Spring 1-1-2015

# Assessment of Anisotropy Effects on the Thermal Volume Change of Unsaturated Bonny Silt Using a Thermo-Hydro-Mechanical True-Triaxial Cell

Mahmud Mousa Shanina
*University of Colorado at Boulder*, mahmud.shanina@colorado.edu

## Recommended Citation

Shanina, Mahmud Mousa, "Assessment of Anisotropy Effects on the Thermal Volume Change of Unsaturated Bonny Silt Using a Thermo-Hydro-Mechanical True-Triaxial Cell" (2015). *Civil Engineering Graduate Theses & Dissertations*. 192.
https://scholar.colorado.edu/cven_gradetds/192

# ASSESSMENT OF ANISOTROPY EFFECTS ON THE THERMAL VOLUME CHANGE OF UNSATURATED BONNY SILT USING A THERMO-HYDRO-MECHANICAL TRUE-TRIAXIAL CELL

By

Mahmud Shanina

M.S., Almergib University - Libya
B.S., Tripoli University - Libya

A thesis submitted to the
Faculty of the Graduate School of the
University of Colorado in partial fulfillment
of the requirement for the degree of
Doctor of Philosophy
Department of Civil, Environmental, and Architectural Engineering
2015

This thesis entitled:

Assessment of Anisotropy Effects on the Thermal Volume Change of Unsaturated Bonny Silt
Using a Thermo-Hydro-Mechanical True-Triaxial Cell

Written by Mahmud Shanina

has been approved by the Department of Civil, Environmental, and Architectural Engineering

_____________________________________________
Professor John McCartney (committee chair)

_____________________________________________
Professor Dobroslav Znidarčić

_____________________________________________
Professor Petros Sideris

_____________________________________________
Professor Nien Y. Chang

_____________________________________________
Dr. Ingrid Tomac

Date_________________

The final copy of this thesis has been examined by the signatories, and we
find that both the content and the form meet the acceptable presentation standards
of scholarly work in the above mentioned discipline.

Mahmud Shanina (Ph.D. Civil Engineering, Department of Civil, Environmental, and Architecture Engineering)

Assessment of Anisotropy Effects on the Thermal Volume Change of Unsaturated Bonny Silt Using a Thermo-Hydro-Mechanical True-Triaxial Cell

Thesis directed by Professor John McCartney

## ABSTRACT

A technique used to improve the energy efficiency of heat pumps for building heating and cooling systems is to embed closed-loop heat exchangers into drilled shaft foundations to form energy foundations. Fluid is circulated through the embedded heat exchangers to transfer heat in the soil surrounding the energy foundations to or from the building. When the soil surrounding the foundations changes temperature, irreversible soil volume changes may occur depending on the soil mineralogy, degree of saturation, and stress state. These volume changes may affect the lateral stress distribution along the energy foundation, and may lead to relative movement between the foundation and surrounding soil. The thermal volume change of the soil has not been considered in design methods that have been developed for energy foundations. Despite the experimental data available on the recoverable and permanent deformations of unsaturated soil during heating and cooling, the impact of thermal deformation of unsaturated soils under anisotropic conditions still needs to be better understood before the design methods can be improved.

This study extends the database of thermal volume change measurement of soils under different conditions by performing several series of thermo-mechanical compression tests on unsaturated, compacted silt specimens using a thermo-hydro-mechanical (THM) true-triaxial cell. The THM true-triaxial cell has the capabilities of being able to control the temperature on all six boundaries of a cubical soil specimen, as well as the suction within the specimen to provide drained conditions during loading or temperature changes. The testing series are focused on understanding the roles of stress-induced anisotropy on the thermal volume change. Six non-isothermal tests were performed, each involving suction application, isotropic consolidation, heating and cooling, and isotropic unloading. Specifically, three tests having different minor to major principal stress ratios of 1.0, 0.7, and 0.5 were performed at a degree of saturation 0.7, and three tests having different stress ratios of 1.0, 0.7, and 0.5 were performed at a degree of saturation of 0.8. Each test required nearly 3 weeks to set up and perform. The results from these tests were compared with each other as well as with results from tests on saturated specimens of the same soil performed in a previous study. Although compressive thermal axial strains were measured in both the major and minor stress directions, a greater thermal axial strain was observed in the direction of major principal stress for stress ratios less than 1.0. This observation is consistent with the previous study on this soil. A small effect of inherent anisotropy due to the compaction process was observed. Specimens with a lower initial degree of saturation were observed to have greater thermal volume changes that specimens closer to saturation, which is proposed to be due to thermal collapse of the air-filled voids during heating. An elasto-plastic model developed for saturated soils under isotropic conditions was modified to consider the effects of anisotropy and variable degrees of saturation, and a good fit was obtained between the measured and predicted results. A discussion of the results from this study indicates that the greater thermal axial strains in the major stress direction may lead to thermal dragdown in normally-consolidated soil layers, with a greater effect in unsaturated soils.

# ACKNOWLEDGEMENT

The author wishes to thank his advisor, Professor John Scott McCartney, for his guidance, assistance, and positive attitude, which helped immensely through the completion of this project. Special recognition is given to Professors Dobroslav Znidarčić, Petros Sideris, Nien Y. Chang, and Dr. Ingrid Tomac for serving on my thesis committee. Deserving of additional thanks for their enthusiasm and assistance are the many geotechnical engineering students and professors at the University of Colorado Boulder, of whom there are far too many to list. A special thanks goes to my wife, and my family, who have inspired me to achieve my goals. Funding from Libyan government and NSF CMMI 1054190 is greatly appreciated.

**Table of Contents**

## List of Tables

## List of Figures

# 1. INTRODUCTION

## 1.1. Motivation

A technique used to improve the energy efficiency of heat pumps for building heating and cooling systems is to embed closed-loop heat exchangers into drilled shaft foundations to form energy foundations (Brandl 2006; Laloui et al. 2006; Adam and Markiewicz 2009; McCartney 2011; McCartney and Murphy 2012; Murphy and McCartney 2015; Murphy et al. 2015). Fluid is circulated through the embedded heat exchangers to transfer heat in the soil surrounding the energy foundations to or from the building. A schematic showing the circulation of fluid from a heat pump to a series of energy foundations beneath a building is presented in Figure 1.1. When the soil surrounding the foundations changes temperature, irreversible soil volume changes may occur depending on the soil mineralogy, degree of saturation, and stress state (Campanella and Mitchell 1968; Demars and Charles 1982; Hueckel and Baldi 1990; Towhata et al. 1993; Burghignoli et al. 2000; Delage et al. 2000; Sultan et al. 2002; Cekerevac and Laloui 2004; Uchaipichat and Khalili 2009). These volume changes (or tendency for volume change) may affect the lateral stress distribution along building foundation, and may lead to relative movement between the foundation and surrounding soil (Vega and McCartney 2014). The thermal volume change of the soil has not been considered in design methods that have been developed for energy foundations, such as that of Knellwolf et al. (2011). Although constitutive models are available to consider the thermal volume change of soils (Hueckel and Pellegrino 1989; Hueckel and Borsetto 1990; Cui et al. 2000; Cekeravac and Laloui 2003; Abuel-Naga et al. 2009), an isotropic stress state is typically assumed, with the same thermal expansion or contraction is expected to occur in both the major principal stress (vertical) and minor principal stress (horizontal) directions when simulating the behavior of soils surrounding energy foundations. Despite the experimental data available on the recoverable and permanent deformations of unsaturated soil during heating and cooling, the impact of thermal deformation of unsaturated soils under anisotropic conditions still needs to be better understood.

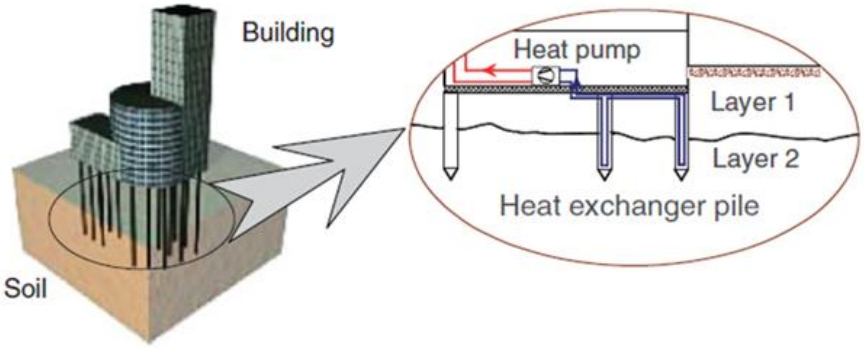

Figure 1.1: Schematic representation of a heat exchanger pile system (Laloui et al. 2006).

Coccia and McCartney (2012) studied the effect of stress-induced anisotropy on thermal volume changes in saturated specimens of compacted Bonny silt using a specially-designed thermo-hydro-mechanical true-triaxial cell. The results from their testing program showed that the stress-induced anisotropy does not have a significant impact on the thermally-induced volumetric strain. However, the initial anisotropic stress state does a significant impact on the magnitude and trend of thermal axial strain in the directions of major and minor principal stresses. Specifically, during heating of anisotropically-consolidated specimens, plastic contraction was observed in the major principal stress direction was observed while less contraction (or even expansion) was observed in the minor principal stress direction, depending on the ratio of the minor to major principal stresses (the stress ratio K). These results indicate that the plastic contraction in the major principal stress direction was proposed to be due to a lower overconsolidation ratio (OCR) as the specimens were loaded to normally-consolidated conditions isotropically then unloaded in the minor principal stress direction. This explanation was proposed as it is in agreement with the trends in the results of thermal volume change of saturated soils having different OCR values presented by Baldi et al. (1988), Towhata et al.

(1993), and Sultan et al. (2002). During cooling, Coccia and McCartney (2012) observed additional contraction for both the axial and volumetric strains, regardless of the initial anisotropic stress states. The volume change behavior during cooling is still not well understood, as other studies such as Hueckel and Baldi (1990) observed a combination of expansion and contraction during cooling.

As only four tests were performed by Coccia and McCartney (2012) on saturated soil specimens, it is clear the more in-depth testing is needed to fully understand the importance of stress-induced anisotropy on the thermal volume change of soils. Coccia and McCartney (2012) identified an issue with their experimental approach in that the intermediate principal stress may not have been representative of plane strain conditions in the intermediate principal stress direction. Accordingly, it is important to implement better control of the principal stresses in future testing with this device. Although Coccia and McCartney (2012) designed their cell with the capability to evaluate unsaturated soils, they only focused on the behavior of saturated soils, which provides an opportunity for further investigations with this device.

## 1.2. Objectives

The objective of this research project is to understand the role of anisotropy on the thermal volume change response of compacted, unsaturated silt. The specific research objectives are as follows:

1. Understand the role of stress-induced anisotropy on the thermally induced volume change of compacted Bonny silt under constant suction conditions.
2. Incorporate the new understanding from this research into a novel constitutive model for the thermal volume change of unsaturated soils under anisotropic stress states.

The objectives will be reached through an experimental testing program and analysis of the results. The improved understanding from these experiments will permit modification and enhancement of available thermal Cam clay-type constitutive models that can be used to describe the response of soils to mechanical loading and heating or cooling in order to reach the second objective.

During heating and cooling, normally consolidated clays may experience changes in volume, which will lead to changes in the apparent preconsolidation stress. Heating of saturated soils typically leads to generation of excess pore water pressure due to the differential expansion between the pore water and soil solids, which may lead to volume change after subsequent drainage. This drainage results in time-dependent, irrecoverable volumetric contraction of the soil as the pore water pressure continues to dissipate for lightly overconsolidated to normally consolidated stress states (Campanella and Mitchell 1968).

A modified true-triaxial cell system shown in Figure 1.2 was developed to achieve the objectives listed above. The modified system will permit incorporation temperature control on each face of the cell, which is an improvement over the approach used by Coccia and McCartney (2012) who only heated two of the six faces. Further, the modified system also permits application of the principal stress in all three orthogonal directions. This permits application of anisotropic stress states to a cubical soil specimen that correspond with the bedding planes associated with compaction of the soil specimen (i.e., major principal stress in the vertical direction orthogonal to the bedding planes and minor principal stresses applied equally in the two horizontal directions parallel to the bedding planes). This approach also permits independent measurement of the principal strains in all three orthogonal directions, which is an improvement over the approach used by Coccia and McCartney (2012).

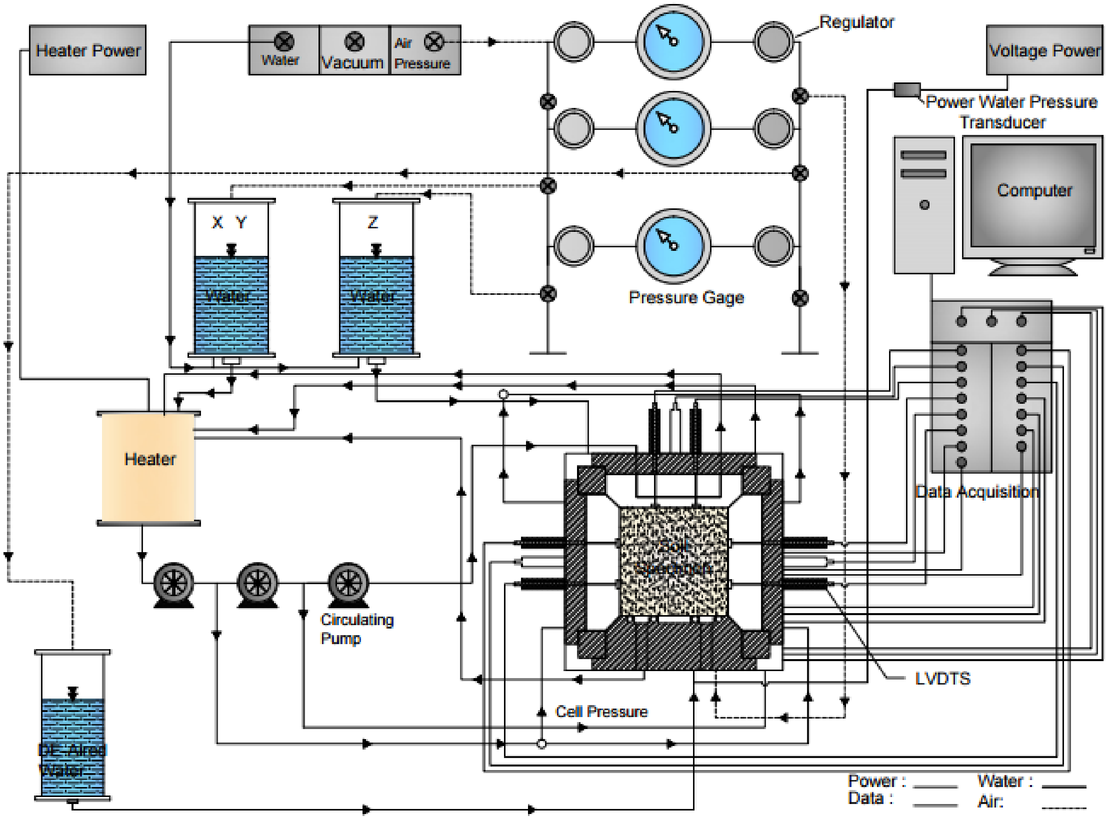

Figure 1.2: Schematic of the modified THM true-triaxial cell with the details of the control systems for temperature, stress, and pore fluid pressures

As shown in the sketch of the true-triaxial cell in Figure 1.2, the bottom face of the specimen is a rigid plate that contains porous disks that independently apply pore air pressure ($u_a$) or water pressures ($u_w$), while the other faces are flexible bladders that apply total principal stresses. The pore water pressures are applied through a high air-entry porous ceramic disk that only allows water to pass until reaching a suction of 100 kPa. The pore air pressures are applied through coarse porous disks that have a very low air entry suction (less than 0.1 kPa). Matric suction in the specimens can either be measured or controlled using the ports at the base of the cell. To measure the matric suction, the air pressure is maintained at atmospheric conditions and the pressure in the water reservoir behind the high air entry ceramic is measured in the same manner as a tensiometer. If a compacted soil is placed atop the ceramic, there will be a tendency to draw water from the stone into the specimen due to the initial suction in the specimen. Alternatively, the suction can be controlled using the axis translation technique (Hilf 1956). In this case, positive pore air and water pressures can be applied independently to the base of the specimen, with a difference ($u_a$ – $u_w$) being equal to the matric suction in the specimen. Although possible, suction control in the configuration of the true-triaxial cell shown in Figure 1.2 is not optimal because water must flow from the bottom face of the specimen to the upper corners of the specimen through capillarity. However, it is possible to measure the suction in the specimen using the tensiometer approach, and then subsequently apply this suction using the axis translation technique, which avoids the need to wait for complicated water flow processes before applying thermo-mechanical loads to the specimen.

## 1.3. Approach

This study extends the database of thermal volume change measurement of soils under different conditions by performing several series of thermo-mechanical compression tests on unsaturated, compacted silt specimens using a thermo-hydro-mechanical (THM) true-triaxial cell. The THM true-triaxial cell has capabilities to control the temperature at the boundaries of the specimen, and has the capability to control the suction in the specimen using the axis translation technique (Hilf 1956). The testing series are focused toward understanding the roles of stress-induced anisotropy on the thermal volume change. Six non-isothermal tests were performed, each involving suction application, isotropic consolidation, heating and cooling, and isotropic unloading. Three tests will be performed on the unsaturated compacted Bonny silt at low constant suction with an initial degree of saturation 0.7, and the other three tests will be performed with low constant suction and degree of saturation 0.8. The improved understanding gained from these experiments will permit modification and enhancement of available thermal Cam Clay-type constitutive models for saturated soils under isotropic conditions such as those of

Hueckel and Pellegrino (1989), Hueckel and Borsetto (1990), Hueckel and Pellegrino (1994), Cui et al. (2000), Laloui and Cekeravac (2003) or Abuel-Naga et al. (2009) that can be used to describe the response of soils to mechanical loading and heating or cooling.

## 1.4. Scope

Relevant background related to the thermal volume change of saturated and unsaturated soils is presented in Chapter 2, including both a literature review as well as a theoretical background section. Particular emphasis is placed on the effect of temperature on fundamental soil properties, thermal volume change behavior, and the impact of anisotropy on the thermal volume changes in saturated soils. The literature review also includes a discussion on the role of the effective stress state in unsaturated soils. The theoretical background section includes a review of a discussion on suction control in unsaturated soils and thermo-elasto-plastic constitutive models that have been used for saturated soils. A preliminary modification to these models to account for the impact of stress-induced anisotropy by Coccia (2011) is also presented.

The properties of the soil used in this study, Bonny silt, are described in Chapter 3. The relevant parameters presented include the grain size distribution, specific gravity, Atterberg limits, and compression behavior using conventional oedometer testing. This chapter also includes details of the procedures used to prepare the cubical soil specimens. The experimental setup developed to evaluate the role of stress-induced anisotropy on the thermal response of unsaturated soils is presented in Chapter 4. Specifically, the details of the updated thermo-hydro-mechanical (THM) true-triaxial cell are presented, including the stress control system and the suction control system. This chapter includes a description of the instrumentation and data acquisition system used in this study, along with the development of the mechanical and thermal machine deflection curves for the THM true-triaxial cell are also presented in this chapter. An outline of the tests performed along with an explanation of the experimental procedures are described in Chapter 5. The experimental results from the true-triaxial cell testing are presented in Chapter 6, which includes results from tests on unsaturated specimens having two different initial degrees of saturation under non-isothermal conditions and isotropic and anisotropic stress states. The analysis of results from the experimental tests is presented in Chapter 7, which includes a synthesis of the results along with the development of an elasto-plastic model to predict the effects of stress induced anisotropy and unsaturated conditions on the thermal volume change of soils. A discussion on the implications of thermal volume change on the behavior of an energy foundation and how the analysis developed in this study can be incorporated into a finite element model are presented in Chapter 8. The conclusions drawn from this work are presented in Chapter 9.

# 2. BACKGROUND

## 2.1 Theoretical Background

### *2.1.1 Suction Control in Unsaturated Soils under Low Suction Magnitudes*

Difficulties arise in testing unsaturated soils that may exhibit negative pore water pressures approaching -1 atm (i.e., -101.3 kPa gage or zero absolute pressure). Water in the measuring system may begin to cavitate as the pore water pressures approaches -1 atm. To avoid the cavitation of an unsaturated soil specimen, the axis translation technique is used to translate the pore water pressure ($u_w$) and air pressure ($u_a$) to positive value in the soil specimen. Hilf (1956) proposed the axis-translation technique for evaluating total stress and pore-air pressure to increase pore-water pressure for preventing cavitation during the drainage process. This technique provides a method of measuring pore-water pressure in a laboratory test without altering soil structure so that it has been widely used to control matric suction of unsaturated soil (Bishop 1959; Matyas and Radhakrishna 1968; Fredlund and Morgenstern 1977; Wheeler and Sivakumar 1995; Hoyos and Macari 2001; Delage et al. 2008). Figure 2.1 illustrates the application of the technique to an unsaturated soil specimen undergoing the matric suction of 101 kPa. The pore water pressure ($u_w$) is measured below, a saturated high air entry ceramic disk with an air entry value of 202 kPa. The water phase of the specimen is originally under 101 kPa tension. An air pressure of 202 kPa is then applied directly to the specimen in order to increase the pore air pressure ($u_a$) to the same magnitude. As a result, the pore water pressure ($u_w$) is increased by an equal amount, with a final positive of 101 kPa. Under these conditions, there is no problem associated with the cavitation of the water in the measuring system. Despite the translation of reference pore air pressure ($u_a$) from 0 to 202 kPa, the matric suction experienced by the soil, $\psi = (u_a - u_w)$, remains constant at 101 kPa.

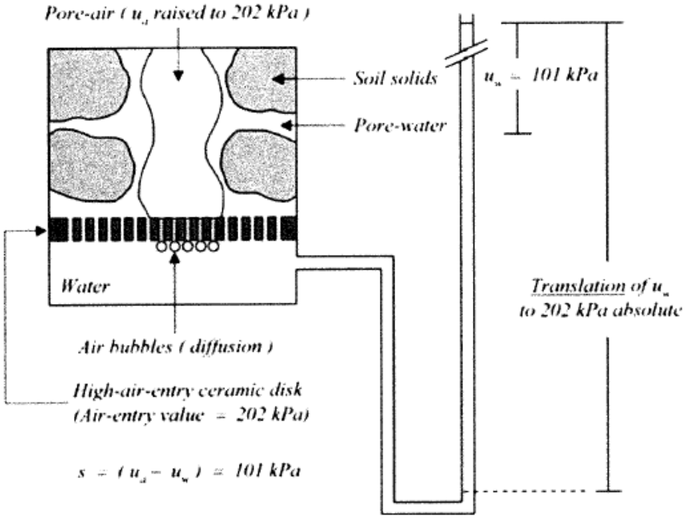

Figure 2.1: Basic concept of the axis translation technique (from Hoyos and Macari 2001).

### *2.1.2 Effective Stress State in Unsaturated Soils*

In nature, pavement subgrades and shallow foundation soils above the ground water table may be subject to three-dimensional stress gradients attributable to changes in the stress state variables ($\sigma_{ij}$ - $u_a$ $\delta_{ij}$) and ($u_a - u_w$)$\delta_{ij}$ as illustrated in Figure 2.2. A relationship for the effective stress in unsaturated soils, which incorporates an effective stress parameter $\chi$ to account for soil-specific material behavior, has been formulated by Bishop (1959), as follows:

$$\sigma' = \sigma_n + \chi\psi \tag{2.1}$$

where $\sigma'$ is the mean effective stress; $\sigma_n$ is the mean net stress (equal to the difference between the mean total stress $\sigma$ and the pore air pressure $u_a$, $\sigma_n = (\sigma - u_a)$; $\psi$ is the matric suction (equal to the difference between the pore air pressure $u_a$ and the pore water pressure $u_w$, $\psi = u_a - u_w$ , and $\chi$ is the effective stress parameter.

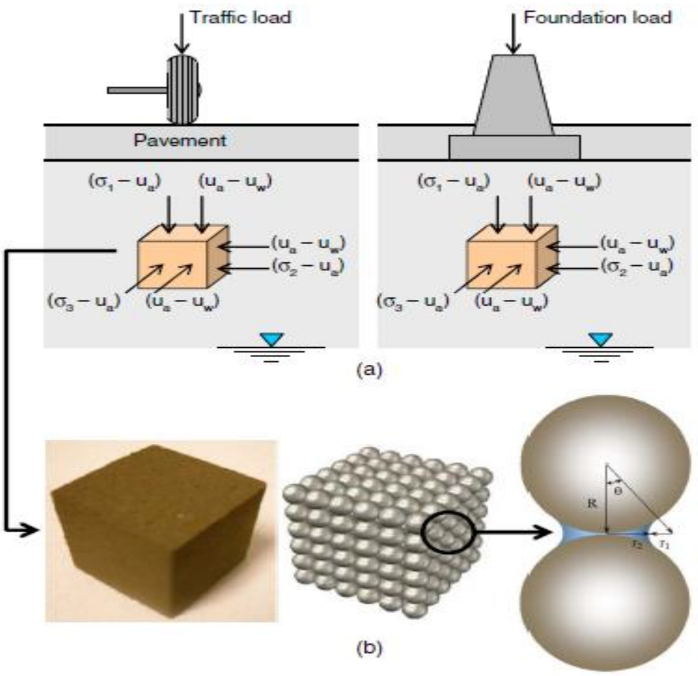

Figure 2.2: Unsaturated soil system: (a) multi-axial stress states; (b) idealized cubical soil samples (Hoyos et al. 2012).

Several approaches have been developed (Vanapalli et al. 1996; Khalili and Khabbaz 1998; Gallipoli et al. 2003; Wheeler et al. 2003; Tamagnini 2004; Nuth and Laloui 2008; Lu and Likos 2006; Lu et al. 2010; Khalili and Zargarbashi 2010) to define the effective stress parameter $\chi$. Bishop (1959) proposed the value of stress parameters $\chi = S_r$, where $S_r$ is the degree of saturation. This approach has the advantage of being simple, but Khalili and Zargarbashi 2010 found that it may not be suitable for characterizing the effective stress during hydraulic hysteresis. Another approach used by Lu et al. (2010) is to assume that $\chi = S_e$, where $S_e$ is equal to the effective saturation ($S_e = \frac{(S_r - S_{r,res})}{(1 - S_{r,res})}$, where $S_{r,res}$ is the residual degree of saturation). The main advantage of this approach is that the parameters of the van Genuchten (1980) soil-water retention curve (SWRC) model can be incorporated into the definition of the effective stress (Alsherif and McCartney 2015).

Khalili and Khabbaz (1998) and Khalili et al. (2004) defined the effective stress parameter as a function of the air entry suction, as follows:

$$\chi = \begin{cases} 1 & for \quad \dfrac{S}{S_e} \le 1 \\ \left(\dfrac{S}{S_e}\right)^{-\Omega} & for \quad \dfrac{S}{S_e} \ge 1 \end{cases} \tag{2.2}$$

where $S_e$ is the suction value marking the transition between saturated and unsaturated states, and $\Omega$ is the material parameter with a best fit-value of 0.55 (Khalili and Khabbaz 1998). For the wetting path $S_e = S_{ex}$, and for the drying path $S_e = S_{ae}$ in which $S_{ex,}$ is the air expulsion value and $S_{ae}$ is the air entry value.

Lu and Likos (2006) proposed an empirical approach to determine the suction stress characteristic curve (SSCC) that relates the suction stress $\sigma_s$ with the suction or degree of saturation in the soil. They defined the SSCC using shear strength failure envelopes defined from drained shear strength tests performed on unsaturated soil specimens under controlled values of matric suction, as shown in Figure 2.3. Specifically, the failure envelopes were extrapolated to the normal stress axis in order to define the suction stress for a particular value of matric suction. As such, the suction stress can be calculated based on the apparent cohesion, c′, and friction angle, $\phi'$, shown below:

$$\sigma_s = c' / \tan(\phi') \tag{2.3}$$

In this approach, the apparent cohesion for saturated soil tested under drained conditions is assumed to be zero. It is also assumed that the friction angle does not change when different suction values are applied to the soil. These assumptions were made in to order correctly define the SSCC. In theory, this assumption is valid only for the case of rigid soils that do not change in volume during changes in matric suction. The validity of the assumption of a constant effective friction angle for both saturated and unsaturated soils has been validated in the literature (Uchaipichat and Khalili 2009).

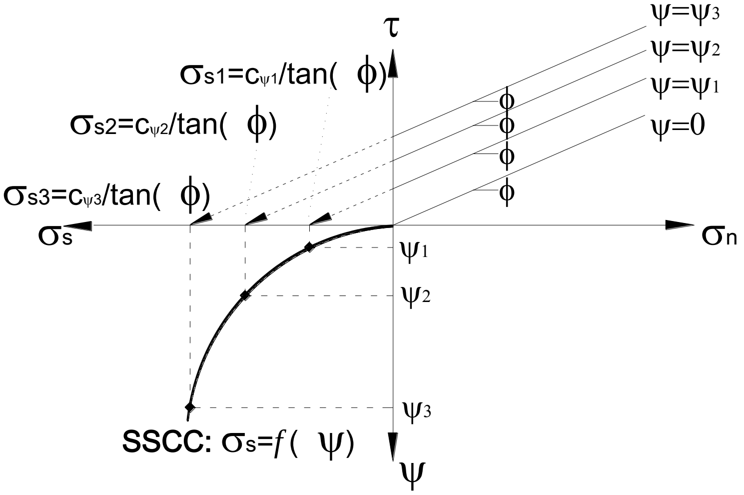

Figure 2.3: Definition of the suction stress versus matric suction relationships using shear strength failure envelopes (after Lu and Likos 2006).

A closed-form equation for the suction stress was proposed by Lu et al. (2010) for the full range of matric suction by employing effective saturation as the effective stress parameter χ. As mentioned, this permits integration of the van Genuchten (1980) SWRC into the definition of the suction stress, as follows:

$$\sigma_s = -\frac{u_a - u_w}{\left(1 + (\alpha(u_a - u_w))^n\right)^{\frac{n-1}{n}}} \tag{2.4}$$

$$\sigma_s = u_a - u_w \geq 0$$

where n and α are empirical fitting parameters, with α being the inverse of air entry pressure for saturated soil and n being the pore size distribution parameter. By substituting Equation 2.4 into Equation 2.1, the effective stress for unsaturated soil can be defined as:

$$\sigma' = (\sigma - u_a) + \frac{u_a - u_w}{\left(1 + (\alpha(u_a - u_w))^n\right)^{\frac{n-1}{n}}} \tag{2.5}$$

### 2.1.3 Elasto-Plasticity Concepts for Saturated Soils

Consolidation is defined as the time rate of volume change of a soil specimen due to a change in effective stress. If the volume of soil solids in soil specimen remains constant, the contraction in volume of the specimen is equal to the decrease in the volume of voids of the specimen. Considering undrained saturated soils, a change in total stress will lead to an identical increase of excess pore water pressure, constituting a hydraulic gradient within the specimen. After this, water will flow from the soil at a rate depending on the hydraulic conductivity.

This study involves an investigation in the impact of temperature on the compression curve, which in this study is expressed as the relationship between the specific volume ν and the mean effective stress. The specific volume, ν, is defined as follows:

$$e = 1 + \nu \tag{2.6}$$

while the mean effective stress p' is defined as follows:

$$p' = \frac{\sigma'_1 + \sigma'_2 + \sigma'_3}{3} \tag{2.7}$$

In this study, the mean effective stress will be calculated using the suction-stress concept as presented in Equation 2.1, so the most of the relationships used in the modified Cam-Clay model are applicable for unsaturated soils. The relationship between p' and ν is typically assumed to be linear when plotted in against the natural logarithm of p', and the slope of the relationship depends on the stress history of the soil. The break in the curve is related to the maximum applied mean effective stress experienced by the soil before undergoing plastic compression, and is referred to as the preconsolidation stress, $p'_c$. The indications that stress state must be reached in order for the soil to exhibit irrecoverable plastic deformations are shown by utilizing preconsolidation stress as a yield limit. In critical state soil mechanics, this process is referred to as yielding. For effective stresses applied higher than preconsolidation stress, the soil will exhibit a softened behavior which undergoes both elastic and plastic strain. For stresses applied lower than the preconsolidation stress, the soil will maintain a stiff and elastic behavior. The compression plane diagram of the ln(p') vs specific volume ν is presented in Figure 2.4. The behavior is characterized by the normal compression line (ncl) and unloading-reloading line (url).

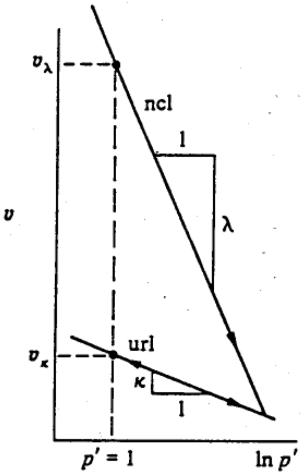

Figure 2.4: Normal compression line (ncl) and unloading-reloading line (url) in (lnp'ν) compression plane.

The equation for the normal compression line (ncl) takes following form:

$$v = v_\lambda - \lambda \ln(p') \tag{2.8}$$

where λ is the slope of the ncl and $\nu_\lambda$ is the intercept of the line at p' = 1 kPa. Similarly, the equation of the unloading-reloading (url) line takes the following form:

$$v = v_k - k \ln(p') \tag{2.9}$$

where κ is the slope of the url and $\nu_k$ is the intercept of the line at p' = 1 kPa. The incremental elastic and plastic volumetric strains due to a change in mean effective stress can be calculated using the parameters λ and κ. Considering a change in mean effective stress from $p'_A$ to $p'_C$, as shown in Figure 2.5, the resulting decrease in specific volume can be calculated as follows:

$$\delta v^e = v_c - v_a \tag{2.10}$$

This can be simplified as follows:

$$\delta v^e = -\kappa\left[\ln p'_c - \ln p'_a\right] \tag{2.11}$$

Assuming that the change in mean effective stress is small, this can be simplified as follows:

$$\delta v^e = -\kappa \frac{\delta p'}{p_a'} \tag{2.12}$$

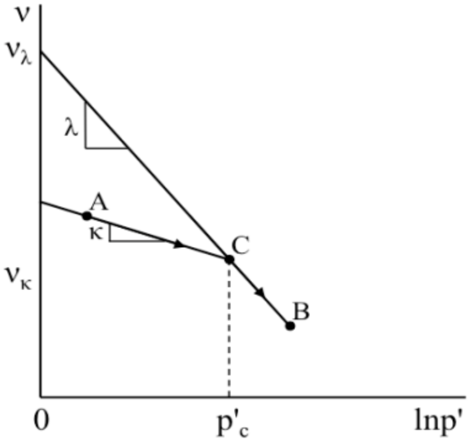

Figure 2.5: Stress path in the ln(p'):ν space

To interpret Equation 2.12 in terms of incremental elastic volumetric strain, the relationship between incremental changes in specific volume and volumetric strain is established:

$$\frac{\delta v^e}{v} = \frac{\delta v_T^e / VS}{VT / VS} = \frac{\delta v_T^e}{VT} = -\delta\varepsilon_v^e \tag{2.13}$$

By substituting Equation 2.12 into Equation 2.13, the incremental elastic volumetric strain due to a change in mean effective stress can be calculated:

$$\delta\varepsilon_v^e = \frac{\kappa}{v}\frac{\delta p'}{p'} \tag{2.14}$$

Finally, writing Equation 2.14 in terms of the elastic bulk modulus, K:

$$\delta\varepsilon_v^e = \frac{\delta p'}{K} \tag{2.15}$$

This equation implies that the elastic bulk modulus is a function of the mean effective stress and void ratio, as follows:

$$K = \frac{vp'}{\kappa} \tag{2.16}$$

Considering the impact of changes in void ratio is assumed to be much smaller than that of changes in mean effective stress (Wood 1990), K can be written as a function of mean effective stress:

$$K(p') = K_{ref}\left(\frac{p'}{p'_{ref}}\right)^n \tag{2.17}$$

where $K_{ref}$ is a reference elastic bulk modulus measured at a reference mean effective stress, $p'_{ref}$, and n is a material parameter defining the change in K due to changes in p′.

For an increase in mean effective stress exceeding the preconsolidation pressure, the soil will undergo both an elastic and plastic volumetric strain response governed by the slope of the (ncl), λ, as follows:

$$\delta\varepsilon_v = \delta\varepsilon_v^e + \delta\varepsilon_v^p \tag{2.18}$$

The incremental total strain (elastic plus plastic) due to an increase in mean effective stress exceeding the preconsolidation pressure is determined to be:

$$\delta\varepsilon_v = \frac{\lambda}{v}\frac{\delta p'}{p'} \tag{2.19}$$

Solving for $\delta\varepsilon_v^p$, the incremental plastic volumetric strain may be defined as follows:

$$\delta\varepsilon_v^p = \frac{(\lambda - \kappa)}{v}\frac{\delta p'}{p'_c} \tag{2.20}$$

By defining the plastic compressibility modulus, *β*, as follows:

$$\beta = \frac{v}{\lambda - \kappa} \tag{2.21}$$

Equation 2.21 can be simplified if re-written in terms of β:

$$\delta\varepsilon_v^p = \frac{1}{\beta}\frac{\delta p'}{p'_c} \tag{2.22}$$

### 2.1.4 Preliminary Modification of Cui et al. (2000) Equations to Account for Stress Anisotropy

Coccia (2011) modified the Cui et al. (2000) equations to account for stress anisotropy. The Cui et al. (2000) equation is presented in Equation 2.23. The thermo-mechanical model by Cui et al. (2000) was developed to define the elastic and plastic volumetric strain of a triaxial specimen due to both mechanical and thermal loading. Four tests were performed to study the effect of anisotropy on the thermal volume changes of saturated soil (Coccia 2011). The results indicated that no effect is observed on the thermal volumetric strain, on the other hand the stress-induced anisotropy was observed to influence the thermal axial strains of specimen during heating. Accordingly, a modification to the Cui et al. (2000) model was used to capture the thermal axial strain characteristics of soil specimen during heating under stress-induced anisotropy conditions. Cui et al. (2000) assumed that the incremental thermal volumetric strain was the sum of the incremental elastic thermal volumetric strain and the incremental plastic thermal volumetric strain as follows:

$$d\varepsilon_{vT} = d\varepsilon_{vT}^e + d\varepsilon_{vT}^P \tag{2.23}$$

The increment in elastic thermal volumetric strain for a heated specimen is defined as follows:

$$d\varepsilon_{vT}^{e} = a_2 dT \tag{2.24}$$

where the parameter $\alpha_2$ is the drained coefficient of thermal expansion of a soil obtained from a cooling test performed at slow rate. The sign of $\alpha_2$ is negative so that expansive strains are predicted during heating. An empirical equation to predict the increment in plastic thermal volumetric strain was defined by Cui et al. (2000) as follows:

$$d\varepsilon_{vT}^{p} = \alpha_p \left[ \exp\left(\alpha_p \Delta T\right) - a \right] dT \tag{2.25}$$

where $\alpha_p$ is a parameter that depends on the overconsolidation ratio, and a is a fitting parameter (Coccia 2011).

As no effect of stress anisotropy on the magnitude of thermal volumetric strains was observed in the experimental results of Coccia and McCartney (2012), modifications were be made to the existing equations by breaking the thermal volumetric component into its x, y and z-axial components, as follows:

$$\varepsilon_{vT} = \varepsilon_{xT} + \varepsilon_{yT} + \varepsilon_{zT} - (\varepsilon_{xT}\varepsilon_{yT} + \varepsilon_{xT}\varepsilon_{zT} + \varepsilon_{yT}\varepsilon_{zT}) - \varepsilon_{xT}\varepsilon_{yT}\varepsilon_{zT} \tag{2.26}$$

The multiplication of strains is assumed to be near zero and therefore may be canceled out of Equation 2.26. In addition, due to the plain strain configuration of the thermo-hydro-mechanical cubical cell, zero total strain is encountered in the *z*-direction; therefore all thermal axial components in the *z*-direction may be canceled. Applying these assumptions to Equation 2.27 gives:

$$\varepsilon_{vT} = \varepsilon_{xT} + \varepsilon_{yT} \tag{2.27}$$

By dividing both sides of Equation 2.27 by $\varepsilon_{xT}$, the following expression is obtained:

$$\varepsilon_{vT} / \varepsilon_{xT} = (\varepsilon_{xT} + \varepsilon_{yT}) / \varepsilon_{xT} \tag{2.28}$$

The thermal axial strain ratio Ω was defined as follows:

$$\Omega = \varepsilon_{yT} / \varepsilon_{xT} \tag{2.29}$$

which allows Equation 2.28 to be simplified as follows:

$$\varepsilon_{vT} / \varepsilon_{xT} = 1 + \Omega \tag{2.30}$$

The value of $\varepsilon_{xT}$ becomes:

$$\varepsilon_{xT} = \frac{\varepsilon_{vT}}{(1+\Omega)} \tag{2.31}$$

This equation can be written differential form as follows:

$$d\varepsilon_{xT} = \frac{d\varepsilon_{vT}}{(1+\Omega)} \tag{2.32}$$

By substituting Equation 2.27 in Equation 2.31, the following equation is obtained:

$$d\varepsilon_{xT} = \frac{(d\varepsilon_{vT}^{e} + d\varepsilon_{vT}^{p})}{(1+\Omega)} \tag{2.33}$$

Substituting the equation for the elastic and plastic volumetric strains from the model of Cui et al. (2000) into Equation 2.33 permits the thermal axial strain in the major stress direction to be defined as follows:

$$d\varepsilon_{xT} = \frac{1}{(1+\Omega)}(\alpha_2 dT + \alpha_p(\exp(\alpha_p \Delta T) - a)dT) \tag{2.34}$$

Similarly, the thermal axial strain in the minor stress direction can be defined as follows:

$$d\varepsilon_{yT} = \frac{\Omega}{(1+\Omega)}(\alpha_2 dT + \alpha_p(\exp(\alpha_p \Delta T) - a)dT) \tag{2.35}$$

## 2.2 Literature Review

### *2.2.1 Thermal Effects on the Index Properties of Soils*

Early research on the effects of temperature on soil behavior focused on changes in the compaction behavior, index properties (such as the liquid limit and plastic limit), and specific gravity with temperature. Hogentogler (1936) investigated the effect of temperature on the compaction of soil with high clay content. He conducted laboratory compaction tests on several predominantly clay soils and reported that the maximum dry unit weight increased and the optimum gravimetric water content decreased with increasing temperature. Youssef et al. (1961) performed a series of tests on compacted clay samples and concluded that heating caused a decrease in both the liquid and plastic limits at temperatures ranging from 14 and 35°C. Comparable tests were performed by Lagurous (1969) on kaolinite, illite, monmorillonitic and monmorillonitic-illite clays at temperatures ranging from 1.7 to 40.6 °C, who concluded that the effects of temperature were most significant for monmorillonitic clays. Wang et al. (1990) observed there were no thermal effects on the Atterberg limits over temperatures ranging from 20 to 400 °C for kaolinite and 20 to 500 °C for bentonite. They also noticed that the specific gravity of kaolinite and bentonite did not change with temperature in the range of 20 to 400 °C. Towhata et al. (1993) reported that there was no significant impact of preheating up to 200 °C on the liquid and plastic limits of the kaolin and bentonite clay.

### *2.2.2 Effects of Temperature on the Compression Index*

Several studies have evaluated the impact of temperature on the shape of the compression curve of saturated soils (Campanella and Mitchell 1968; Eriksson 1989; Boudali et al. 1994; Cekerevac and Laloui 2004; Uchaipichat and Khalili 2009). A general conclusion from these studies is that temperature does not have a significant impact on the compression index, $C_c$ for most soils. The results for $C_c$ values obtained from 1D compression tests on different soils at different initial temperatures is summarized in Figure 2.6. Because these soils were loaded mechanically under a constant initial temperature, they do not reflect the impact of thermal volume change, which is the change in volume of soils due to a change in temperature. Although researchers have not necessarily focused on the effect of temperature on the unloading-reloading curve, it is also assumed that temperature has no effect on the recompression index $C_r$.

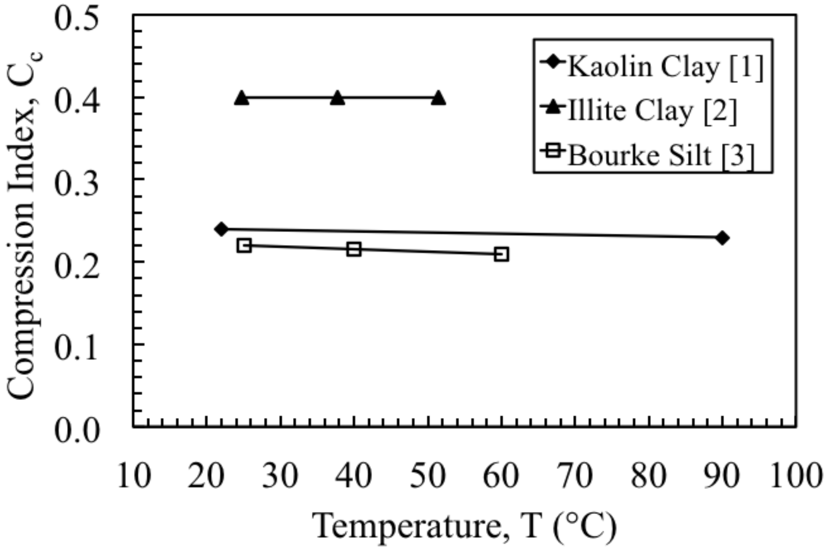

Figure 2.6: Influence of temperature on the compression index ([1] Cekerevac and Laloui 2004; [2] Campanella and Mitchell 1968; [3] Uchaipichat and Khalili 2009)

### *2.2.3 Effects of Temperature on the Preconsolidation Stress*

Although temperature does not have a significant impact on the shape of the compression curve measured under isothermal conditions, other studies have observed that heating a soil under a given stress state then applying an increase in stress will lead to a change in the preconsolidation stress. Tidfors and Sällfors (1989) performed conventional incremental oedometer tests as well as constant rate of strain to study the effect the temperature on the preconsolidation stress. The results from tests on a clay specimen showed that the preconsolidation stress clearly decreases with increasing temperature as illustrated in Figure 2.7. Tidfors and Sällfors (1989) and Boudali et al. (2004) observed a linear decrease in preconsolidation stress with temperature.

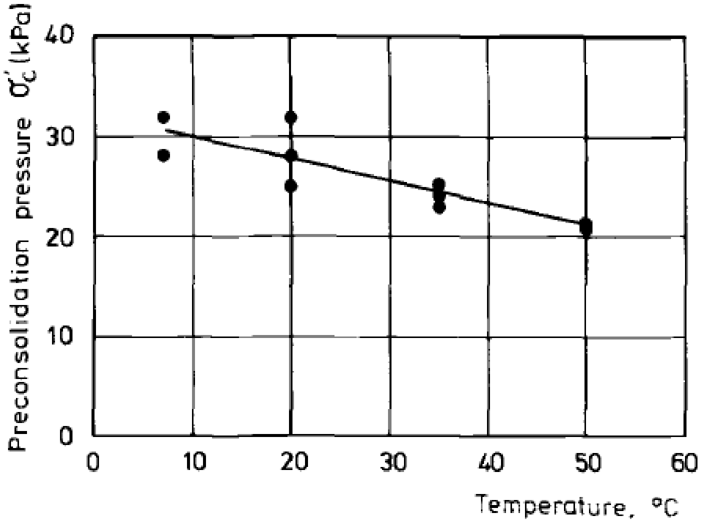

Figure 2.7: Preconsolidation stress as a function of test temperature (Tidfors and Sällfors 1989).

Isothermal oedometer tests at various temperatures were conducted on a sample of intact Lulea clay with a plasticity index of 60 by Eriksson (1989). The results from this study are shown in Figure 2.8, and indicate that the preconsolidation pressure decreased nonlinearly with increasing temperature unlike the results from Tidfors and Sällfors (1989) and Boudali et al. (2004). The results of Eriksson (1989) are in agreement with those of Cekerevac and Laloui (2004) and François and Laloui (2008a).

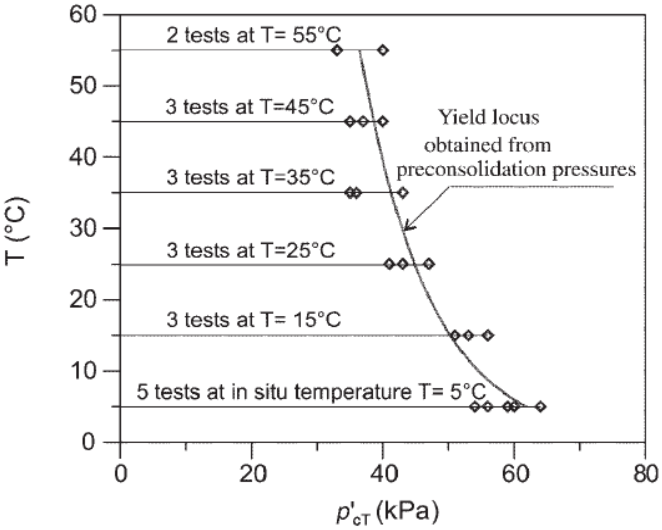

Figure 2.8: Change in preconsolidation stress $p'_c$ with temperature (Cui et al. 2000)

The trend of a decrease in preconsolidation stress with a change in temperature is not observed in all studies. Sultan (1997) loaded a sample of Boom clay to normally consolidated conditions at a constant temperature of 20 °C and then heated the sample to 70 °C. Following heating, the sample was loaded until a normally consolidated state was again achieved. An increase in preconsolidation stress from 0.8 to 1.12 MPa was observed due to heating, indicating a potential “overconsolidation” effect induced by heating. That because when the Boom clay heated under the first loading, the partial collapse of the soil structure occurred, which turn in decrease the void ratio and the soil becomes more stiff before second load was again achieved. Similar results were found by Plum and Esrig (1969) and Towhata et al. (1993).

### *2.2.4 Effect of Temperature on the Soil Water Retention Curve*

The effect of temperature on the SWRC of compacted unsaturated soils has been investigated in several studies. Early studies in the area of soil physics by Grant and Salehzadeh (1996) and She and Sleep (1998) observed that an increase in temperature leads to a decrease in degree of saturation for a given suction. A shift in the SWRC to lower degrees of saturation for elevated temperatures was also observed in the studies that involved control of the stress state and measurement of volume change as shown in Figure 2.9, including Romero et al. (2001), Salager et al. (2007), and Uchaipichat and Khalili (2009) for low suction values. The decrease in degree of saturation was from the reduction in surface tension of water with increasing temperature, which in turn reduces the air entry value as temperature increases. Also the soil-water characteristic is observed independent of stress level by Uchaipichat and Khalili (2009).

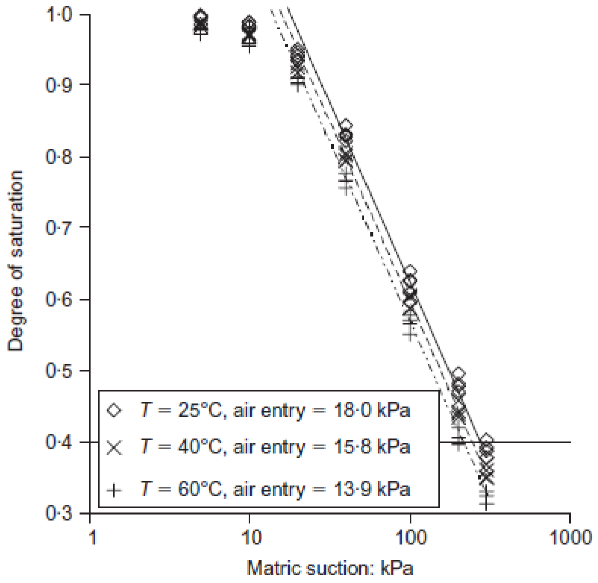

Figure 2.9: Shift in the SWRC with increasing temperature (Uchaipichat and Khalili 2009).

### *2.2.5 Effect of Overconsolidation Ratio on the Thermal Volume Change*

The previous studies have observed that the overconsolidation ratio to have a significant effect on the thermal volume change of a soil specimen when heated under a constant net stress. Soils with larger overconsolidation ratio values trend to expand during heating while soils with lower OCR values trend to contracted behavior. Cekerevac and Laloui (2004) performed heating tests on Kaolinite clay between 22 and 90 °C at different overconsolidation ratios using a temperature-controlled triaxial cell. The results data in Figure 2.10 shows that the thermally induced volumetric strain with temperature for different OCR values. Thermal contraction was observed for lower OCR values of 1.0, 1.5, and 2.0 while thermal expansion followed by contraction was measured for specimens at higher values of OCR of values 6.0 and 12.0. It may be deduced from Figure 2.10 that the magnitude of initial thermal expansion increases with increasing OCR. This impact of stress state on thermal volume change is in agreement with other authors (Plum and Esrig 1969; Baldi et al. 1988; Graham et al. 2001; Towhata et al. 1993; Sultan et al. 2002; Abuel-Naga et al. 2007).

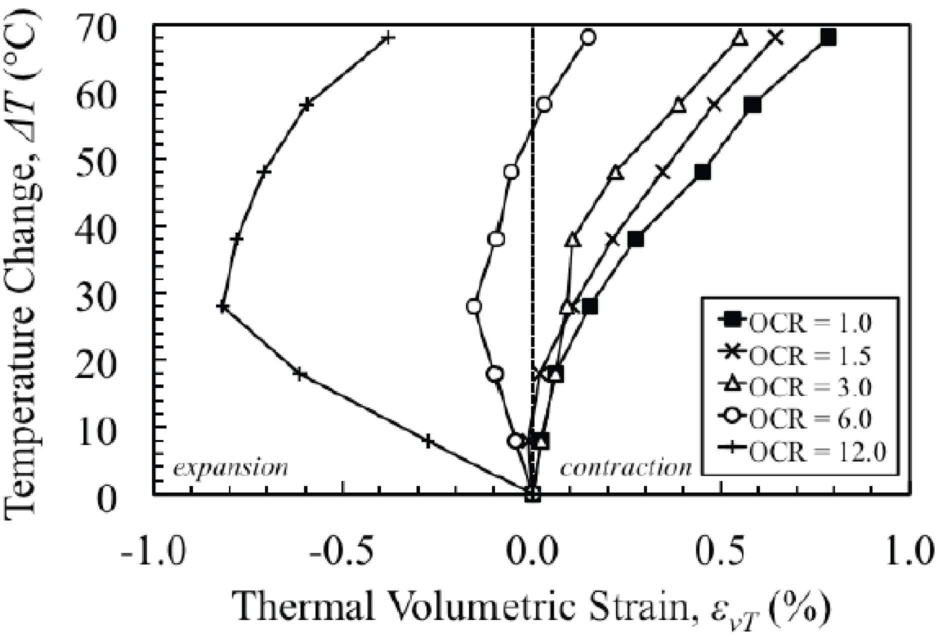

Figure 2.10:Thermal volumetric strain versus temperature during heating of a Kaolin clay (Cekerevac and Laloui 2004).

### *2.2.6 Impact of Anisotropy on the Thermal Volume Changes of Saturated Soils*

Hueckel and Pellegrini (1996) studied the thermo-mechanical anisotropy of clays. Two deep clays, Belgian Boom clay and Spanish clay, were tested during mechanical and thermo-mechanical loading. The results exhibited pronounced strain anisotropy both during mechanical loading as well as during heating and cooling at constant stresses in drained conditions. In the mechanical loading test, vertical strain was larger than the horizontal one. During heating, the vertical strain was larger than the horizontal one within the elastic region; however, the opposite was observed in the elasto-plastic range. This behavior is presented in Figure 2.11.

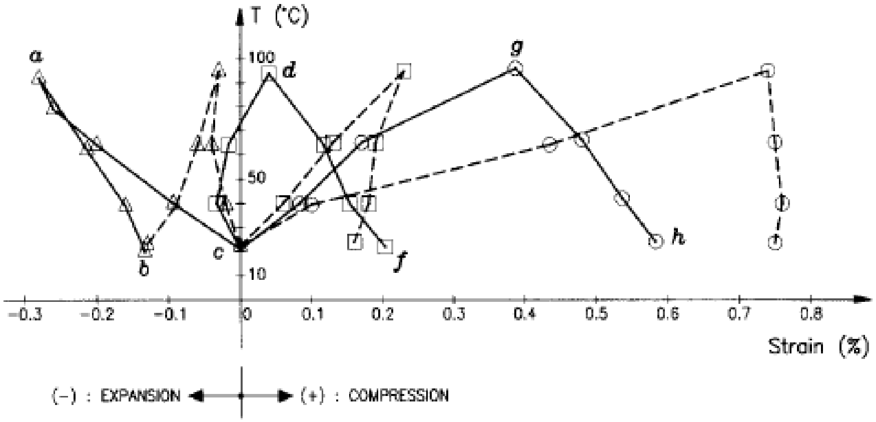

Figure 2.11: Drained heating test on Boom clay; axial strain versus temperature at three different confining stresses; vertical strain solid line Δ 1MPa; □ 3MPa; O 6 MPa and lateral strain dash line Δ 1MPa; □ 3MPa; O 6 MPa.

Coccia and McCartney (2011) evaluated the impact of stress induced anisotropy on thermally induced volume chances of saturated soil. The result showed that the anisotropic stress states may lead to thermal expansion and contraction in different directions in the same soil specimen. For saturated Bonny silt, expansion was observed in the direction of greater overconsolidation ratio (lower stress), while contraction was observed in the direction of lower overconsolidation ratio (greater stress) as shown in Figure 2.12.

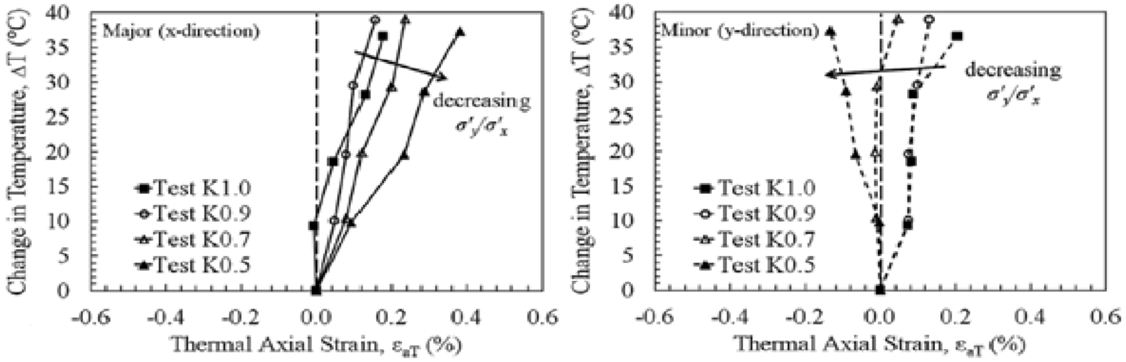

(a) (b)

Figure 2.12: Thermal axial strain during heating of saturated Bonny silt with different anisotropic stress ratios K (Coccia and McCartney 2012): (a) Major stress direction; (b) Minor stress direction.

When examined from a volumetric perspective, contractile volumetric strains were observed in all four tests, regardless of the initial stress state, as shown in Figure 2.13. This is an important observation as it indicates that the constitutive models for isotropic soils may provide useful results from a volumetric response, and may be easily adapted to account for stress induced anisotropy.

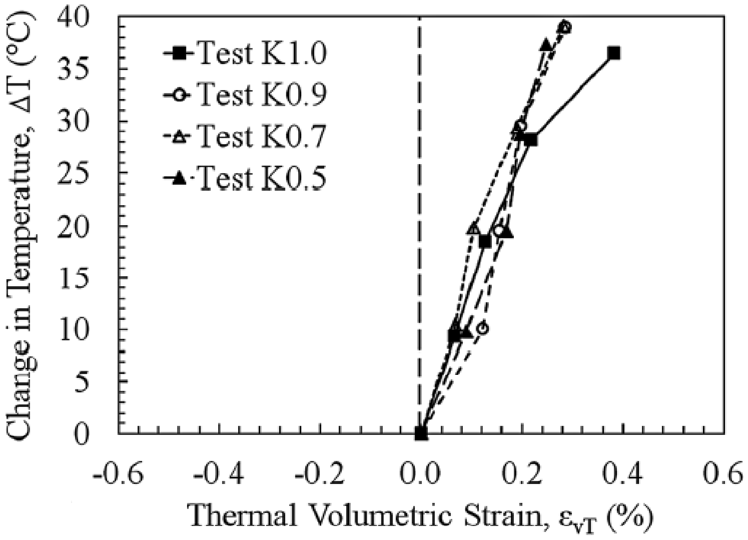

Figure 2.13: Thermal volumetric strain during heating of saturated Bonny silt with different anisotropic stress ratios K (Coccia and McCartney 2012)

### *2.2.7 Effect of Temperature on Volume Change Behavior of Unsaturated Soils*

The effect of temperature on the volume change behavior of unsaturated soils has been evaluated in several studies (Romero et al. 2003; Francois et al. 2007; Salager et al. 2008; Tang et al. 2008; Uchaipichat and Khalili 2009; McCartney 2012; Alsherif and McCartney 2015). Romero et al. (2003) studied the effect of suction and temperature on volumetric Boom clay samples. These tests were performed using an oedometer apparatus with simultaneous control of suction and temperature. Suction up to 0.45 MPa and temperature up to 80 °C were applied. The isothermal wetting drying tests were carried out at two constant temperatures of 22 and 80 °C and a constant vertical net stress 0.026 MPa. The results from these tests indicated that the specimens expanded at lower suction and higher temperature. However, the expansion and water content of the specimens decreased as suction increased and temperature decreased. Tang et al. (2008) investigated an unsaturated compacted bentonite specimen by performing thermo-mechanical tests following a wetting path from an initial suction of 110 MPa to a target suction of 9 MPa under constant confining stress. The results shown in Figure 2.14 indicate that the unsaturated compacted bentonite specimens expanded during heating at low confining stress; but contracted during heating at high confining stress

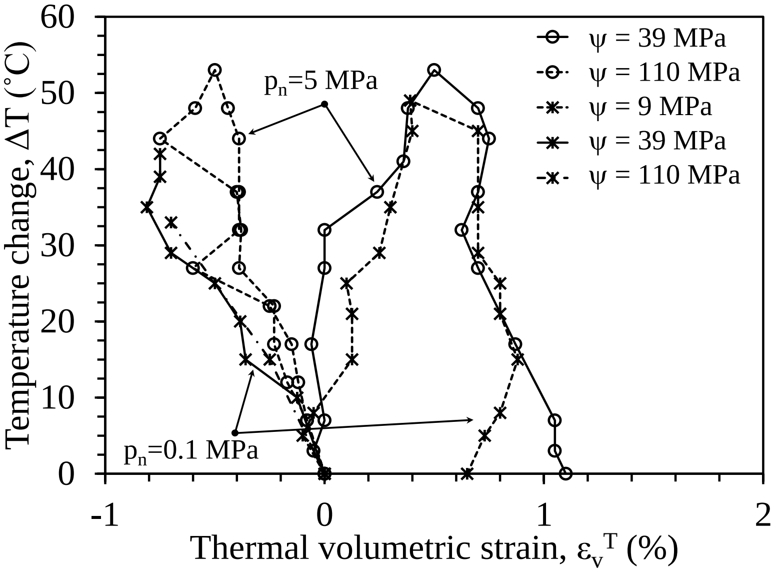

Figure 2.14: Thermal volumetric strain versus temperature during heating (Tang 2008).

Uchipichat and Khalili (2009) studied the effect of the thermal volume change of normally consolidated and over consolidated soils. In this study they performed a total of three thermal loading and unloading tests at constant matric suction. Temperatures used in the experiments ranged from 25 to 60 °C. The objective in these tests was to investigate the volume change due to the changes in temperature. Prior to each test, the temperature of the sample was set at 25°C under an isotropic net stress of 50 kPa. The water temperature in the triaxial cell was then increased from 25 to 60 °C and lowered to 25 °C under constant suction and constant net stress. After completion of the first cycle of thermal loading and unloading, the samples were loaded to isotropic net stresses of 100, 150 and 200 kPa, and the cyclic thermal loading and unloading was repeated for each of the net stresses. The tests results showed the dilation occurred with low net stress of 50 kPa and was recovered during cooling. However, the tendency to dilation reduced with increasing net stress of 150 and 200 kPa. They observed from tests results that the dilation occurred in the overconsolidated samples at low net stress of 50 kPa, but contraction occurred at lower overconsolidation ratio. The results are presented in Figure 2.15.

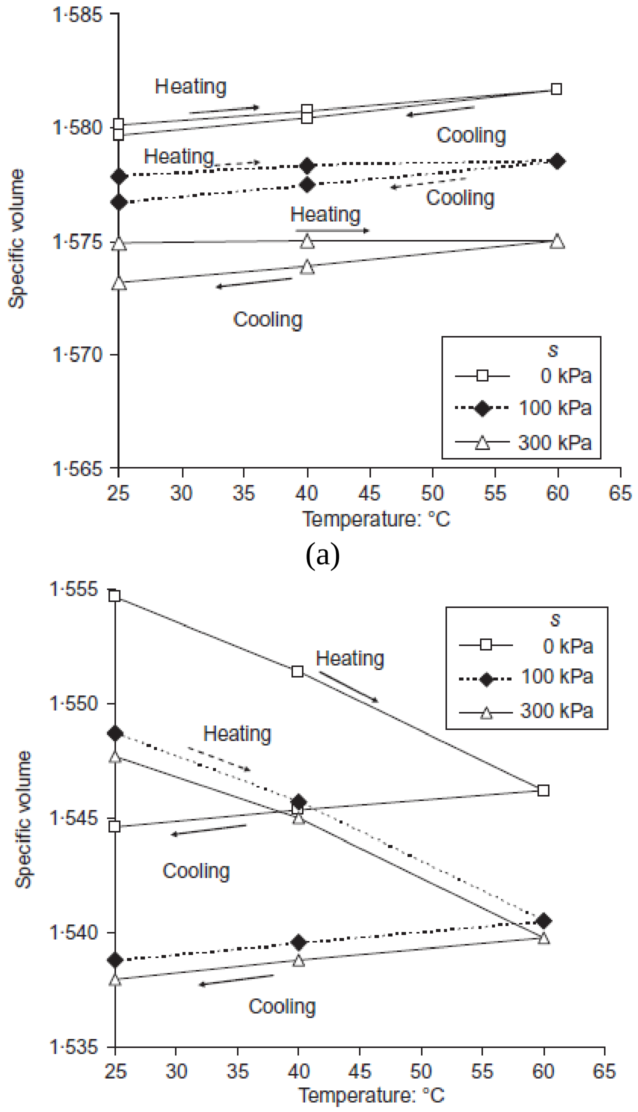

(a)

(b)

Figure 2.15: Specific volume against temperature at different matric suction with net stress values of (Uchaipichat and Khalili 2009): (a) 50kPa; (b) 200 kPa.

### *2.2.8 Effect of Suction on Volume Change Behavior of Unsaturated Soils*

Most studies on the thermal effects on the behavior of unsaturated soils have involved heating under constant suction values. Lloret et al. (2003) studied the effect of different values of matric suction (0, 4, 14, 127 and 500MPa) on the compacted bentonite. The test was performed using a suction-controlled oedometer capable of applying high suctions and large vertical loads. Results showed that the stiffness of the soil is reduced slightly as the suction applied during loading increases. The most noticeable effect of suction is the shifting of the point at which there is a change in the slope of these lines, indicated by a vertical arrow. In the framework of elasto-plasticity, this change is interpreted as the crossing of a yield surface, and the load at which it takes place can be considered as an apparent preconsolidation pressure as shown in Figure 2.16.

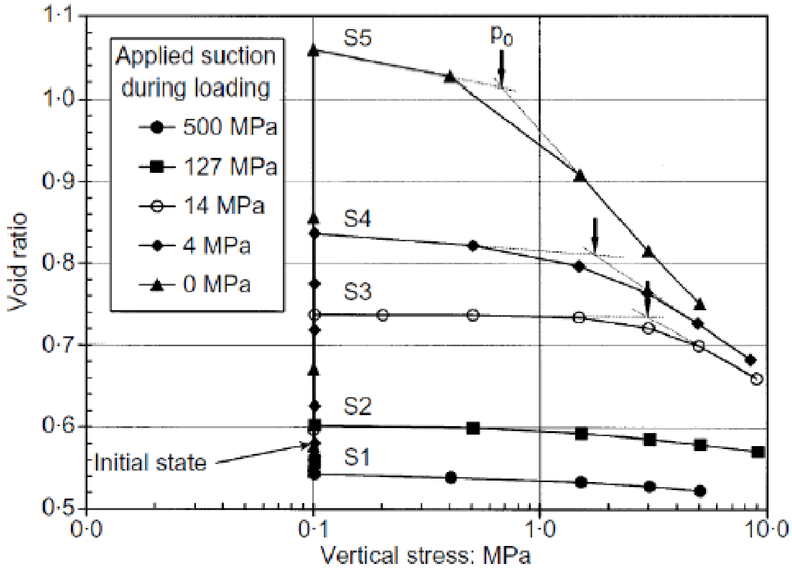

Figure 2.16: Variation of void for compacted bentonite during the initial stage of suction variation and subsequent loading (Lloret et al. 2003).

Uchaipichat (2010) performed a series of suction-controlled shear tests on specimens under different values of suctions and isotropic loading using the modified triaxial equipment for testing unsaturated soils. The results from these tests are presented as compression curves in Figure 2.17. These curves, which are presented in terms of void ratio versus logarithm of effective stress, show that the slope of the normal compression lines (λ) and the slope of the unloading lines (κ) are independent of matric suction. Javadi (2012) also investigated the effect of suction on the compressibility of unsaturated soils by performing controlled-suction isotropic loading tests in a triaxial device and observed similar results.

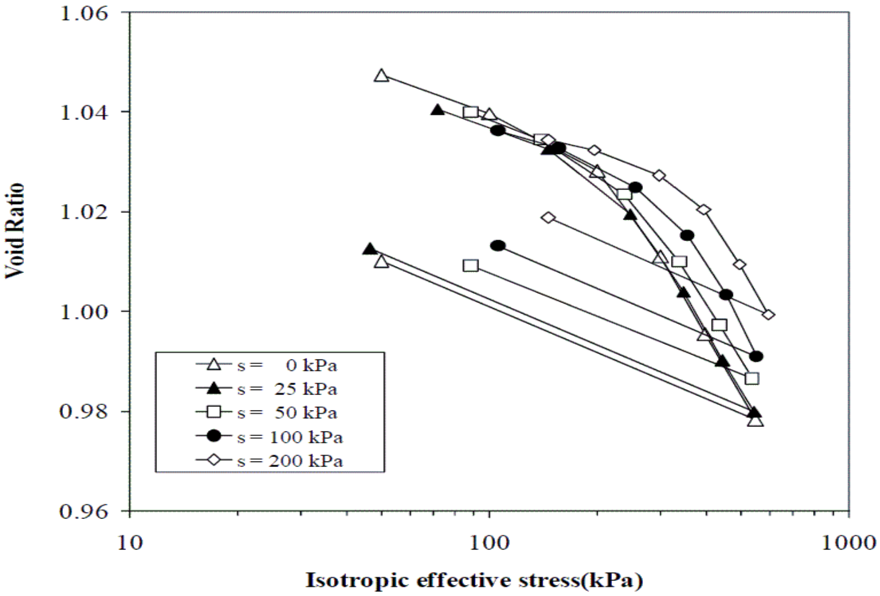

Figure 2.17: Compression curves for unsaturated soil (Uchaipichat 2010).

# 3. MATERIALS

## 3.1 Soil Properties

### *3.1.1 Overview*

Silt obtained from the Bonny dam, located near the Colorado and Kansas border in Yuma County and referred to as Bonny silt, was used in this experimental study. This soil has been characterized in several previous experimental studies at the University of Colorado at Boulder. This chapter summarizes the various physical properties of Bonny silt, including its particle-size distribution, Atterberg limits, and specific gravity. Further, the compaction curve, compression properties, and thermal conductivity ranges for Bonny silt are presented at the end of the chapter.

### *3.1.2 Grain Size Analysis*

The distribution of particle size longer than 75 μm was determined using a sieve analysis, while all particles smaller than 75 μm were determined using a hydrometer. This particle size distribution of the soil was obtained in accordance with ASTM D422.

**Table 3.1 Grain-size distribution properties of Bonny silt.**

| Parameter | Value |
|---|---|
| $D_{10}$ | ‹0.0013 mm |
| $D_{30}$ | 0.022 mm |
| $D_{50}$ | 0.039 mm |
| %Passing No.200 sieve | 83.9% |
| %Clay size | 14% |
| %Silt size | 69.9% |
| % Sand size | 16.1% |

### *3.1.3 Specific Gravity*

In soils, specific gravity (SG) refers to the mass of solid matter of a given soil sample as compared to an equal volume of water. The SG indicates how much heavier/lighter a material is than water. The SG of solids for Bonny silt was measured using a water pycnometer in accordance with ASTM D854, and was found to be 2.63. The unit weight of water used corresponds to de-aired distilled water at room temperature.

### *3.1.4 Atterberg Limits*

The liquid and plastic limits of the soil are 25 and 21, respectively, measured in accordance with ASTM D4318. Because the fines content is greater than 50% and the plasticity index is 4, Bonny silt is classified as ML (inorganic low plasticity silt) according to the Unified Soil Classification System (ASTM D 2487). An activity of 0.29 indicates that Bonny silt does not contain a significant amount of active clay minerals.

### *3.1.5 Compaction Curve*

A standard compaction test ASTM 698 and the modified Proctor compaction test ASTM D1557 were performed on Bonny silt to define the relationship between compaction water content and dry unit weight for different compaction energies. The compaction curves a long with the zero air void (ZAV) line and the initial conditions are shown in Figure 3.1. The maximum dry unit weights of the silt are 16.6 and 19.1 kN/m$^3$ for specimens compacted using the standard and modified Proctor compaction efforts, respectively. The optimum water content for the standard Proctor effort is approximately 14%, while that for the modified Proctor effort is approximately 11%. The initial conditions for the soil specimens in this study are listed in Table 3.2. The initial compaction points for the specimens are also shown in Figure 3.1.

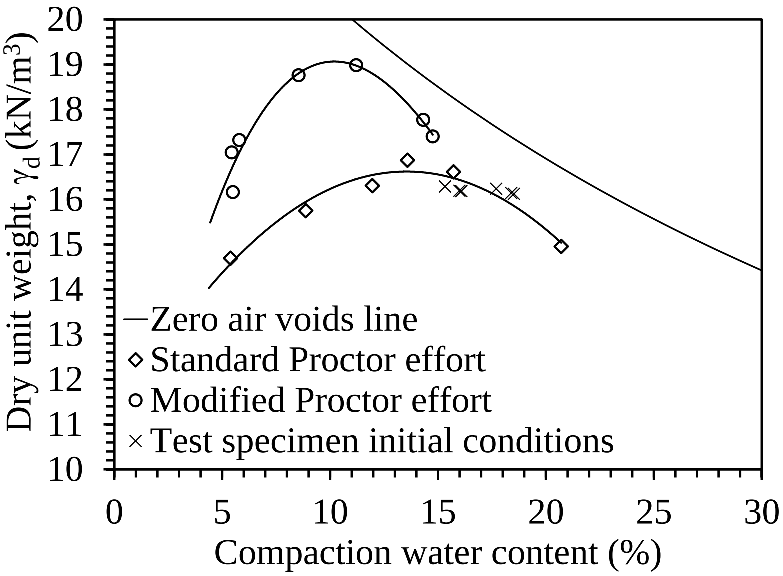

Figure 3.1: Compaction curves for Bonny silt along with initial conditions for the soil specimens evaluated in this study.

Table 3.2: Initial conditions of the soil specimens evaluated in this study.

| Test | Stress ratio, $K = \sigma_y/\sigma_z$ | Gravimetric water content, w (%) | Total density, $\rho_t$ (kg/m$^3$) | Dry density, $\rho_d$ (kg/m$^3$) | Initial void ratio | Initial degree of saturation, $S_r$ | Measured initial suction (kPa) |
|---|---|---|---|---|---|---|---|
| K1.0-S0.7 | 1.00 | 16.08 | 1915 | 1650 | 0.594 | 0.712 | 20.0 |
| K0.7-S0.7 | 0.70 | 15.32 | 1915 | 1661 | 0.584 | 0.690 | 20.0 |
| K0.5-S0.7 | 0.50 | 15.99 | 1915 | 1651 | 0.593 | 0.709 | 20.0 |
| K1.0-S0.8 | 1.00 | 18.52 | 1948 | 1644 | 0.600 | 0.812 | 10.0 |
| K0.7-S0.8 | 0.70 | 18.39 | 1948 | 1646 | 0.598 | 0.808 | 10.0 |
| K0.5-S0.8 | 0.50 | 17.70 | 1948 | 1655 | 0.589 | 0.790 | 10.0 |

The initial suction in the specimens within the cell was measured using the tensiometer technique. An example of the initial suction measurement for one of the $S_r = 0.7$ specimens is shown in Figure 3.2(a). The van Genuchten (1980) SWRC for Bonny silt inferred from tests performed by Khosravi and McCartney (2012) that incorporate the axis translation technique is shown in Figure 3.2(b). The specimens tested by Khosravi and McCartney have an initial void ratio of 0.6, which is similar to that evaluated in this study. The initial suction values measured for the different specimens using the tensiometer technique are also shown in this figure, which are consistent with the SWRC. It should be noted that the SWRC for compacted specimens likely changes with the compaction water content used in the tests, so that SWRC shown here is only shown for guidance purposes.

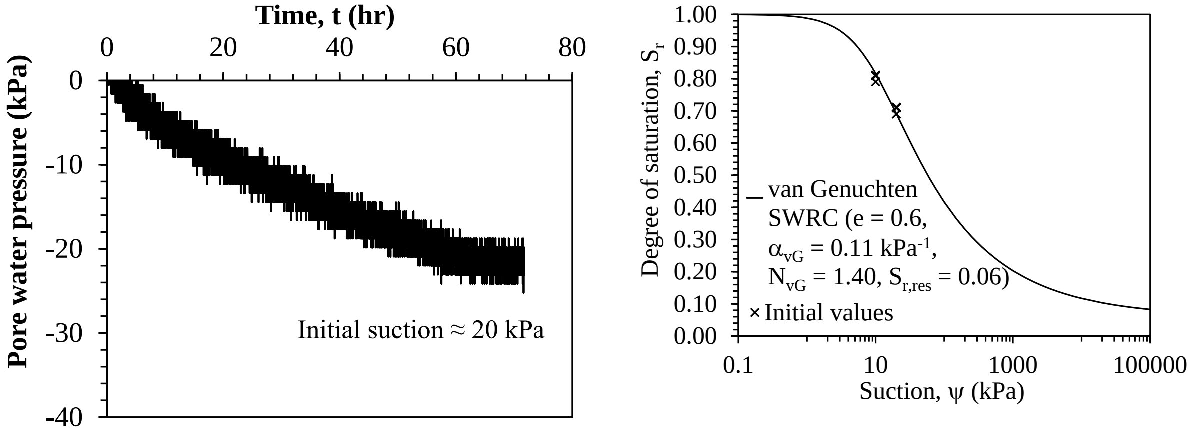

(a) (b)

Figure 3.2: (a) Example of initial suction measurement; (b) SWRC for Bonny silt along with the initial degrees of saturation and initial suctions for the compacted soil specimens.

### *3.1.6 Compression Characteristics of Saturated Specimens*

The compression properties of a saturated specimen of compacted Bonny silt were measured using an oedometer test, with loading increments applied until reaching the end of primary consolidation at each stress level. The compression curve with the compression indices and apparent preconsolidation stress are shown in Figure 3.3.

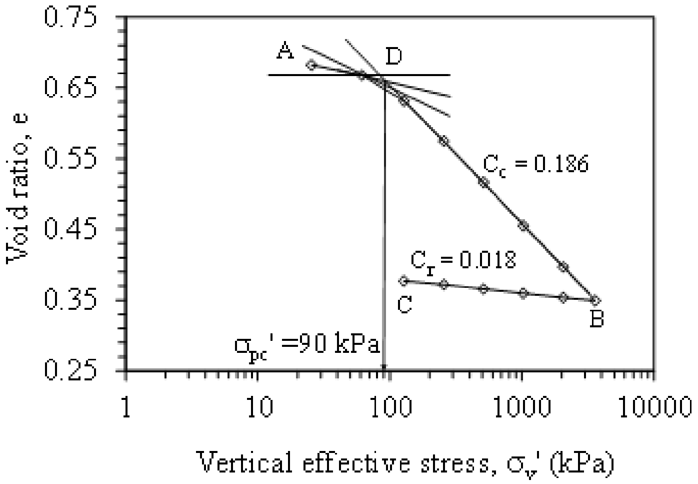

Figure 3.3: Compression curve for saturated Bonny silt measured in an oedometer.

### 3.1.7 Thermal Properties

The thermal conductivity tests were performed using a thermal needle on compacted silt specimen, using the methodology described by McCartney et al. (2013). This test permits assessment of the thermal conductivity of soil as a function of void ratio using a triaxial cell modified to permit a thermal needle to probe to be inserted into the soil specimen through the top platen. The thermal conductivity of Bonny silt was measured after consolidation of specimen to different void ratios. The result indicated that the thermal conductivity ranges from 1.37 to 1.47 W/mK for void ratios of 0.59 to 0.52. The change in thermal conductivity corresponding to the change in void ratio is shown in Figure 3.4.

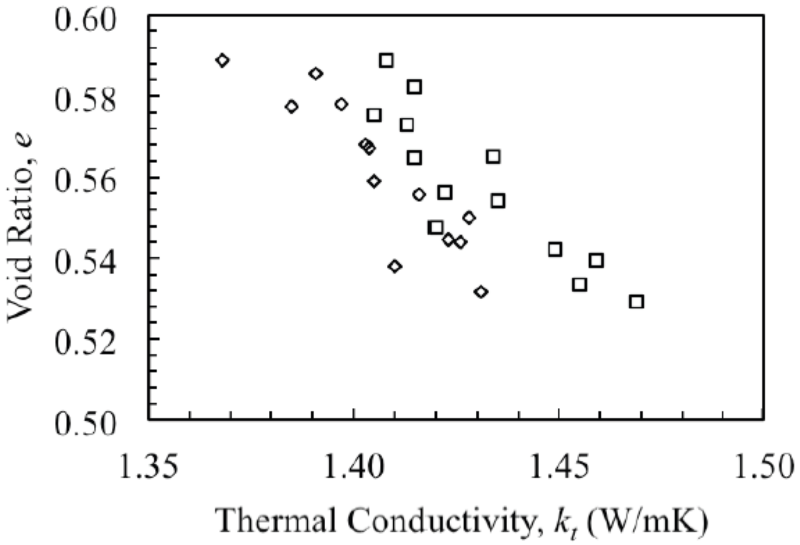

Figure 3.4: Relationship between thermal conductivity and void ratio.

### 3.2 Soil Preparation Procedures

All cubical soil specimens were prepared using static compaction to reach the same initial dry density of 1660 kg/m³, which corresponds to an initial void ratio of 0.53. This dry density corresponds with about 90% of the maximum dry density from the standard Proctor compaction curve as shown in Figure 3.1. The target gravimetric water content values investigated in this study were 15.5 and 17.5%, which correspond to initial degrees of saturation of 70% and 80%, respectively. Before compaction, the soil was mixed with water until the target gravimetric water content was reached. It was then sealed within a five-gallon bucket for 24 hours to allow the water content to homogenize within the soil. A mechanical press was next used to compress the specimen in six lifts of equal height within a 178 mm cubical aluminum mold, this cubical aluminum mold is presented in Figure 3.5.

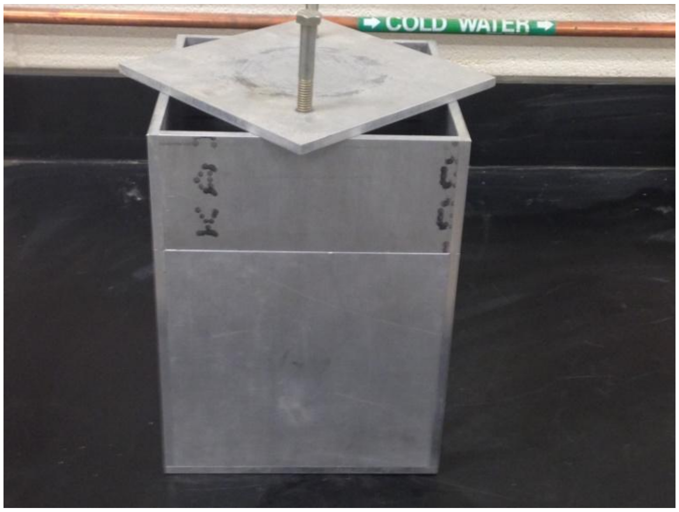

Figure 3.5: Cubical aluminum mold.

The under-compaction technique was used to ensure uniform compaction of each lift and to avoid over compaction of the underlying lifts as the upper lifts were compacted (Ladd 1978). The top of each compacted lift was scarified to minimize any potentially weak planes within the cubical specimen, as shown in Figure 3.6(a). To remove the specimen from the mold, the specimen was first pushed from the mold using the press before removing the side walls so that removal of the walls does not pull on the surfaces of the specimen. The specimen after removal of the walls is shown in Figure 3.6(b). The compacted specimen was covered immediately with plastic to avoid changes in the degree of saturation while the rest of the components of the cubical cell were being assembled, as shown in Figure 3.6(c).

(a) (b) (c)

Figure 3.6: Cubical specimen of Bonny silt after compaction: (a) Compacted lift scarified; (b) Soil specimen; (c) Soil specimen wrapped in plastic.

# 4. EXPERIMENTAL SET-UP AND EQUIPMENT

## 4.1. Thermo-Hydro-Mechanical (THM) True-Triaxial Device

This study involves characterization of the impact of stress-induced anisotropy on the thermal volume changes in compacted soils using a thermo-hydro-mechanical (THM) true-triaxial device. The device is capable of accommodating a cubical soil specimen with a side length of 178 mm, and can apply principal stresses to the faces of the cube in stress-controlled conditions. A photograph of the system is shown in Figure 4.1.

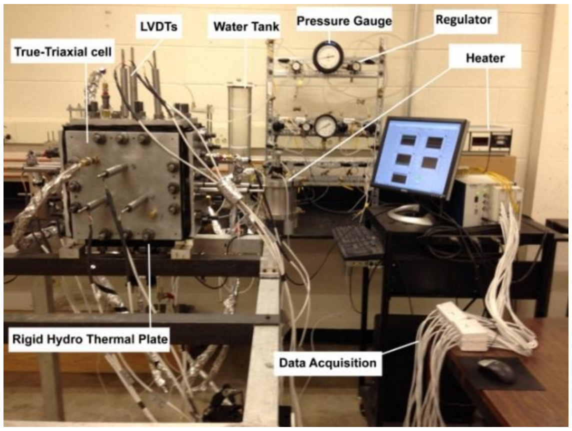

Figure 4.1: Photo of the overall THM true-triaxial cell system.

The true-triaxial cell was originally developed by Mould (1983) and subsequently modified by Takata (2000). In its typical configuration, this cell uses six flexible latex bladders to apply principal stresses to the faces of the soil specimen, following the approach outlined by Ko and Scott (1967). The deformations of each face of the cubical cell are measured using spring-loaded linearly variable differential transformers (LVDTs).

The cell was adapted for thermo-hydro-mechanical testing by replacing the top (and/or bottom) faces of the cell with rigid face plates by Coccia and McCartney (2012) similar to the approach of Macari and Hoyos (2001), Hoyos et al. (2008), and Hoyos et al. (2012). These rigid face plates incorporate heating elements to control temperature and hydraulic ports to control pore water pressure and pore air pressure. These rigid face plates are referred to as hydro-thermal face plates.

Different than the setup used by Coccia and McCartney (2012), five flexible latex bladders were used to apply principal stresses to the faces of the cubical soil specimen, and one rigid face was used to control the suction. This configuration permits application of stresses and measurement of corresponding deformations of the unsaturated soil specimen in the x, y and z directions. Coccia and McCartney (2012) were only able to measure the soil deformation in the x and y directions, and plane strain conditions were assumed in the z direction. However, plane strain conditions cannot be applied when the system is heated, as the cell will likely expand in the z direction during both loading and heating. Further, Coccia and McCartney (2012) only controlled the temperature at the top and bottom of the cubical specimen, and used air to pressurize the bladders. This required long times to reach thermal equilibrium. In order to provide a more uniform change in temperature to the faces of the cubical specimen, the temperatures were applied using the rigid face as well as by circulating heated water through the pressurized bladders. A schematic showing the approach used to apply stresses and temperatures to the cubical specimen is shown in Figure 4.2.

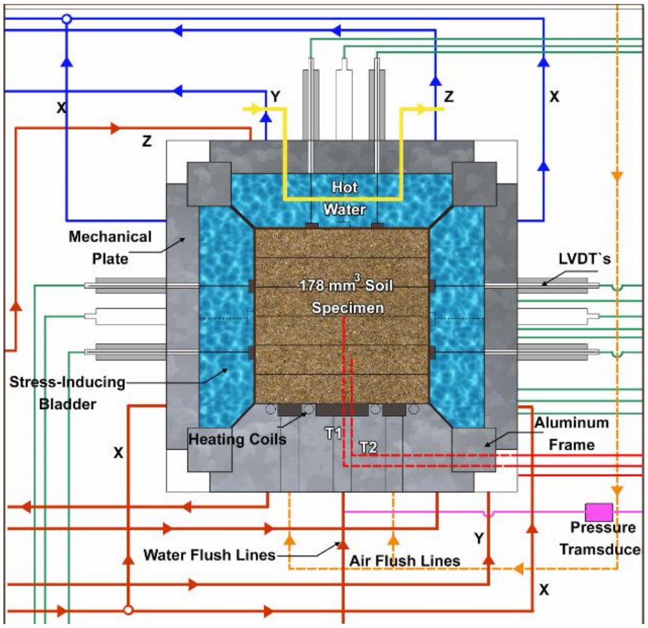

Figure 4.2: Hydro-thermal bottom face plate and side bladders filled by pressurized hot water with soil specimen.

## 4.2 Mechanical Loading System

An aluminum space frame acts as the core of the true-triaxial cell. The space frame is shown in Figure 4.3. Latex rubber bladders are placed within the space frame, and a reaction wall is placed on top of each bladder to form pressurized chambers between the reaction wall and the bladder that can be used to apply principal stresses to the soil specimen within the space frame. Rubber sheets were used to improve the hydraulic seals between the reaction walls and the space frame, as shown in Figure 4.4.

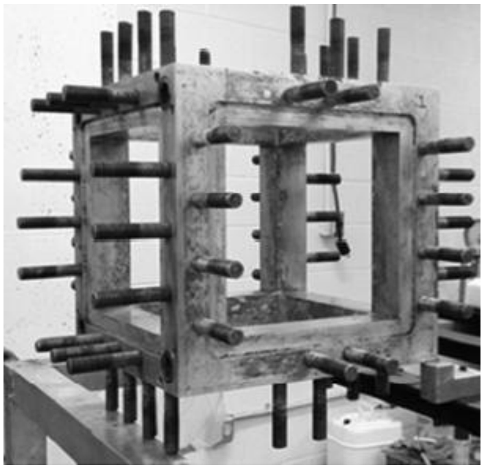

Figure 4.3: Photo of aluminum space frame core of the true-triaxial cell.

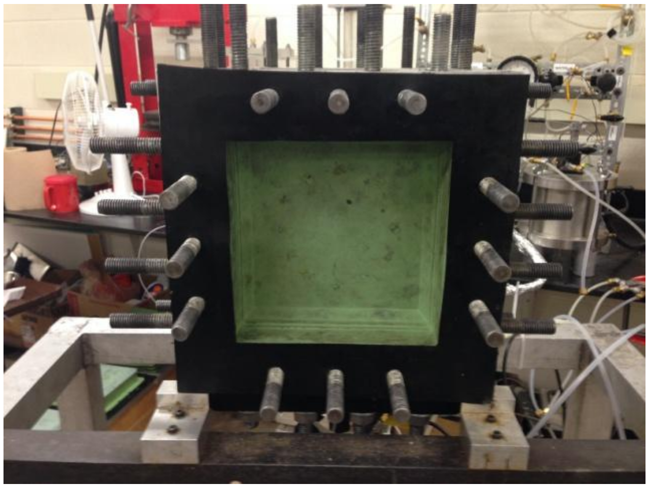

Figure 4.4: Photo of aluminum frame core of the true-triaxial cell with rubber sheet and bladder.

The sides of the bladders are configured so that they are thinner than the face of the bladder, with the goal of having the bladders deform toward the specimen as uniformly as possible. As mentioned, water is used to pressurize the bladders. The pressurized water is heated to the same temperature applied to the base of the specimen, which helps ensure the uniformity of temperature on all sides of the specimen. This was a modification from the approach used by Coccia and McCartney (2012) so that thermal equilibrium could be reached in a faster time period. The axial stresses are applied to the x and y-faces using pressurized reservoirs with embedded heat exchange coils. The pressure in the upper z-face was applied independently from x and y-axis. However, in order to apply the same temperature, the fluid in the z-axis bladder was heated with the same x,y pressurized reservoir embedded heat exchange by circulating heated water through a closed-loop pipe installed in the z plate. This feature of the cell will be discussed in the chapter on experimental procedures. The pressures applied to the water reservoirs for pressurizing the horizontal (x-and y-faces) and vertical (z-face) faces are controlled independently using two Kendall Model 10 pneumatic pressure regulators manufactured by Fairchild Industrial Products Company and having a range of 34.5 to 2758 kPa. The deformations of the five faces of the specimen in the x, y and z-directions are monitored during application of mechanical stresses, temperature changes and low constant suction conditions using linearly variable differential transformers (LVDTs). The fact that the bladders are pressurized requires a creative means for measuring displacements with the LVDTs. Specifically, the cores for the LVDTs are placed within sealed aluminum tubes, and their movement is tracked by the LVDT through the aluminum core. The cores are spring-loaded so that they maintain intimate contact with the specimen during mechanical and thermal loading as shown in Figure 4.5.

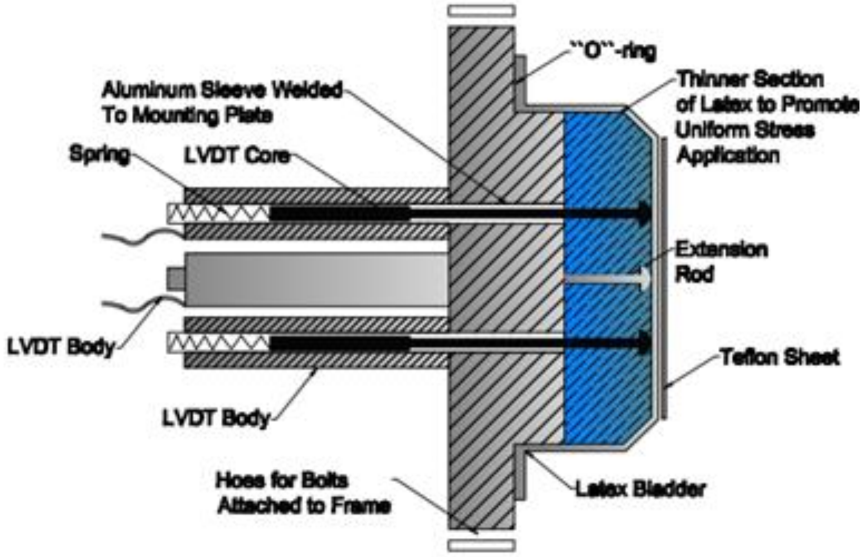

Figure 4.5: LVDT configuration with the mechanical backing plate.

The LVDTs used were manufactured by Measurement Specialties, Inc. (Model number HR 500) and have a range of -12.7 to +12.7 mm, and can measure deformations with a precision of 0.05 mm. The reason for using three LVDTs on each of the five faces in the x, y and z-directions is that three points of deformation are required to define the position and orientation of a plane. Accordingly, they can be used to infer if the specimen is deforming uniformly. Although the cubical specimen is intended to remain plane for the range of stresses applied to the specimen, it is possible that friction between the bladder and frame may lead to a slight bulging of the bladders. Accordingly, the average reading of the three LVDTs is assumed to be representative of the deformation of the center of the face. Several precautions were taken to minimize bulging of the specimen. A well-greased 6 mm-thick acrylic spacer was used to close the gap between the bladders, which reduced friction at the boundaries and prevented the intrusion of particles in the gap. The acrylic spacers are shown in Figure 4.6. To prevent the development of shear stresses on the faces of the specimens, Polytetrafluoroethylene (Teflon) sheets were adhered to the face of each bladder using vacuum grease to reduce friction between the bladder and the soil as indicated in Figure 4.7. In addition, the maximum magnitude of deformations applied to the specimen was limited to 10 mm.

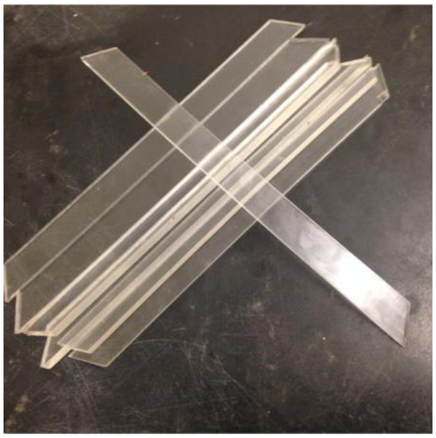

Figure 4.6: Acrylic spacers used between the flexible bladders.

Takata (2000) found that if the bladders deformed by more than 25 mm, they became distorted and the LVDT measurements the assumption of uniform deformations is no longer reliable. The maximum tilt angle of the bladders inferred with the LVDTs was approximately 0.6 degrees from vertical, which indicates that the faces remained relatively plane. Furthermore, post-test disassembly of the system indicated that the specimen remained close to plane without visible evidence of bulging.

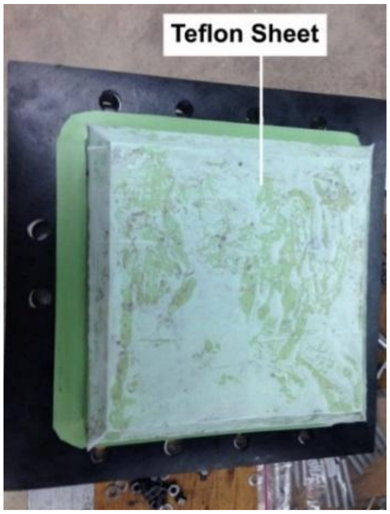

Figure 4.7: Bladder with Teflon sheet adhered with vacuum grease.

### 4.3 Temperature Control System

The temperature of the water used to pressurize the five flexible bladders was heated in a reservoir that is pressurized using fluid from the x- and y-face reservoir. Pictures of the reservoir are shown in Figure 4.8.

Figure 4.8: Pictures of the pressurized reservoir containing the heating coil.

Water was used as the heat exchange fluid in all of the experiments because it has a relatively low viscosity. The viscosity of water varies from 1.310 to 0.470 centipoises for temperatures ranging from 10 to 60 °C, respectively. The heat exchange fluid within the pressurized reservoir was heated using the resistance coil heater, the temperature of which was controlled using an automated Watlow model 88-10 temperature controller, shown in Figure 4.9. The temperature controller can control the temperature of the water within a range -17.8 to +204.5 °C.

Figure 4.9: Temperature controller (WATLOW 88-10).

To heat the soil specimen, the water was circulated through the four bladders, the heat exchange tube in the z-face, and the heat exchange tube in the rigid hydro-thermal plate on the bottom of the specimen using a circulating pump. A circulation pump (Heliatos model TS5 15PV) was used to circulate the water from the pressurized reservoir through the different faces of the cell. A picture of the circulating pump is shown in Figure 4.10. The circulating pump can supply a fluid pressure up to 145 psi and a flow rate up to 11.4 lpm. During circulation of the heated water throughout the system, heat is transferred from the hydro-thermal face plate and the five flexible bladders to the soil through conduction.

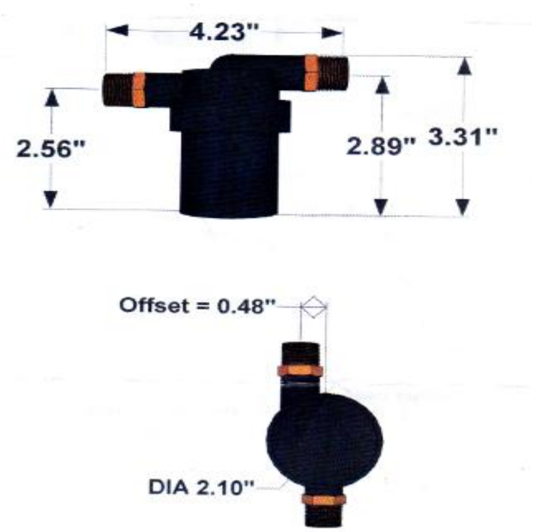

Figure 4.10: Schematics of the circulating pump.

The hydro-thermal face plate on the bottom of the specimen consists of an Acetal face plate that is in direct contact with the soil specimen to control temperature as well as pore air and water pressure, and an anodized aluminum backing plate which connects to the frame and incorporates connection ports for the temperature, pore air and water pressure control. The heat exchange tubing consists of two individual 6.3 mm copper heating coils embedded within the Acetal face plates. The copper heating coils are connected to the circulator pump through 6.3 mm insulated polyethylene tubing. This tubing is connected to the heating coils using quick connect fittings to prevent loss of the heat exchanger fluid during assembly of the setup. The hydro-thermal face plate consist of an Acetal face plate is shown in Figure 4.11.

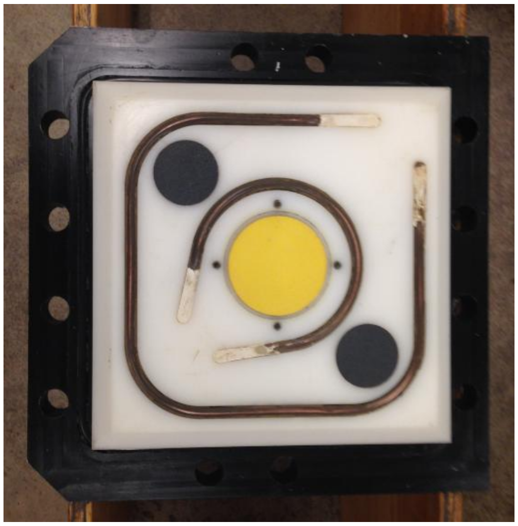

Figure 4.11: Pictures of the hydro-thermal face plate on the bottom of the specimen.

Internal soil temperatures are measured using two K-type thermocouples which were carefully inserted into the center of the soil specimen at different distances from the base plate using a needle (labeled as T1 and T2 in Figure 4.2). This information can be used to infer the heat flux into or out of the specimen during heating and cooling, respectively. Pictures of the thermocouples placed within the cell will be shown in Chapter 5 during the discussion of the experimental procedures.

## 4.4 Pore Air and Water Pressure Control System

Air and water pressure in the specimen has been controlled by using a hydro-thermal plate incorporating recesses to hold two 35 mm-diameter coarse porous discs which can be used to control air pressure in the specimen. Furthermore, the hydro-thermal plate incorporates a central port which can accommodate a 40 mm-diameter high air entry (HAE) ceramic disc to control pore water pressure using the axis translation technique as shown in Figure 4.12. The system was designed so that independent air and water pressures would be applied to the bottom of the soil specimen to induce flow of air and water across the specimen. The layout of the pressure control system is described in Figure 1.2 (objectives section). The de-aired water pressure on the bottom of the specimen was controlled independently through tanks pressurized with air regulated by type 70 manual pneumatic pressure regulators, manufactured by Bellofram Co. and having ranges of 13 to 1035 kPa.

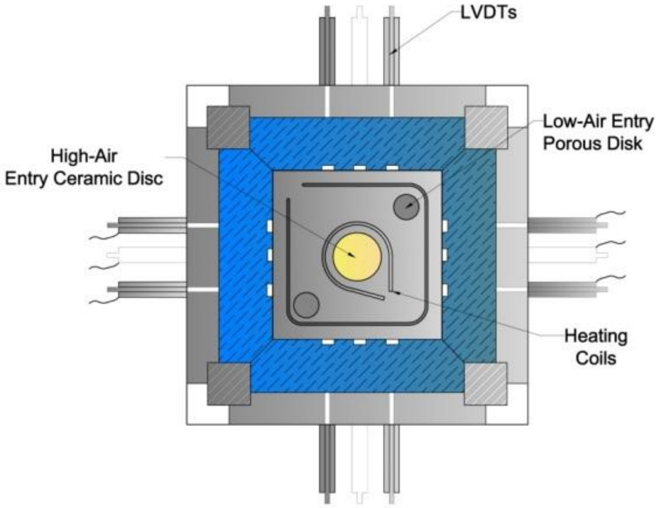

Figure 4.12: Top view of the THM cell showing the hydro-thermal control plate.

### 4.5. Mechanical Machine Deflections

During isothermal or non-isothermal tests using the THM true-triaxial cell, application of stresses or changes in temperature may lead to expansion of the space frame of the cell. The expansion of the space frame will affect the measurements of the displacements of the face of each specimen in the directions of principal stresses as the body of each LVDT is mounted to the space frame. Accordingly, machine deflections of the true-triaxial during mechanical loading were first characterized by evaluating the response of the space frame during compression of an aluminum cube with the same dimensions as the typical soil specimen. The aluminum cube is shown in Figure 4.13. In this approach, the elastic deflections of the aluminum cube for a given change in stress are known.

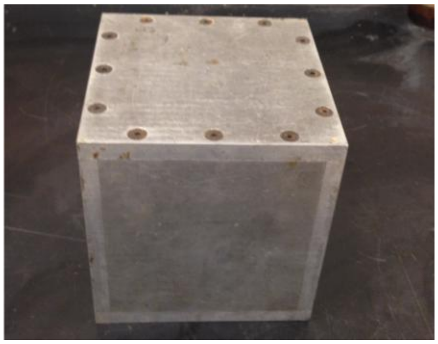

Figure 4.13: Aluminum cube used for thermo-mechanical cell deflection evaluation.

Stresses were applied to the aluminum cube in order to reach three different values anisotropic stress states ($K = \sigma_h/\sigma_v$, where $\sigma_h = \sigma_x = \sigma_y$ and $\sigma_v = \sigma_z$), corresponding to K = 1.0, 0.7 and 0.5. Although the space frame is expected to be linear elastic and isotropic, it is possible that application of anisotropic stresses to the space frame may result in different machine deflections. During mechanical loading, cold water was used to pressurize the flexible bladders around the aluminum cube. Stresses were applied to the aluminum isotropically up to 350 kPa, then the stresses in the z direction were increased to reach the different target K values. The changes in applied stresses are presented in Figure 4.14. Deflections of the aluminum cube and the average face deflections of the space frame are shown in Figure 4.15.

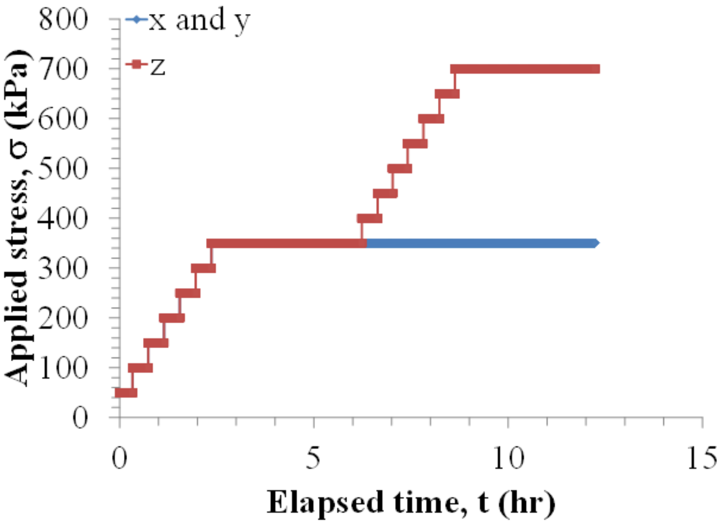

Figure 4.14: Applied stress during the machine deflection test.

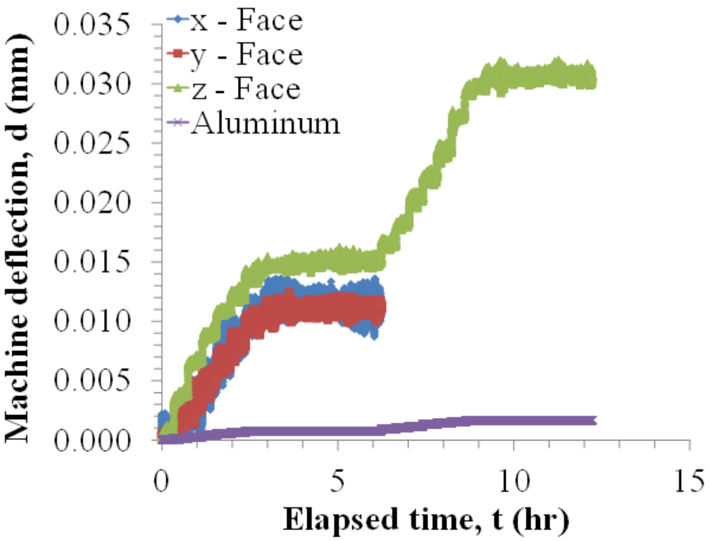

Figure 4.15: Deflections of the aluminum cube and the average face deflections of the space frame.

The mechanical machine deflections were calculated by subtracting the elastic deflection of the aluminum cube from the average deflections of the space frame. The deflection of the aluminum cube was calculated as follows:

$$\delta = \frac{\sigma \times L}{E} \tag{4.1}$$

where δ is the elastic deflection of the aluminum cube, σ is the stress for each stage in kPa, L is the length of the aluminum cube, which is equal to 178 mm and E is the Young's modulus of the aluminum cube, which is equal to 69000000 kPa. A positive machine deflection is defined as compression. The slopes of machine deflections in each principal stress direction $M_x$, $M_y$ and $M_z$ were calculated as follows:

$$M = \frac{d_m}{\sigma} \tag{4.2}$$

where M is the slope of machine deflection (mm/kPa), $d_m$ is the mechanical machine deflection (mm) and σ is the axial stress (kPa).

The mechanical machine deflections and the values of machine deflections slope in each direction during loading are presented in Figure 4.16. The values of mechanical machine deflections can be subtracted from the measured deformation results from non-isothermal compression tests on soils during changes in stress. The z face showed a softer response than the other directions possibly because the bottom face in the z direction is a rigid plate. The application of anisotropic stresses in the z direction still resulted in linear elastic behavior, reflected in the same slope of the mechanical machine deflection curve.

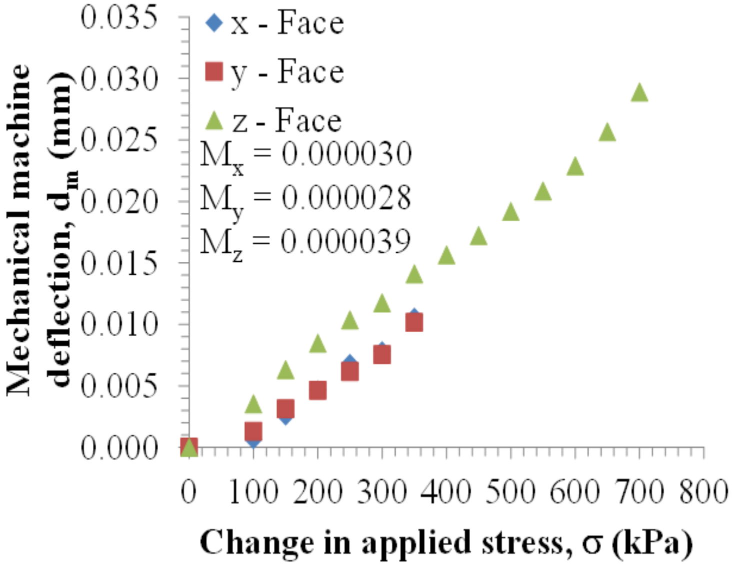

Figure 4.16: Mechanical machine deflections for the true-triaxial cell.

## 4.6 Thermal Machine Deflection

It is important to consider the deformation of the true-triaxial cell during heating and cooling in order to consider the effects of thermal expansion of the space frame when inferring the thermally induced volume change of soil specimens. At the same mechanical machine deflection test, thermal deformations were measured by unloading aluminum cube from anisotropic stress state, which is corresponding to K = 0.50 to isotropically loading, which corresponds to K = 1. Then aluminum cube was heated from the ambient room temperature of 20 °C to a temperature of approximately 50 °C in three stages in 10 °C intervals, then cooled back to ambient room temperature in one stage. The aluminum cube was heated under an isotropic stress of 350 kPa, because this range of stresses is associated with normally consolidated conditions for unsaturated, compacted Bonny silt. The change in temperature of the cell during heating and cooling is shown in Figure 4.17.

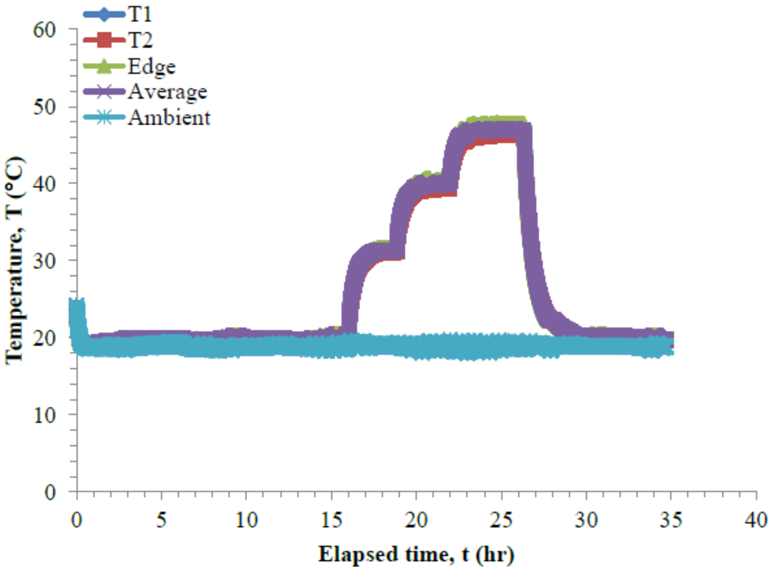

Figure 4.17: Change in temperature of the cell during the machine deflection test.

The thermal machine deflections were calculated by subtracting the expected thermo-elastic deflection of the aluminum cube from the measured deflections. The LVDTs were used to measure the deflections of the five faces in the x, y and z directions during thermal cycling. The theoretical aluminum cubic displacement was calculated as follows:

$$d_{T,al} = \alpha_{al} \times L_{al} \times \Delta T \tag{4.3}$$

where $d_{T,al}$ is the thermal displacement of the aluminum cube, $\alpha_{al}$ is the coefficient of thermal expansion of the aluminum ($\alpha_{al} = 23\times10^{-6}$ m/m°C), $L_{al}$ is the initial length of aluminum cube and $\Delta T$ is the change in temperature applied during the test. The machine deflections were calculated as the difference between the measured deflections from the LVDTs and the theoretical value of $d_{T,al}$ for a given change in temperature. Because the thermal machine deflections were found to be thermo-elastic, the slopes of the thermal machine deflection curves during heating $C_x$, $C_y$ and $C_z$ were calculated as follows:

$$H = d_T / \Delta T \tag{4.4}$$

where H is the slope of thermal machine deflection (mm/°C), $d_T$ is the thermal machine deflection (mm) and ΔT is the change in temperature (°C). The slopes of the thermal machine deflection curves during cooling were also relatively linear, so the values during cooling $C_x$, $C_y$ and $C_z$ were calculated as follows:

$$C = d_T / \Delta T \tag{4.5}$$

where C is the slope of thermal machine deflection (mm/°C), $d_T$ is the thermal machine deflection (mm) and ΔT is the change in temperature (°C).

The thermal machine deflections for all faces in the x, y and z directions and the values of the thermal machine deflections slopes $H_x$, $H_y$ and $H_z$ during heating along with the values of the thermal machine deflections slopes $C_{x,}$ $C_y$ and $C_Z$ during cooling are plotted in Figure 4.18(a). Because the slopes during cooling were relatively similar to those during heating, the slopes during heating were used to correct the thermal machine deflections through the entire test for simplicity. Accordingly, the thermal machine deflections for all faces x,y and z directions without the data during cooling are shown in Figure 4.18(b).

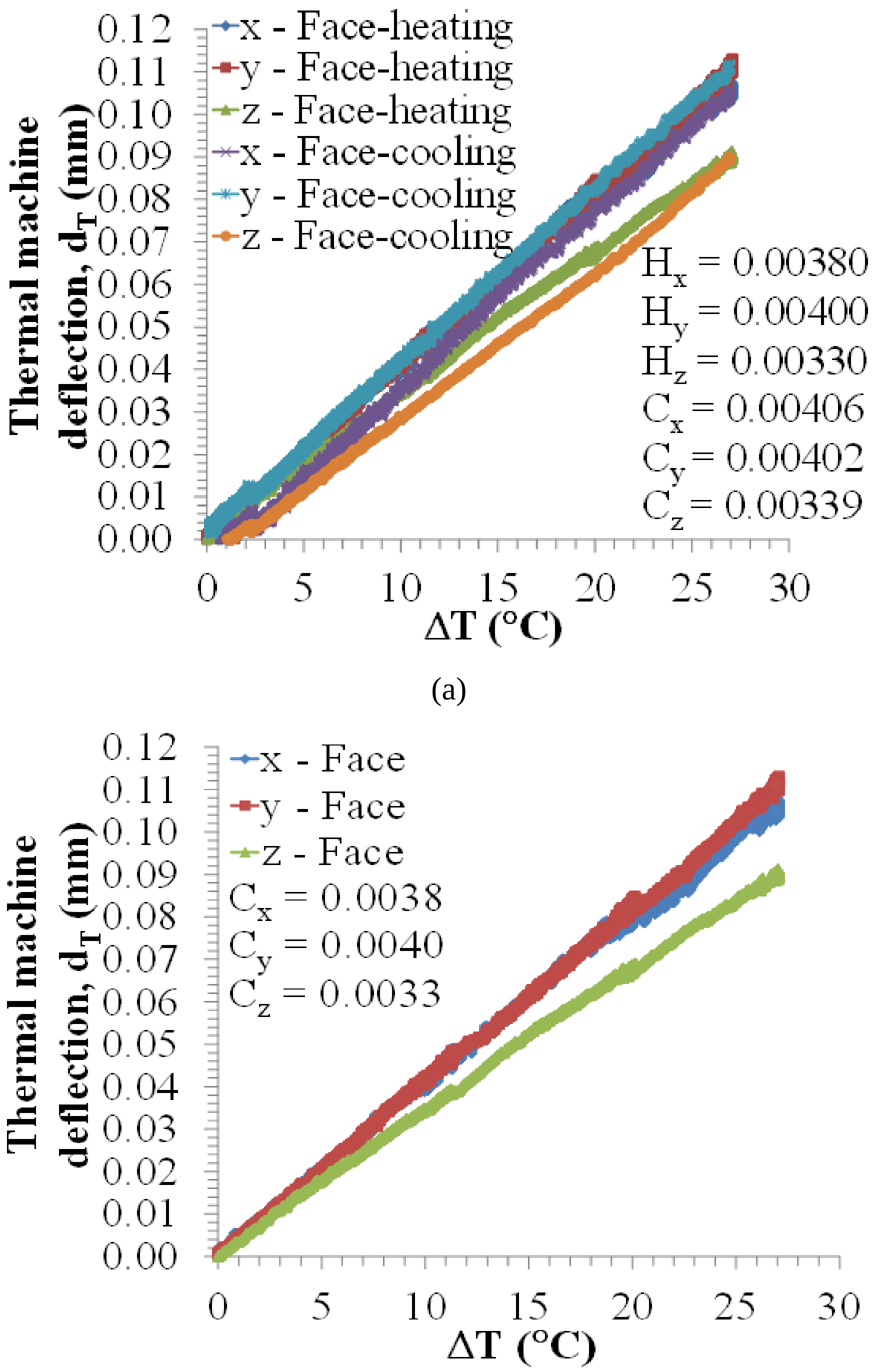

(a)

(b)

Figure 4.18: (a) Thermal machine deflections of the faces x,y and z directions during heating and cooling; (b) Thermal machine deflections of the faces x,y and z without cooling.

# 5. PROCEDURES

The first step in preparing the THM triaxial cell for a test is to saturate the high air entry (HAE) ceramic disc. The specific HAE ceramic disc used in this study has an air entry suction of 300 kPa, and is shown in Figure 5.1. This HAE ceramic disc is used to facilitate measurement of the negative water pressure in unsaturated soils using the tensiometer approach, and to apply water pressures using the axis translation technique. It is critical for the HAE ceramic disc to be saturated with water before beginning a test.

Figure 5.1: High air entry (HAE) ceramic disc.

The HAE ceramic disc was first placed into the recess in the rigid bottom platen of the THM true-triaxial cell in air-dry conditions. Then a bead of RTV silicon sealant was placed around the edge of the ceramic to provide a hydraulic seal that prevents short-circuiting of air around the edges of the HAE ceramic disc. After the silicon sealant cured, water was flushed through the channel beneath the ceramic disc. Next, a special pressure-saturation device was placed on top of the ceramic disc, as shown in Figure 5.2.

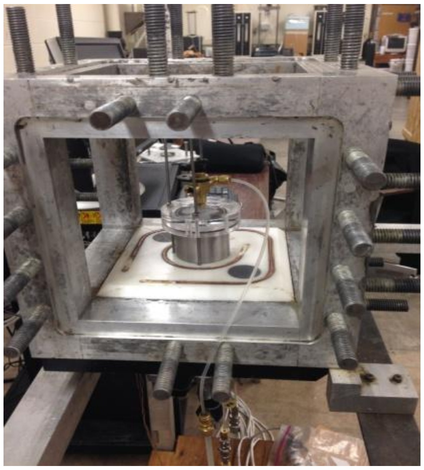

Figure 5.2: Setup used to saturate the high air entry ceramic disc in the rigid platen.

The device, shown in the schematic in Figure 5.3, consists of a steel cylinder with an O-ring seal at the base that is tightened onto the face of the rigid platen using three screws. This chamber was then filled with water under a pressure of 70 kPa, and the water on the bottom side of the HAE ceramic disc was placed under vacuum. De-aired water was then permitted to flush downward through the HAE ceramic disc overnight. Water flow was oriented downward to avoid putting upward stresses on the seal between the hydro-thermal plate and the HAE disc. After this, the HAE ceramic was assumed to be water-saturated.

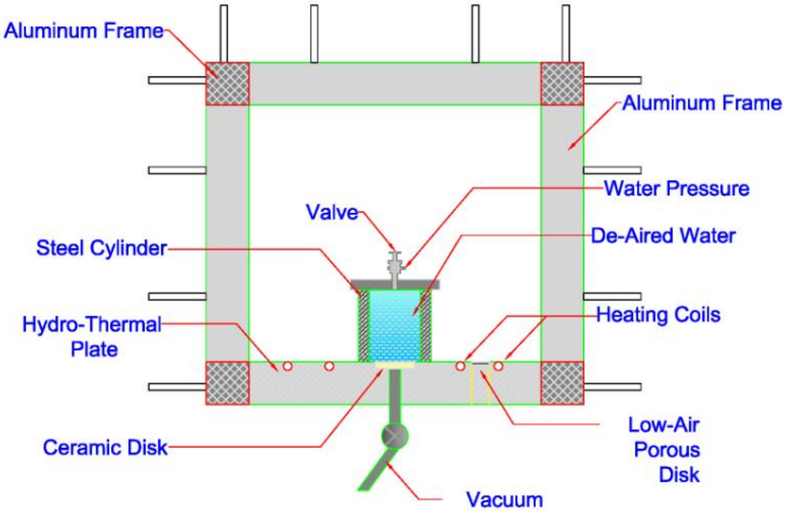

Figure 5.3: Cross-section schematic of the device used for saturation of the HAE disc.

Next, the compacted soil specimen was placed carefully on top of one of the flexible latex bladders outside of the THM cell so that the compaction lifts are perpendicular to the bladder face. The THM cell incorporates a tilting apparatus that can be used to facilitate placement of the soil specimen within the frame, which is described in detail by Mould (1983). After attaching the hydrothermal face plate to the bottom of the frame (which is aligned with the z-axis), the frame was tilted 90° around the hinge-point. The specimen and the flexible bladder were then inserted into the THM cell so that the z-face of the specimen, which is perpendicular to the compaction lifts, was placed in contact with the rigid platen. A picture of the soil specimen inside of the THM cell after completion of this process is shown in Figure 5.4. Then the frame was tilted back into the normal configuration.

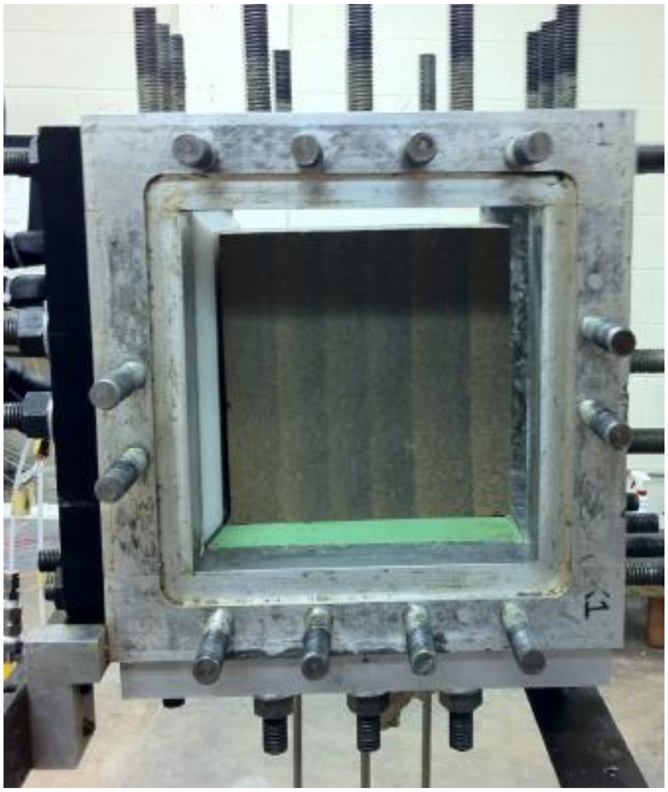

Figure 5.4: Orientation of the cubical cell during insertion of soil specimen.

In the initial orientation, four thermocouples were installed into the system to measure the spatial distribution in temperature during the test. Two thermocouples were inserted into the compacted soil specimen as shown in Figure5.5, a third thermocouple was placed between the face of compacted soil specimen and the bladder, and the fourth thermocouple was left outside to measure the changes in the ambient room temperature. The thermocouples in the soil specimen were inserted using a needle so that they would measure the temperature near the mid-plane of the specimen, in between two lifts at similar distances from the lower hydro-thermal plate and the upper z-direction bladder. Next, the thermocouples were connected to the data acquisition system as shown in Figure 5.6.

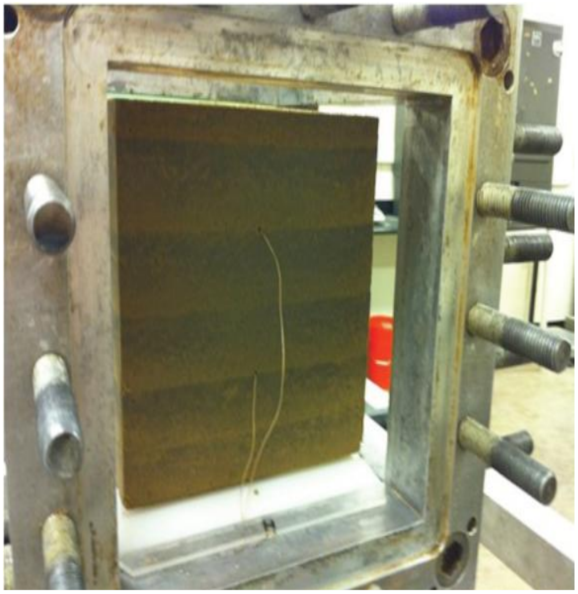

Figure 5.5: Compacted soil specimen in the upright configuration with two thermocouples inserted into the soil specimen.

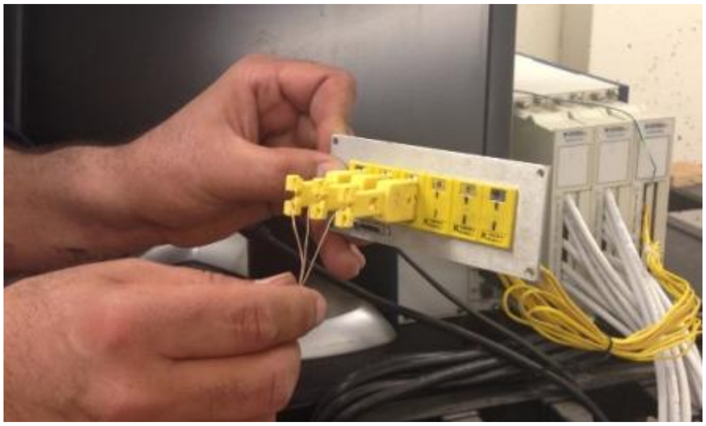

Figure 5.6: Thermocouple connections.

The mechanical loading plates were then assembled onto the true-triaxial cell frame. In the next step, fifteen DC linearly variable differential transformers (LVDTs) were placed on the top of the mechanical loading plates of the true triaxial cell. Each loading face contains three LVDTs. O-rings were then set behind the LVDTs to avoid the LVDTs from moving along the core during testing, and all instrumentation drainage pipes were connected. The assembly of the mechanical loading plates and the placement of the LVDTs are shown in Figure 5.7.

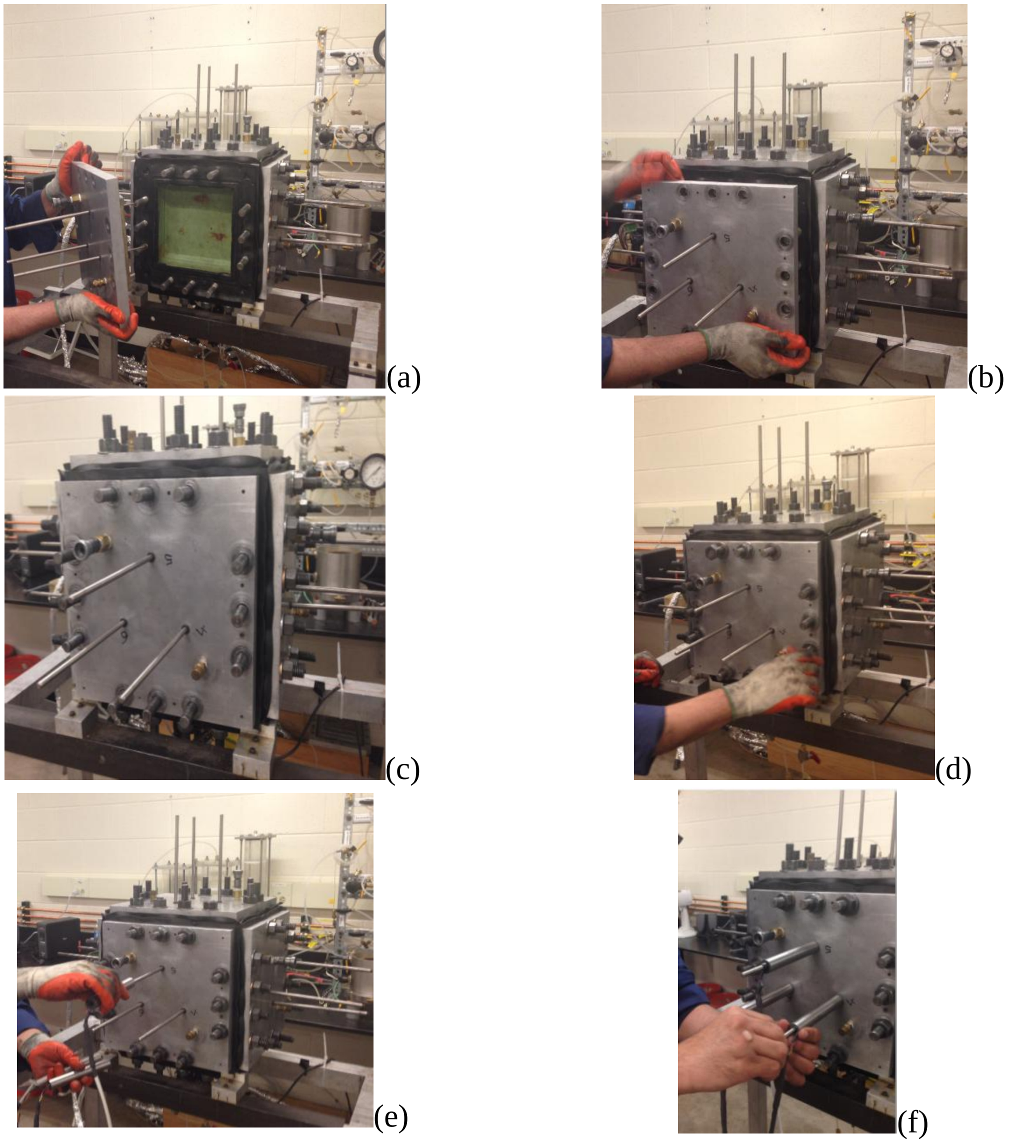

Figure: 5.7. Processes assembling the true-triaxial cell: (a) bladder and rubber sheet assembly; (b) mechanical loading plate fitting the screws; (c) placed the mechanical loading plate onto the true-triaxial frame; (d) mechanical loading plate tighten using twelve screws; (e) LVDTs placing on the top of mechanical loading plate; (f) small O-ring behind LVDT.

Once the true-triaxial cell is assembled as shown in Figure 5.8, the initial suction in the compacted, unsaturated silt was measured using the tensiometer approach. Specifically, the water pressure within the reservoir beneath the high air entry ceramic disc was monitored using a pressure sensor. In this approach, water has the tendency to flow from the ceramic disc into the relatively dry soil, which makes the water within the reservoir behind the disc go into tension as long as the air pressure within the specimen is equal to zero. Negative water pressures up to approximately -80 kPa can be measured using this approach. At equilibrium, the negative water pressure measured within the reservoir is expected to be approximately equal to the suction within the unsaturated specimen as the pore air pressure is assumed to be zero.

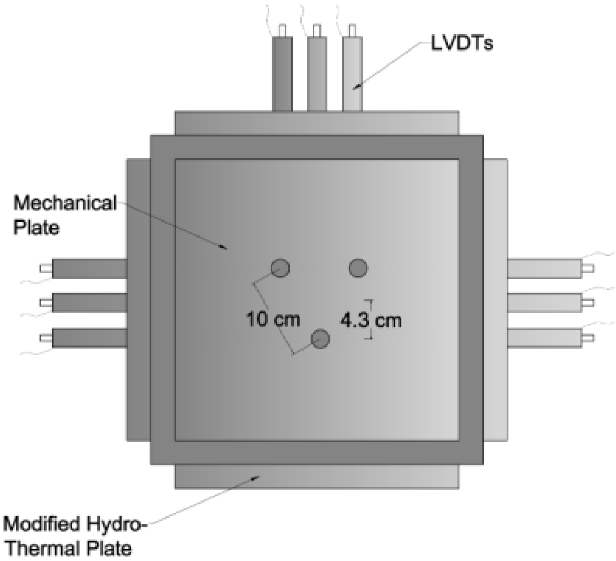

Figure 5.8: Schematic of the true-triaxial cell assembly showing the configuration of the mechanical plates and the rigid face plate.

After reaching hydraulic equilibrium, a seating normal stress of 10 kPa was applied to all of the bladders on the x- y- z-faces of the cubical soil specimen. This initial total stress was applied to ensure initial contact between the flexible latex bladders and the cubical specimen without causing significant deformations to the compacted specimen. The LVDT readings measured after equilibration under this initial seating stress were then zeroed to serve as a baseline reading from which to base further deformations of the specimen.

After application of the seating stress, the initial value of suction measured within the specimen was applied using the axis translation technique. This involved increasing the total stress, pore air pressure, and pore water pressure in stages to maintain a constant suction within the specimen equal to the initial suction. An example of the pressure stages corresponding to a constant suction during suction application and subsequent mechanical loading are shown in Figure 5.9. The axis translation approach permits the pore water pressure applied to the bottom of the specimen to be positive, which minimizes the likelihood that the water will cavitate.

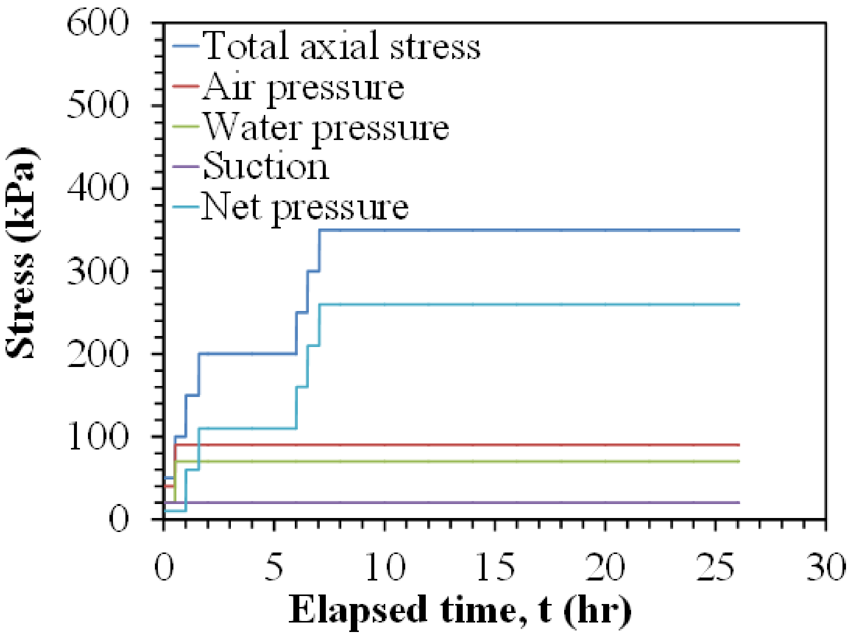

Figure 5.9: Application of different values of total stress, pore air pressure and pore water pressure in stages to maintain constant suction using the axis translation technique.

The constant matric suction pressure was achieved by directly measuring the difference between the pore water and air pressures of the specimen ($u_a$-$u_w$ = 20 kPa) for 0.7 degree of saturation and ($u_a$-$u_w$ = 10 kPa) for 0.8 degree of saturation. The value of air pressure ($u_a$) should be maintained greater than the value of water pressure ($u_w$), and both less than the value of total net stress. The isotropic and anisotropic loading-unloading tests were performed by increasing and decreasing the pressurized water through the bladders in increments and allowing the excess pore water pressure to dissipate.

Stresses were applied to the compacted soil specimens in order to reach three different values anisotropic stress states ($K = \sigma_h/\sigma_v$, where $\sigma_h = \sigma_x = \sigma_y$ and $\sigma_v = \sigma_z$), corresponding to K = 1, 0.70 and 0.50, these values are shown in the plot in Figure 5.10.

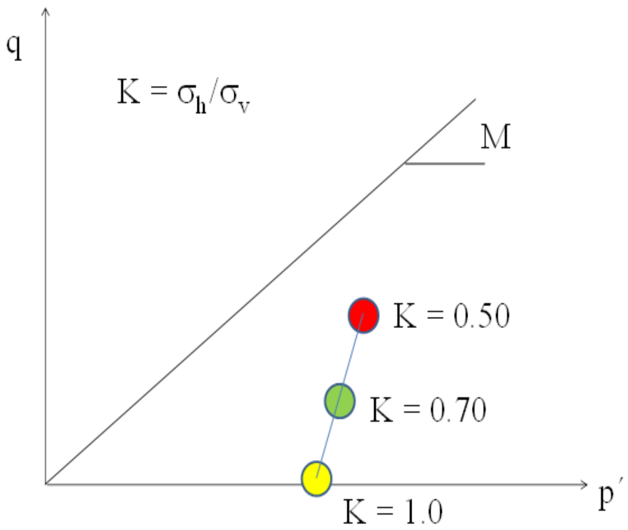

Figure 5.10: Schematic of the initial anisotropic stress states applied to the soil specimens.

During mechanical loading, cold water was used to pressurize the flexible bladders around the soil specimen. The specimen was first loaded isotropically up to 350 kPa in all cases, then the stresses in the z direction were increased to reach the different target K values. After reaching the desired value of the anisotropy coefficient K, the soil specimens were heated in three stages then cooled in one stage. The target rate of increasing water temperature was 0.5°C/hr to follow the approach of Uchaipichat and Khalili (2009). During heating, the water within the bladders was circulated through a pressurized reservoir that contains a heating coil. When the heating coil is activated, the water which used to pressurize the flexible bladders heats up, and applies the same temperature to all sides of the cubical specimen.

Because only one heated reservoir was available, and because the temperature at all six faces of the specimen should be the same, a special copper circulation coil was run through the bladder on the upper z-face. The pressure within this face was controlled using a separate pressure reservoir. This permitted independent application of pressures to the z face, but uniform temperatures on all of the faces. This copper circulation coil is shown in Figure 5.11.

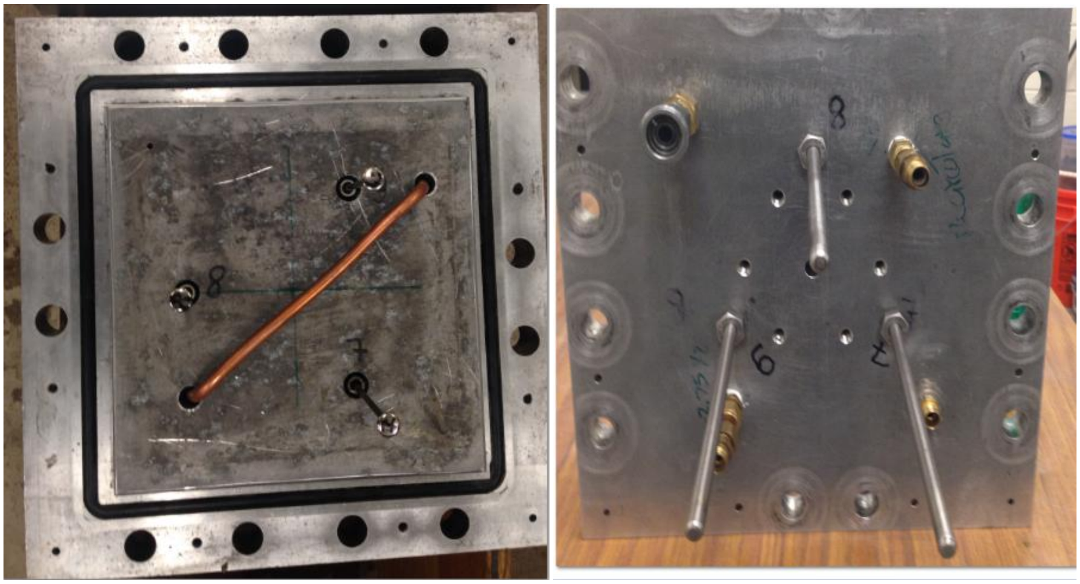

Figure 5.11. Pictures of the z-face loading face with the copper circulation coil used to maintain the same temperature at the x- and y-faces but independent temperatures.

# 6. RESULTS

## 6.1. Overview

Six non-isothermal tests were conducted using the THM true-triaxial cell under constant suction conditions to characterize the effect of stress-induced anisotropy on the thermal volume changes of unsaturated soils. These tests were performed on compacted, cubical specimens of Bonny silt having different initial degrees of saturation and under different stress ratios K. The compaction conditions for these specimens were summarized in Table 3.2. In this study, it is assumed that the horizontal principal stresses are equal to the minor principal stress ($\sigma_2=\sigma_3=\sigma_x=\sigma_y$), and that the vertical stress is the major principal stress ($\sigma_1=\sigma_z$). As mentioned, the stress ratio is equal to the ratio of the minor principal stress to the major principal stress ($K = \sigma_3/\sigma_1 = \sigma_y/\sigma_z$). Three tests were performed on soil specimens compacted to an initial degree of saturation of 0.70, while three other tests were performed on specimens with an initial degree of saturation of 0.8. These tests were performed to complement the tests on saturated specimens of Bonny silt evaluated by Coccia and McCartney (2012). The name designations for each test along with the axial stresses applied to the specimens in the different tests are summarized in Table 6.1. The initial matric suction values measured in the specimen using the tensiometer approach are also presented in this table.

Table 6.1: Applied stresses in the tests having different stress ratios K

| Test | Stress ratio, $K = \sigma_y'/\sigma_z'$ | Stresses at the start of heating | | | | Void ratio at the start of heating |
|---|---|---|---|---|---|---|
| | | $\sigma_x'$ (kPa) | $\sigma_y'$ (kPa) | $\sigma_z'$ (kPa) | p' (kPa) | |
| K1.0-S0.7 | 1.0 | 274 | 274 | 274 | 274 | 0.580 |
| K0.7-S0.7 | 0.7 | 274 | 274 | 424 | 324 | 0.571 |
| K0.5-S0.7 | 0.5 | 274 | 274 | 624 | 391 | 0.567 |
| K1.0-S0.8 | 1.0 | 268 | 268 | 268 | 268 | 0.590 |
| K0.7-S0.8 | 0.7 | 268 | 268 | 418 | 318 | 0.577 |
| K0.5-S0.8 | 0.5 | 268 | 268 | 618 | 385 | 0.571 |

## 6.2. Results from Test K1.0-0.7

After application of the seating stress in this test, the initial value of suction measured within the specimens using the tensiometer approach was applied using the axis translation technique. This involved increasing the total stress, pore air pressure, and pore water pressure in stages to maintain a constant suction of 20 kPa. The stages corresponding to application of a constant suction value using the axis translation technique are shown in Figure 6.1. The increases in total stress applied to the specimen to mechanically load the specimen in isotropic conditions are also shown in this figure.

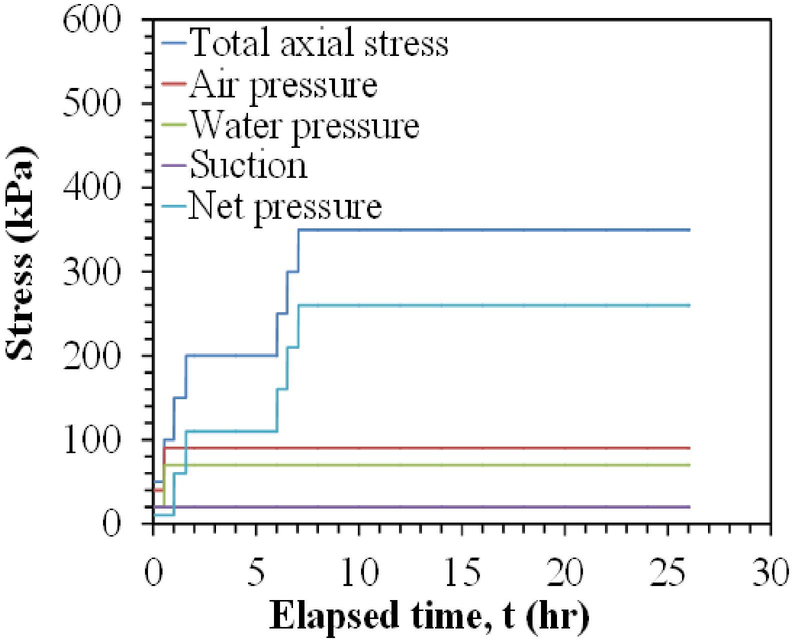

Figure 6.1: Application of total stress, pore air pressure and pore water pressure in stages to maintain constant suction using the axis translation technique for the K1.0-0.7 test.

The changes in applied effective stresses with time are presented in Figure 6.2. Effective stress was calculated from Equation 2.1. The test was mechanically loaded to a total isotropic stress of 350 kPa in the x, y and z directions, which corresponds to a mean effective stress of 274 kPa. The isotropic total stresses were applied by increasing the water pressure in the bladders in stages and allowing sufficient time for the excess pore water pressure to dissipate. Specifically, each loading increment was applied until all of the face deformations had stabilized.

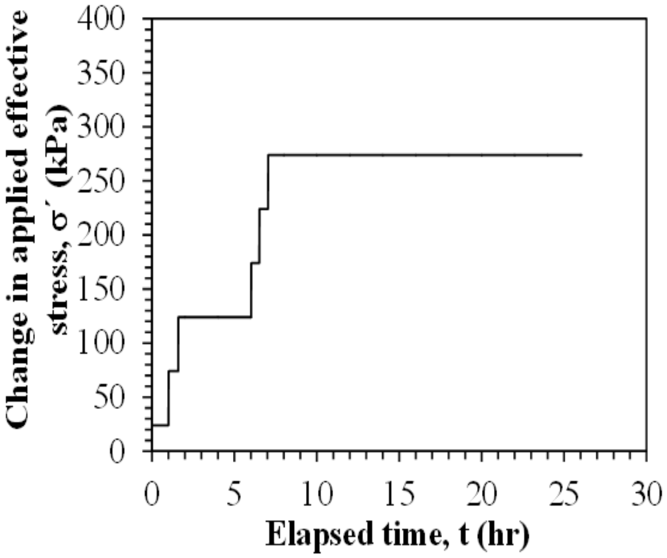

Figure 6.2: Change in effective stress on the soil specimen in the K1.0-0.7 test.

The time series of displacement for the K1.0-0.7 test are shown in Figures 6.3(a) through 6.3(e) for each of the faces. The displacement values shown in these figures were corrected for the effects of mechanical machine deflection of the cell using Equation 4.2. The average displacement for each of the faces is shown in Figure 6.3(f). The average compression of the specimen in each direction was calculated by summing the average displacements on the two opposite faces in each direction, assuming that there is no displacement of the ZZ face due to the presence of the rigid THM plate. The compressions of each face are shown in Figure 6.3(f). The averages of three LVDTs readings on each face of the soil specimen were calculated for measuring displacements except face XX, which used the average of two LVDTs (LVDTXX13 and LVDXXT15), because LVDTXX14 was not functional during testing.

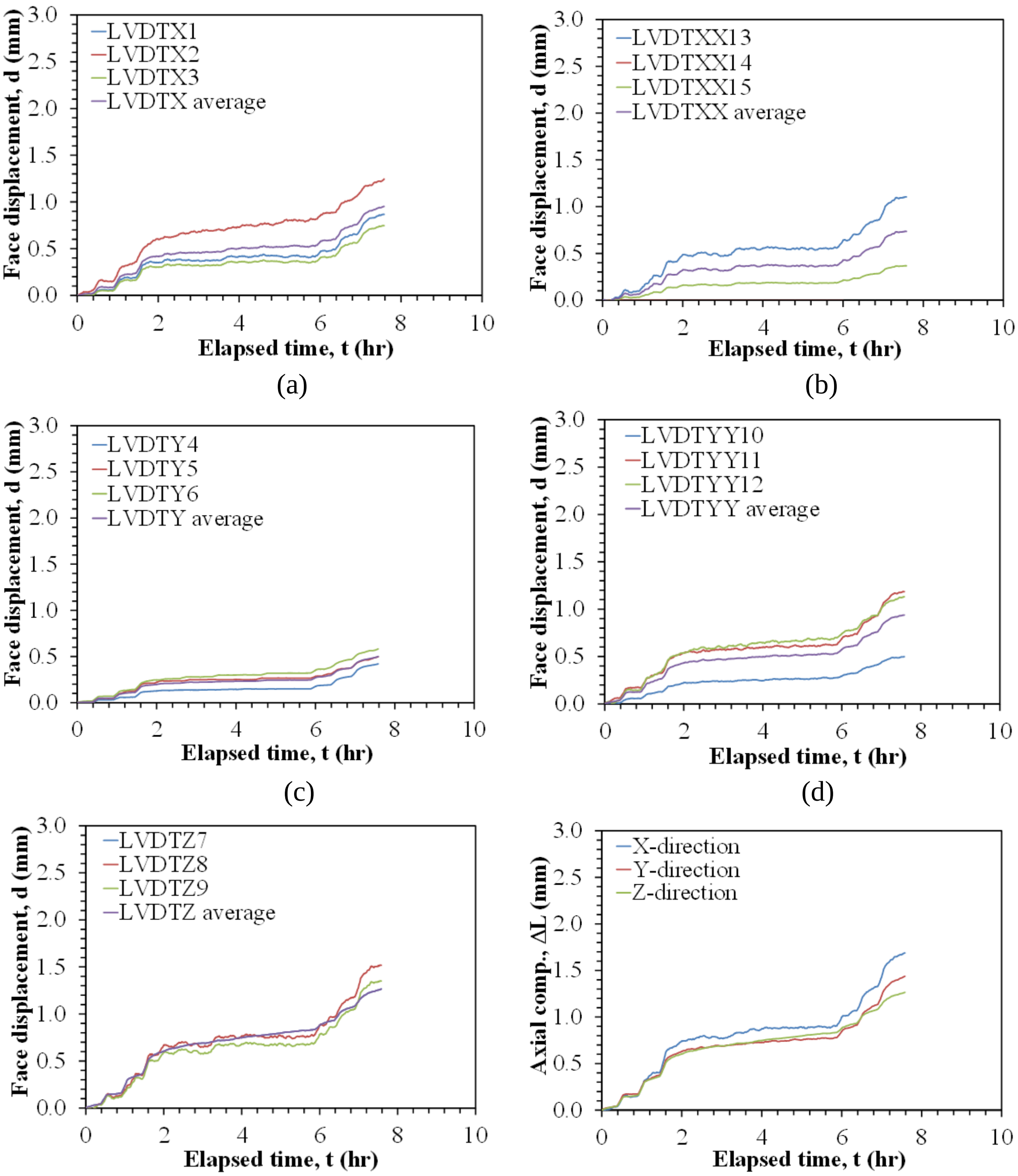

(a) (b)

(c) (d)

(e) (f)

Figure 6.3: Time series for the individual face displacements along with the average value: (a) X face; (b) XX face; (c) Y face; (d) YY face; (e) Z face; (f) Summary of average face displacements.

The time series of the mechanical axial strains for the K1.0-0.7 test were calculated from the values of displacements in Figure 6.3 using the following equation:

$$\varepsilon_a = \frac{\Delta L_i}{L_O} * 100 \tag{6.1}$$

where $\varepsilon_a$ is the mechanical axial strain of the soil specimen in the $_i$ direction (%), $\Delta L_i$ is the axial compression in the i direction (mm), and $L_o$ is the initial side-length of the soil specimen equal to 178 mm. The mechanical axial strain values are plotted in Figure 6.4.

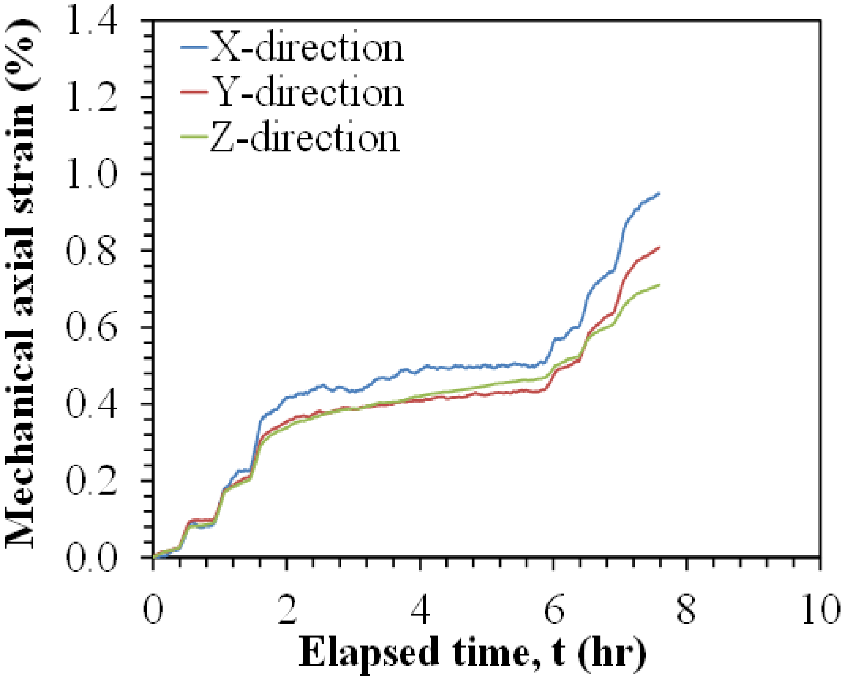

Figure 6.4: Time series for the mechanical strain values in Test K1.0-0.7.

The compression curve for the soil specimen in the K1.0-0.7 test up to the point at which heating was started is shown in Figure 6.5. The void ratio values were calculated from the average mechanical axial strains presented in Figure 6.4. The compression curve indicates that the compacted specimen initially behaves like an overconsolidated soil.

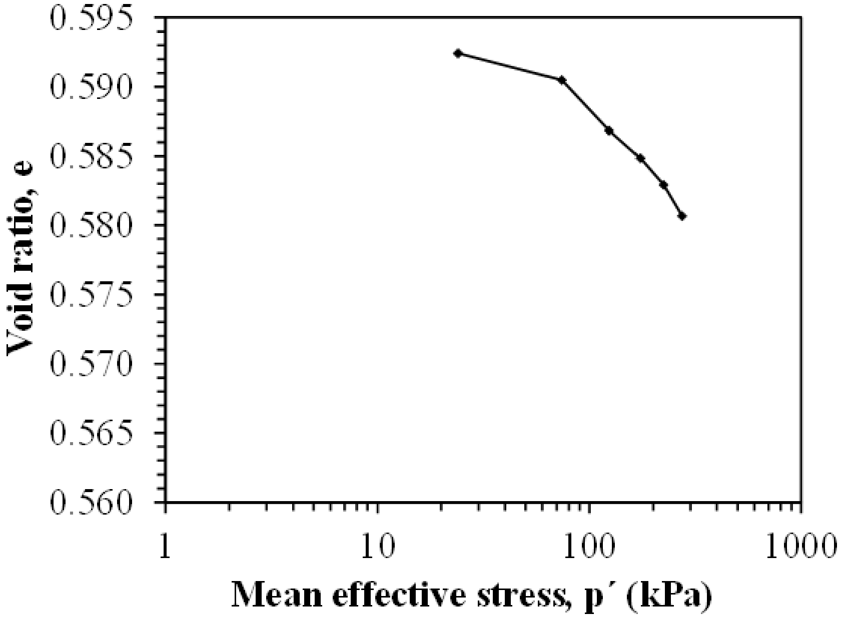

Figure 6.5: Compression curve obtained during application of isotropic stress state to unsaturated Bonny silt specimen for test K1.0-0.7.

Once the mechanical stresses were applied to the specimen, the temperature applied to the faces of the specimen was increased from the ambient room temperature of approximately 20 °C to a temperature of approximately 50 °C in three 10 °C stages, after which it was cooled back to ambient room temperature in one stage. The changes in temperature of the soil specimen at the edges and within the specimen during heating and cooling are shown in Figure 6.6(a). The rate of temperature change versus time is shown in Figure 6.6(b). The temperature changes of the soil specimen reached a stable value at each interval, which was maintained until the thermal axial strains reached equilibrium. The temperature within the specimen was within 4 °C of the temperature applied at the boundary.

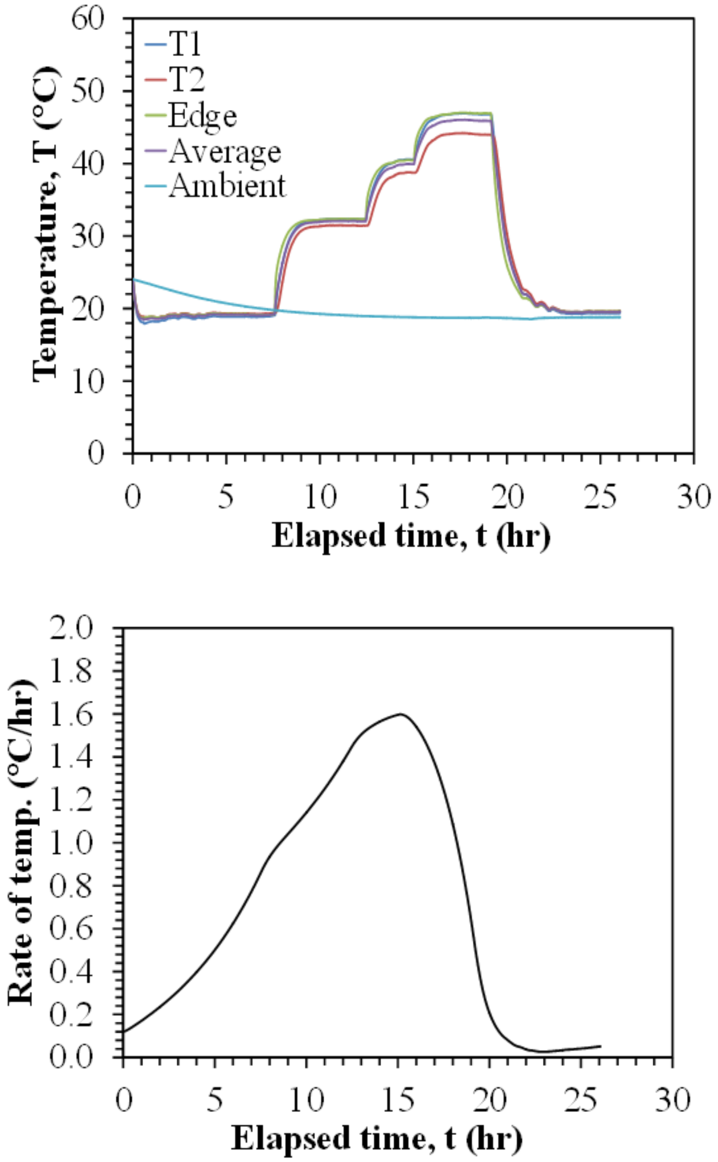

Figure 6.6: Results from the K1.0-0.7 test: (a) Change in temperature of the soil specimen; (b) The rate of temperature of the soil specimen.

The time series of thermal displacement for the K1.0-0.7 test are shown in Figures 6.7(a) through 6.7(e) for each of the faces. The thermal displacement values shown in these figures were corrected for the effects of mechanical machine deflection of the cell using Equation 4.2 and thermal machine deflection using Equation 4.4. The average thermal displacement for each of the faces is shown in Figure 6.7(f). The average axial strain of the specimen in each direction

was calculated by summing the average thermal displacements on the two opposite faces in each direction. The compressions of each face are shown in Figure 6.7(f).

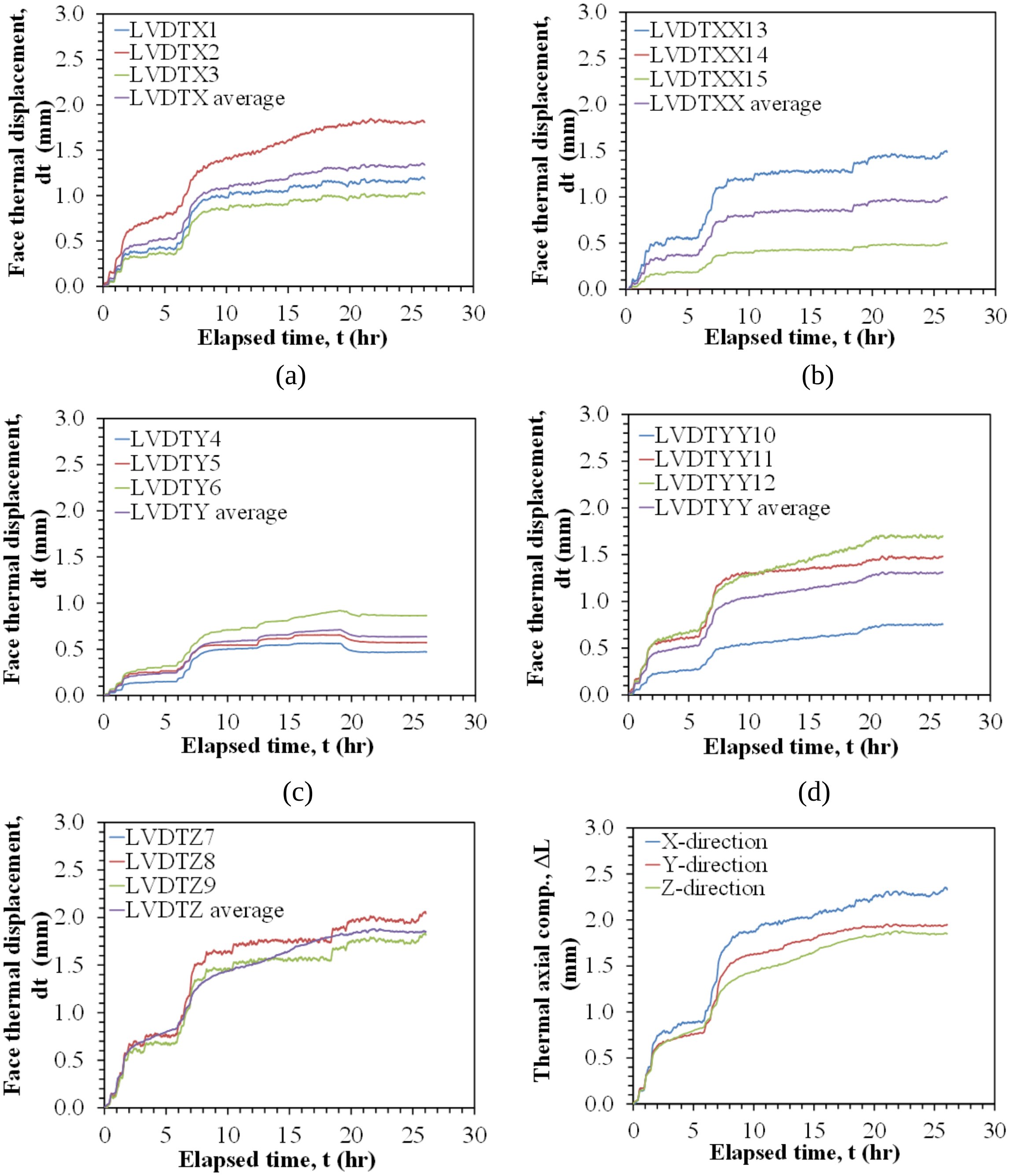

(a) (b)

(c) (d)

(e) (f)

Figure 6.7: Time series for the individual face thermal displacements along with the average value: (a) X face; (b) XX face; (c) Y face; (d) YY face; (e) Z face; (f) Summary of average face thermal displacements.

The time series of the thermal axial strains for the K1.0-0.7 test were calculated from the values of thermal displacements in Figure 6.7 using Equation 6.1. The axial strain values are plotted in Figure 6.8.

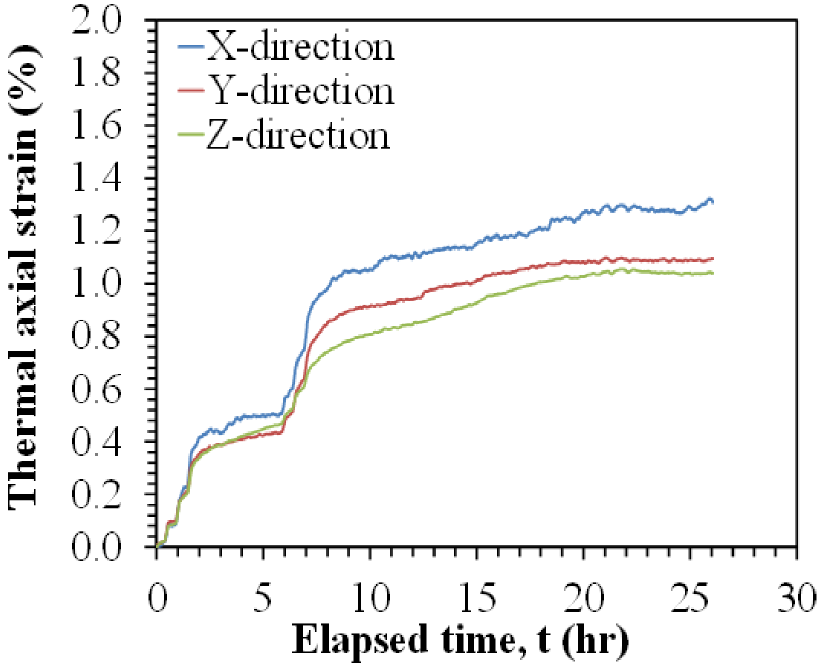

Figure 6.8: Time series for the axial strain values in Test K1.0-0.7.

The thermally-induced axial strains during the heating-cooling cycle are shown in Figure 6.9(a). The same data without the cooling stage is shown in Figure 6.9(b). Change of temperature versus thermal axial strain during heating for the points of equilibrium is shown in Figure 6.9(c). The data in these figures show that the thermal axial strain in the x, y and z directions indicate contractile behavior during heating as expected for a normally-consolidated soil specimen (Uchaipichat and Khalili 2009). This behavior is in agreement with the isotropic test on normally-consolidated, saturated Bonny silt reported by Coccia and McCartney (2012).

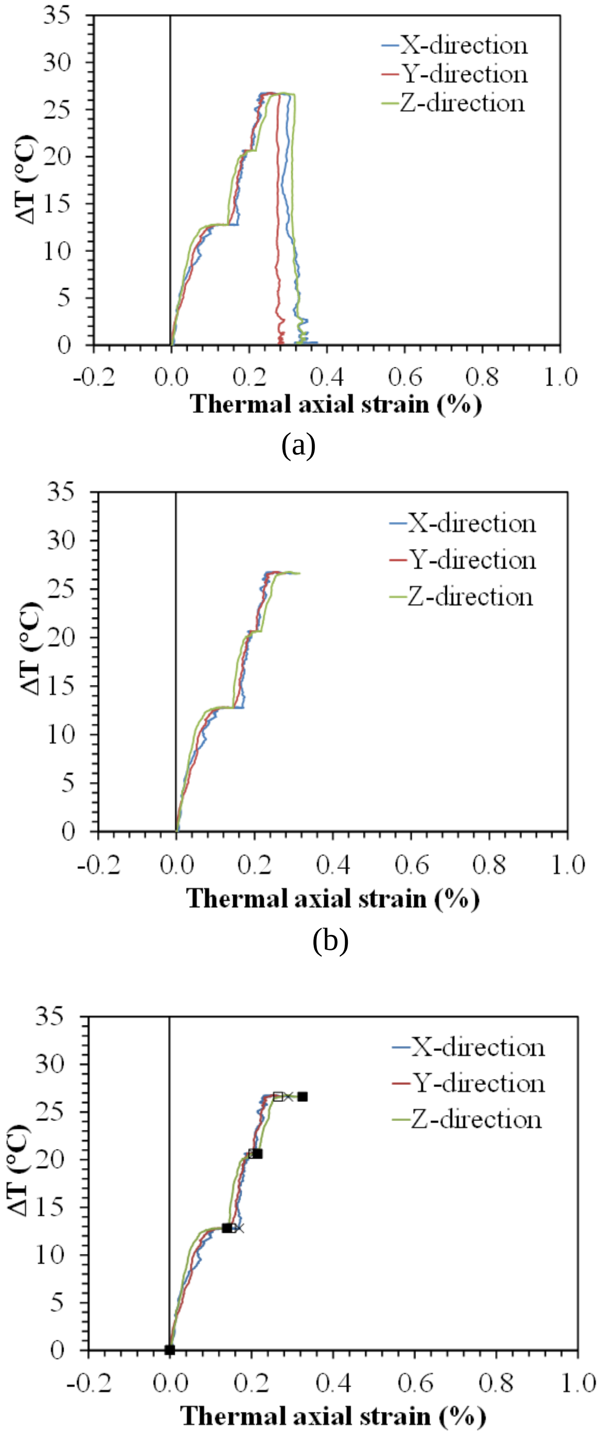

(a)

(b)

(c)

Figure 6.9: Results from the K1.0-0.7 test: (a) Change in temperature versus thermal axial strain for the full heating-cooling cycle; (b) Change in temperature versus thermal axial strain during heating; (c) Change of temperature versus thermal axial strain during heating for the points of equilibrium.

The thermal volumetric strain was calculated from the thermal axial strains as follows:

$$\varepsilon_v = \varepsilon_x + \varepsilon_y + \varepsilon_z \tag{6.2}$$

The thermal volumetric strain as a function of the change in temperature is shown in Figure 6.10(a) during heating and cooling. The thermal volumetric strain as a function of the change in temperature for the points of the equilibrium during heating is shown in Figure 6.10(b). The thermal volumetric strain indicates contractile behavior during heating, consistent with the observations for the normally consolidated, saturated Bonny silt specimen tested by Coccia and McCartney (2012). During cooling, the thermal volumetric strain was not recoverable, and additional thermo-elastic contraction was observed during cooling. This is consistent with the constitutive relationship of Cui et al. (2000). A total volumetric strain of 0.90% was observed for a change in temperature of 27 °C.

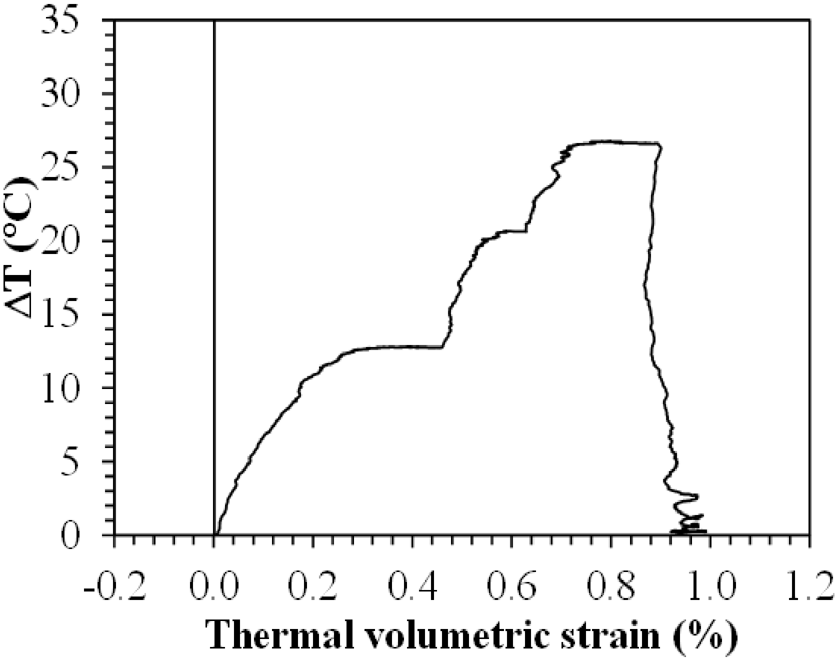

(a)

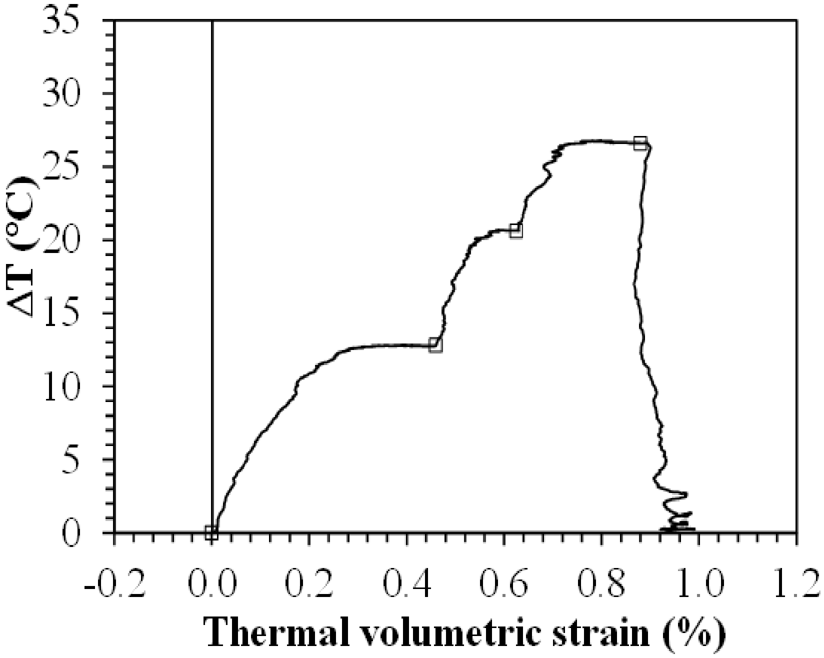

(b)

Figure 6.10: Results from the K1.0-0.7 test: (a) Temperature versus thermal volumetric strain; (b) Temperature versus thermal volumetric strain for points of equilibrium.

The compression curve considering the thermal volume change and the unloading path is shown in Figure 6.11. The compression index $C_c$ and recompression index $C_r$ are equal to 0.014 and 0.0013 respectively. The curve reflects compression during after loading the specimen to normally consolidated conditions.

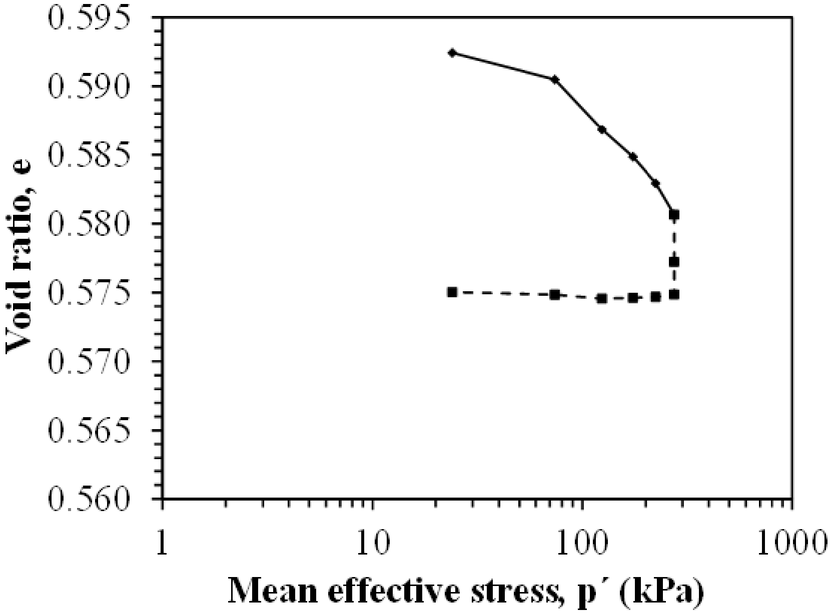

Figure 6.11: Compression curve obtained during application of isotropic stress state to unsaturated Bonny silt specimen for test K1.0-0.7 considering the thermal volume change and unloading path.

### 6.3. Results from Test K0.7-0.7

Test K0.7 was conducted to analyze the effect of stress-induced anisotropy on the thermal volume change. The stages corresponding to the application of a constant suction value along with the subsequent mechanical loading are shown in Figure 6.12.After application of the seating stress in this test, the initial value of suction within the compacted specimen was measured using the tensiometer approach to be 20 kPa. Next, this same suction value was applied to the specimen using the axis translation technique. This involved increasing the total stress, pore air pressure, and pore water pressure in stages to maintain a constant suction of 20 kPa.

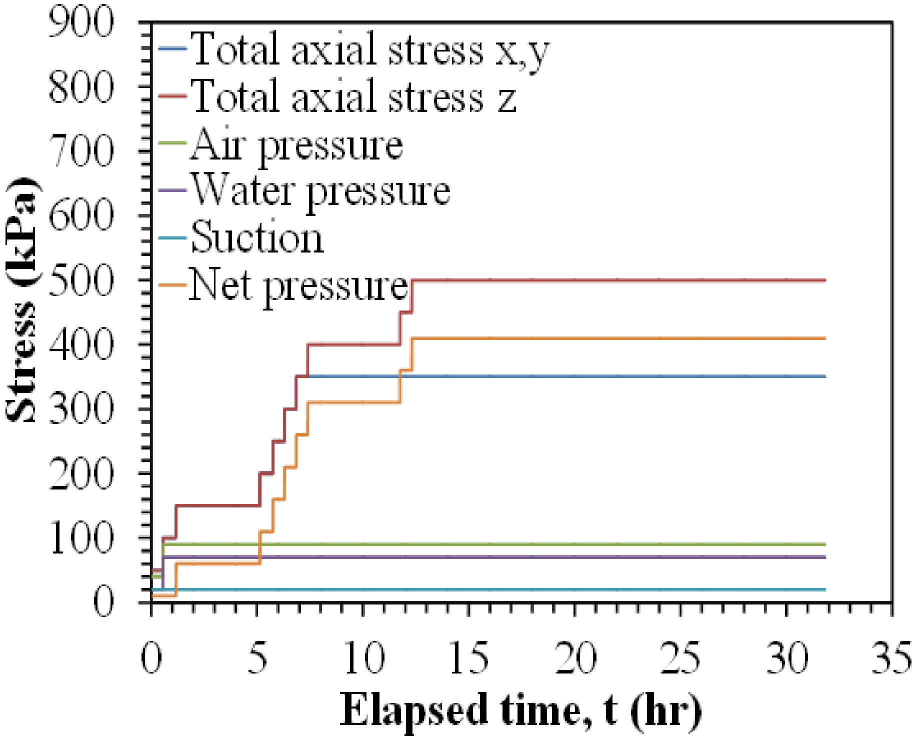

Figure 6.12: Application of total stress, pore air pressure and pore water pressure in stages to maintain constant suction using the axis translation technique for the K0.7-0.7 test.

The changes in applied effective stresses are presented in Figure 6.13. As shown in Figure 6.12, mechanical stresses were applied to the specimen isotropically up to a stress of 350 kPa in the x, y and z directions, then the stress applied in z direction was increased up to 500 kPa to reach a stress ratio of K = 0.7. This approach is different from the approach used by Coccia and McCartney (2012), who unloaded the specimen in one direction to apply different stress ratios.

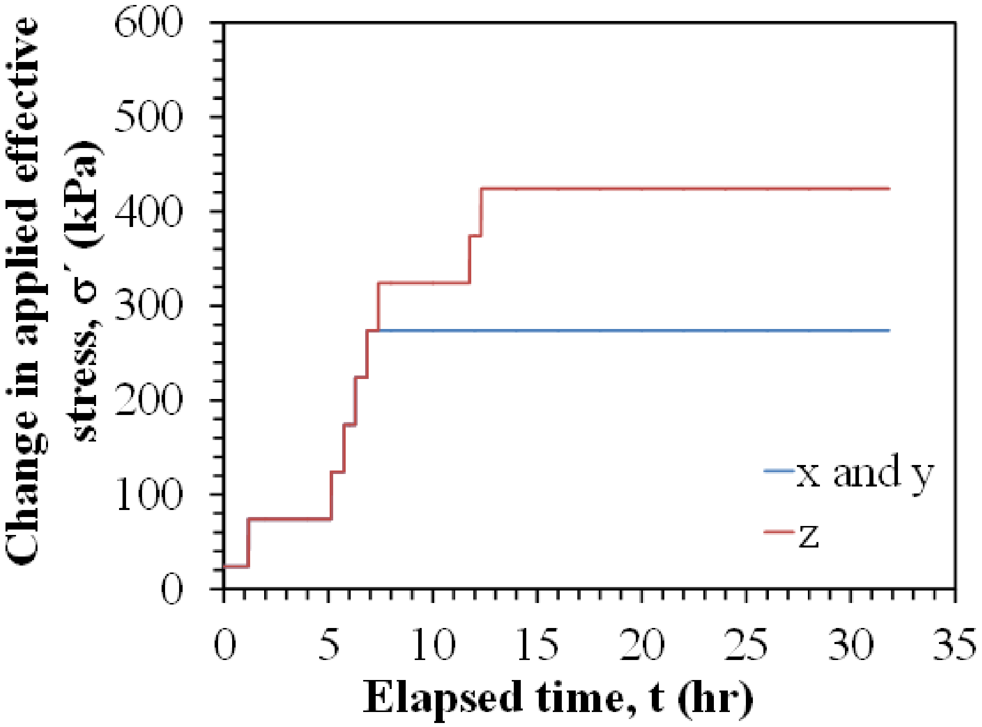

Figure 6.13: Change in effective stress on the soil specimen in the K0.7-0.7 test.

The time series of displacement for the K0.7-0.7 test are shown in Figures 6.14(a) through 6.14(e) for each of the faces. The displacement values shown in these figures were corrected for the effects of mechanical machine deflection of the cell using Equation 4.2. The average displacement for each of the faces is shown in Figure 6.14(f). The average compression of the specimen in each direction was calculated by summing the average displacements on the two opposite faces in each direction. The compressions of each face are shown in Figure 6.14(f). The averages of three LVDTs readings on each face of the soil specimen were calculated for measuring displacements except face X,XX and YY which used the average of two LVDTs (LVDTX1and LVDTX2), (LVDTXX13 and LVDXXT15) and (LVDTYY10 and LVDTYY11), because LVDTX3, LVDTXX14 and LVDTYY12 were not functional during testing.

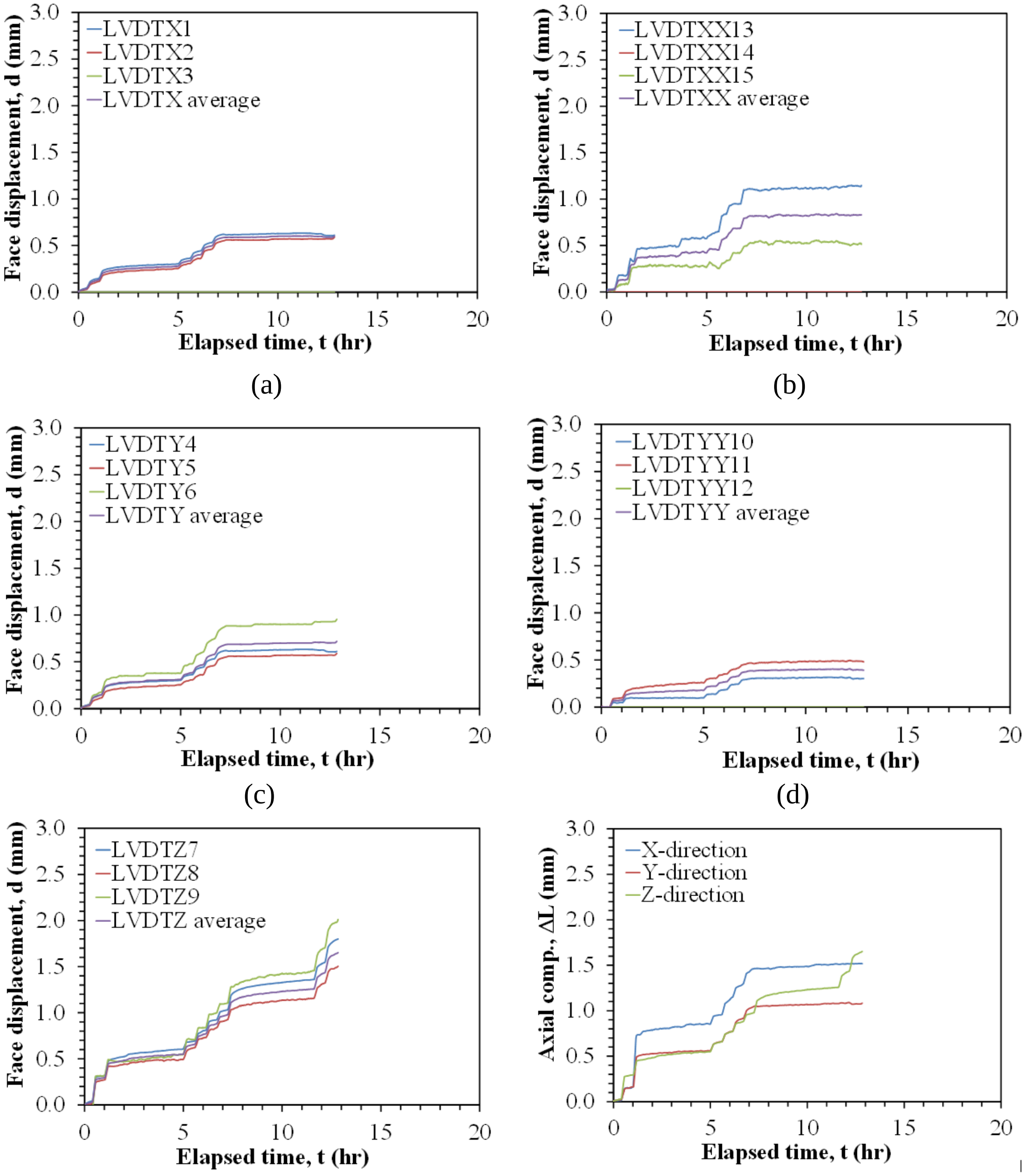

(a) (b)

(c) (d)

(e) (f)

Figure 6.14: Time series for the individual face displacements along with the average value: (a) X face; (b) XX face; (c) Y face; (d) YY face; (e) Z face; (f) Summary of average face displacements.

The time series of the mechanical axial strains for the K0.7-0.7 test were calculated from the values of displacements in Figure 6.14 using Equation 6.1. The mechanical axial strain values are plotted in Figure 6.15.

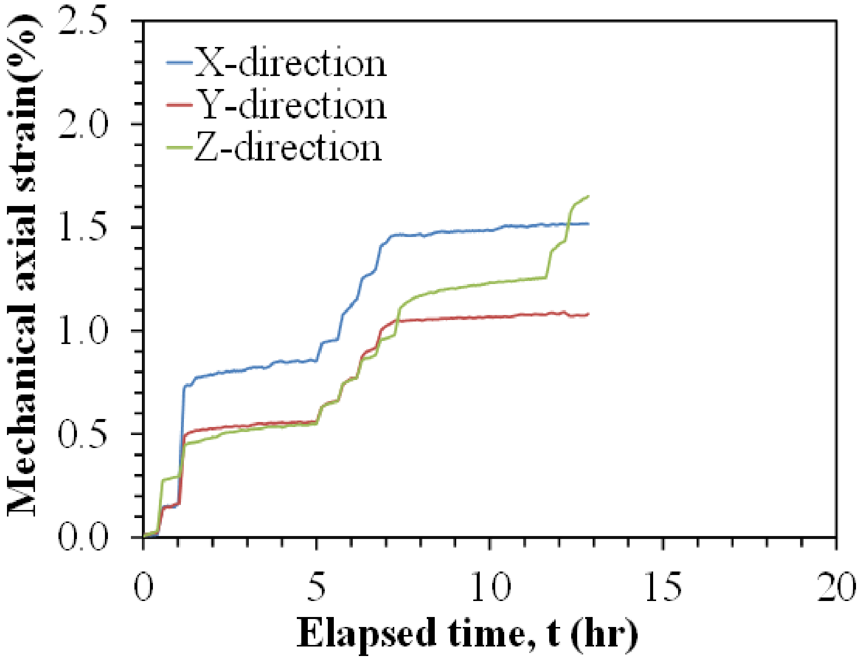

Figure 6.15: Time series for the mechanical strain values in Test K0.7-0.7.

The compression curve for the soil specimen in the K0.7-0.7 test up to the point at which heating was started is shown in Figure 6.16. The void ratio values were calculated from the average mechanical axial strains presented in Figure 6.15. The compression curve indicates that the compacted specimen initially behaves like an overconsolidated soil.

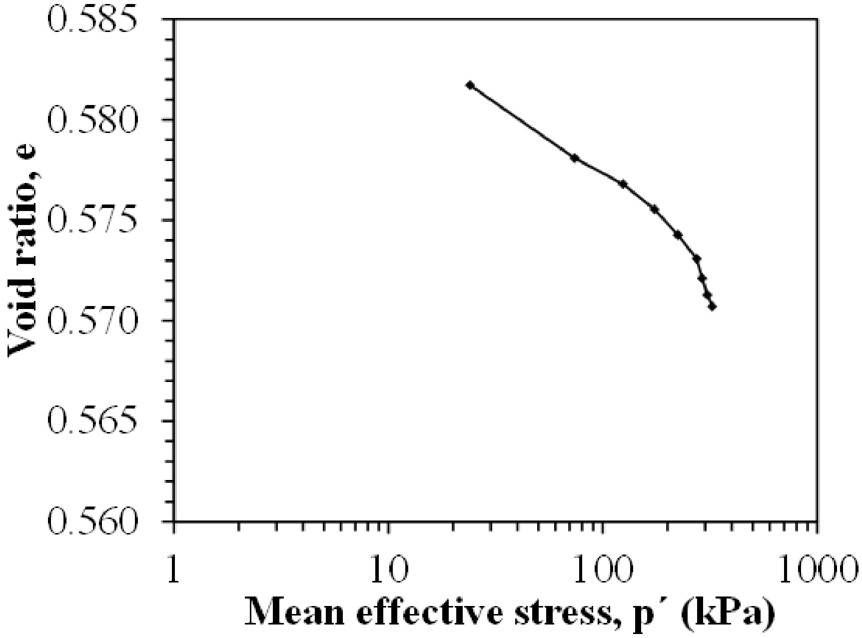

Figure 6.16: Compression curve obtained during application of anisotropic stress state to unsaturated Bonny silt specimen for test K0.7-0.7.

After reaching equilibrium under the final stress state, the temperature of the compacted cubical soil specimen was increased from ambient room temperature to approximately 50 °C in three increments of 10 °C, then cooled back to ambient room temperature in one stage. The change in temperature of the soil specimen during heating and cooling is shown in Figure 6.17(a). The rate of temperature change versus time is shown in Figure 6.17(b). The temperature changes of the soil specimen during testing indicated that the temperature was uniform throughout the specimen at each of the three intervals. Each interval was maintained until the thermal axial strains stabilized.

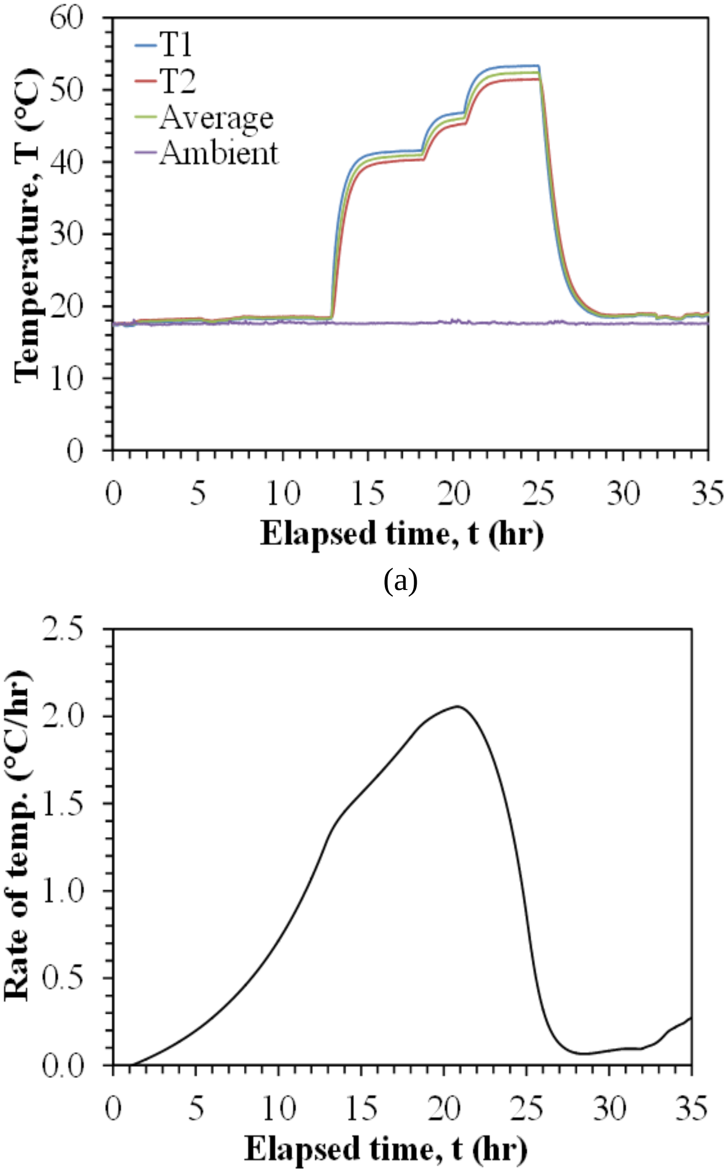

(a)

(b)

Figure 6.17: Results from the K0.7-0.7 test: (a) Change in temperature of the soil specimen; (b) The rate of temperature of the soil specimen.

The time series of thermal displacement for the K0.7-0.7 test are shown in Figures 6.18(a) through 6.18(e) for each of the faces. The thermal displacement values shown in these figures were corrected for the effects of mechanical machine deflection of the cell using Equation 4.2 and thermal machine deflection using Equation 4.4. The average of the thermal displacement for each of the faces is shown in Figure 6.18(f). The average axial strain of the specimen in each direction was calculated by summing the average thermal displacements on the two opposite faces in each direction. The compressions of each face are shown in Figure 6.18(f).

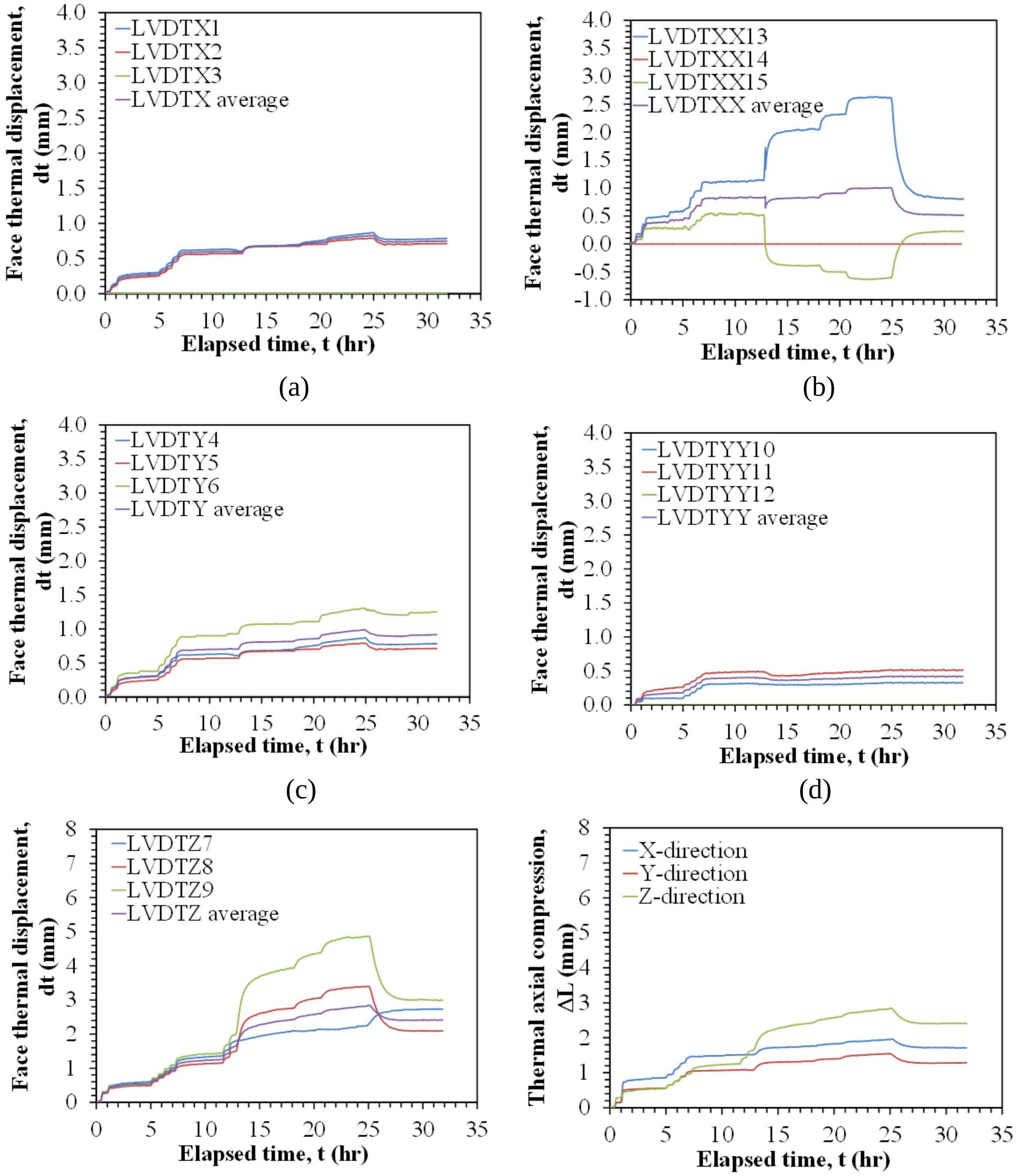

(a) (b) (c) (d) (e) (f)

Figure 6.18: Time series for the individual face thermal displacements along with the average value: (a) X face; (b) XX face; (c) Y face; (d) YY face; (e) Z face; (f) Summary of average face thermal displacements.

The time series of the thermal axial strains for the K0.7-0.7 test were calculated from the values of thermal displacements in Figure 6.18 using Equation 6.1.The axial strain values are plotted in Figure 6.19.

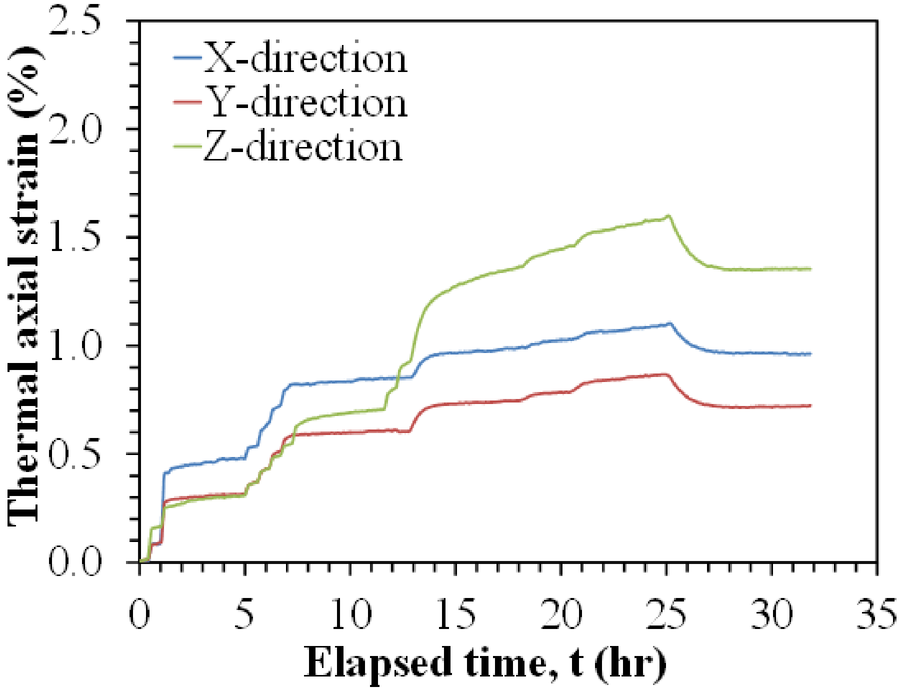

Figure 6.19: Time series for the axial strain values in Test K0.7-0.7

The thermally-induced axial strains during heating-cooling are shown in Figure 6.20(a). The same data without the cooling stage is shown in Figure 6.20(b). Change of temperature versus thermal axial strain during heating for the points of equilibrium is shown in Figure 6.20(c). The data in these figures shows that the thermal axial strains in the x, y and z directions is contractile during heating. However, different from the behavior of the compacted soil specimen tested under isotropic conditions, a greater amount of contraction was observed in the z direction, which was under a greater principal stress. This is consistent with the trend from Coccia and McCartney (2012) for this stress range.

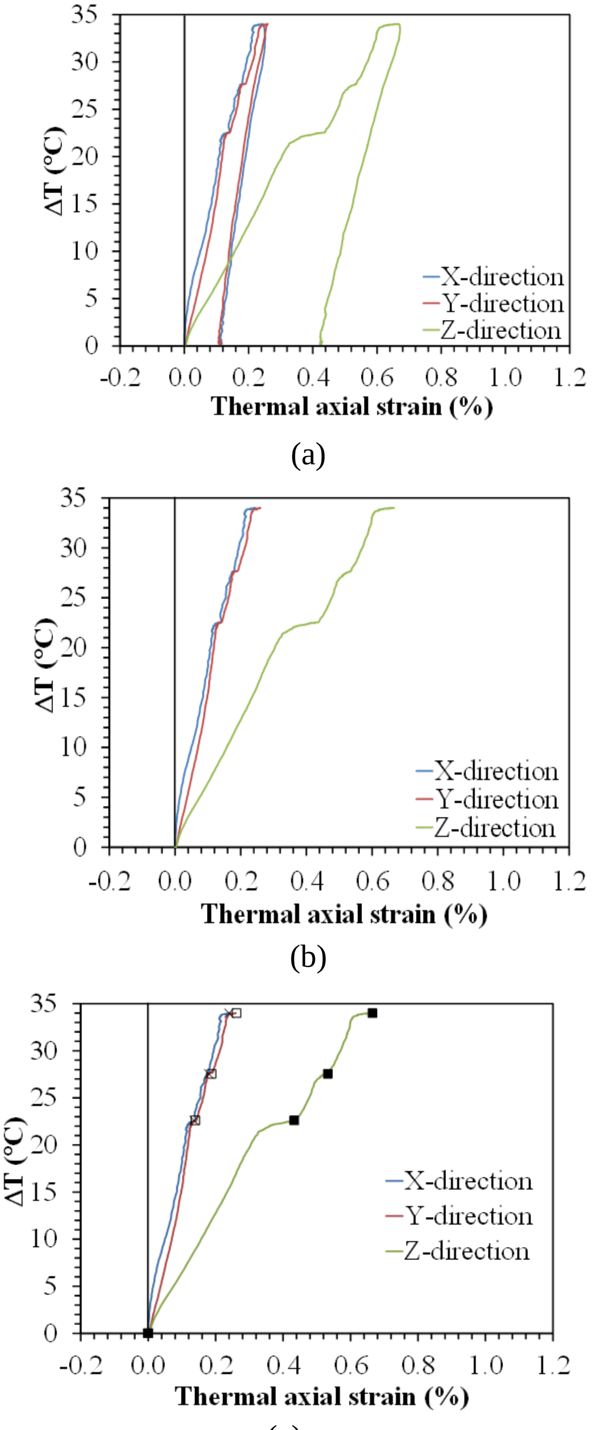

(a)

(b)

(c)

Figure 6.20: Results from the K0.7-0.7 test: (a) Change in temperature versus thermal axial strain for the full heating-cooling cycle; (b) Change in temperature versus thermal axial strain during heating; (c) Change of temperature versus thermal axial strain during heating for the points of equilibrium.

The thermal volumetric strain as a function of the change in temperature is shown in Figure 6.21(a) during heating and cooling. The thermal volumetric strain as a function of the change in temperature for the points of the equilibrium during heating is shown in Figure 6.21(b). Volumetric strain was calculated from Equation 6.2. The thermal volumetric strain indicates contractile behavior during heating, consistent with the observations for the normally consolidated, saturated Bonny silt specimen tested by Coccia and McCartney (2012). During cooling, the thermal volumetric strain was not recoverable, this is consistent with the Laloui and Cekerevac (2008).

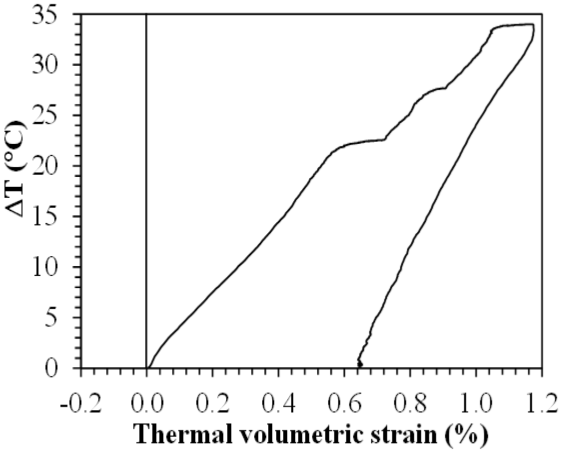

(a)

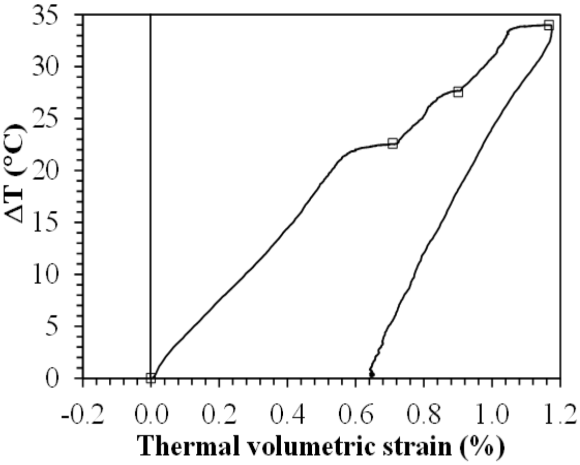

(b)

Figure 6.21: Results from the K0.7-0.7 test: (a) Temperature versus thermal volumetric strain; (b) Temperature versus thermal volumetric strain for points of equilibrium.

The compression curve considering the thermal volume change and the unloading path is shown in Figure 6.22. The compression index $C_c$ and recompression index $C_r$ are equal to 0.025 and 0.0025, respectively.

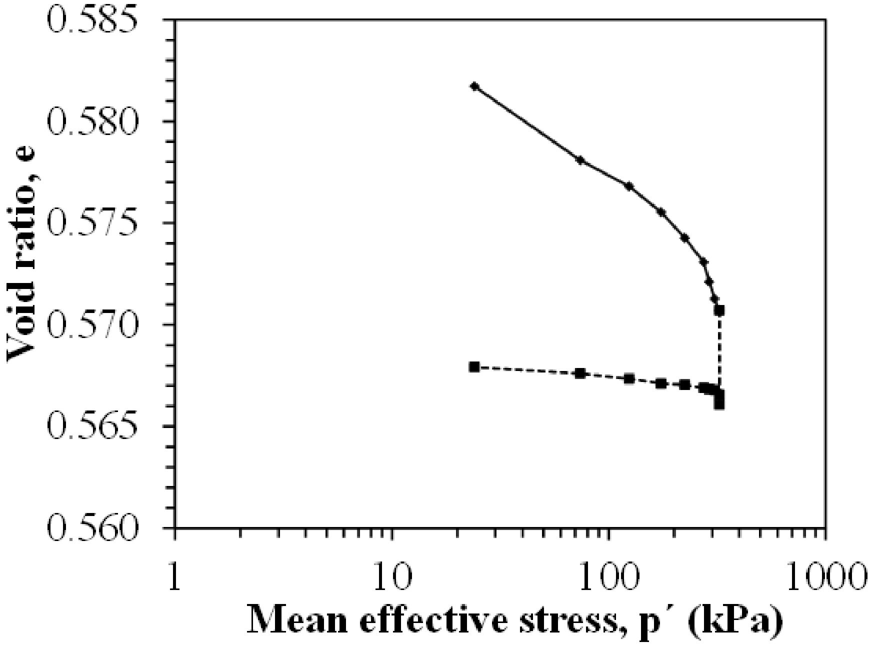

Figure 6.22: Compression curve obtained during application of anisotropic stress state to unsaturated Bonny silt specimen for test K0.7-0.7 considering the thermal volume change and unloading path.

### 6.4. Results from Test K0.5-0.70

Test K0.5 was conducted to analyze the effect of stress state anisotropy on the thermal volume change. After application of the seating stress in this test, the initial value of suction measured within the specimen was applied using the axis translation technique. This involved increasing the total stress, pore air pressure, and pore water pressure in stages to maintain a constant suction 20kPa. The pressure stages corresponding to a constant suction during suction application and subsequent mechanical loading are shown in Figure 6.23.

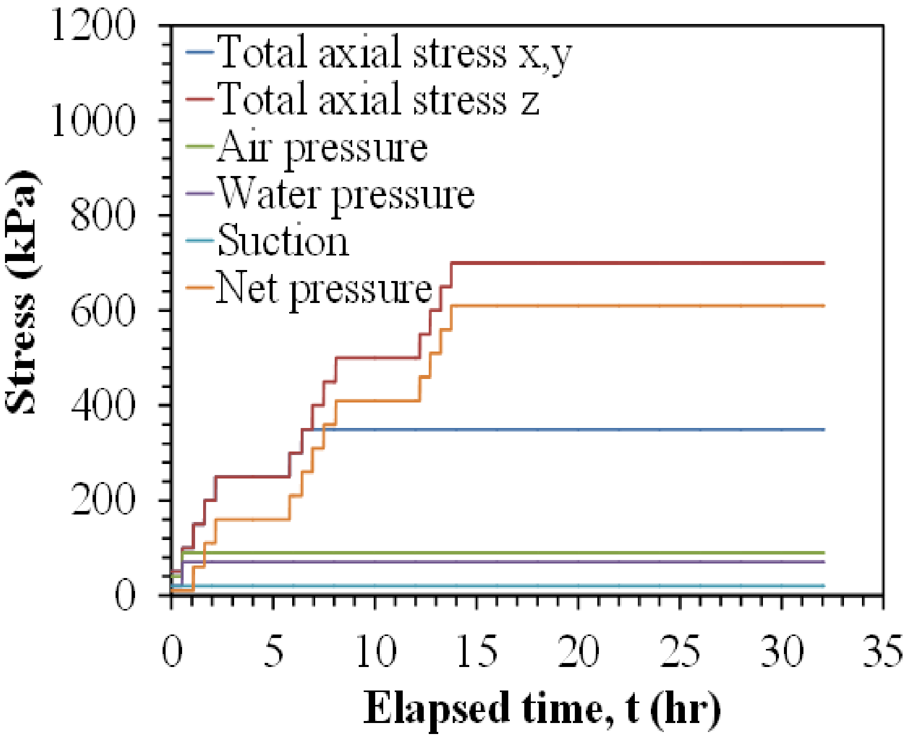

Figure 6.23: Application sequence of total stress, pore air pressure and pore water pressure in stages to maintain constant suction using the axis translation technique for the K0.5-0.7 test.

The changes in applied effective stresses in the K0.5 test are presented in Figure 6.24. Similar to the other tests, an isotropic stress of 350 kPa was applied to the specimen in the x, y and z directions, after which the axial stress in the z direction was increased up to 700 kPa to reach a stress level of K = 0.5.

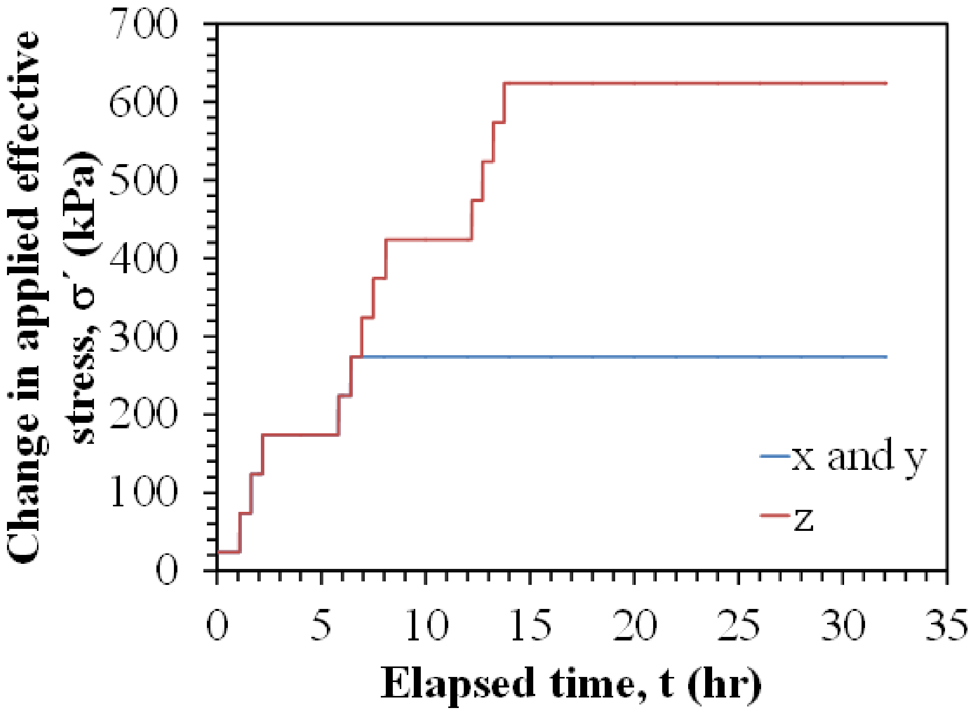

Figure 6.24: Change in effective stress on the soil specimen in the K0.5-0.7 test.

The time series of displacement for the K0.5-0.70 test are shown in Figures 6.25(a) through 6.25(e) for each of the faces. The displacement values shown in these figures were corrected for the effects of mechanical machine deflection of the cell using Equation 4.2. The average displacement for each of the faces is shown in Figure 6.25(f). The average compression of the specimen in each direction was calculated by summing the average displacements on the two opposite faces in each direction. The compressions of each face are shown in Figure 6.25(f). The averages of three LVDTs readings on each face of the soil specimen were calculated for measuring displacements except face X and XX, which used the average of two LVDTs (LVDTX1and LVDTX2), (LVDTXX13 and LVDXXT15), because LVDTX3 and LVDTXX14 were not reading during testing.

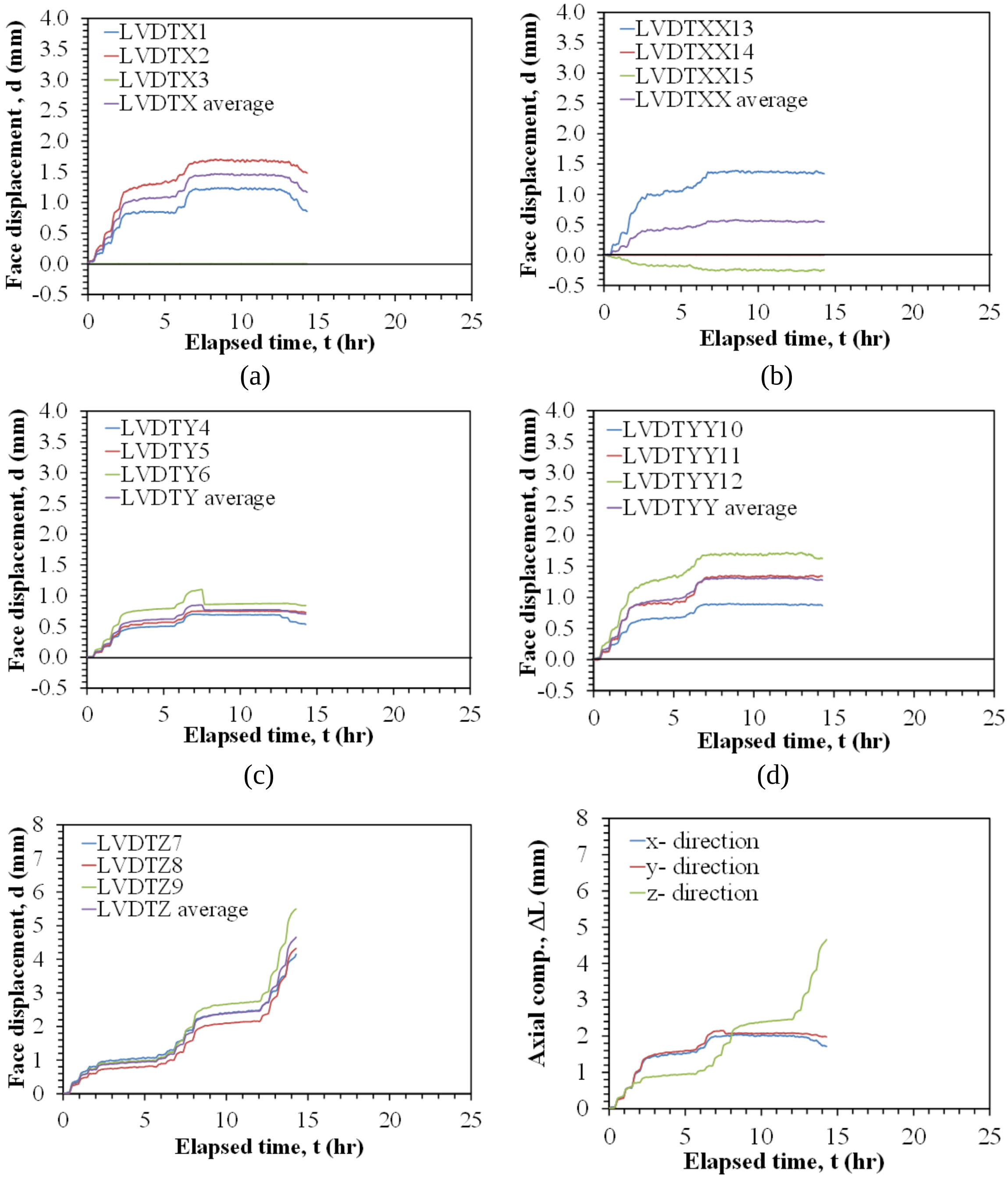

(a) (b) (c) (d) (e) (f)

Figure 6.25: Time series for the individual face displacements along with the average value: (a) X face; (b) XX face; (c) Y face; (d) YY face; (e) Z face; (f) Summary of average face displacements.

The time series of the mechanical axial strains for the K0.5-0.70 test were calculated from the values of displacements in Figure 6.25 using Equation 6.1. The mechanical axial strain values are plotted in Figure 6.26.

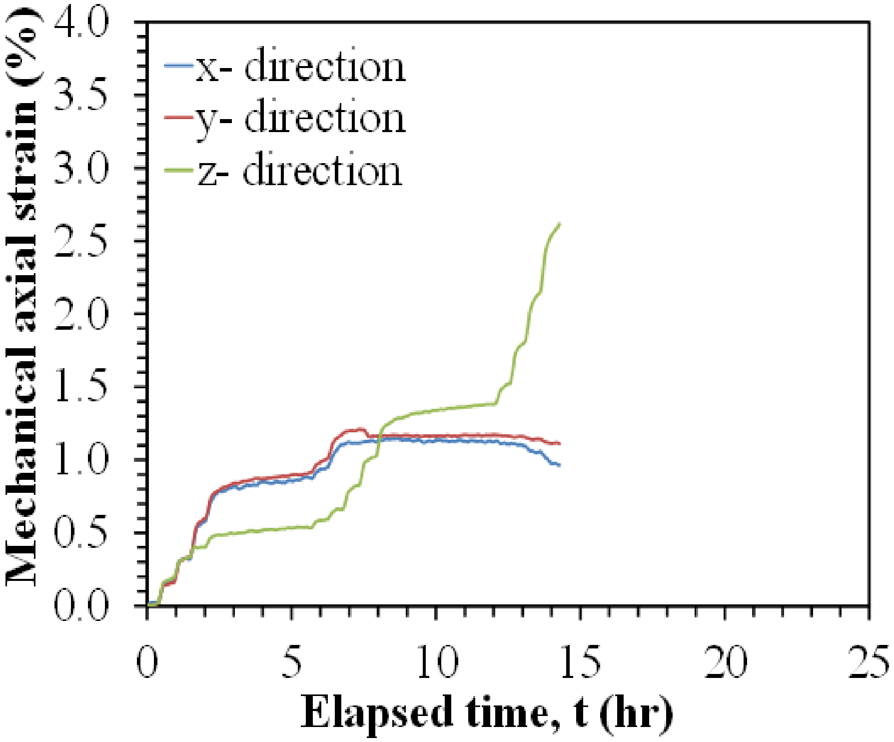

Figure 6.26: Time series for the mechanical strain values in Test K0.5-0.7.

The compression curve for the soil specimen in the K0.5-0.7 test up to the point at which heating was started is shown in Figure 6.27. The void ratio values were calculated from the average mechanical axial strains presented in Figure 6.26. The compression curve indicates that the compacted specimen initially behaves like an overconsolidated soil.

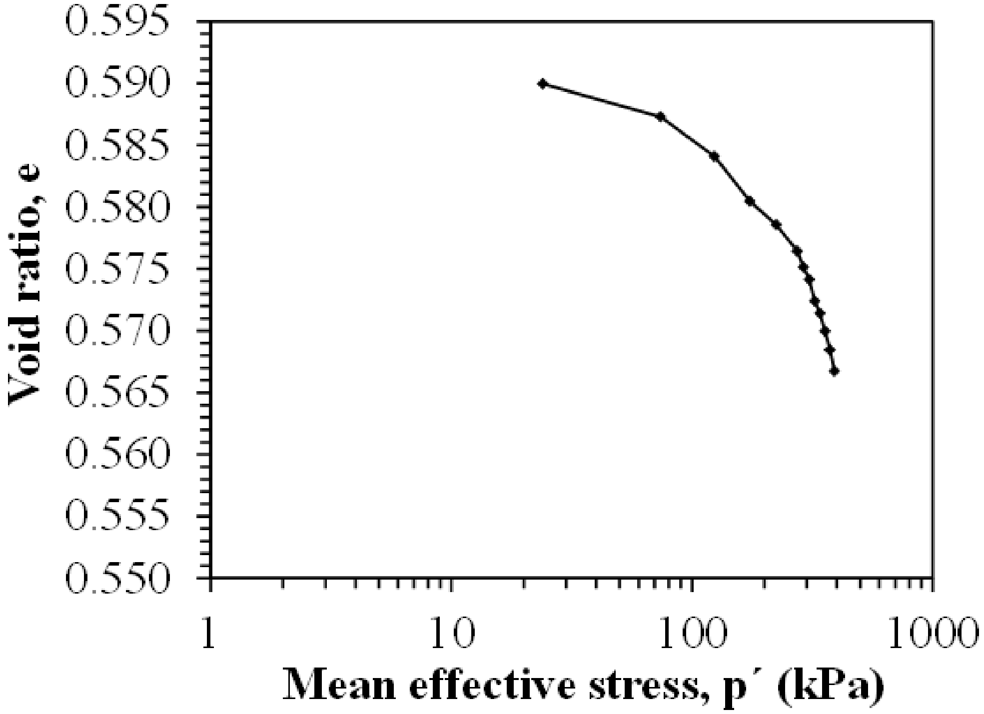

Figure 6.27: Compression curve obtained during application of anisotropic stress state to unsaturated Bonny silt specimen for test K0.5-0.7.

Once the mechanical loading was completed, the temperature of the compacted cubical soil specimen was increased from ambient room temperature to approximately 50 °C in three stages for 10 °C interval, then cooled back to ambient room temperature in one stage. The change in temperature of the soil specimen during heating and cooling is shown in Figure 6.28(a). The rate of temperature change versus time is shown in Figure 6.28(b). The temperature changes of the soil specimen during testing indicated that the temperature was uniformity at lower and higher temperature. Each interval was maintained until the thermal axial strains stabilized.

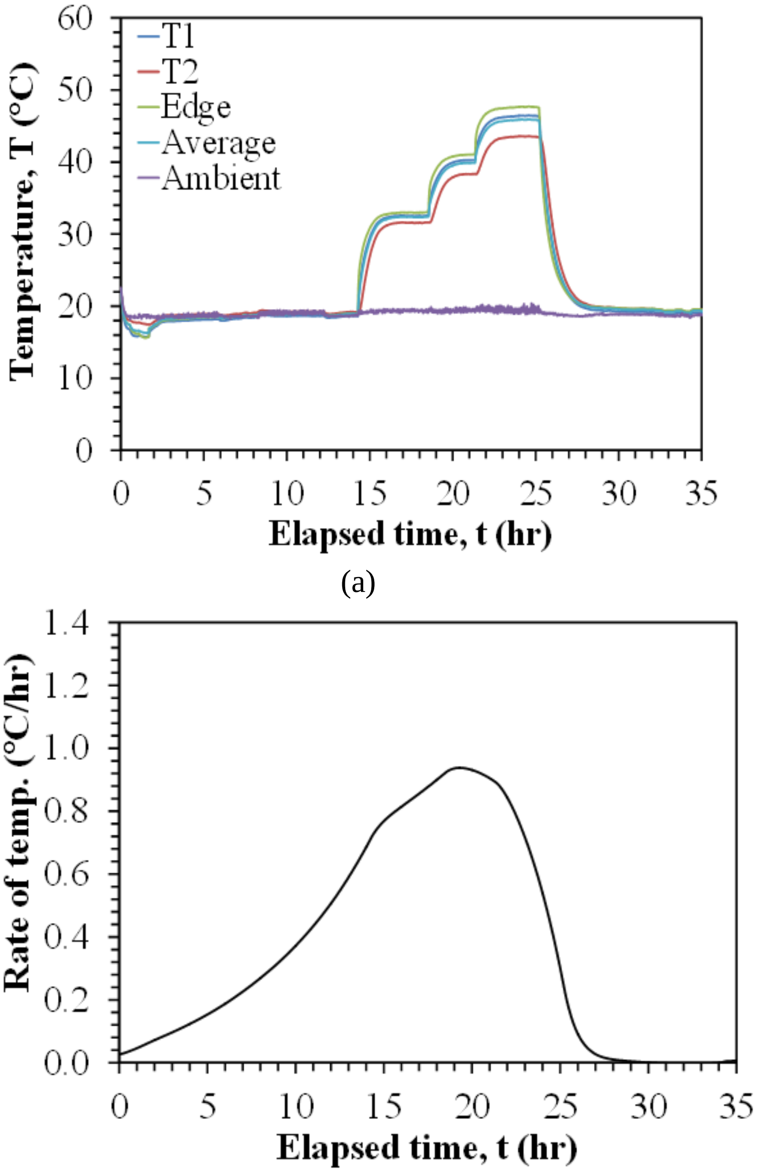

(a)

(b)

Figure 6.28: Results from the K0.5-0.7 test: (a) Change in temperature of the soil specimen; (b) The rate of temperature of the soil specimen.

The time series of thermal displacement for the K0.5-0.7 test are shown in Figures 6.29(a) through 6.29(e) for each of the faces. The thermal displacement values shown in these figures were corrected for the effects of mechanical machine deflection of the cell using Equation 4.2 and thermal machine deflection using Equation 4.4. The average thermal displacement for each of the faces is shown in Figure 6.29(f). The average axial strain of the specimen in each direction

was calculated by summing the average thermal displacements on the two opposite faces in each direction. The compressions of each face are shown in Figure 6.29(f).

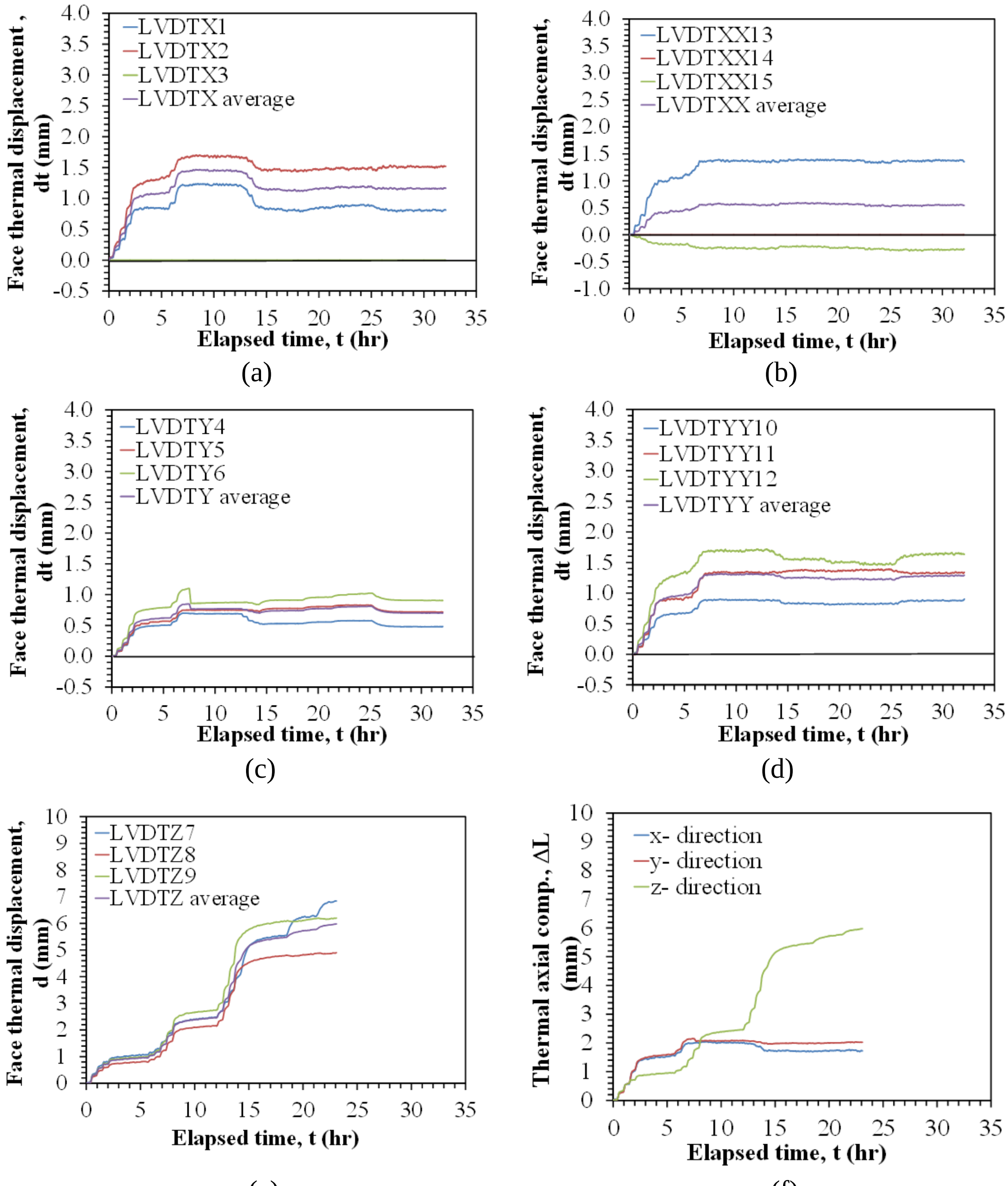

(a) (b) (c) (d) (e) (f)

Figure 6.29: Time series for the individual face thermal displacements along with the average value: (a) X face; (b) XX face; (c) Y face; (d) YY face; (e) Z face; (f) Summary of average face thermal displacements

The time series of the thermal axial strains for the K0.5-0.7 test were calculated from the values of thermal displacements in Figure 6.29 using Equation 6.1. The axial strain values are plotted in Figure 6.30.

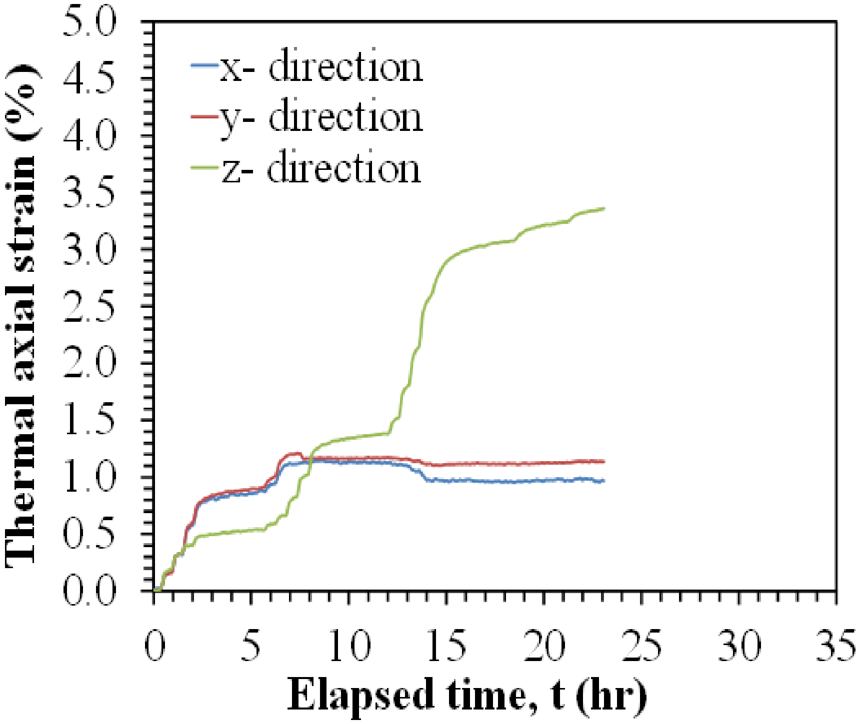

Figure 6.30: Time series for the axial strain values in Test K0.5-0.7.

The thermally-induced axial strains during heating-cooling are shown in Figure 6.31(a). The same data without the cooling stage is shown in Figure 6.31(b). Change of temperature versus thermal axial strain during heating for the points of equilibrium is shown in Figure 6.31(c). The data in these figures show that the thermal axial strain in the x, y and z directions indicate contractile behavior during heating as expected for a normally-consolidated soil specimen. This is consistent with the trend from Coccia and McCartney (2012) for this stress range.

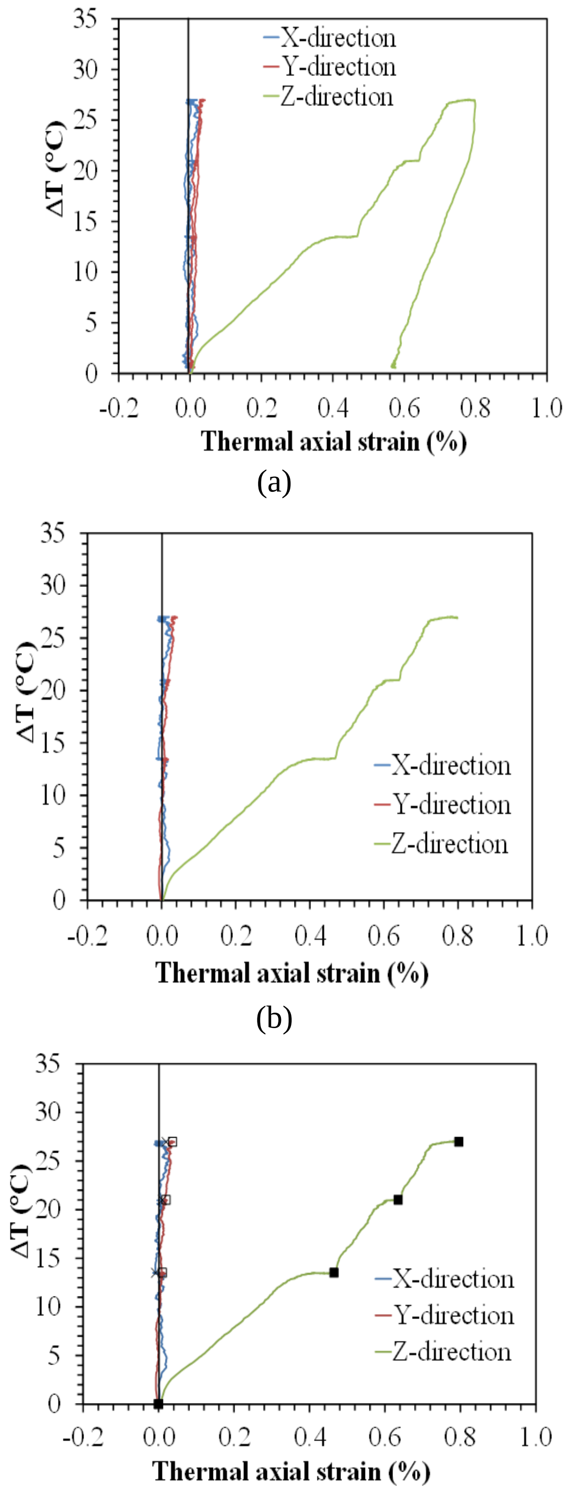

(a)

(b)

(c)

Figure 6.31: Results from the K0.5-0.7 test: (a) Change in temperature versus thermal axial strain for the full heating-cooling cycle; (b) Change in temperature versus thermal axial strain during heating; (c) Change of temperature versus thermal axial strain during heating for the points of equilibrium.

The thermal volumetric strain was calculated from the thermal axial strains using Equation 6.2.The thermal volumetric strain as a function of the change in temperature is shown in Figure 6.32(a) during heating and cooling. The thermal volumetric strain as a function of the change in temperature for the points of the equilibrium during heating is shown in Figure 6.32(b). The thermal volumetric strain indicates contractile behavior during heating, consistent with the observations for the normally consolidated, saturated Bonny silt specimen tested by Coccia and McCartney (2012). During cooling, the thermal volumetric strain was not recoverable. This is consistent with the constitutive relationship of Cui et al. (2000). A total volumetric strain of 0.8% was observed for a change in temperature of 28 °C.

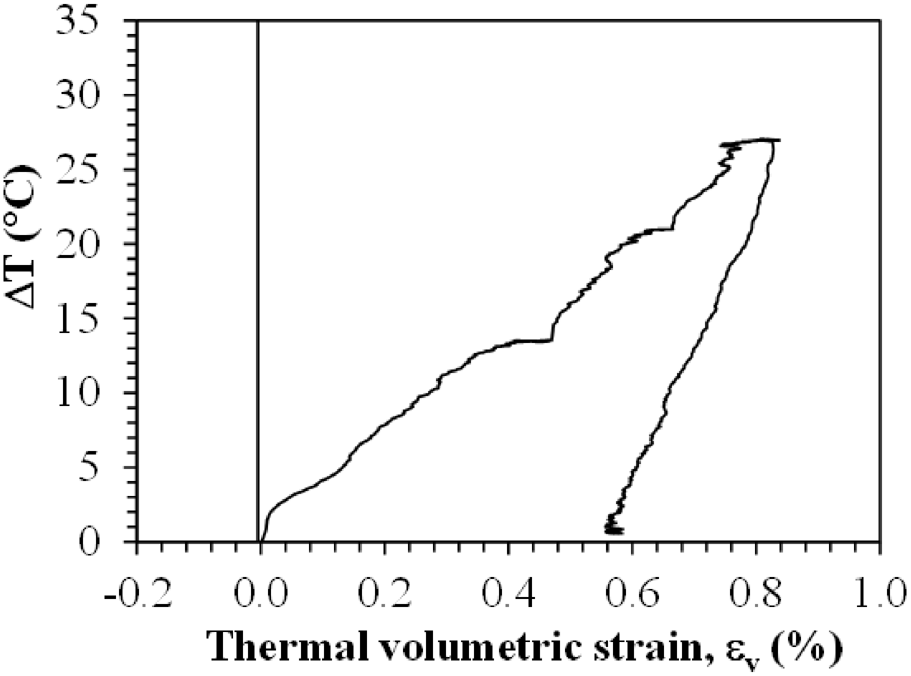

(a)

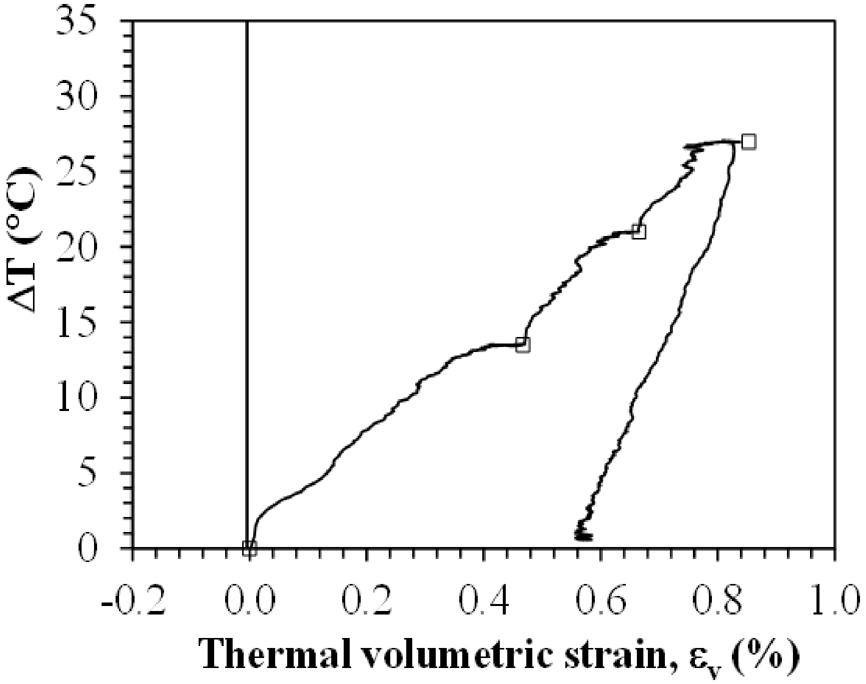

(b)

Figure 6.32: Results from the K0.5-0.7 test: (a) Temperature versus thermal volumetric strain; (b) Temperature versus thermal volumetric strain for points of equilibrium.

The compression curve considering the thermal volume change and the unloading path is shown in Figure 6.33. The compression index $C_c$ and recompression index $C_r$ are equal to 0.051 and 0.0051, respectively.

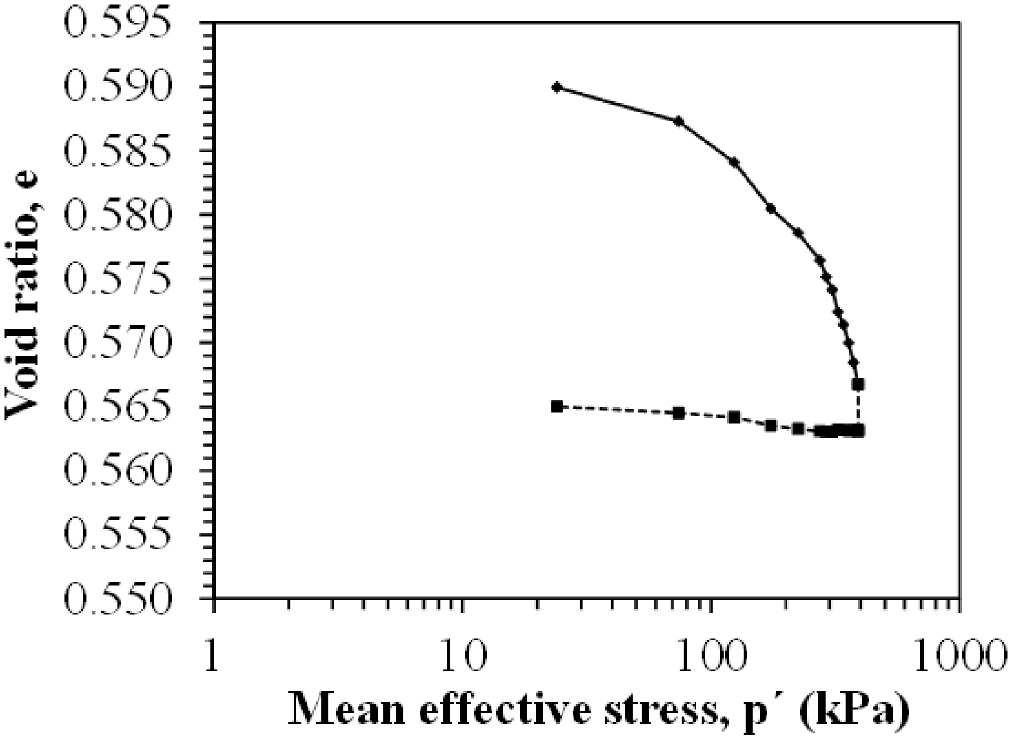

Figure 6.33: Compression curve obtained during application of anisotropic stress state to unsaturated Bonny silt specimen for test K0.5-0.7considering the thermal volume change and unloading path.

### 6.5. Results from Test K1.0-0.8

After application of the seating stress in this test, the initial value of suction measured within the specimen using the tensiometer approach of 10 kPa was applied using the axis translation technique. This involved increasing the total stress, pore air pressure, and pore water pressure in stages to maintain a constant suction of 10 kPa. The stages corresponding to application of a constant suction value using the axis translation technique are shown in Figure 6.34. The increases in total stress applied to the specimen to mechanically load the specimen in isotropic conditions are also shown in this figure.

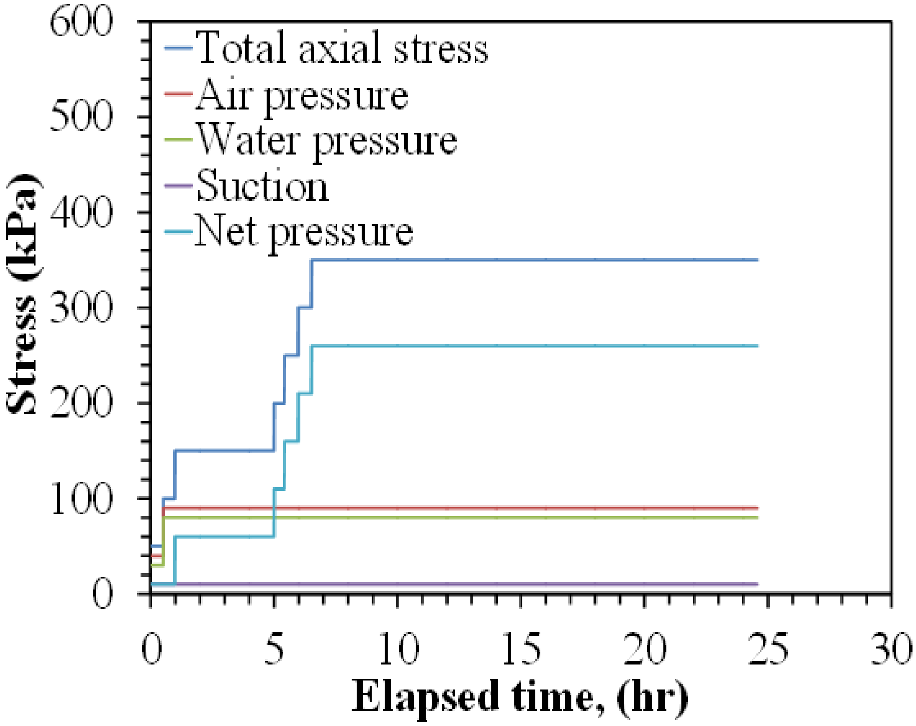

Figure 6.34: Application of total stress, pore air pressure and pore water pressure in stages to maintain constant suction using the axis translation technique for the K1.0-0.8 test.

The changes in applied effective stresses with time are presented in Figure 6.35. Effective stress was calculated from Equation 2.1. The test was mechanically loaded to a total isotropic stress of 350 kPa in the x, y and z directions, which corresponds to a mean effective stress of 268 kPa. The isotropic total stresses were applied by increasing the water pressure in the bladders in stages and allowing sufficient time for the excess pore water pressure to dissipate. Specifically, each loading increment was applied until all of the face deformations had stabilized.

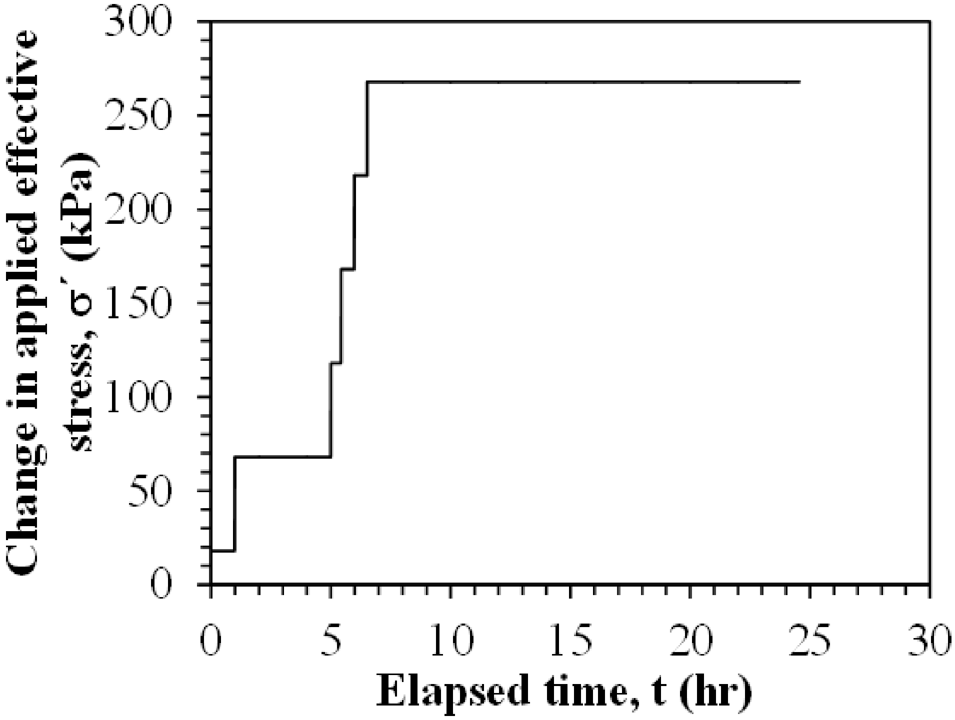

Figure 6.35: Change in effective stress on the soil specimen in the K1.0-0.8 test.

The time series of displacement for the K1.0-0.8 test are shown in Figures 6.36(a) through 6.36(e) for each of the faces. The displacement values shown in these figures were corrected for the effects of machine deflection of the cell using Equation 4.2. The average displacement for each of the faces is shown in Figure 6.36(f). The average compression of the specimen in each direction was calculated by summing the average displacements on the two opposite faces in each direction. The compressions of each face are shown in Figure 6.36(f). The averages of three LVDTs readings on each face of the soil specimen were calculated for measuring displacements except face X, XX,Y and Z which used the average of two LVDTs (LVDTX1 and LVDTX2),(LVDTXX14 and LVDXXT15), (LVDTY5 and LVDTY6) and (LVDTZ7 and LVDTZ8) because LVDTX3, LVDTXX13, LVDTY4 and LVDTZ9 were not functional during testing.

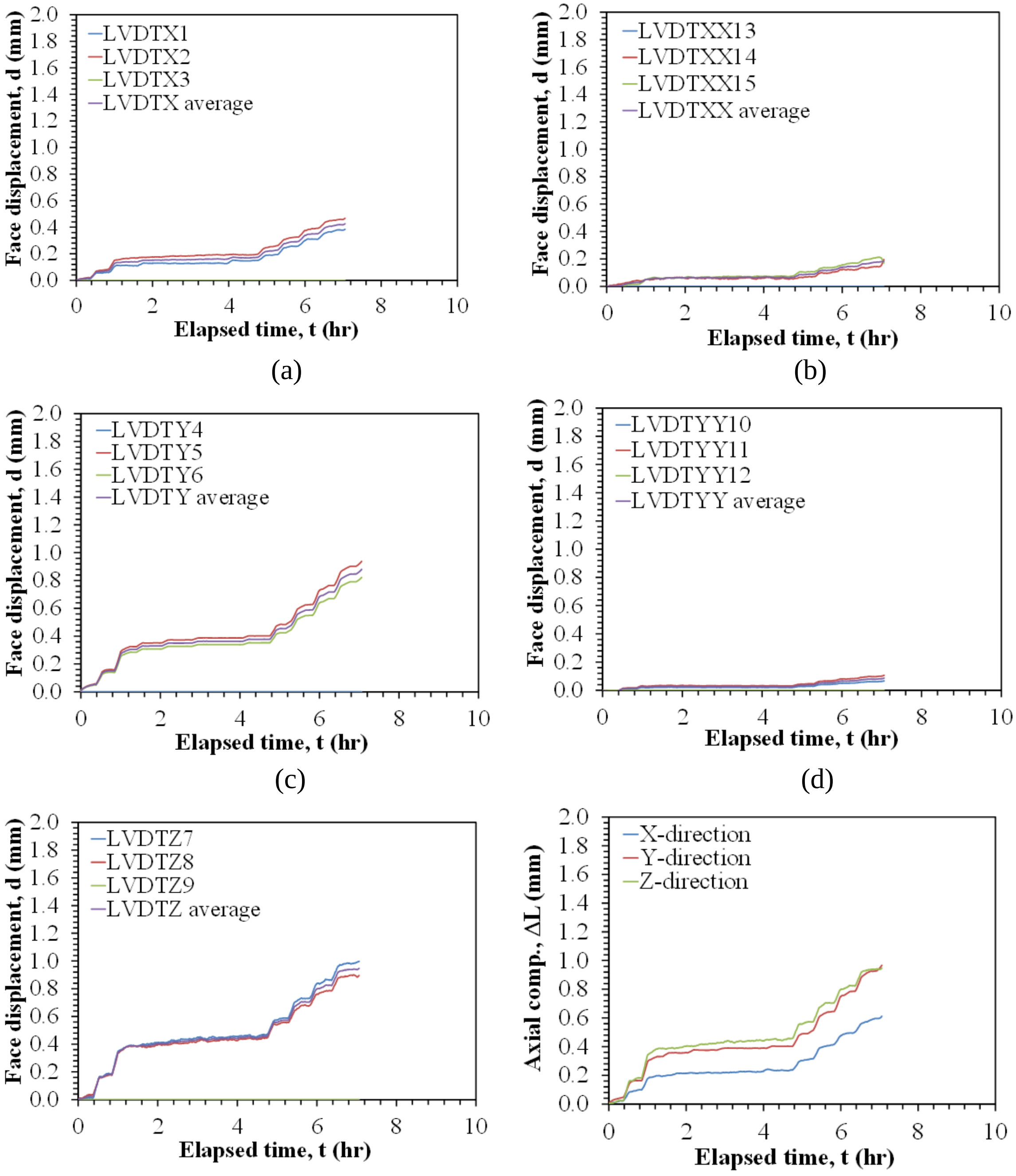

(a) (b) (c) (d) (e) (f)

Figure 6.36: Time series for the individual face displacements along with the average value: (a) X face; (b) XX face; (c) Y face; (d) YY face; (e) Z face; (f) Summary of average face displacements.

The time series of the mechanical axial strains for the K1.0-0.8 test were calculated from the values of displacements in Figure 6.36 by using Equation 6.1. The mechanical axial strain values are plotted in Figure 6.37.

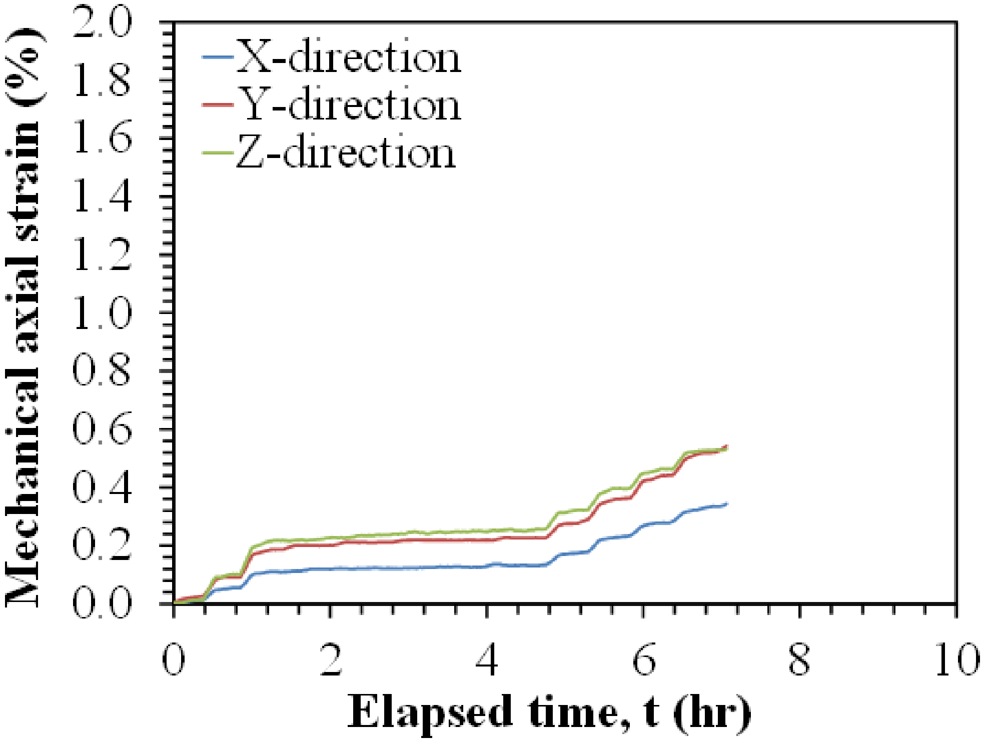

Figure 6.37: Time series for the mechanical strain values in Test K1.0-0.8.

The compression curve for the soil specimen in the K1.0-0.8 test up to the point at which heating was started is shown in Figure 6.38. The void ratio values were calculated from the average mechanical axial strains presented in Figure 6.37. The compression curve indicates that the compacted specimen initially behaves like an overconsolidated soil.

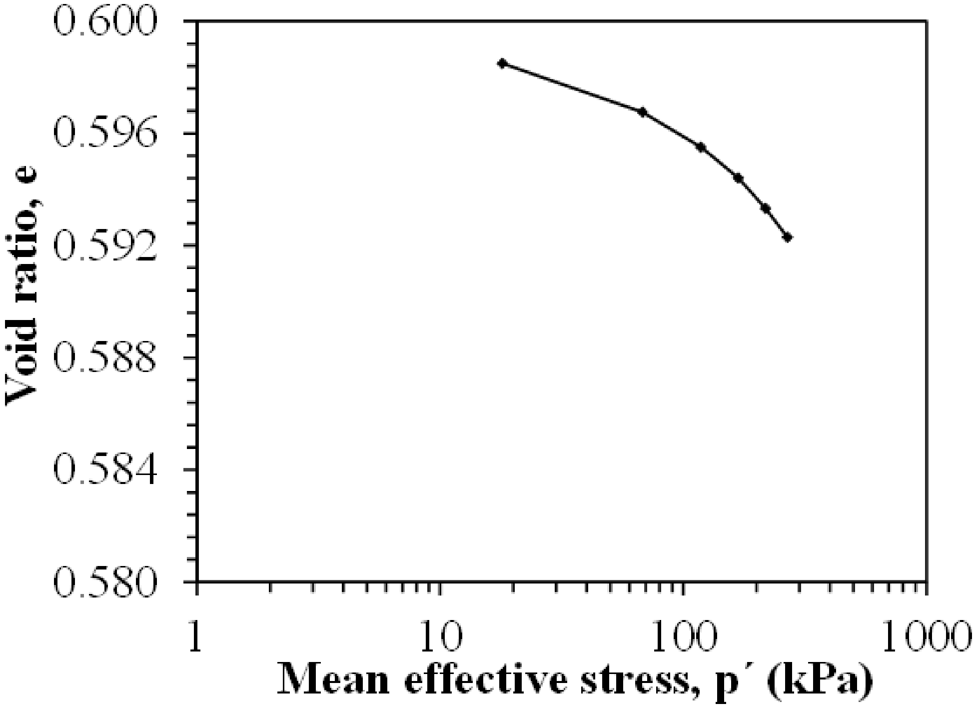

Figure 6.38: Compression curve obtained during application of isotropic stress state to unsaturated Bonny silt specimen for test K1.0-0.8.

Once the mechanical stresses were applied to the specimen, the temperature applied to the faces of the specimen was increased from the ambient room temperature of approximately 20 °C to a temperature of approximately 50 °C in three 10 °C stages, after which it was cooled back to ambient room temperature in one stage. The changes in temperature of the soil specimen at the edges and within the specimen during heating and cooling are shown in Figure 6.39(a). The rate of temperature change versus time is shown in Figure 6.39(b). The temperature changes of the soil specimen reached a stable value at each interval, which was maintained until the thermal axial strains reached equilibrium.

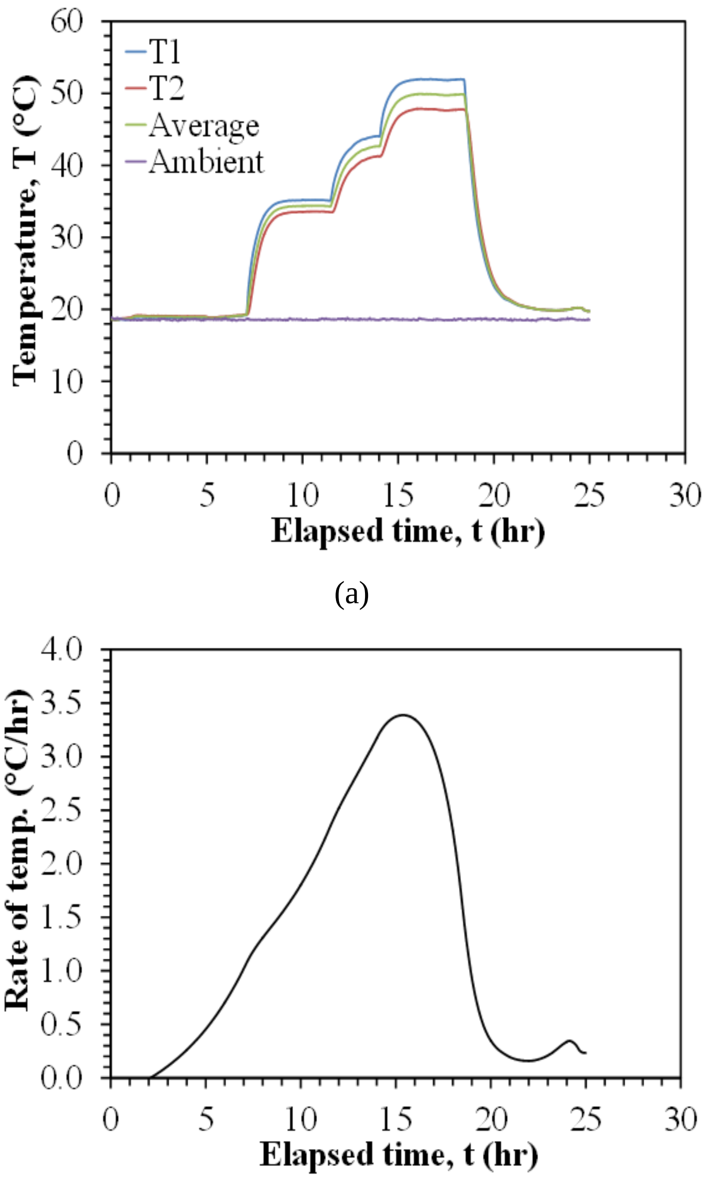

(a)

(b)

Figure 6.39: Results from the K1.0-0.8 test: (a) Change in temperature of the soil specimen; (b) The rate of temperature of the soil specimen.

The time series of thermal displacement for the K1.0-0.8 test are shown in Figures 6.40(a) through 6.40(e) for each of the faces. The thermal displacement values shown in these figures were corrected for the effects of mechanical machine deflection of the cell using Equation 4.2 and thermal machine deflection using Equation 4.4. The average thermal displacement for each of the faces is shown in Figure 6.40(f). The average axial strain of the specimen in each direction

was calculated by summing the average thermal displacements on the two opposite faces in each direction. The compressions of each face are shown in Figure 6.40(f).

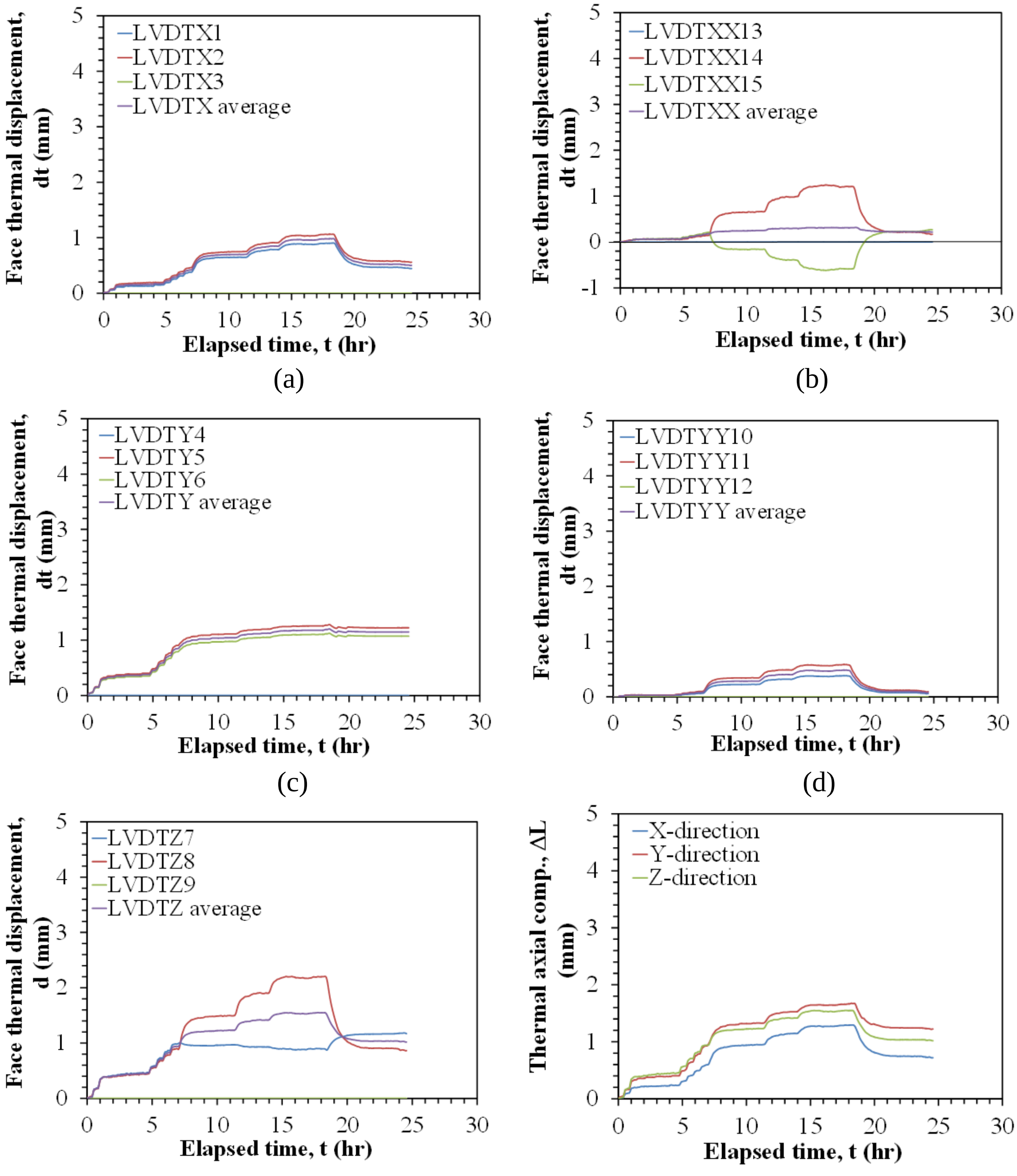

(a) (b) (c) (d) (e) (f)

Figure 6.40: Time series for the individual face thermal displacements along with the average value: (a) X face; (b) XX face; (c) Y face; (d) YY face; (e) Z face; (f) Summary of average face thermal displacements.

The time series of the thermal axial strains for the K1.0-0.8 test were calculated from the values of thermal displacements in Figure 6.40 by using Equation 6.1. The axial strain values are plotted in Figure 6.41.

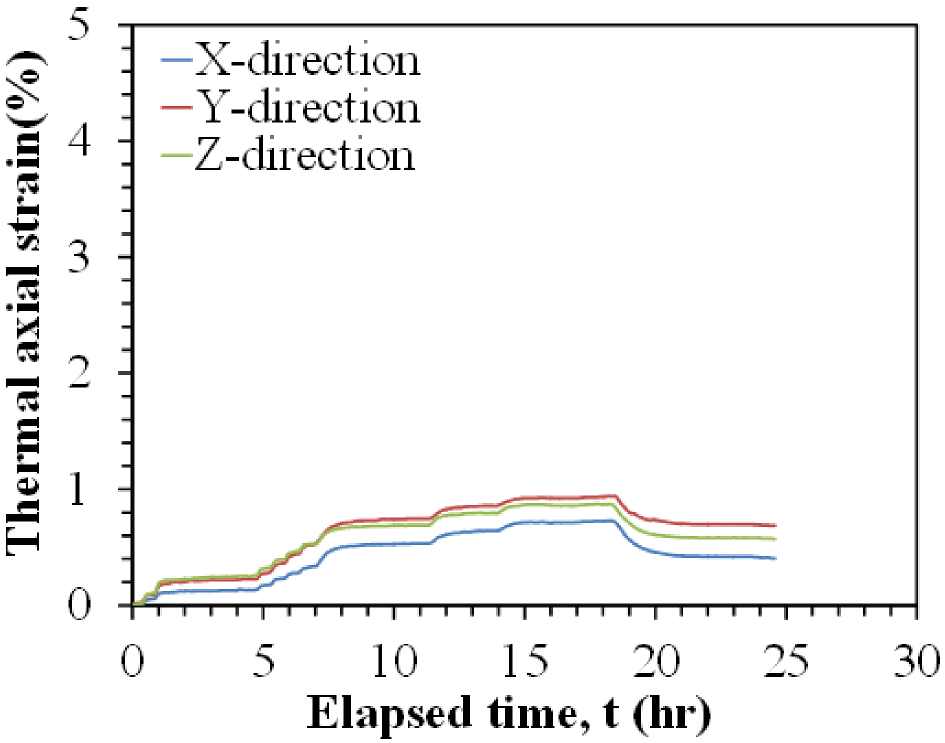

Figure 6.41: Time series for the axial strain values in Test K1.0-0.8.

The thermally-induced axial strains during the heating-cooling cycle are shown in Figure 6.42(a). The same data without the cooling stage is shown in Figure 6.42(b). Change of temperature versus thermal axial strain during heating for the points of equilibrium is shown in Figure 6.42(c). The data in these figures show that the thermal axial strain in the x, y and z directions indicate contractile behavior during heating as expected for a normally-consolidated soil specimen (Uchaipichat and Khalili 2009). This behavior is in agreement with the isotropic test on normally-consolidated, saturated Bonny silt reported by Coccia and McCartney (2012).

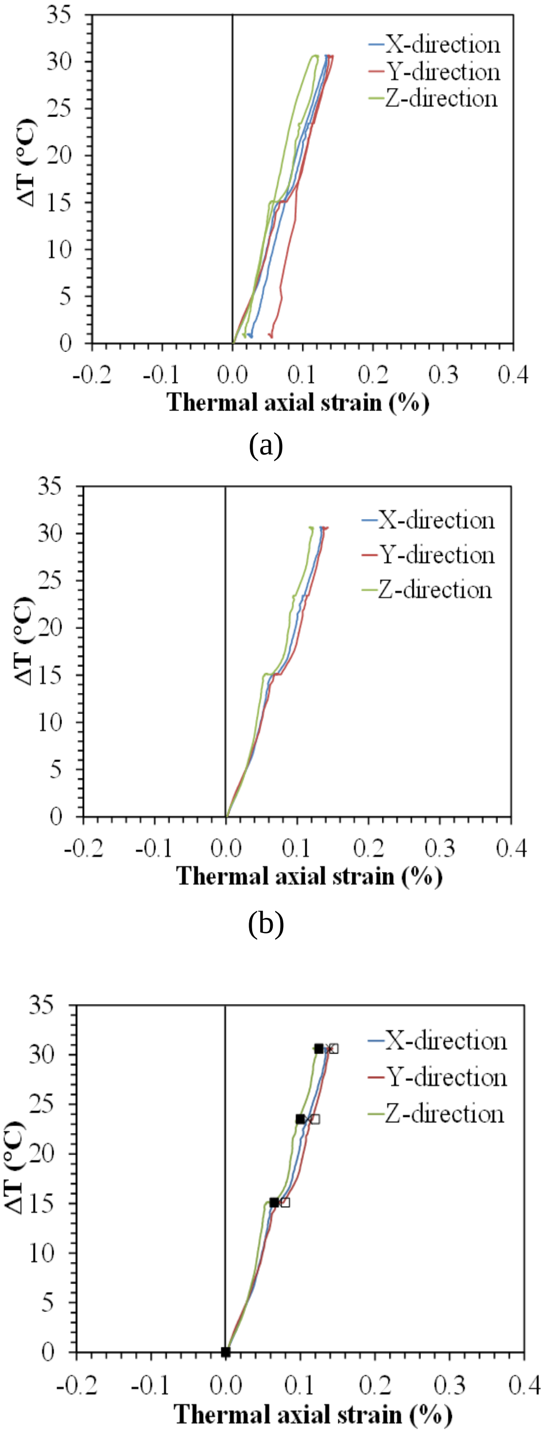

(a)

(b)

(c)

Figure 6.42: Results from the K1.0-0.8 test: (a) Change in temperature versus thermal axial strain for the full heating-cooling cycle; (b) Change in temperature versus thermal axial strain during heating; (c) Change of temperature versus thermal axial strain during heating for the points of equilibrium.

The thermal volumetric strain was calculated from the thermal axial strains by using Equation 6.2. The thermal volumetric strain as a function of the change in temperature is shown in Figure 6.43(a) during heating and cooling. The thermal volumetric strain as a function of the change in temperature for the points of the equilibrium during heating is shown in Figure 6.43(b). The thermal volumetric strain indicates contractile behavior during heating, consistent with the observations for the normally consolidated, saturated Bonny silt specimen tested by Coccia and McCartney (2012). During cooling, the thermal volumetric strain was not recoverable.

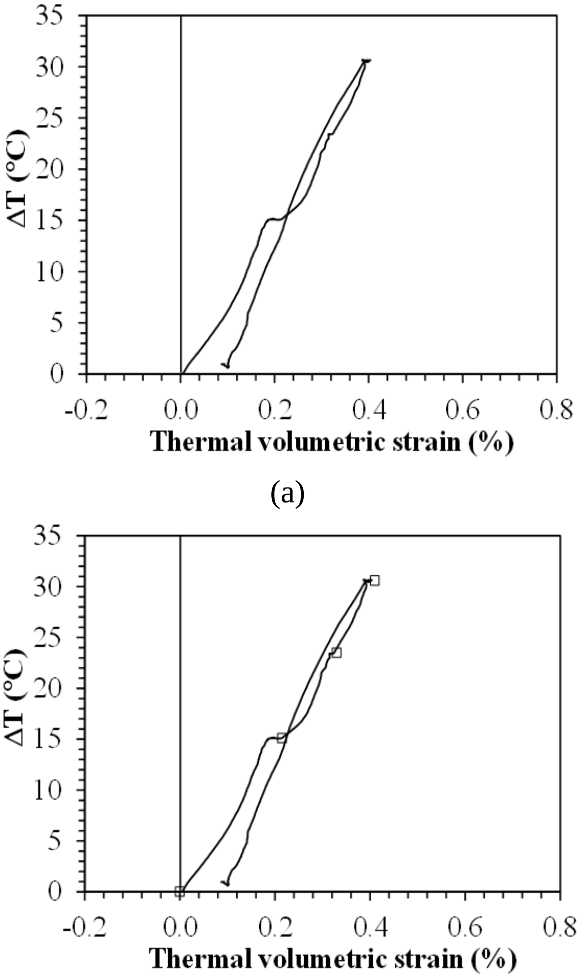

(a)

(b)

Figure 6.43: Results from the K1.0-0.8 test: (a) Temperature versus thermal volumetric strain; (b) Temperature versus thermal volumetric strain for points of equilibrium

The compression curve considering the thermal volume change and the unloading path is shown in Figure 6.44. The compression index $C_c$ and recompression index $C_r$ are equal 0.01 and 0.0009, respectively.

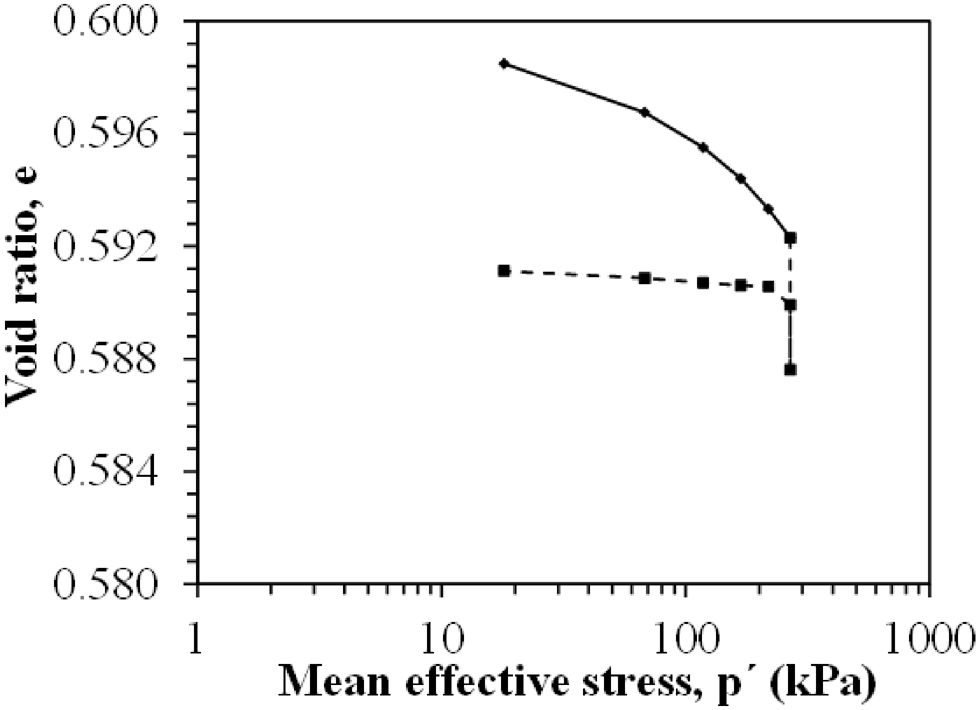

Figure 6.44: Compression curve obtained during application of isotropic stress state to unsaturated Bonny silt specimen for test K1.0-0.8 considering the thermal volume change and unloading path.

### 6.6. Results from Test K0.7-0.8

Test K0.7 was conducted to analyze the effect of stress state anisotropy on the thermal volume change. After application of the seating stress in this test, the initial value of suction measured within the specimen was applied using the axis translation technique. This involved increasing the total stress, pore air pressure, and pore water pressure in stages to maintain a constant low suction 10 kPa. The pressure stages corresponding to a constant suction during suction application and subsequent mechanical loading are shown in Figure 6.45.

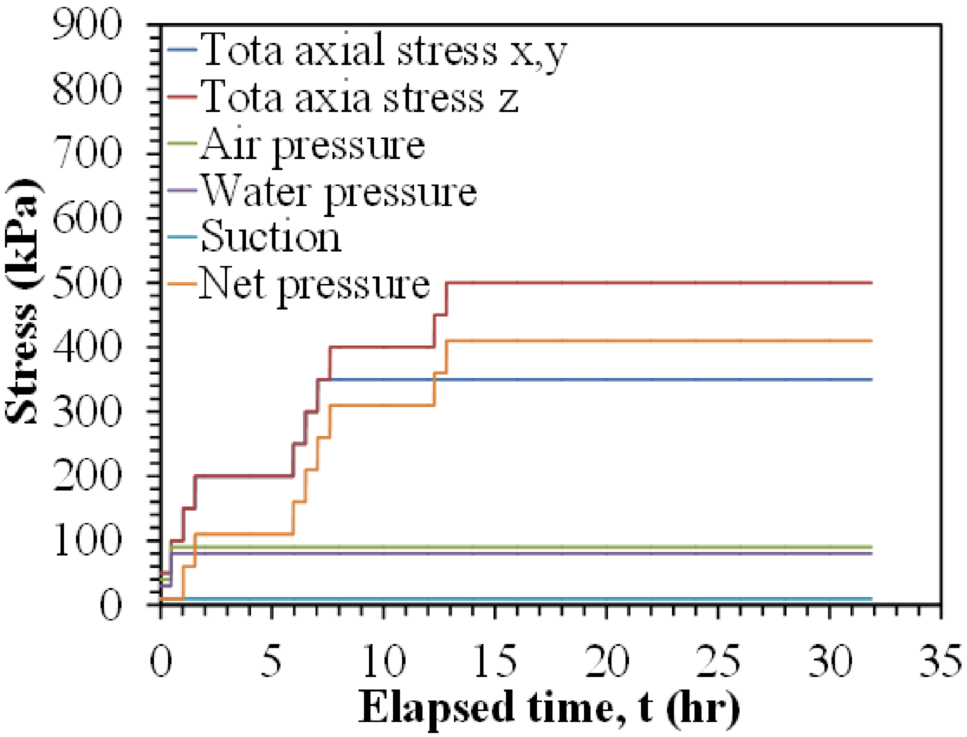

Figure 6.45: Application of total stress, pore air pressure and pore water pressure in stages to maintain constant suction using the axis translation technique for the K0.7-0.8 test.

The test was mechanically loaded to a total isotropic loading 350 kPa in x, y and z directions, then the load in z direction was increased up to 500 kPa t to reach a stress ratio of K = 0.7. The changes in applied effective stresses are presented in Figure 6.46.

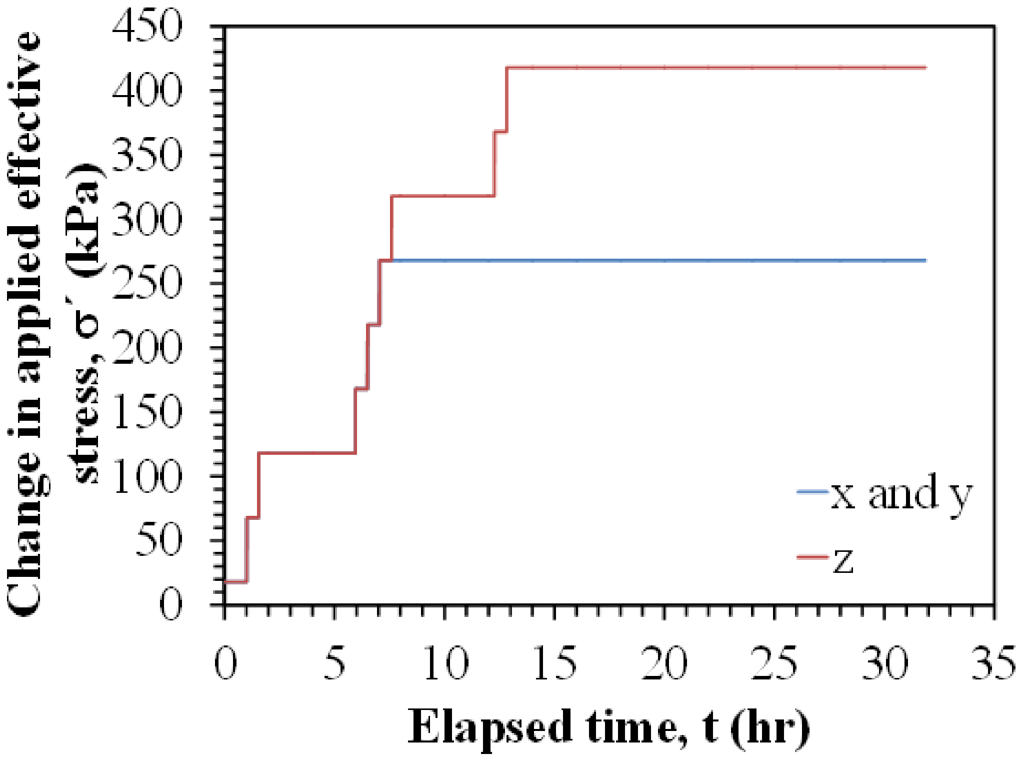

Figure 6.46: Change in effective stress on the soil specimen in the K0.7-0.8 test.

The time series of displacement for the K0.7-0.8 test are shown in Figures 6.47(a) through 6.47(e) for each of the faces. The displacement values shown in these figures were corrected for the effects of mechanical machine deflection of the cell using Equation 4.2. The average displacement for each of the faces is shown in Figure 6.47(f). The average compression of the specimen in each direction was calculated by summing the average displacements on the two opposite faces in each direction. The compressions of each face are shown in Figure 6.47(f). The averages of three LVDTs readings on each face of the soil specimen were calculated for measuring displacements except face X and XX, which used the average of two LVDTs (LVDTX1 and LVDTX2) and (LVDTXX13 and LVDXXT15), because LVDTXX3 and LVDTX14 were not functional during testing.

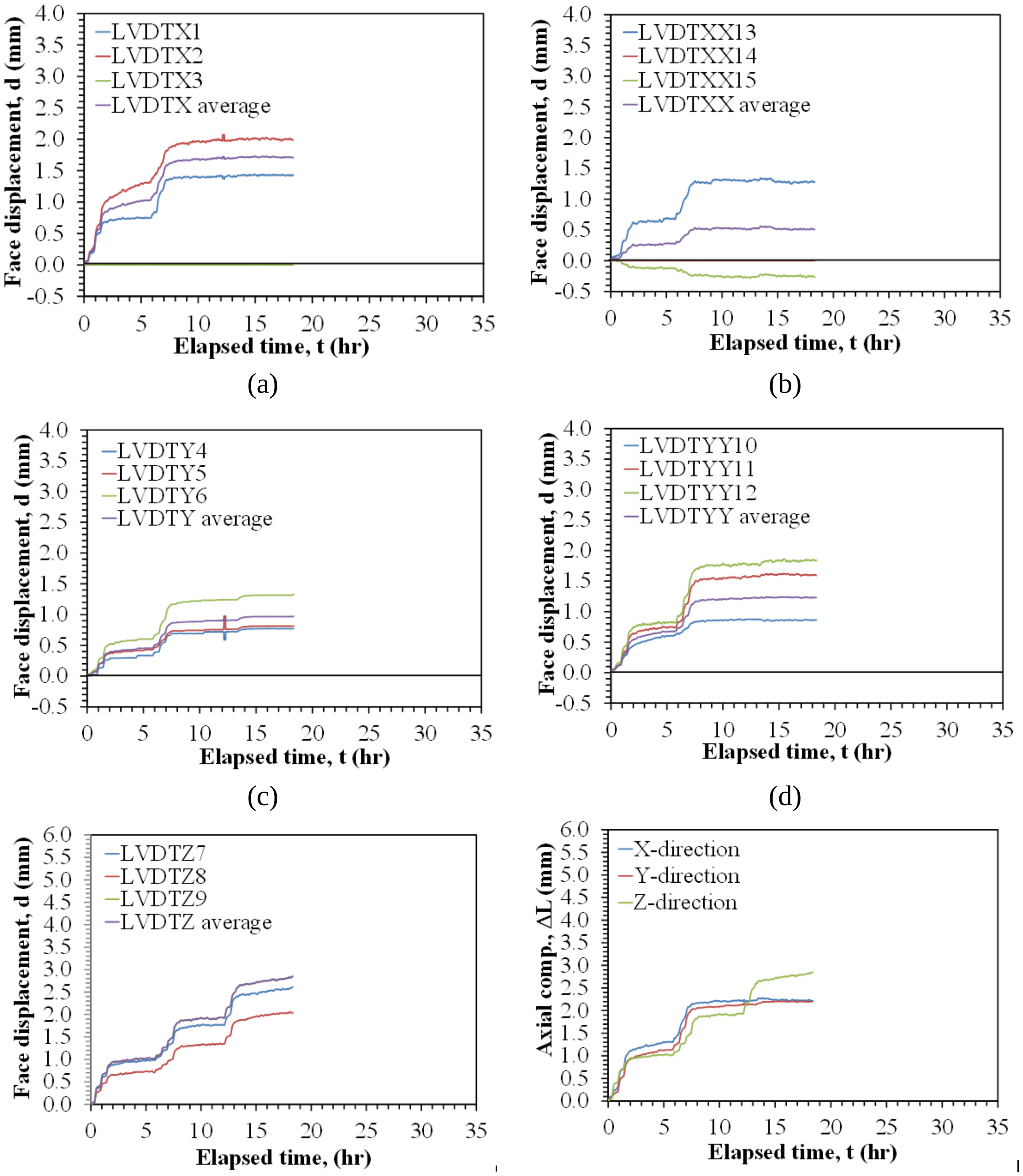

(a) (b)

(c) (d)

(e) (f)

Figure 6.47: Time series for the individual face displacements along with the average value: (a) X face; (b) XX face; (c) Y face; (d) YY face; (e) Z face; (f) Summary of average face displacements.

The time series of the mechanical axial strains for the K0.7-0.8 test were calculated from the values of displacements in Figure 6.47 by using Equation 6.1. The mechanical strain values are plotted in Figure 6.48.

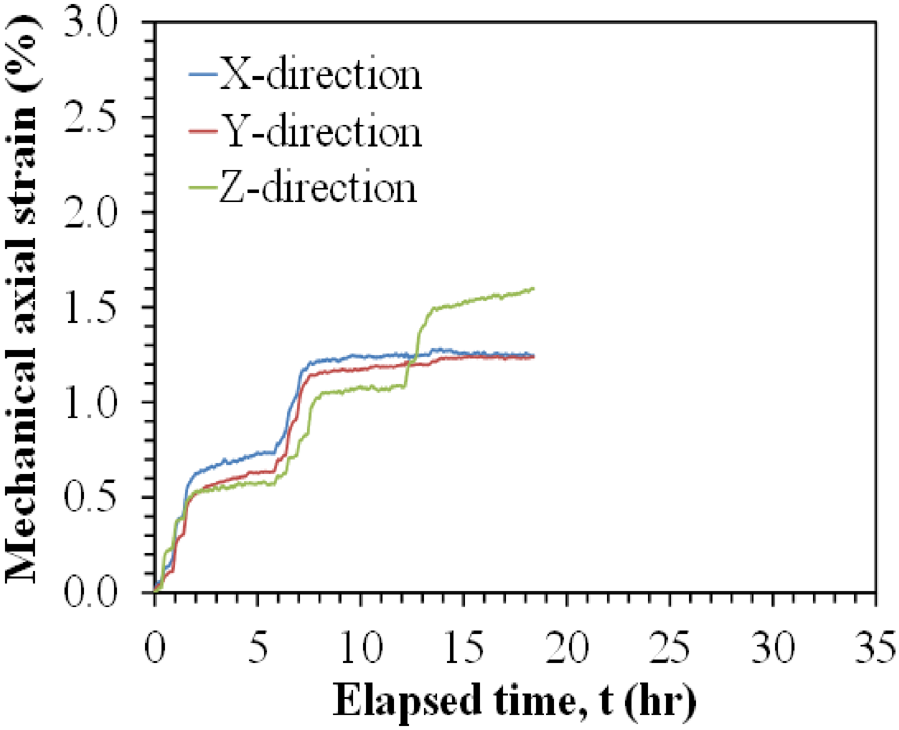

Figure 6.48: Time series for the mechanical strain values in Test K0.7-0.8.

The compression curve for the soil specimen in the K0.7-0.8 test up to the point at which heating was started is shown in Figure 6.49. The void ratio values were calculated from the average mechanical axial strains presented in Figure 6.48. The compression curve indicates that the compacted specimen initially behaves like an overconsolidated soil.

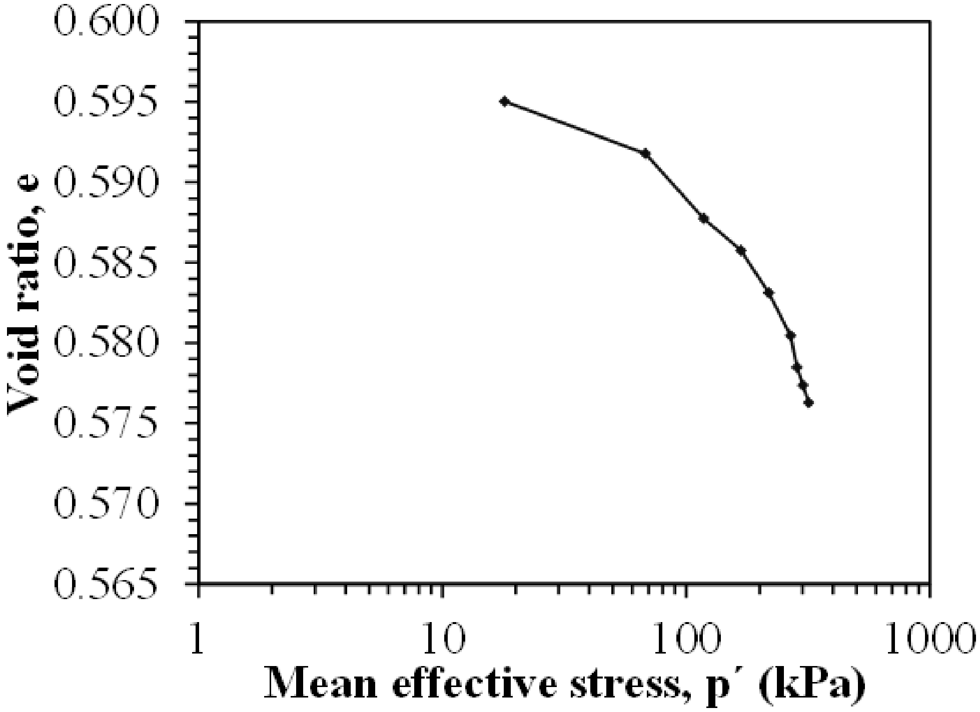

Figure 6.49: Compression curve obtained during application of anisotropic stress state to unsaturated Bonny silt specimen for test K0.7-0.8.

Once the mechanical loading was completed, the temperature of the compacted cubical soil specimen was increased from ambient room temperature to approximately 50 °C in three stages for 10 °C interval, then cooled back to ambient room temperature in one stage. The change in temperature of the soil specimen during heating and cooling is shown in Figure 6.50(a). The rate of temperature change versus time is shown in Figure 6.50(b). The temperature changes of the soil specimen during testing indicated that the temperature was uniform throughout the specimen at each of the three intervals. Each interval was maintained until the thermal axial strains stabilized.

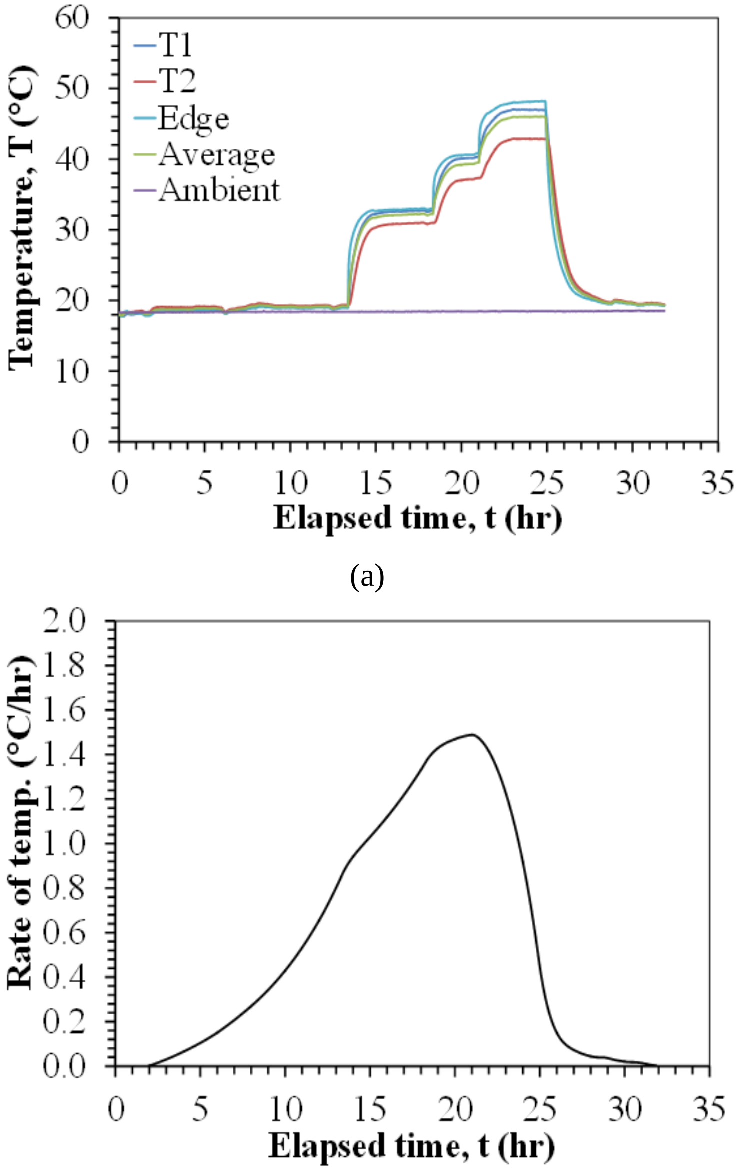

(a)

(b)

Figure 6.50: Results from the K0.7-0.8 test: (a) Change in temperature of the soil specimen; (b) The rate of temperature of the soil specimen.

The time series of thermal displacement for the K0.7-0.8 test are shown in Figures 6.51(a) through 6.51(e) for each of the faces. The thermal displacement values shown in these figures were corrected for the effects of mechanical machine deflection of the cell using Equation 4.2 and thermal machine deflection using Equation 4.4. The average thermal displacement for each of the faces is shown in Figure 6.51(f). The average axial strain of the specimen in each direction

was calculated by summing the average thermal displacements on the two opposite faces in each direction. The compressions of each face are shown in Figure 6.51(f).

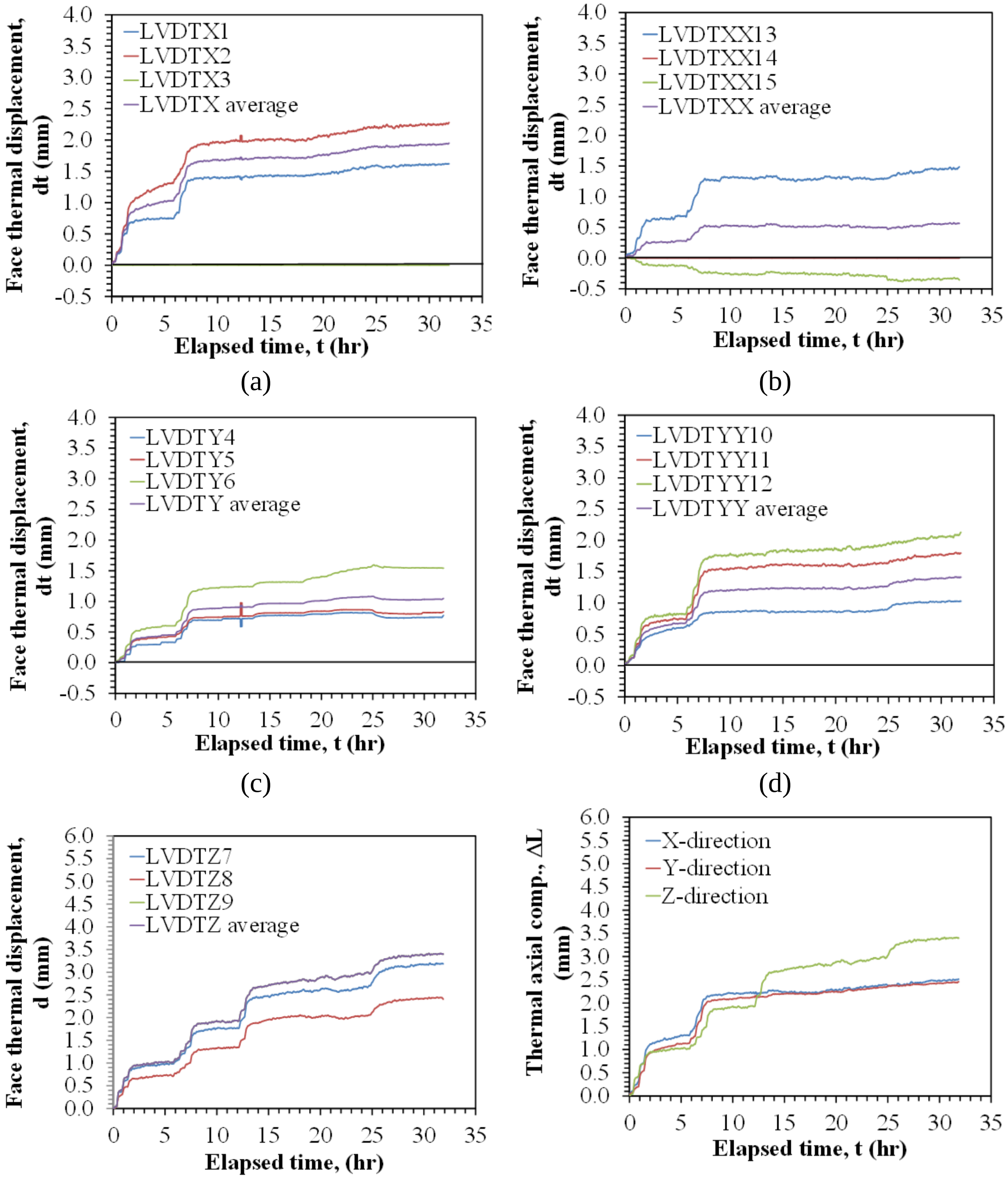

(a)

(b)

(c)

(d)

(e)

(f)

Figure 6.51: Time series for the individual face thermal displacements along with the average value: (a) X face; (b) XX face; (c) Y face; (d) YY face; (e) Z face; (f) Summary of average face thermal displacements.

The time series of the thermal axial strains for the K0.7-0.8 test were calculated from the values of thermal displacements in Figure 6.50 by using Equation 6.1. The axial strain values are plotted in Figure 6.52.

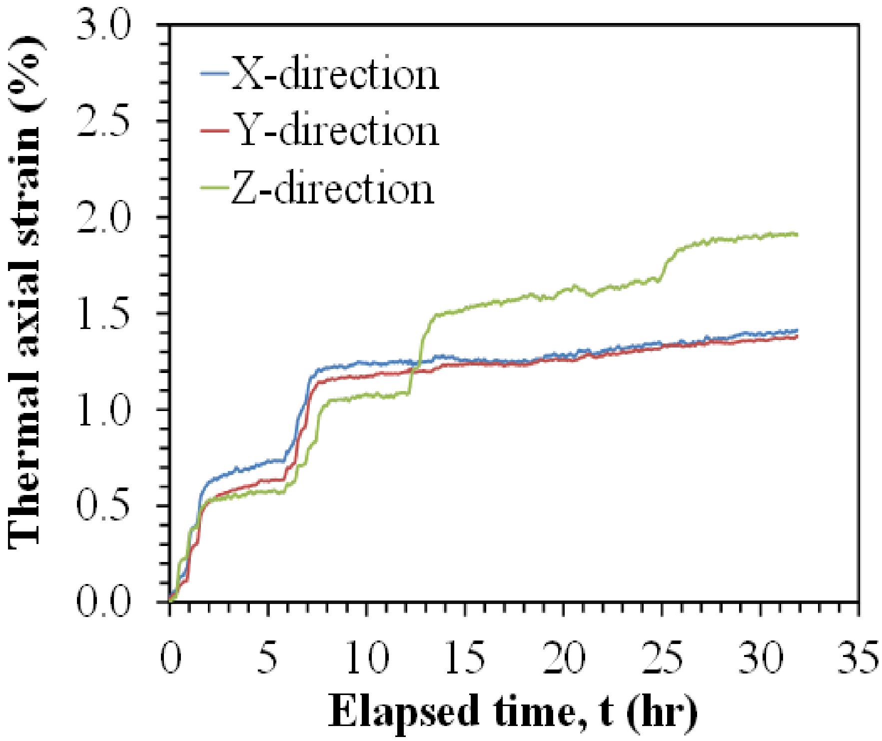

Figure 6.52: Time series for the axial strain values in Test K0.7-0.8.

The thermally-induced axial strains during heating-cooling are shown in Figure 6.53(a). The same data without the cooling stage is shown in Figure 6.53(b). Change of temperature versus thermal axial strain during heating for the points of equilibrium is shown in Figure 6.53(c). The data in these figures shows that the thermal axial strains in the x, y and z directions is contractile during heating. However, different from the behavior of the compacted soil specimen tested under isotropic conditions, a greater amount of contraction was observed in the z direction, which was under a greater principal stress. This is consistent with the trend from Coccia and McCartney (2012) for this stress range.

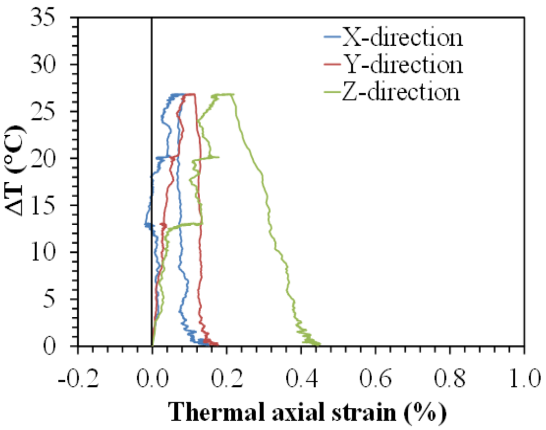

(a)

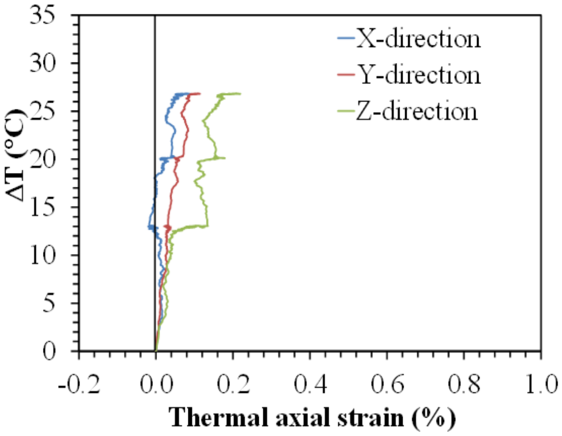

(b)

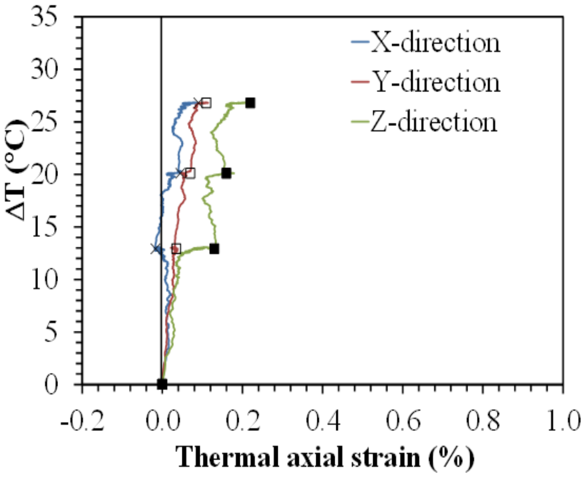

(c)

Figure 6.53: Results from the K0.7-0.8 test: (a) Change in temperature versus thermal axial strain for the full heating-cooling cycle; (b) Change in temperature versus thermal axial strain during heating; (c) Change of temperature versus thermal axial strain during heating for the points of equilibrium.

The thermal volumetric strain as a function of the change in temperature is shown in Figure 6.54(a) during heating and cooling. The thermal volumetric strain as a function of the change in temperature for the points of the equilibrium during heating is shown in Figure 6.54(b).Volumetric strain was calculated by using Equation 6.2. The thermal volumetric strain indicates contractile behavior during heating, consistent with the observations for the normally consolidated, saturated Bonny silt specimen tested by Coccia and McCartney (2012). During cooling, the thermal volumetric strain was not recoverable.

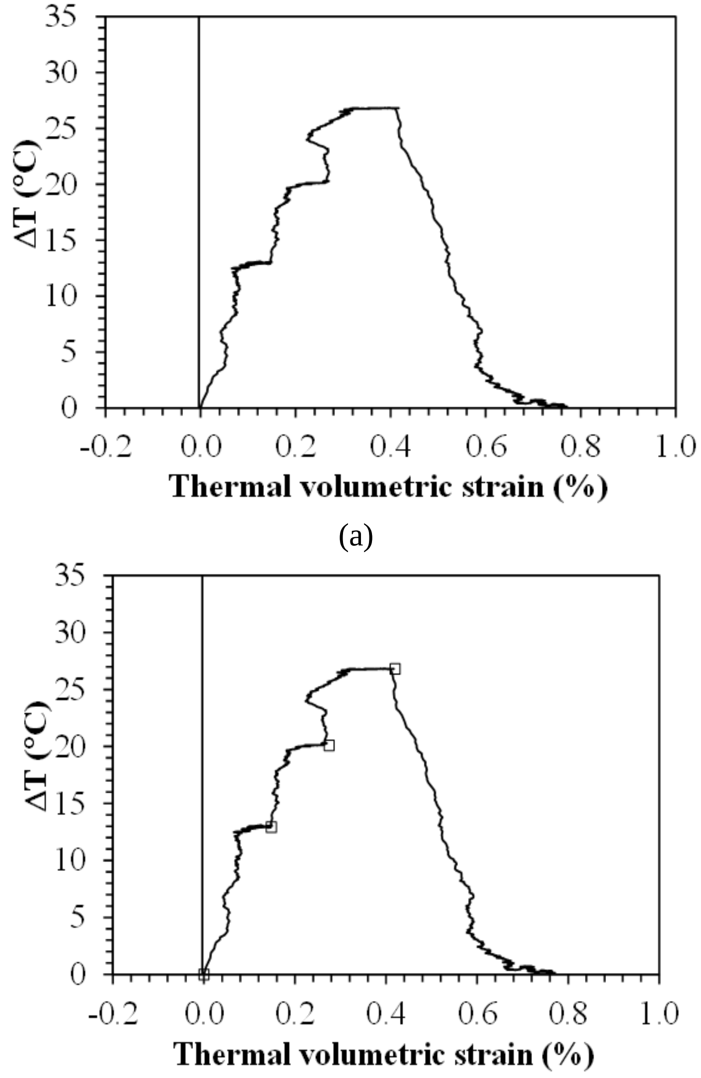

(b)

Figure 6.54: Results from the K0.7-0.8 test: (a) Temperature versus thermal volumetric strain; (b) Temperature versus thermal volumetric strain for points of equilibrium

The compression curve considering the thermal volume change and the unloading path is shown in Figure 6.55. The compression index $C_c$ and recompression index $C_r$ are equal to 0.05 and 0.005, respectively.

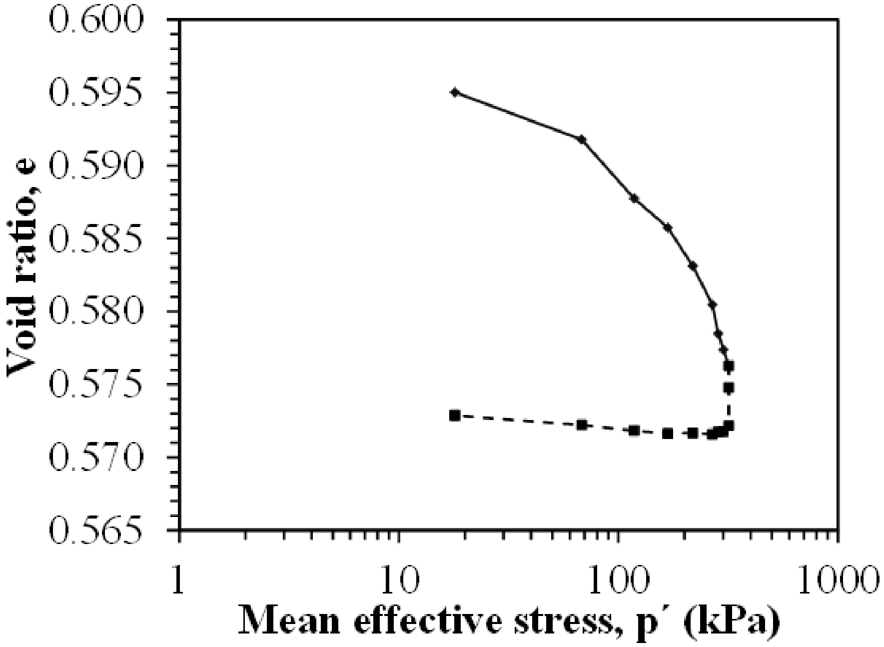

Figure 6.55: Compression curve obtained during application of anisotropic stress state to unsaturated Bonny silt specimen for test K0.7-0.8 considering the thermal volume change and unloading path.

### 6.7. Results from Test K0.5-0.8

Test K0.5 was conducted to analyze the effect of stress state anisotropy on the thermal volume change. After application of the seating stress in this test, the initial value of suction measured within the specimen was applied using the axis translation technique. This involved increasing the total stress, pore air pressure, and pore water pressure in stages to maintain a constant low suction 10kPa. The pressure stages corresponding to a constant suction during suction application and subsequent mechanical loading are shown in Figure 6.56.

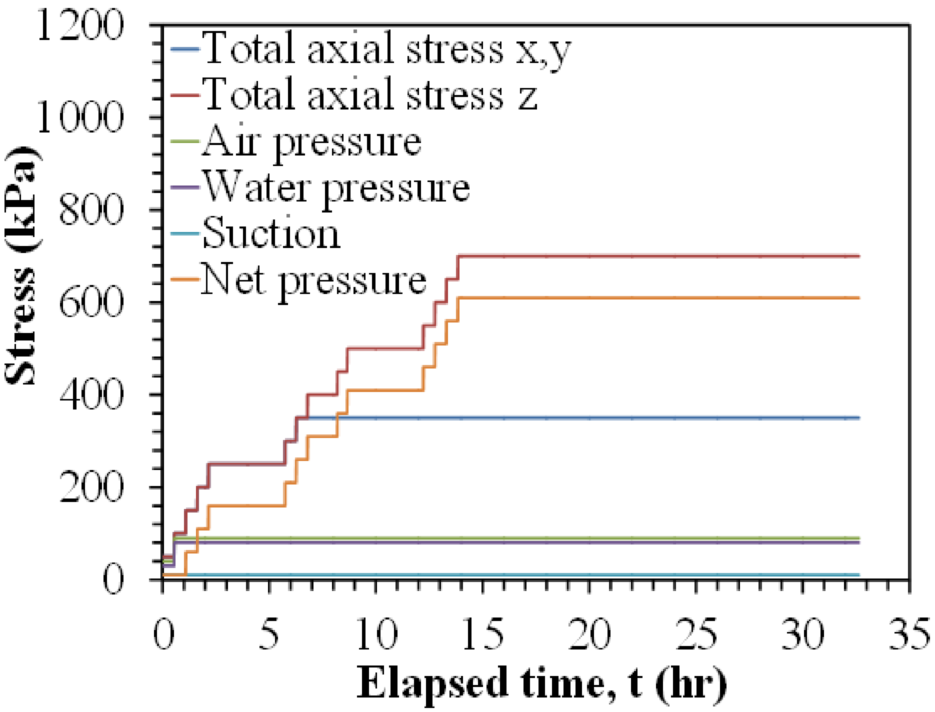

Figure 6.56: Application sequence of total stress, pore air pressure and pore water pressure in stages to maintain constant suction using the axis translation technique for the K0.5-0.8 test.

The changes in applied effective stresses in the K0.5 test are presented in Figure 6.57. Similar to the other tests, an isotropic stress of 350 kPa was applied to the specimen in the x, y and z directions, after which the axial stress in the z direction was increased up to 700 kPa to reach a stress level of K = 0.5.

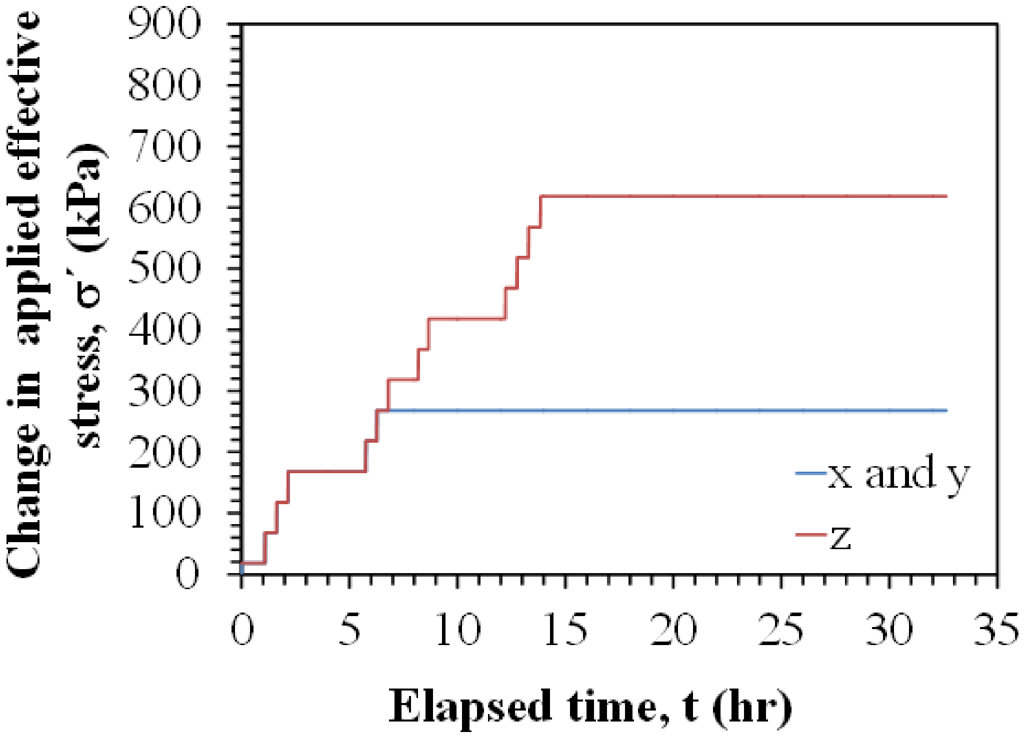

Figure 6.57: Change in effective stress on the soil specimen in the K0.5-0.8 test.

The time series of displacement for the K0.5-0.8 test are shown in Figures 6.58(a) through 6.58(e) for each of the faces. The displacement values shown in these figures were corrected for the effects of mechanical machine deflection of the cell using Equation 4.2. The average displacement for each of the faces is shown in Figure 6.58(f). The average compression of the specimen in each direction was calculated by summing the average displacements on the two opposite faces in each direction. The compressions of each face are shown in Figure 6.58(f). The averages of three LVDTs readings on each face of the soil specimen were calculated for measuring displacements except face XX, which used the average of two LVDTs (LVDTXX13 and LVDXXT15), because LVDTXX14 was not functional during testing.

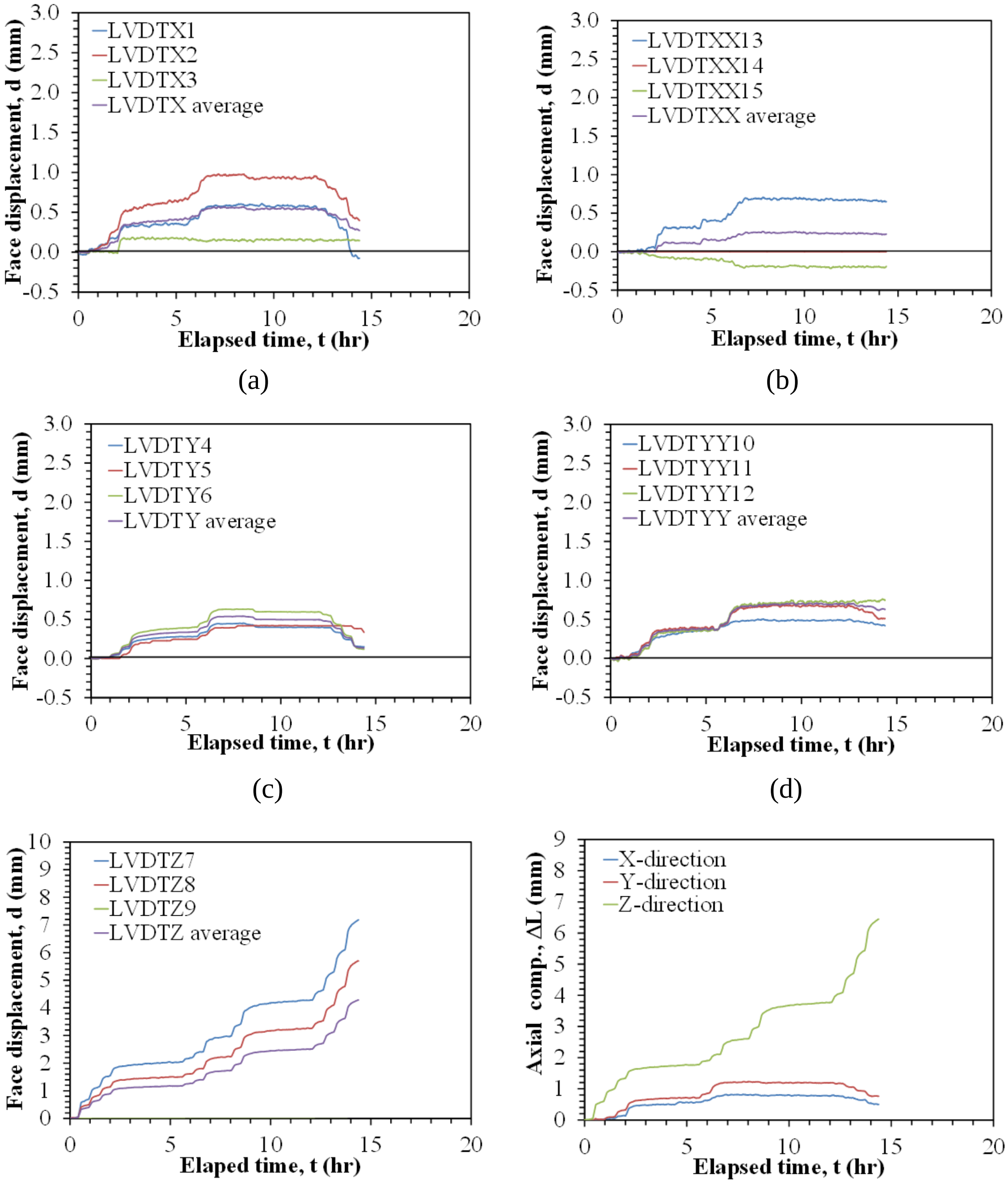

(a) (b) (c) (d) (e) (f)

Figure 6.58: Time series for the individual face deflections along with the average value: (a) X face; (b) XX face; (c) Y face; (d) YY face; (e) Z face; (f) Summary of average face deflections

The time series of the mechanical axial strains for the K0.5-0.8 test were calculated from the values of displacements in Figure 6.58 by using Equation 6.1. The mechanical strain values are plotted in Figure 6.59.

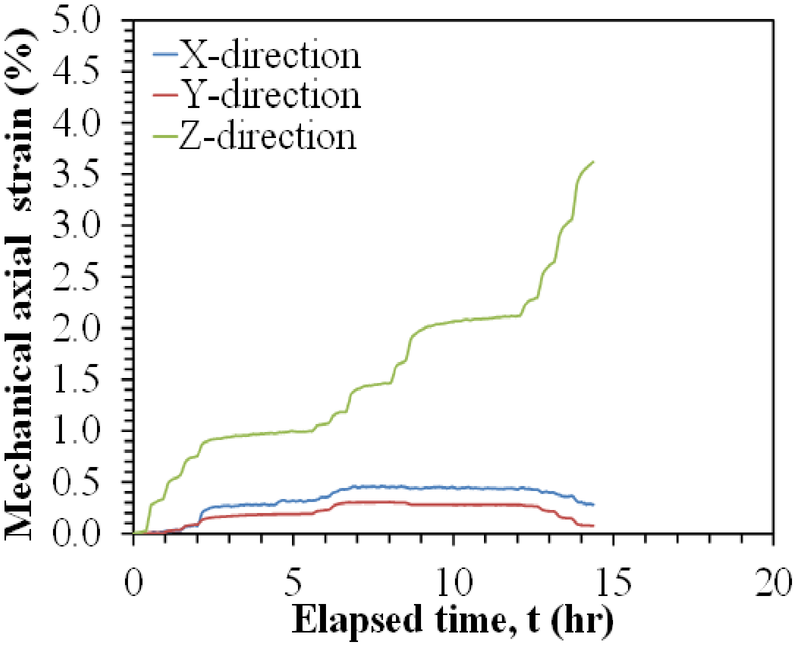

Figure 6.59: Time series for the mechanical strain values in Test K0.5-0.8.

The compression curve for the soil specimen in the K0.5-0.8 test up to the point at which heating was started is shown in Figure 6.60. The void ratio values were calculated from the average mechanical axial strains presented in Figure 6.59. The compression curve indicates that the compacted specimen initially behaves like an overconsolidated soil.

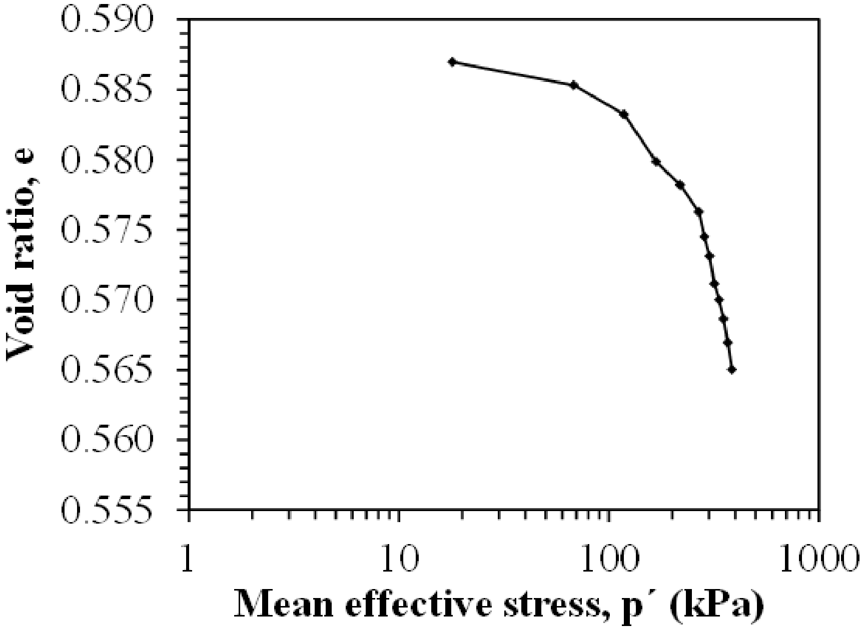

Figure 6.60: Compression curve obtained during application of anisotropic stress state to unsaturated Bonny silt specimen for test K0.5-0.8.

After the compacted cubical soil specimen reaching equilibrium under the final stress state, the temperature of the compacted cubical soil specimen was increased from ambient room temperature to approximately 50 °C in three increments of 10 °C, then cooled back to ambient room temperature in one stage. The change in temperature of the soil specimen during heating and cooling is shown in Figure 6.61(a). The rate of temperature change versus time is shown in Figure 6.61(b). The temperature changes of the compacted cubical soil specimen during testing indicated that the temperature was uniform throughout the specimen at each of the three intervals. Each interval was maintained until the thermal axial strains stabilized.

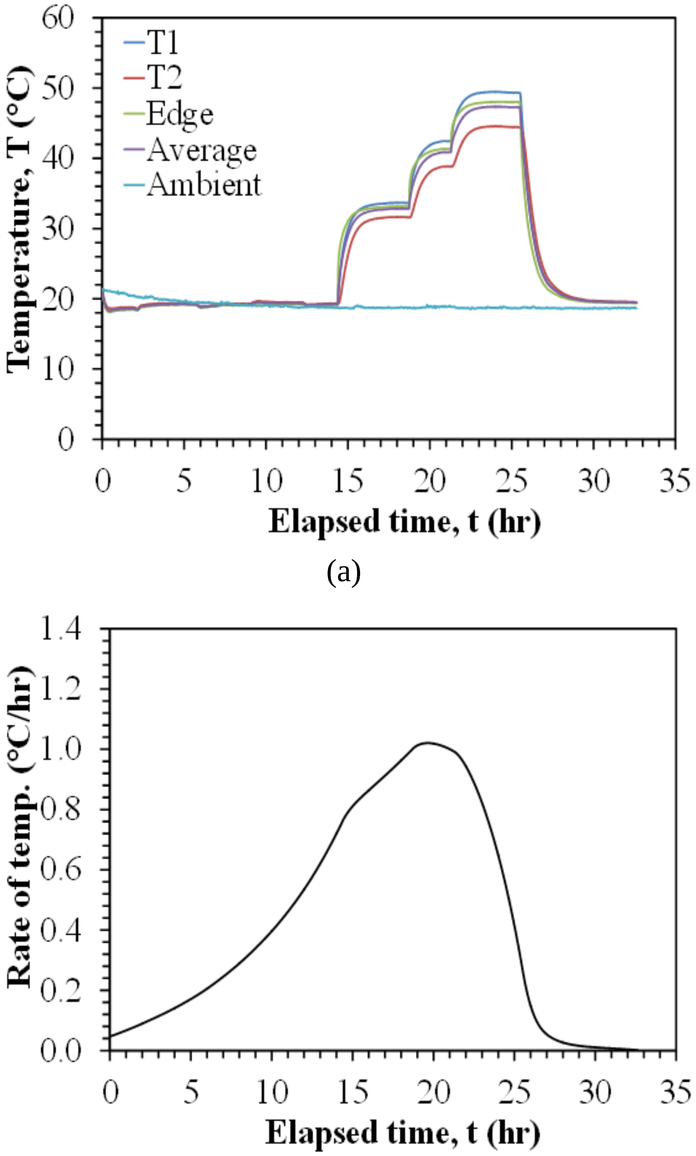

(a)

(b)

Figure 6.61: Results from the K0.5-0.8 test: (a) Change in temperature of the soil specimen; (b) The rate of temperature of the soil specimen.

The time series of thermal displacement for the K0.5-0.8 test are shown in Figures 6.62(a) through 6.62(e) for each of the faces. The thermal displacement values shown in these figures were corrected for the effects of mechanical machine deflection of the cell using Equation 4.2 and thermal machine deflection using Equation 4.4. The average thermal displacement for each of the faces is shown in Figure 6.62(f). The average axial strain of the specimen in each direction

was calculated by summing the average thermal displacements on the two opposite faces in each direction. The compressions of each face are shown in Figure 6.62(f).

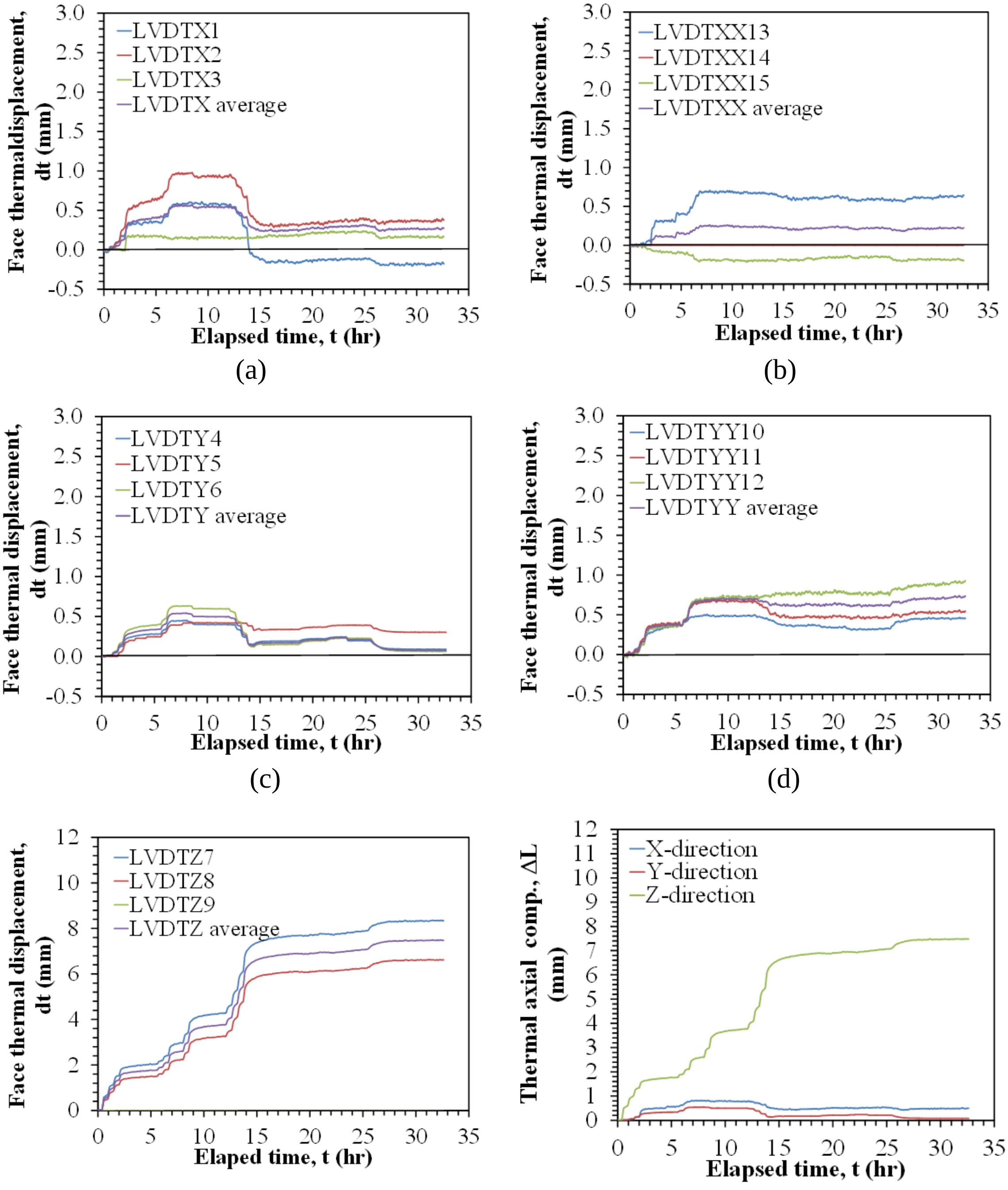

(a) (b)

(c) (d)

(e) (f)

Figure 6.62: Time series for the individual face thermal displacements along with the average value: (a) X face; (b) XX face; (c) Y face; (d) YY face; (e) Z face; (f) Summary of average face thermal displacements.

The time series of the thermal axial strains for the K0.5-0.8 test were calculated from the values of thermal displacements in Figure 6.62 by using Equation 6.1. The axial strain values are plotted in Figure 6.63.

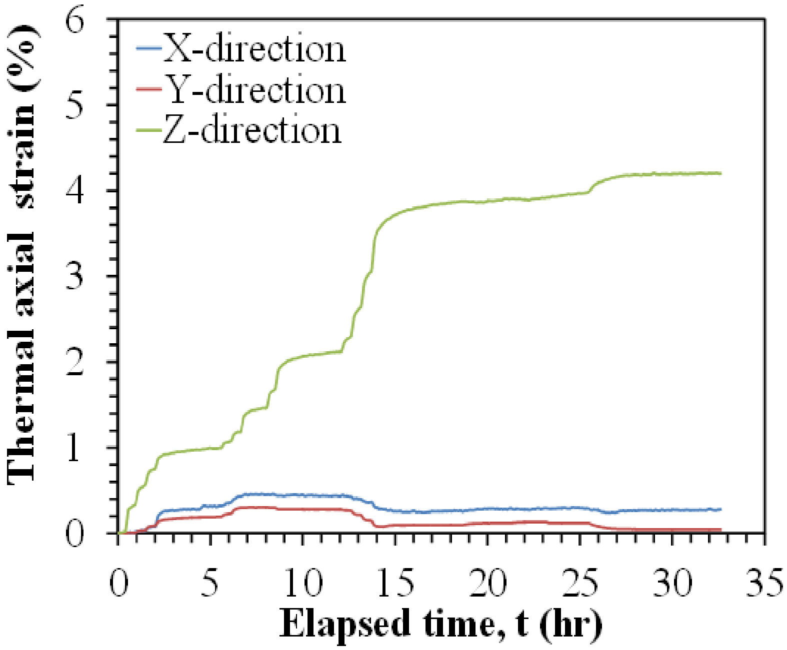

Figure 6.63: Time series for the axial strain values in Test K0.5-0.8.

The thermally-induced axial strains during heating-cooling are shown in Figure 6.64(a). The same data without the cooling stage is shown in Figure 6.64(b). Change of temperature versus thermal axial strain during heating for the points of equilibrium is shown in Figure 6.64(c). The data in these figures show that the thermal axial strain in the x, y and z directions indicate contractile behavior during heating as expected for a normally-consolidated soil specimen. Although the data in these figures indicates that the thermal axial strain in the x direction shows expansive behavior at lower temperatures, after which the axial strain transitioned from expansive to contractile behavior.

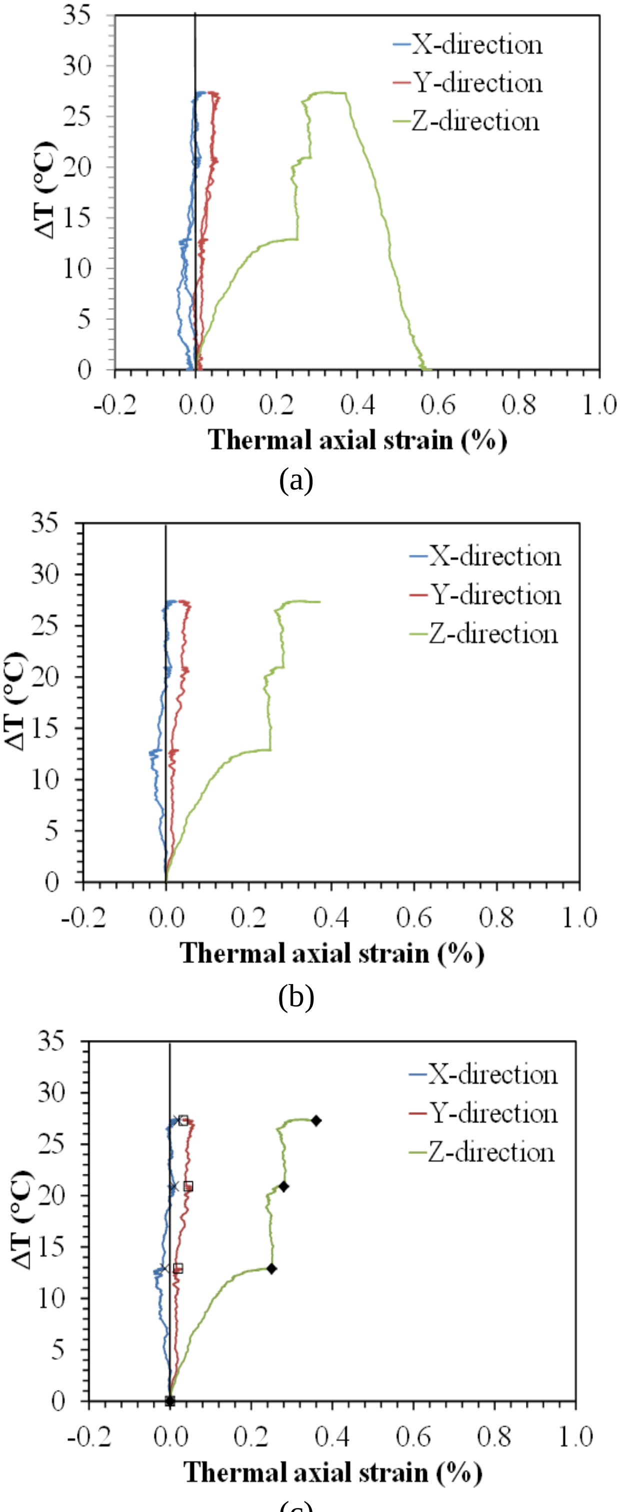

Figure 6.64: Results from the K0.5-0.8 test: (a) Change in temperature versus thermal axial strain for the full heating-cooling cycle; (b) Change in temperature versus thermal axial strain during heating; (c) Change of temperature versus thermal axial strain during heating for the points of equilibrium.

The thermal volumetric strain was calculated from the thermal axial strains by using Equation 6.2. The thermal volumetric strain as a function of the change in temperature is shown in Figure 6.65(a) during heating and cooling. The thermal volumetric strain as a function of the change in temperature for the points of the equilibrium during heating is shown in Figure 6.65(b). The thermal volumetric strain indicates contractile behavior during heating, consistent with the observations for the normally consolidated, saturated Bonny silt specimen tested by Coccia and McCartney (2012). During cooling, the thermal volumetric strain was not recoverable, and additional thermo-elastic contraction was observed during cooling. This is consistent with the constitutive relationship of Cui et al. (2000). A total volumetric strain of 0.4% was observed for a change in temperature of 27 °C.

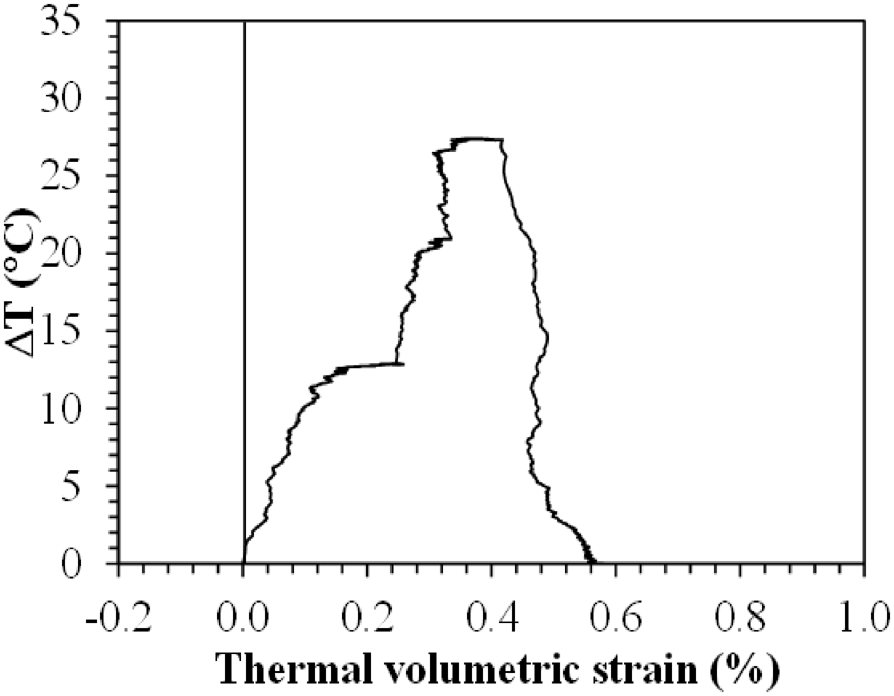

(a)

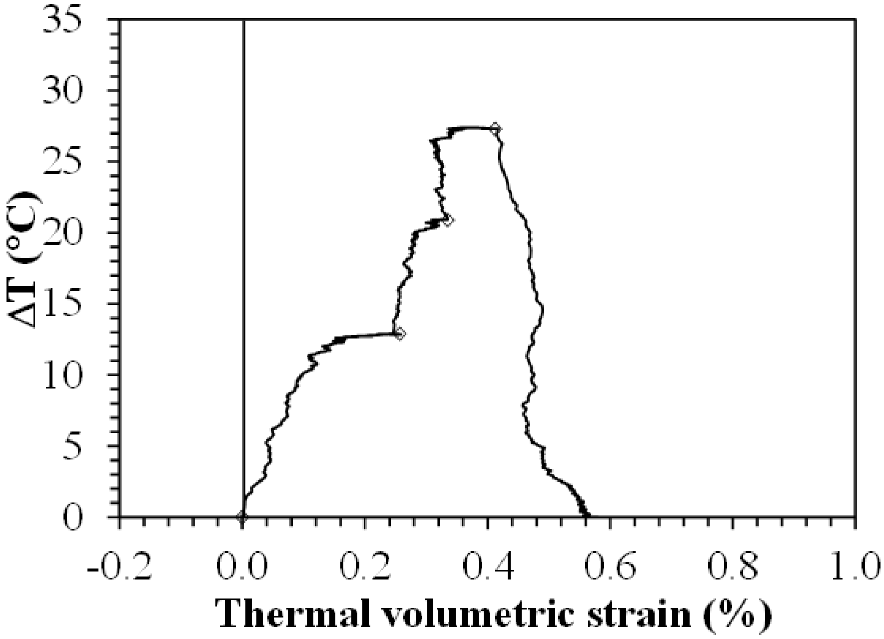

(b)

Figure 6.65: Results from the K0.5-0.8 test: (a) Temperature versus thermal volumetric strain; (b) Temperature versus thermal volumetric strain for points of equilibrium

The compression curve considering the thermal volume change and the unloading path is shown in Figure 6.66. The compression index $C_c$ and recompression index $C_r$ are equal to 0.05 and 0.005, respectively.

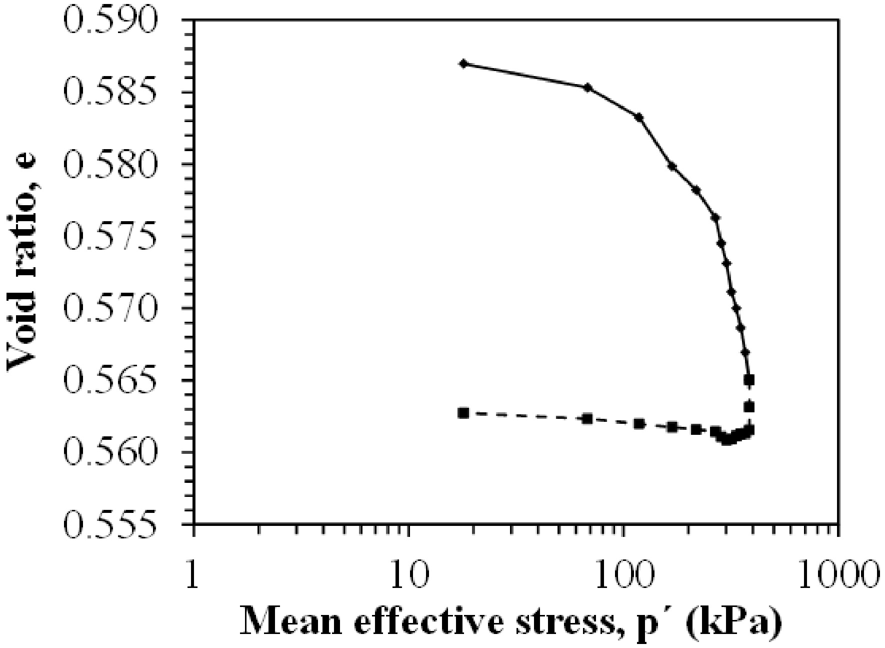

Figure 6.66: Compression curve obtained during application of isotropic stress state to unsaturated Bonny silt specimen for test K0.5-0.8 considering the thermal volume change and unloading path.

# 7. ANALYSIS

## 7.1 Impact of Stress-Induced Anisotropy on the Thermo-mechanical Response

This section provides a comparison of the results from the tests having different initial stress ratios at the beginning of heating, for Bonny silt specimens having two different initial degrees of saturation of 0.7 and 0.8. The thermally-induced axial strains for the specimens with an initial degree of saturation of 0.7 having different initial stress ratios are shown in Figure 7.1(a). The same data without the cooling stage is shown in Figure 7.1(b). The first observation from the data is that the thermal axial strains are contractile for all of the different stress ratios. This is consistent with the behavior of normally consolidated unsaturated silts observed by Uchaipichat and Khalili (2009). The second observation is that with decreasing stress ratio, the thermal axial strain in the major stress direction (z) is observed to increase, while the thermal axial strains in the minor stress directions (x and y) are observed to decrease. For the isotropic test with K=1.0, the thermal axial strains in the x, y and z directions are similar, while for the anisotropic test with K=0.5, the thermal axial strain in the z direction is significant while it is negligible in the x and y directions. This observation is consistent with that of Coccia and McCartney (2012), who tested saturated specimens of Bonny silt. A comparison of the magnitude of thermal axial strains with those of Coccia and McCartney (2012) will be discussed later in this chapter.

A comparison between the thermal axial strains for the tests with an initial degree of saturation of 0.8 are shown in Figure 7.2(a). The same data without the cooling stage is shown in Figure 7.2(b). The observations are consistent with those for the specimens with an initial degree of saturation of 0.7, although the magnitude of thermal axial strains are slightly smaller for the specimens with an initial degree of saturation of 0.8.

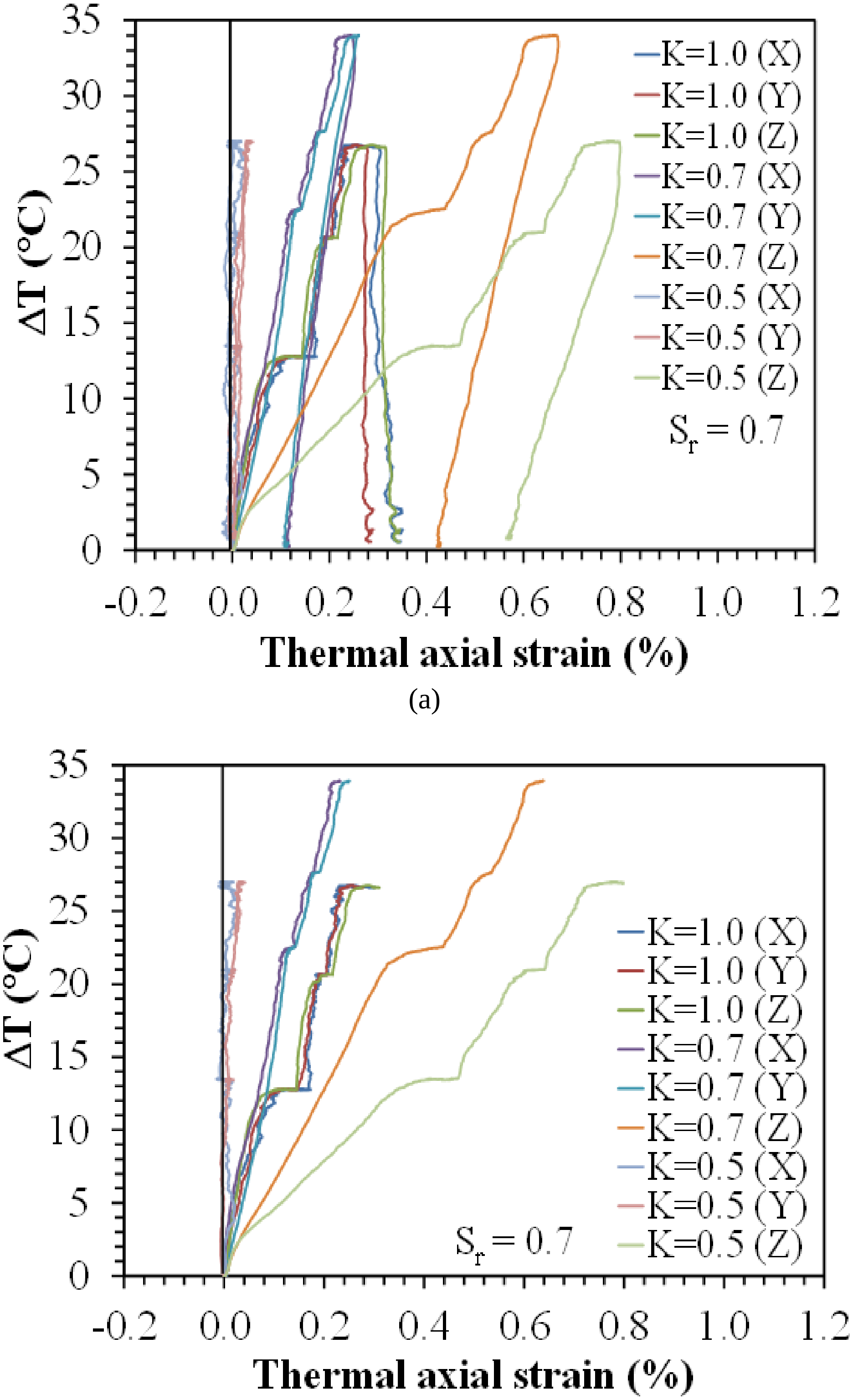

(a)

(b)

Figure 7.1: Thermal axial strains for the specimens with $S_r = 0.7$ and different stress ratios K: (a) With cooling stage; (b) without cooling stage.

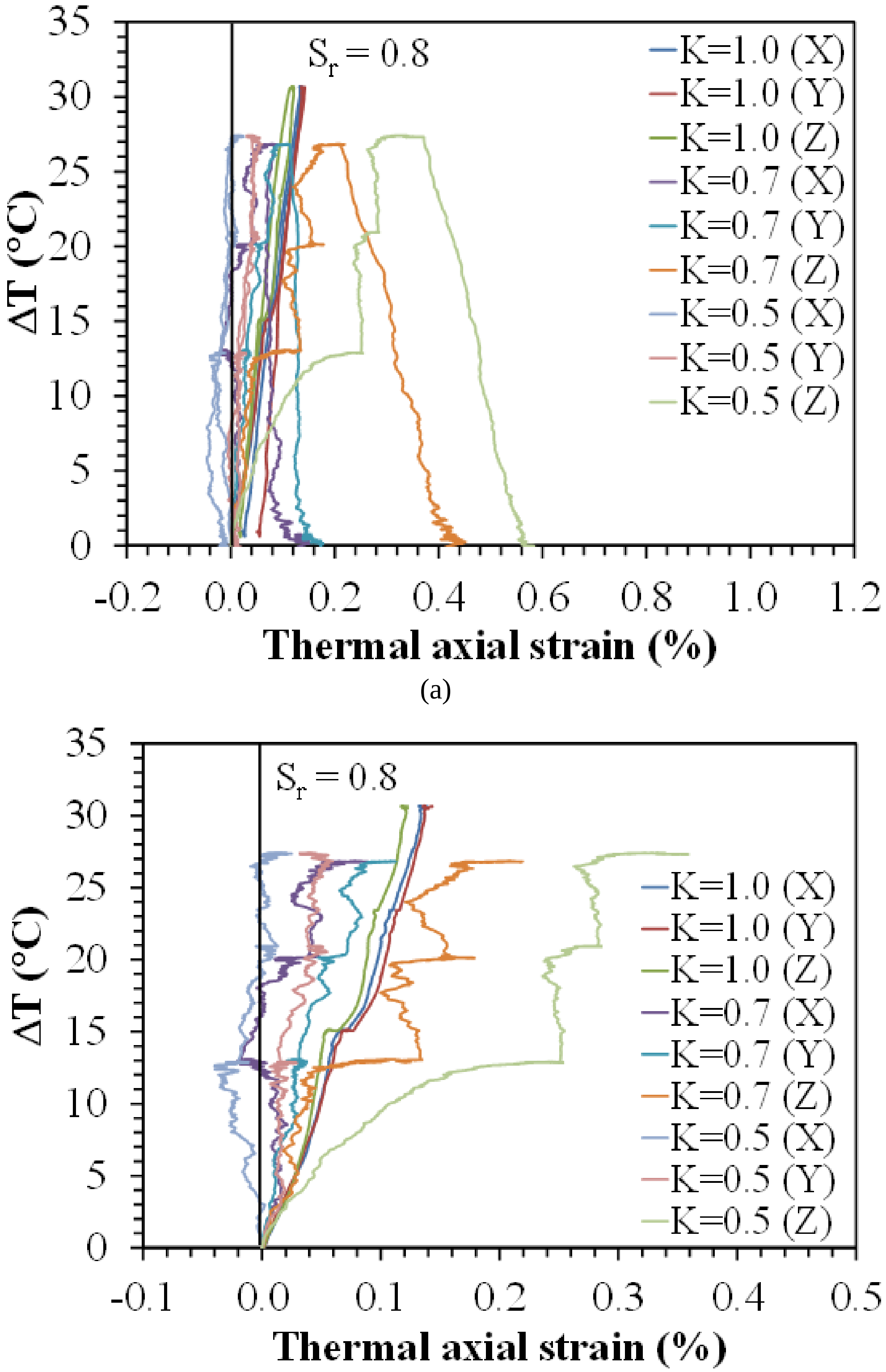

(a)

(b)

Figure 7.2: Thermal axial strains for the specimens with $S_r$ = 0.8 and different stress ratios K: (a) With cooling stage; (b) without cooling stage.

The thermal volumetric strains for the three tests with an initial degree of saturation of 0.7 are shown in Figure 7.3(a). The thermal volumetric strain is equal to the sum of the three axial strains measured in Figure 7.1. The same data without the cooling stage is shown in Figure 7.3(b). The first observation is that the thermal volumetric strain for the three tests is relatively consistent despite the different stress ratios. This is consistent with the observation from Coccia and McCartney (2012) for saturated specimens of Bonny silt. The cooling stage data shown in Figure 7.3(a) shows inconsistent behavior from test to test. It is expected that additional contractile strains would be observed during cooling, which was the case for the specimen with K=1.0, but was not observed for the other two tests. Although this could be due to the impact of the stress anisotropy, it could also be due to the fact that the thermal machine deflection is hysteretic during cooling, and the thermal machine deflection for heating was used to correct the entire data series. A more complex thermal machine deflection curve may improve the evaluation of the thermal strains during cooling.

The thermal volumetric strains for the specimens with an initial degree of saturation of 0.8 are shown in Figure 7.4(a). The same data without the cooling stage is shown in Figure 7.4(b). A similar observation can be drawn that the thermal volumetric strains are relatively consistent despite the difference in stress ratio. However, the trends in the strains during cooling is opposite from that observed in Figure 7.3. This indicates that the thermal machine deflection is an issue that needs to be evaluated in the future.

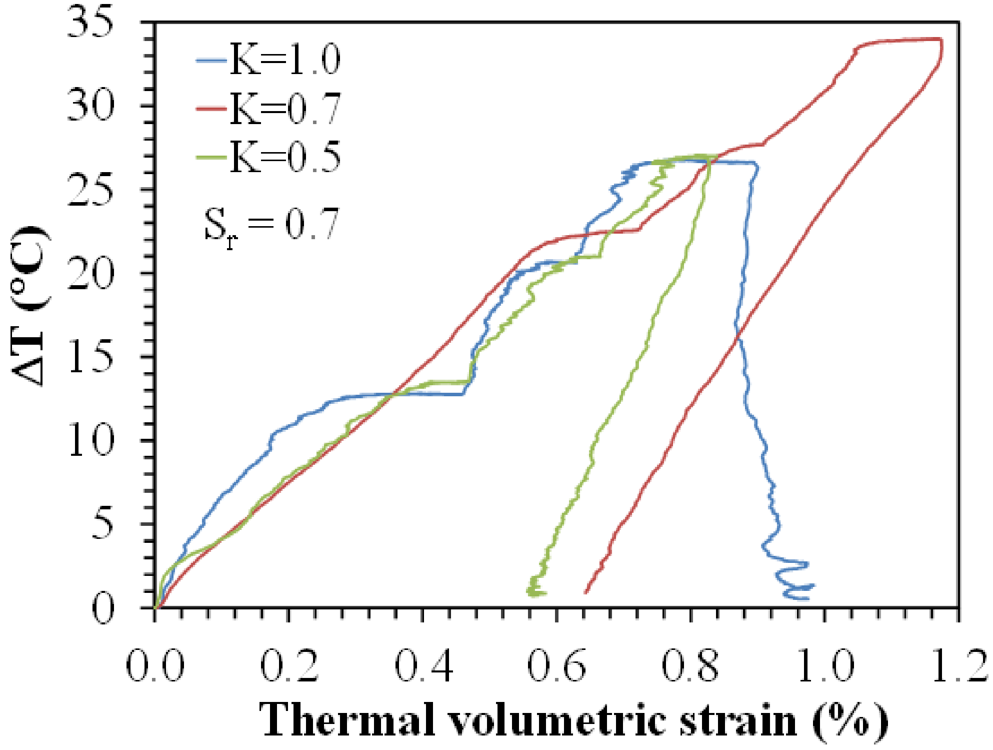

(a)

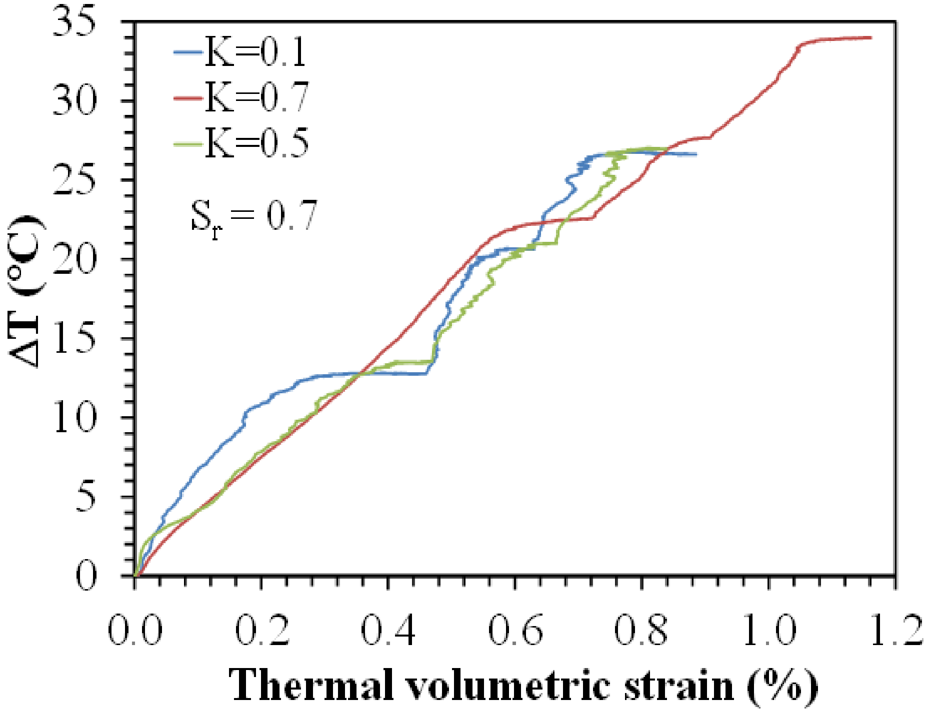

(b)

Figure 7.3: Thermal volumetric strains for the specimens with $S_r = 0.7$ and different stress ratios: (a) With cooling stage; (b) Without cooling stage.

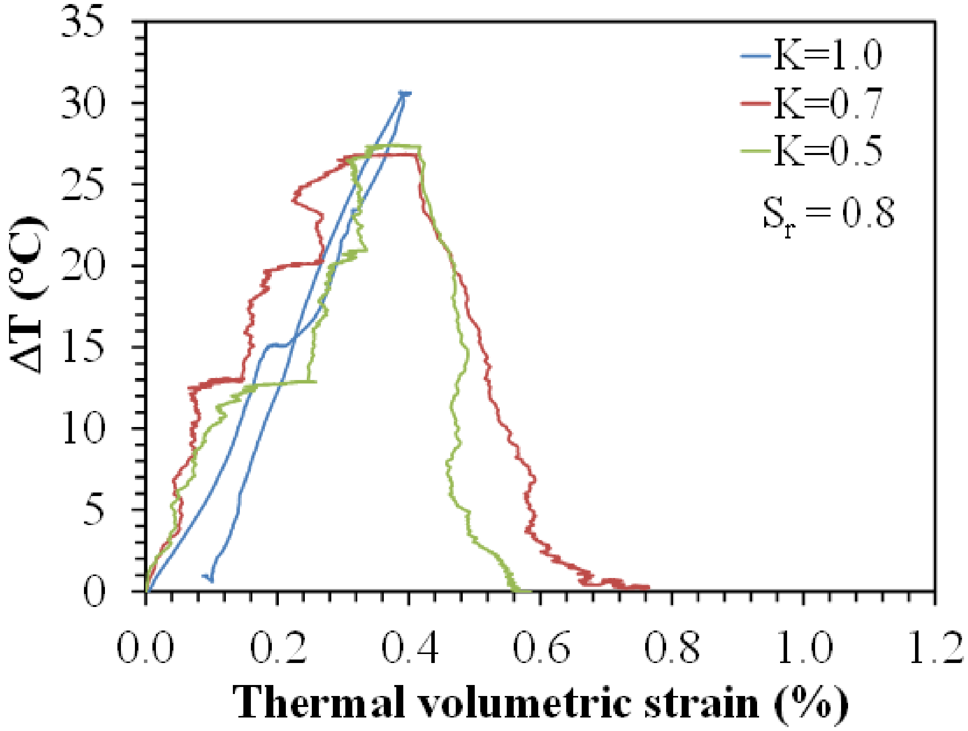

(a)

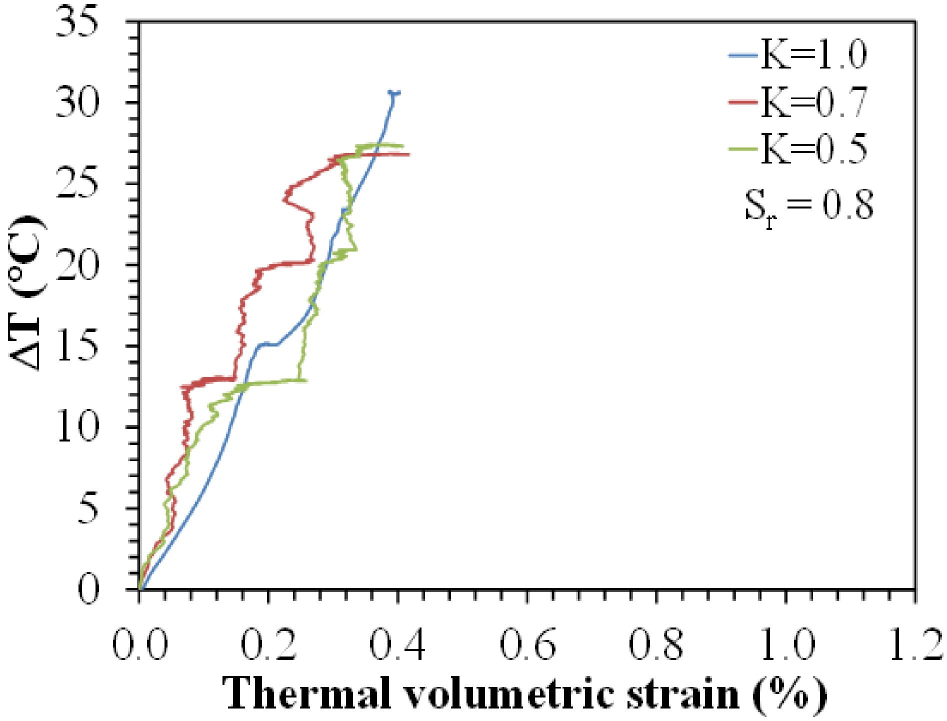

(b)

Figure 7.4: Thermal volumetric strains for the specimens with $S_r = 0.8$ and different stress ratios: (a) With cooling stage; (b) Without cooling stage.

The comparison of the rate of the cooling for each test is shown in Figure 7.5. The results in this figure indicate that the rate of the cooling was not the same for all the tests. This is likely be function of the ambient lab temperature, and may change the slope of the strain versus change in temperature curves for the different tests.

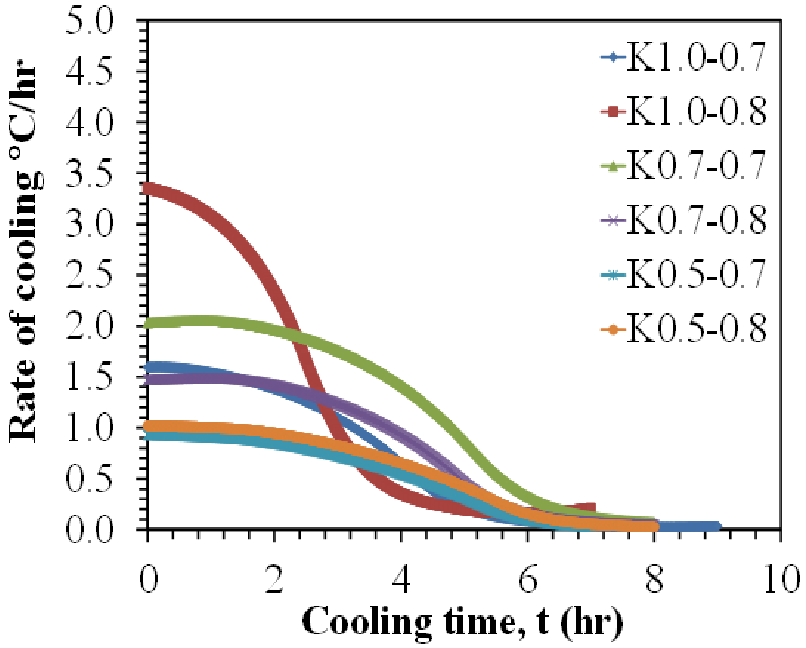

Figure 7.5: Rate of cooling versus cooling time.

A synthesis of the thermal axial strains for the thermal axial strains at a change in temperature of 27 °C for all cases in the major and minor principal stress directions versus different K values are presented in Figure 7.6. Some of the tests were performed to higher temperatures, in which case, the results were linearly interpolated to estimate the thermal axial strain at 27 °C. Although the same conclusions drawn from Figures 7.1 to 7.4 can be drawn, and interesting observation is that the soils with an initial degree of saturation of 0.7 show greater thermal axial strains. Further, the difference between the thermal axial strains in the major and minor direction is also greater for the dryer specimen. Consistent with the explanation of Coccia and McCartney (2012), the results in this figure reflects that the thermal axial strain in the major principal stress direction behaves more like a normally consolidated soil due to its high effective stress, while the thermal axial strain in the minor principal stress direction behaves like an overconsolidated soil due to its lower effective stress. However, it should be noted that the minor principal stress was assumed to correspond to normally consolidated conditions, and was not unloaded like that of Coccia and McCartney (2012).

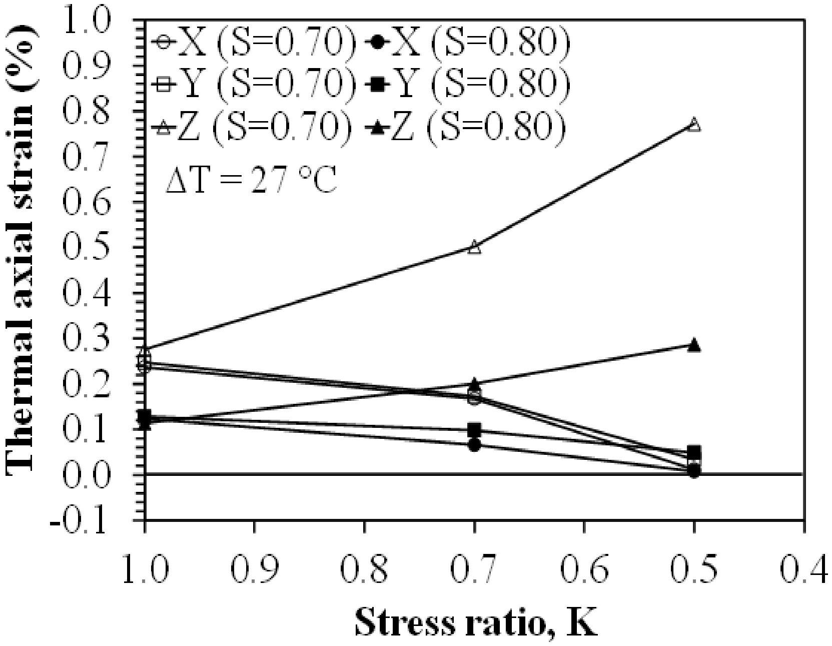

Figure 7.6: Thermal axial strain in the major and minor principal directions versus K.

A synthesis of the volumetric strain versus the stress ratio for the specimens having initial degrees of saturation of 0.7 and 0.8 is shown in Figure 7.7 for a change in temperature of 27 °C and in Figure 7.8 for a change in temperature of 20 °C. The two temperatures were chosen because the volumetric strain curves in Figures 7.2 and 7.4 were observed to follow a nonlinear relationship at higher temperatures. Although there is some slight fluctuation in the curves with K, the thermal volumetric strain is not as sensitive to the value of K as the thermal axial strain. Further, it is clear that the specimens with an initial degree of saturation of 0.8 have a consistently lower thermal volume change that those with an initial degree of saturation of 0.7.

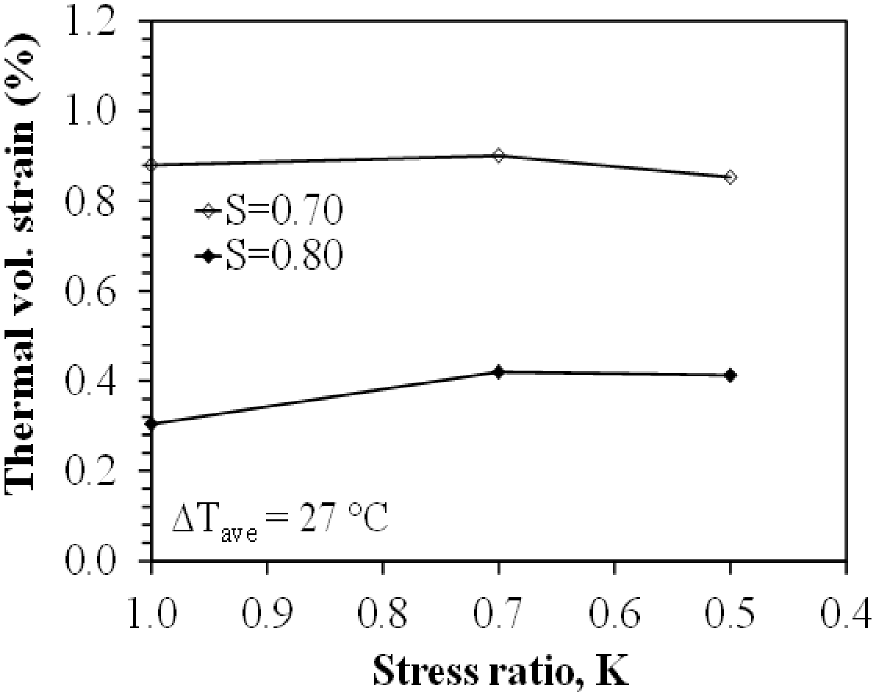

Figure 7.7: Thermal volumetric strains at a change in temperature of 27 °C.

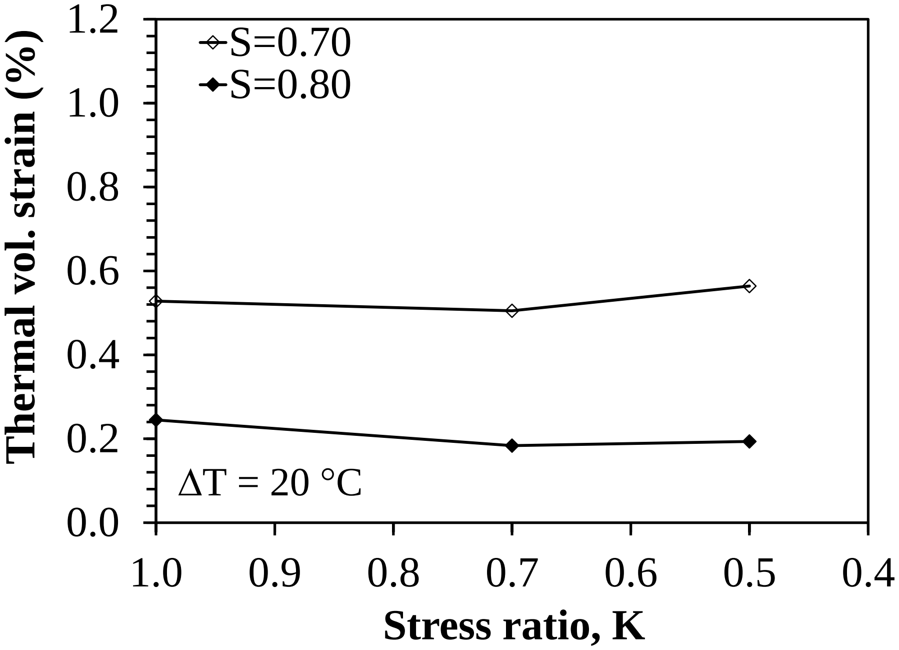

Figure 7.8: Thermal volumetric strains at a change in temperature of 20 °C.

As Coccia and McCartney (2012) evaluated Bonny silt under saturated conditions, their results were compared to those of this study in terms of the thermal volumetric strain in Figure

7.9. It is not possible to fairly compare the thermal axial strains because Coccia and McCartney (2012) applied the major and minor principal stresses in the X and Y directions, and did not control the stress in the Z direction. Nonetheless, the comparison in Figure 7.9 permits further assessment of the impact of initial degree of saturation on the thermal volumetric strain. Although there is some scatter, the thermal volumetric strains for the specimens with an initial degree of saturation of 1.0 are slightly lower on average than those with an initial degree of saturation of 0.8.

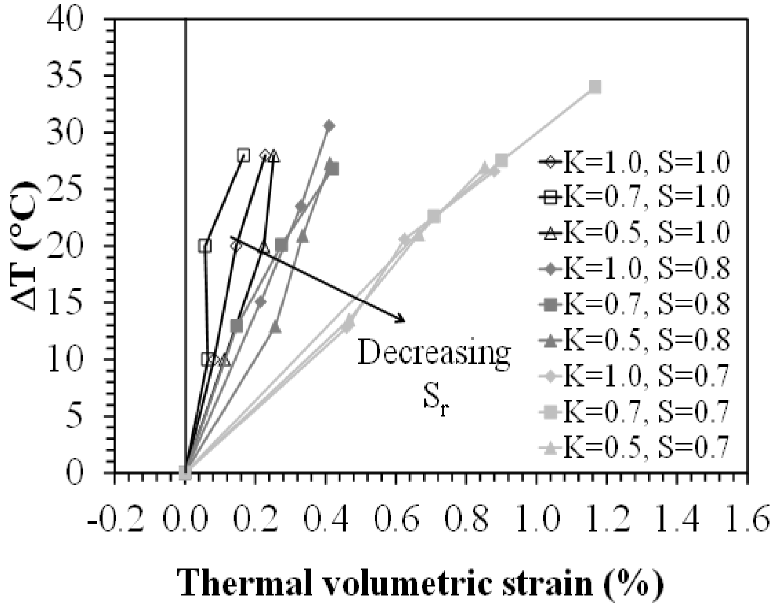

Figure 7.9: Thermal volumetric strains from this study compared with those for saturated specimens from Coccia and McCartney (2012).

Uchaipichat and Khalili (2009) also investigated the impact of unsaturated conditions on the thermal volume change of compacted specimens heated in isotropic conditions. They evaluated the thermal volume change at a range of net normal stresses and suctions. Their results from tests at the highest net normal stress of 200 kPa, corresponding to normally-consolidated conditions, are shown in Figure 7.10. Their results were presented in terms of the specific volume ($v$ = 1+e), as shown in Figure 7.10(a). The thermal volumetric strain was calculated and replotted in Figure 7.10(b) as follows:

$$\varepsilon_v^T = \frac{e - e_0}{1 + e_0} \times 100\% \tag{7.1}$$

where $e_o$ is the void ratio at the start of heating. The results in this figure indicate that they observed thermal contraction in all cases, but that they also observed a slightly lower thermal volumetric strain for the unsaturated specimens. Although this contradicts the observations in this study, the impact of suction in their experiments was not significant. Further, it should be noted that their tests involved application of multiple loading stages and undrained heating and cooling cycles before the drained heating tests.

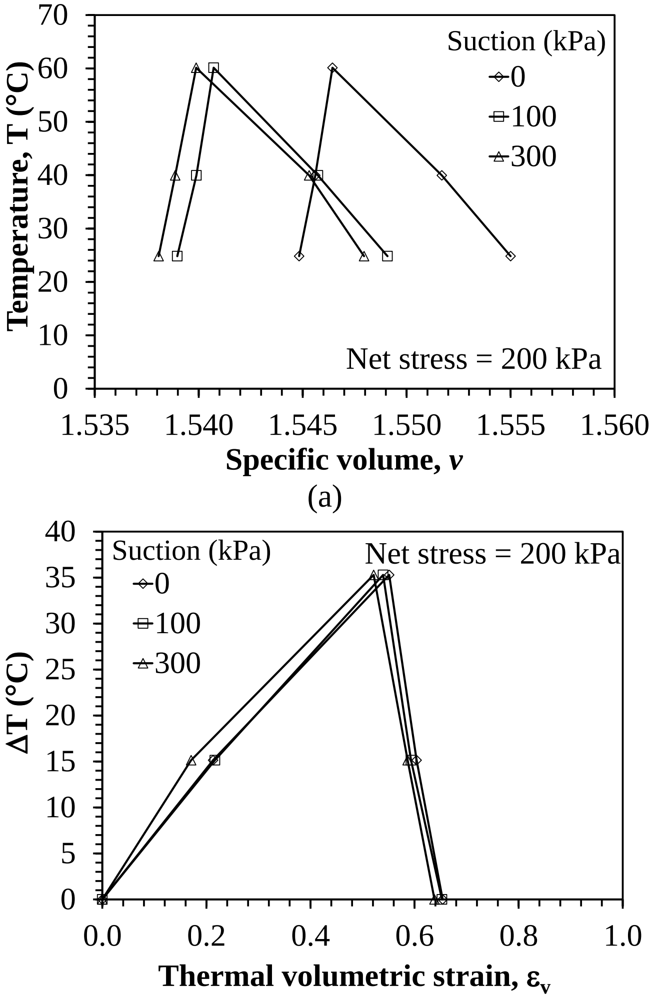

(a)

(b)

Figure 7.10: Thermal volume changes for unsaturated silt observed by Uchaipichat and Khalili (2009): (a) Specific volume; (b) Thermal volumetric strain.

The thermal volume change can be integrated into the compression curves for the different specimens to put the magnitude of thermal volume change into perspective with the mechanical volume change due to loading. The compression curves for the specimens compacted to an initial degree of saturation of 0.7 are shown in Figure 7.11 and the specimens compacted to an initial degree of saturation of 0.8 are shown in Figure 7.12. Although the y-axis range is very narrow, there is some variability in the initial void ratios. As mentioned in the procedures section, the isotropic specimen was compressed to a lower mean effective stress (274 kPa) than the other two specimens. The greater mean effective stress in the anisotropic specimens reflects the increase in the major principal stress to reach the target K value while the minor principal stress was kept constant at 274 kPa.

Evaluation of the compression curves indicates that the specimens were approximately at normally consolidated conditions at the beginning of heating. However, it was difficult to assess the value of preconsolidation stress from the figures because of the highly nonlinear compression curves which are typical of compacted soils. A summary of the values of $C_c$ are listed in Table 7.1. The value for the specimens with lower K values are slightly greater, which may be because the specimen was changing from isotropic to anisotropic conditions at a mean effective stress of 274 kPa. After the thermal volume change was measured and the specimen was cooled, they were unloaded. It is clear that the unloading slopes are similar for all of the specimens. The values of $C_r$ are summarized in Table 7.1 as well.

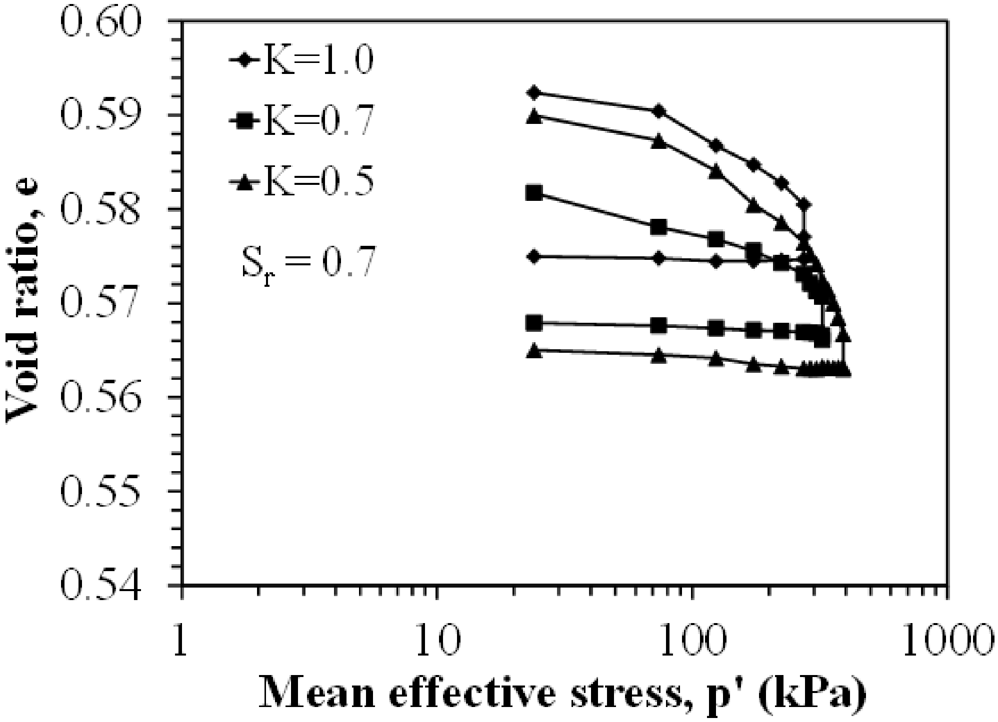

Figure 7.11: Compression curve for the three tests having $S_r = 0.7$ with the superimposed effect of thermal volume change.

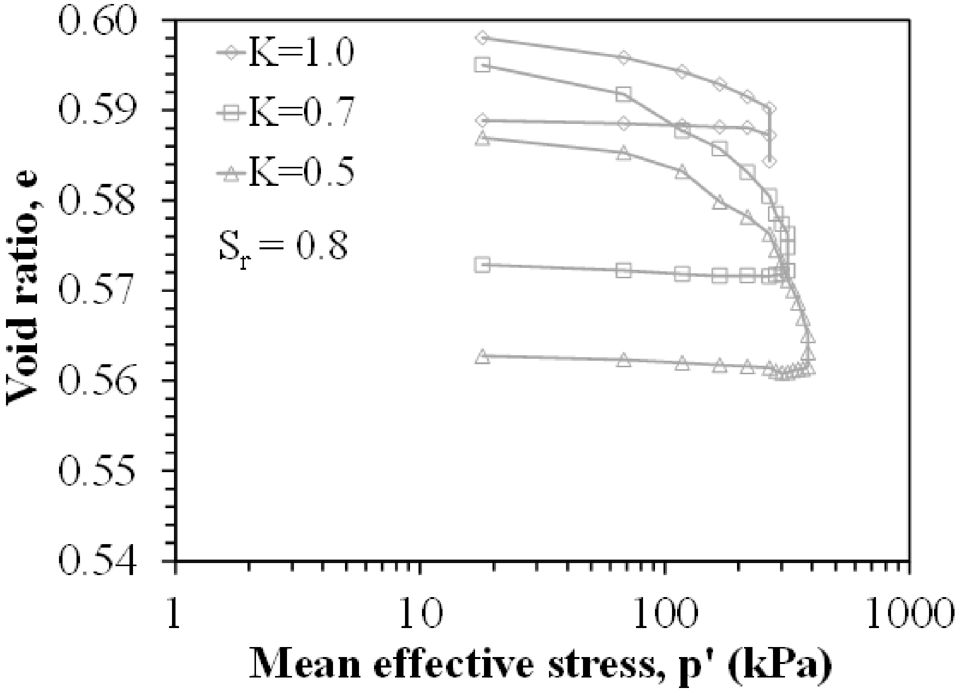

Figure 7.12: Compression curve for the three tests having $S_r = 0.8$ with the superimposed effect of thermal volume change.

Table 7.1: Synthesis of parameters for the compression curves.

| Test | $C_c$ | $C_r$ |
|---|---|---|
| K1.0-S0.7 | 0.014 | 0.0013 |
| K0.7-S0.7 | 0.025 | 0.0025 |
| K0.5-S0.7 | 0.051 | 0.0051 |
| K1.0-S0.8 | 0.010 | 0.0009 |
| K0.7-S0.8 | 0.050 | 0.0050 |
| K0.5-S0.8 | 0.050 | 0.0050 |

## 7.2 Elasto-Plastic Model for Impacts of Anisotropy and Unsaturated Conditions

The thermal volumetric strain for the cubical soil specimen can be calculated from the axial thermal strains as follows:

$$\varepsilon_{vT} = \varepsilon_{xT} + \varepsilon_{yT} + \varepsilon_{zT} - \left(\varepsilon_{xT} \times \varepsilon_{yT} + \varepsilon_{xT} \times \varepsilon_{zT} + \varepsilon_{yT} \times \varepsilon_{zT}\right) - \varepsilon_{xT} \times \varepsilon_{yT} \times \varepsilon_{zT} \quad (7.2)$$

where $\varepsilon_{vT}$ is the total thermal volumetric strain and $\varepsilon_{xT,}$ $\varepsilon_{yT}$, $\varepsilon_{zT}$ are the thermal axial strains in x, y and z directions. This equation can be simplified by assuming that because the thermal axial strains are very small, which implies that the higher order terms are negligible. Accordingly, the thermal volumetric strain can be expressed as follows:

$$\varepsilon_{vT} = \varepsilon_{xT} + \varepsilon_{yT} + \varepsilon_{zT} \quad (7.3)$$

Coccia (2011) defined the thermal axial strain ratio (Ω) for anisotropic stress states as follows in order to quantify the amount of thermal volume changes in different orthogonal directions during heating:

$$\Omega = \varepsilon_{yT} / \varepsilon_{xT} \quad (7.4)$$

The values of Ω can be estimated from experimental data by calculating the ratio between the thermal axial strains after the soil has been heated to a given change in temperature. The trend in Ω observed by Coccia (2011) for saturated Bonny silt under different stress ratios ($K = \sigma_y/\sigma_x$) is shown in Figure 7.13. This figure indicates that greater differences between the thermal axial strains will occur for smaller stress ratio values. Coccia (2011) also provided an empirical expression for estimating the value of Ω as a function of K, also shown in Figure 7.13.

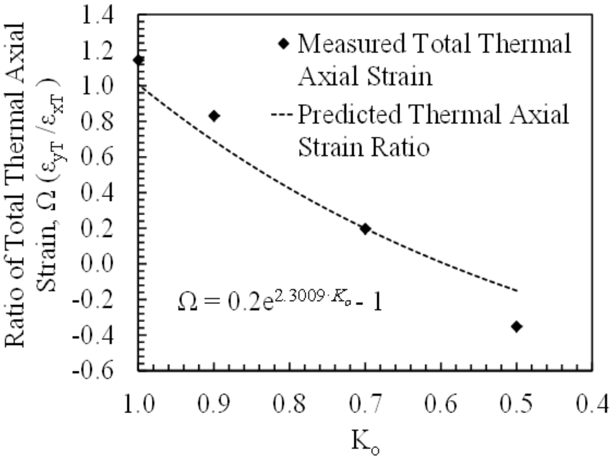

Figure 7.13: Thermal axial strain ratio as a function of stress ratio proposed by Coccia (2011).

As additional information was collected in this study on the effect of anisotropy, this should also be considered in the development of an empirical equation for Ω. In this study, a change in temperature of 27 °C was used for the evaluation of the value of Ω. One difference between the tests in this study and those of Coccia (2011) is that he evaluated the effect of anisotropy on the thermal volume change in only two orthogonal directions x and y. For isotropic conditions, it was assumed that $\sigma_x=\sigma_y$, while for anisotropic conditions it was assumed that $\sigma_x > \sigma_y$. The stress in the z direction was not considered by Coccia (2011). In the current study, principal stresses were applied in all three orthogonal directions. In this case, for isotropic conditions it is assumed that $\sigma_x=\sigma_y=\sigma_z$, while for anisotropic conditions it is assumed that $\sigma_z > \sigma_y = \sigma_x$. Therefore the relationships between the thermal axial strains in the x or y directions compared to the z-direction can be defined as follows:

$$\Omega = \varepsilon_{yT} / \varepsilon_{zT} \tag{7.5}$$

The trend in $\Omega$ observed in the current study for Bonny silt under different stress ratios ($K = \sigma_y/\sigma_z$) and different degrees of saturation is shown in Figure 7.14. This figure also includes the data from Coccia (2011). Although Coccia (2011) observed a nonlinear decreasing trend, the results presented in this study provide a good fit to most of the data except for the strongly negative value of Ω for the saturated specimen. The curve is only shown to a value of K = 0.325, as this is the minimum value of K corresponding to shear failure (corresponding to a friction angle of 33°). The value of Ω for the specimen with K=1 is not equal to 1.0 even though the stress state is isotropic because of inherent anisotropy effects associated with how the specimen was compacted with lifts perpendicular to the z direction.

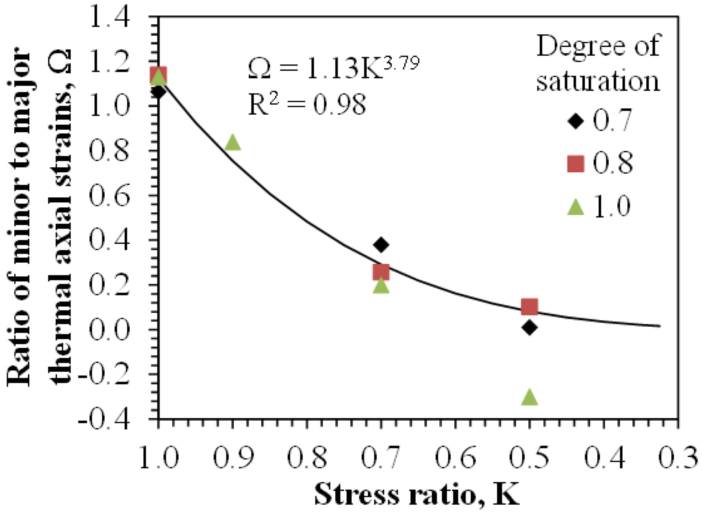

Figure 7.14: Thermal axial strain ratio as a function of stress ratio for Bonny silt with different degrees of saturation proposed in this study.

By dividing Equation 7.3 by $\varepsilon_{zT}$, the thermal volumetric strain can be partitioned into the thermal axial strains as follows:

$$\frac{\varepsilon_{vT}}{\varepsilon_{zT}} = \frac{(\varepsilon_{xT} + \varepsilon_{yT} + \varepsilon_{zT})}{\varepsilon_{zT}} \tag{7.6}$$

Equation 7.6 can be rewritten as follows:

$$\varepsilon_{zT} = \frac{\varepsilon_{vT}}{(\Omega + \Omega + 1)} \tag{7.7}$$

or,

$$\varepsilon_{zT} = \frac{\varepsilon_{vT}}{(2\Omega+1)} \tag{7.8}$$

This equation can be written in differential form as follows:

$$d\varepsilon_{zT} = \frac{d\varepsilon_{vT}}{(2\Omega+1)} \tag{7.9}$$

The thermal axial strain in the y or x directions can be calculated similarly, as follows:

$$d\varepsilon_{yT} = \frac{d\varepsilon_{vT}\Omega}{(2\Omega+1)} \tag{7.10}$$

By incorporating the constitutive equations for the elastic and plastic volumetric strains from the constitutive model of Cui et al. (2000), Equation 7.9 can be rewritten as follows:

$$d\varepsilon_{zT} = \frac{1}{(2\Omega+1)}\left[\alpha_2 dT + \alpha_p\left(\exp\left(\alpha_p \Delta T\right) - a\right)dT\right] \tag{7.11}$$

while Equation 7.10 can be rewritten as follows:

$$d\varepsilon_{yT} = \frac{\Omega}{(2\Omega+1)}\left[\alpha_2 dT + \alpha_p\left(\exp\left(\alpha_p \Delta T\right) - a\right)dT\right] \tag{7.12}$$

where the parameter $\alpha_2$ is the drained coefficient of thermo-elastic expansion of a soil obtained from a cooling test performed at a slow rate, $\alpha_p$ is a parameter that depends on the overconsolidation ratio, a is a shape parameter, ΔT is the total change in temperature (°C), dT is the change between increments in temperature from one step to another (°C). The value of $\alpha_2$ was calculated to be approximately -0.0007/°C from the tests that show contraction during cooling. Cui et al. (2000) noted that $\alpha_p = -\alpha_2/(1-a)$ for normally consolidated soils. In this case, Equation 7.11 can be rewritten as follows:

$$d\varepsilon_{zT} = \frac{1}{(2\Omega+1)}\left[\alpha_2 dT - \frac{\alpha_2}{1-a}\left(\exp\left(-\frac{\alpha_2}{1-a}\Delta T\right) - a\right)dT\right] \tag{7.13}$$

and Equation 7.12 can be rewritten as follows:

$$d\varepsilon_{yT} = \frac{\Omega}{(2\Omega+1)}\left[\alpha_2 dT - \frac{\alpha_2}{1-a}\left(\exp\left(-\frac{\alpha_2}{1-a}\Delta T\right) - a\right)dT\right] \tag{7.14}$$

In addition to the impact of anisotropy, the impact of unsaturated conditions needs to be incorporated into the prediction of the thermal volumetric strain. The thermal axial strain for unsaturated soils was estimated by assuming that the $\alpha_p$ parameter in the model of Cui et al. (2000) is also a function of the degree of saturation. Specifically, Equation 7.13 was updated by modifying the definition of $\alpha_p$ to include the product of a constant parameter b and the effective saturation at the beginning of heating ($S_e = \frac{S_r - S_{r,res}}{1 - S_{r,res}}$), as follows:

$$d\varepsilon_{zT} = \frac{1}{(2\Omega+1)}\left[\alpha_2 dT - \frac{\alpha_2}{bS_e(1-a)}\left(\exp\left(-\frac{\alpha_2}{bS_e(1-a)}\Delta T\right) - a\right)dT\right] \tag{7.15}$$

Similarly the thermal axial strain in the minor stress direction can be calculated as follows:

$$d\varepsilon_{yT} = \frac{\Omega}{(2\Omega+1)}\left[\alpha_2 dT - \frac{\alpha_2}{bS_e(1-a)}\left(\exp\left(-\frac{\alpha_2}{bS_e(1-a)}\Delta T\right) - a\right)dT\right] \tag{7.16}$$

This model assumes that the initial degree of saturation affects the thermal axial strain, and that any potential changes in degree of saturation during heating do not have a major effect on the value of the thermal axial strain. However, this is a topic that requires further study.

A comparison of the measured and simulated thermal axial strains for the specimens with an initial degree of saturation of 0.7 is shown in Figures 7.15(a), 7.145(b), and 7.15(c) for K values of 1.0, 0.7, and 0.5, respectively. A good fit is observed between the model and experimental results for a value of a equal to 0.323 and a value of b equal to 1.95. A plot of the thermal volumetric strains for the same specimens along with the model simulations are shown in Figure 7.16, and a good fit is also observed.

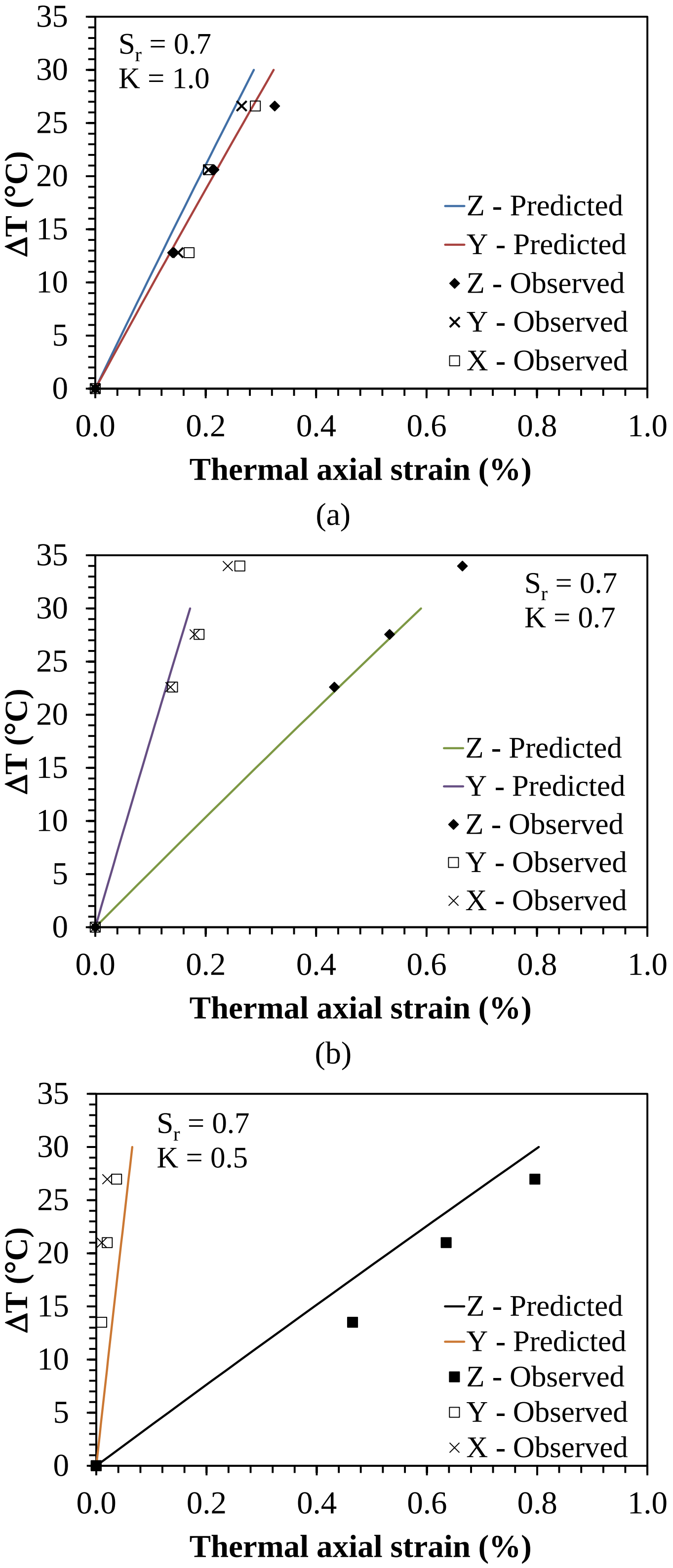

(a)

(b)

(c)

Figure 7.15: Comparison between predicted and observed axial results for the specimens with $S_r$ = 0.7 and different stress ratios: (a) K1.0; (b) K0.7; (c) K0.5.

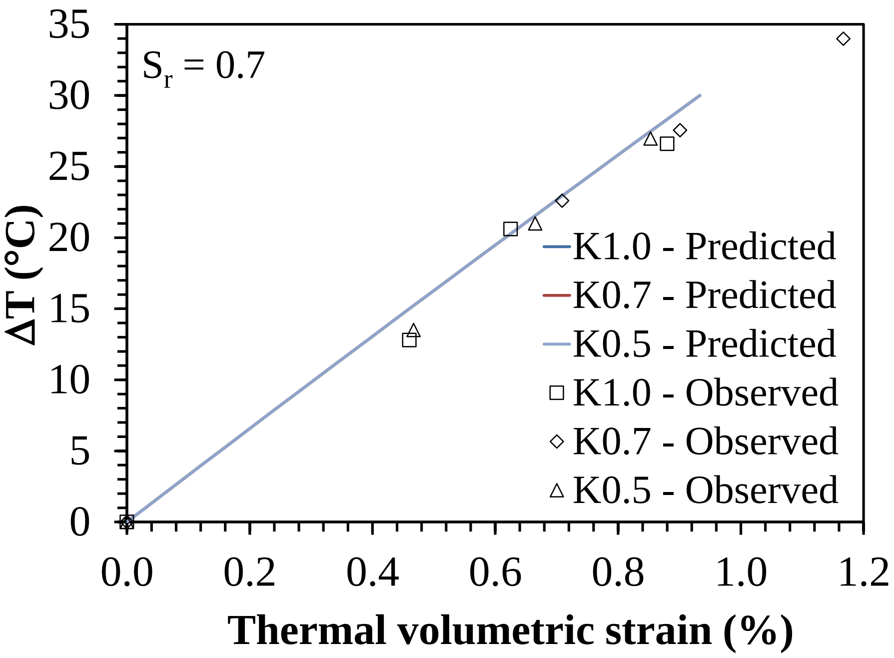

Figure 7.16: Comparison between predicted and observed volumetric results for the specimens with $S_r = 0.7$ and different stress ratios.

Using these same parameters, a comparison between measured and simulated thermal axial strains for the specimens with an initial degree of saturation of 0.8 is shown in Figures 7.17(a), 7.17(b), and 7.17(c) for K values of 1.0, 0.7, and 0.5, respectively. Similar to the comparison for the specimens with a degree of saturation of 0.7, a good match between the experimental thermal axial strains and those of the model is observed. A plot of the thermal volumetric strains for the same specimens along with the model simulations are shown in Figure 7.18. The fit is not as good as to the S = 0.7 data, but the trends in the data are adequately represented.

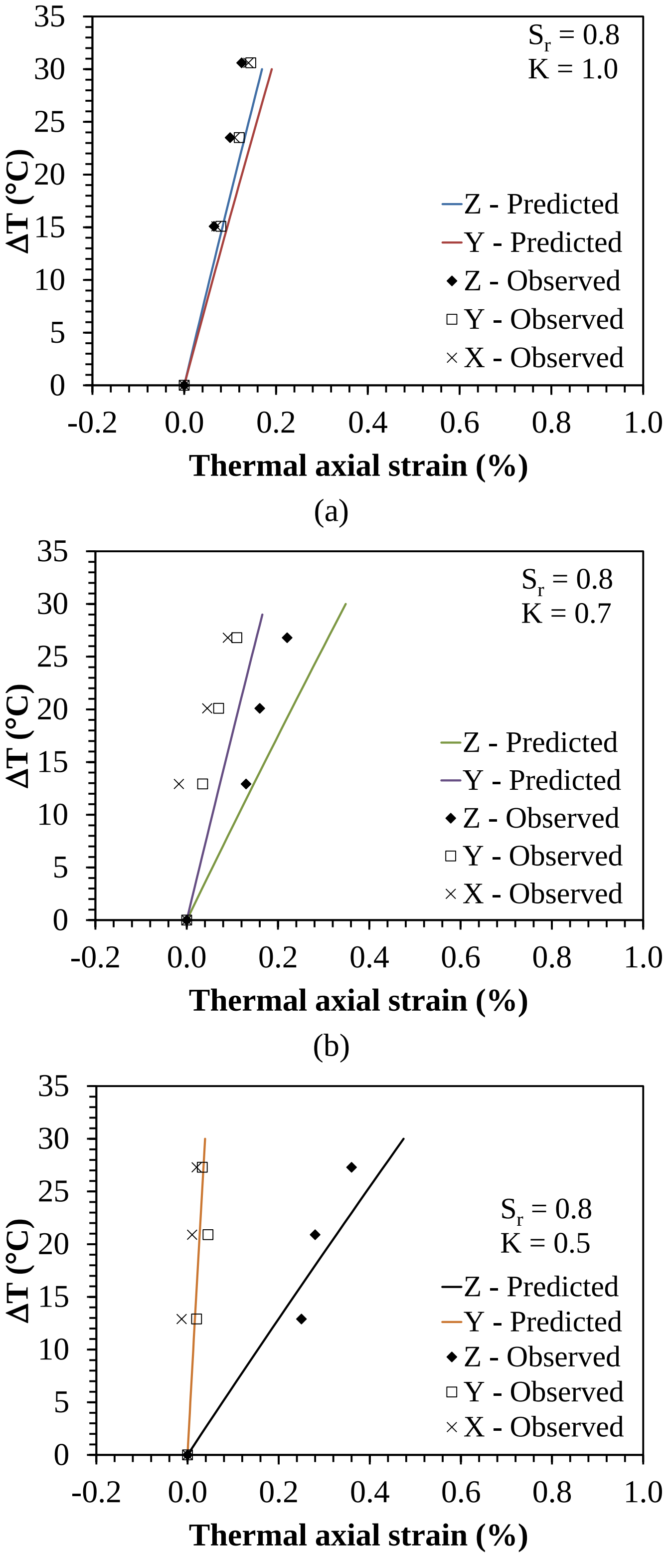

(a)

(b)

(c)

Figure 7.17: Comparison between predicted and observed axial results for the specimens with $S_r$ = 0.8 and different stress ratios: (a) K1.0; (b) K0.7; (c) K0.5.

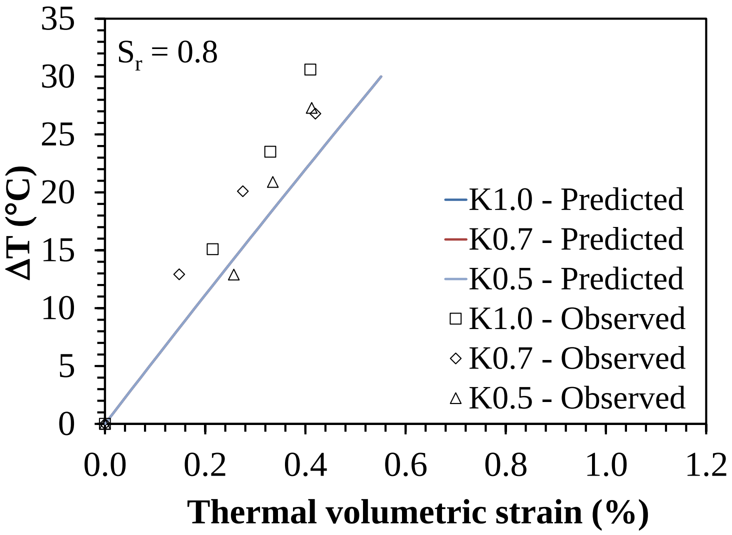

Figure 7.18: Comparison between predicted and observed volumetric results for the specimens with $S_r = 0.8$ and different stress ratios.

Finally, a comparison between the measured and simulated thermal volumetric strains for the specimens from Coccia (2011) with an initial degree of saturation of 1.0 is shown in Figure 7.19. The model predicts a smaller value of thermal volumetric strain than that observed in the results. During selection of the a and b parameters, priority was given to fitting the data with $S_r = 0.7$ and 0.8 because they both had the same stress state and boundary conditions. Nonetheless, the trends in the data is adequately represented.

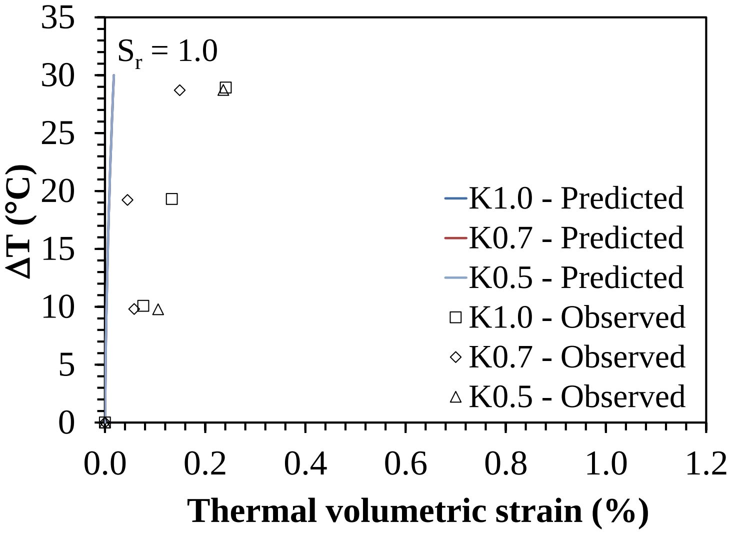

Figure 7.19: Comparison between predicted and observed volumetric results for the specimens with $S_r = 1.0$ and different stress ratios.

Overall, the comparisons shown in this section indicate that the available constitutive relationship of Cui et al. (2000) can be adapted to consider the impact of both stress-induced anisotropy and unsaturated soil conditions in an empirical manner. As the Cui model was developed for saturated soils, it is assumed that the single-value mean effective stress is used to represent the mechanical response of the soil. The calculation of the mean effective stress in unsaturated soils defined by Bishop (1959) is given as follows:

$$p' = p_n + \chi(\psi) \tag{7.17}$$

where p' is the mean effective stress in kPa, $p_n$ is the mean net stress in kPa, $\psi$ is the suction (difference between the pore air and water pressures) in kPa, and $\chi$ is the effective stress parameter. In this study, the effective stress parameter can be assumed equal to the effective saturation ($\chi = S_e$), similar to Lu et al. (2010). As all of the experiments with a given initial degree of saturation performed in this study have the same mean effective stress, the role of the initial effective stress was not considered in the calculations.

## 8. DISCUSSION

The results from this study confirm the importance of considering the role of stress-induced anisotropy in the thermal volume change of soils. Natural soils typically have an inherent stress-induced anisotropy, corresponding to at-rest or $K_0$ conditions. As $K_0$ is typically less than 1, this means that the vertical stress is greater than the horizontal stress. If the soil under this stress state is heated, then different magnitudes of thermal axial strains are expected. The value of K may change more significantly in the case of the installation of an energy pile, which typically involves excavation and a lower K value that is closer to active earth pressure conditions.

When the soil surrounding the energy changes in temperature, irreversible soil volume changes in the soil are expected to occur. If the soil is overconsolidated, it is likely that the soil will expand in both the vertical and horizontal directions elastically. In this case, the thermal volume changes are not expected to be significant. More important changes are expected to occur if the soil is closer to normally consolidated conditions in the vertical direction, in which case contraction would be expected in both the vertical and horizontal directions. The thermal axial strain in the horizontal direction will likely reduce the lateral stress distribution along the energy foundation, and may lead to relative movement due to the existing mechanical stress being transferred from the foundation to the surrounding soil. Further, the thermal axial strain the vertical direction will be greater than that in the horizontal direction, and may lead to dragdown forces on the energy foundation that are superimposed atop any mechanical or thermo-mechanical strains that are predicted to occur using a load-transfer analysis such as that of Knellwolf et al. (2011). Nonetheless, for the soil that was evaluated in this study, the magnitudes of thermal axial strain are all less than 1%, which are relatively small. The only likelihood that these thermal axial strains will affect the performance of the foundation would be if it were heavily loaded close to its ultimate capacity.

The empirical model of Cui et al. (2000) was adapted in this study to consider the effects of stress-induced anisotropy as well as to include the impacts of unsaturated conditions. This model is simple to use in the fact that it can predict the thermal axial strains for a given change in soil temperature. In this case, a finite element model may be used to predict the change in temperature of the soil as a function of space and time using a transient conduction analysis. After this, the model can be used to estimate the thermal axial strains in a de-coupled manner (assuming the thermal axial strains are just due to changes in temperature and are independent of the mechanical stresses). These strains would have to be superimposed on top of a mechanical stress-strain analysis to see if mechanical changes in piles behavior would be expected.

Regarding the role of unsaturated conditions, this study indicates that this is an important variable to consider. Different trends in the magnitude of thermal volume change were observed for the soil tested in this study than in previous studies such as Uchaipichat and Khalili (2009). Nonetheless, the tests in this previous study underwent undrained heating and cooling cycles and several different loading and unloading cycles before heating, which may have had a cumulative effect on the results. A mechanism for the increasing trend in thermal volume change with decreasing thermal volume change was not explicitly proposed in this study due to the relatively limited number of specimens with different degrees of saturation, although this behavior may be due to the collapse of air voids during drained heating. The role of unsaturated conditions was considered empirically in the thermal volume change model using the b parameter, which needs to be more verified through further testing of different soils.

# 9. CONCLUSION

This study involved the development of a thermo-hydro-mechanical true triaxial cell which is capable of measuring the thermal deformations of unsaturated soils under various anisotropic stress states. In addition to calibrating and characterizing the response of the true-triaxial cell, several experiments were performed on specimens having different minor to major stress ratios and to different initial degrees of saturation. The specimens were all loaded to normally consolidated conditions isotropically before application of the different anisotropic stress states. The major conclusions that can be drawn from the evaluation of the results from these test include:

- The thermally-induced axial strains during heating for all tests showed contractile behavior, regardless of the stress state and the initial degree of saturation. Soils with lower initial degrees of saturation exhibited greater thermal volume change than those with higher initial degrees of saturation. Thermally-induced axial strains during cooling for all tests showed that the behavior of soil specimen was not recoverable.
- The plastic thermal contraction trends observed in this study are consistent with those published in the literature with respect to the overconsolidation ratio (OCR).
- With decreasing values of stress ratio K, the thermal axial strains in the major stress direction (z) were observed to increase, while the thermal axial strains in the minor stress directions (x, y) are observed to decrease. However, for isotropic conditions (K = 1), was slightly greater in the x and y directions than in the z directions even though the stresses were the same. This was attributed to the effects of inherent anisotropy associated with how the specimens evaluated in this study were compacted.

- Consistent with the observations of tests on saturated Bonny silt specimens reported by Coccia and McCartney (2012), the thermal volumetric strains were relatively similar regardless of the stress ratio K. This indicates that anisotropy may lead to different thermal deformations in different directions but the same overall volumetric response.
- Specimens with a lower initial degree of saturation were observed to show greater thermal axial strains. The trends with degree of saturation for the unsaturated specimens evaluated in this study are consistent with the saturated specimens evaluated by Coccia and McCartney (2012).
- The trends with degree of saturation differed from that of Uchaipichat and Khalili (2009), who observed a very slight decrease in thermal volume strain with decreasing degree of saturation. However, their tests involved application of multiple loading stages and undrained heating and cooling cycles before the drained heating tests.
- An empirical model based on the elasto-plastic model of Cui et al. (2000) that was originally developed for saturated soil was adapted to fit the trends in the experimental data observed in this study. This model employs a relationship between the anisotropy in thermal axial strains and the stress ratio was developed that appears to be insensitive to the degree of saturation. The adapted model is capable of considering the effects of stress-induced anisotropy, as well as the impacts of unsaturated conditions. The model shows a good prediction of the observed thermal axial strain trends for different degrees of saturation. The parameters governing the impact of the stress-induced anisotropy may be more reliable than the parameters governing the impact of the degree of saturation.

## REFERENCES

Abuel-Naga, H. M., Bergado, D. T., Bouazza, A. and Ramana, G. V. (2007). "Volume change behavior of saturated clays under drained heating conditions: experimental results and constitutive modeling." Canadian Geotechnical Journal. 44(8), 942-956.

Abuel-Naga, H.M., Bergado, D.T., Bouazza, A., and Pender, M. (2009). "Thermomechanical model for saturated clays." Géotechnique, 59(3), 273–278.

Adam, D. and Markiewicz, R. (2009). "Energy from earth-coupled structures, foundations, tunnels and sewers," Géotechnique. 59(3), 229–236.

Alsherif, N.A. and McCartney, J.S. (2015). "Nonisothermal behavior of compacted silt at low degrees of saturation." Géotechnique. DOI: 10.1680/geot./14-P-049.

Baldi, G., Hueckel, T. and Pelegrini, R. (1988). "Thermal volume changes of the mineral-water system in low-porosity clay soils." Canadian Geotechnical Journal. 25, 807-825.

Bishop, A.W. (1959). "The principle of effective stress," Teknisk Ukeblad I Samarbeide Med Teknikk, Oslo, Norway, 106(39), 859–863.

Boudali, M., Leroueil, S. and Murthy, B.R.S. (1994). "Viscous Behaviour of Natural Clays". *In Proceedings of the 13th International Conference on Soil Mechanics and Foundation* Engineering. New Delhi. January 5-10. 1: 411–416.

Brandl, H. (2006). "Energy foundations and other thermo-active ground structures." Géotechnique. 56(2), 81-122.

Burghignoli A., Desideri A., and Miliziano S. (2000). "A laboratory study on the thermomechanical behaviour of clayey soils." Canadian Geotechnical Journal. 37: 764-780.

Campanella, R.G. and Mitchell, J.K. (1968). "Influence of temperature variations on soil behavior." Journal of the Soil Mechanics and Foundation Engineering Division. 94(3), 709–734.

Cekerevac, C. and Laloui, L. (2004). "Experimental study of thermal effects on the mechanical behaviour of a clay." International Journal of Numerical and Analytical Methods in Geomechanics. 28(3), 209–228.

Coccia, C.J.R. and McCartney, J.S. (2012). "A thermo-hydro-mechanical true triaxial cell for evaluation of the impact of anisotropy on thermally induced volume changes in soils." Geotechnical Testing Journal. 35(2), 1-11.

Cui, Y.J., Sultan, N., and Delage, P. (2000). "A thermomechanical model for clays." Canadian Geotechnical Journal, 37(3), 607–620.

Delage, P., Sultan, N., and Cui, Y.J. (2000). "The thermal consolidation of Boom Clay," Canadian Geotechnical Journal. 37, 343-354.

Delage, P., Romero, E., Tarantino, A. (2008). "Recent developments of controlling and measuring suction in unsaturated soils." Proceedings of the 1st European Conference on Unsaturated Soils, Durham, 33-52.

Demars, K.R. and Charles, R.D. (1982). "Soil volume changes induced by temperature cycling." Canadian Geotechnical Journal. 19, 188–194.

Eriksson, L.G. (1989). "Temperature effects on consolidation properties of sulphide clays." In Proceedings of the 12th International Conference on Soil Mechanics and Foundation Engineering. Rio de Janeiro. August 13-18. 12: 2087-2090.

Francois, B. Salager, S., El Youssoufi, M.S., Ubals Picanyoul, D., Laloui, L., and Saix, C. (2007). “Compression tests on a sandy silt at different suction and temperature levels.” GSP 157: Computer Applications in Geotechnical Engineering. 1-10.

Fredlund, D.G. and Morgenstern, N.R. (1977). “Stress state variables for unsaturated soils.” ABB Rev., 103(5), 447–466.

Gallipoli, D., Gens, A., Sharma, R., Vaunat, J., (2003). “An elasto-plastic model for unsaturated soil incorporating the effects of suction and degree of saturation on mechanical behavior.” Géotechnique. 53(1), 123–135.

Grant, S.A. and Salehzadeh, A. (1996). “Calculations of temperature- effects on wetting coefficients of porous solids and their capillary pressure functions.” Water Resources Research. 32, 261–279.

Hilf, J.W. (1956). An Investigation of Pore-water Pressure in Compacted Cohesive Soils. Technical Memo No.654, United States Bureau of Reclamation, Denver.

Hoyos, L.R. and Macari, E.J. (2001). “Development of a stress/suction-controlled true triaxial testing device for unsaturated soils.” Geotechnical Testing Journal. 24(1), 5-13.

Hoyos, L. R., Laikram, A., and Puppala, A. J. (2008). “A novel suction controlled true triaxial apparatus for unsaturated soils.” Chapter 5, Unsaturated Soils: Advances in Geo-engineering. D.G. Toll, C.E. Augarde, D. Gallipoli and S.J. Wheeler, eds., CRC, London, 83–88.

Hoyos, L.R., Pērez-Ruiz, D.D. and Puppala, A.J. (2012). ”Refined true triaxial apparatus for testing unsaturated soil under suction controlled stress path.” International Journal of Geomechanics, 12(3), 281–291.

Hueckel, T. and Baldi, M. (1990). “Thermoplasticity of saturated clays: experimental constitutive study.” Journal of Geotechnical Engineering, 116(12), 1778–1796.

Hueckel, T. and Borsetto, M. (1990). “Thermoplasticity of saturated soils and shales: Constitutive equations.” Journal of Geotechnical Engineering. 116(12), 1765-1777.

Hueckel, T., Pellegrini, R., and Olmo, C.D., (1998). “A constitutive study of thermo-elasto-plasticity of deep carbonatic clays.” International Journal for Numerical and Analytical Methods in Geomechanics. 22, 549-574.

Khalili, N. and Khabbaz, M.H. (1998). “A unique relationship for v for the determination of the shear strength of unsaturated soils.” Géotechnique. 48(5), 681–687.

Khalili, N. and Zargarbashi, S. (2010). “Influence of hydraulic hysteresis on effective stress in unsaturated soils.” Géotechnique. 60(9), 729–734.

Khosravi, A. and McCartney, J.S. (2012). “Impact of hydraulic hysteresis on the small-strain shear modulus of unsaturated soils.” ASCE Journal of Geotechnical and Geoenvironmental Engineering. 138(11), 1326–1333.

Knellwolf, C., Peron, H., and Laloui, L. (2011). “Geotechnical analysis of heat exchanger piles.” ASCE Journal of Geotechnical and Geoenvironmental Engineering. 137(12), 890-902.

Ko, H.Y., and Scott, R.F. (1967). “A new soil testing apparatus.” Géotechnique. 17(1), 40-57.

Laloui, L. and Cekerevac, C. (2003). “Thermo-plasticity of clays: an isotropic yield mechanism.” Computers and Geotechnics. 30(8), 649–660.

Laloui, L., Nuth, M., and Vulliet, L. (2006). “Experimental and numerical investigations of the behavior of a heat exchanger pile.” International Journal of Numerical and Analytical Methods in Geomechanics. 30(8), 763-781.

Lloret, A., Villar, M.V., Sanchez, M., Gens, A., Pintado, X., Alonso, E.E. (2003). “Mechanical behaviour of heavily compacted bentonite under high suction changes.” Géotechnique. 53(1), 27-40.

Lu, N., Godt, J., Wu, D. (2010). “A closed-form equation for effective stress in unsaturated soil.” Water Resources Research. 46, W05515.

Lu, N. and Likos, W. (2006). “Suction stress characteristic curve for unsaturated soil.” Journal of Geotechnical Geoenvironmental Engineering. 132(2), 131-142.

McCartney, J.S. (2011). “Engineering performance of energy foundations.” Invited Theme Paper. 2011 PanAm CGS Geotechnical Conference. Canadian Geotechnical Society. Toronto. Oct. 2-6. 1-14.

McCartney, J.S. (2012). “Issues involved in using temperature to improve the mechanical behavior of unsaturated soils.” Unsaturated Soils, Theory and Practice 2011: Proceedings of 5th Asia-Pacific Unsaturated Soils Conference. A. Jotisankasa, A. Sawangsuriya, S. Soralump and W. Mairaing, eds. Kasetsaert University, Thailand. pp. 509-514.

McCartney, J.S., Jensen, E., and Counts, B. (2013). “Measurement of the impact of volume change on thermal conductivity of subgrade soils.” TRB 2013. Washington, DC. January 13-17, 2013.

McCartney, J.S. and Murphy, K.D. (2012). “Strain distributions in full-scale energy foundations.” DFI Journal. 6(2), 28-36.

Matyas, E.L. and Radhakrishna, H.S. (1968). “Volume change characteristics of partially saturated soils.” Géotechnique. 18(4), 432–448.

Mould, J.C. (1983), Stress Induced Anisotropy in Sand and the Evaluation of a Multi-Surface Elasto-Plastic Material Model. Ph.D. Thesis, Univ. of Colorado.

Murphy, K.D. and McCartney, J.S. (2015). “Seasonal response of energy foundations during building operation.” Geotechnical and Geological Engineering. 33(2), 343-356.

Murphy, K.D., McCartney, J.S., and Henry, K.S. (2015). “Thermo-mechanical response tests on energy foundations with different heat exchanger configurations.” Acta Geotechnica. 10(2), 179-195.

Nuth, M. and Laloui, L. (2008). “Effective stress concept in unsaturated soils: Clarification and validation of a unified framework.” International Journal for Numerical and Analytical Methods in Geomechanics. 32, 771–801.

Plum, R.L. and Esrig, M.I. (1969). “Some temperature effects on soil compressibility and pore water pressure.” Effects of Temperature and Heat on Engineering Behavior of Soils. Highway Research Board. Washington, DC. 103: 231–242.

Romero, E. (1999). Characterisation and Thermo-hydro-mechanical Behaviour of Unsaturated Boom Clay: an Experimental Study. Thése de l’Université Polytechnique de Catalogne, Barcelone. 405 pg.

Romero, E., Gens, A., Lloret, A. (2003). “Suction effects on a compacted clay under non-isothermal conditions.” Géotechnique. 53(1), 65–81.

Salager, S., El Youssoufi, M.S., and Saix, C. (2007). "Influence of temperature on the water retention curve of soils: Modelling and experiments." Experimental Unsaturated Soil Mechanics. Schanz, T. ed. pp. 251-258.

She, H.Y. and Sleep, B.E. (1998). "The effect of temperature on capillary pressure-saturation relationships for air-water and perchloroethylene-water systems." Water Resources Research, 34(10), 2587–2597, doi:10.1029/98WR01199.

Sultan, N. (1997). Etude du Comportement Thermo-mécanique de l'Argile de Boom: Experiences et Modélisation. Ph.D. thesis, Ecole Nationale des Ponts et Chaussées, Paris.

Sultan, N., Delage, P. and Cui, Y.J. (2002). "Temperature effects on the volume change behavior of boom clay." Engineering Geology. 64, 135-145.

Tamagnini, R. (2004). "An extended cam-clay model for unsaturated soils with hydraulic hysteresis." Géotechnique. 54(3), 223–228.

Tang, A.M. and Cui, Y.J. (2005). "Controlling suction by the vapour equilibrium technique at different temperatures and its application in determining the water retention properties of MX80 clay." Canadian Geotechnical Journal, 42(1), 287-296.

Tang, A.M., Cui, Y.J. and Barnel, N. (2008). "Thermo-mechanical behavior of a compacted swelling clay." Géotechnique. 58(1), 45-54.

Takata, S. (2000). Upgrade of a Large Scale True Triaxial Apparatus for Shear Strength Characterization." Master Thesis, University of Colorado.

Tidfors, M. and Sällfors, G. (1989). "Temperature effect on preconsolidation stress." Geotechnical Testing Journal. 12(1), 93-97.

Towhata, I., Kuntiwattanakul, P., Seko, I. and Ohishi, K. (1993). “Volume change of clays induced by heating as observed in consolidation tests.” Soils and Foundations. 33(4), 170-183.

Uchaipichat, A. and Khalili, N. (2009). “Experimental investigation of thermo-hydro-mechanical behaviour of unsaturated silt.” Géotechnique, 59(4), 339-353.

Vanapalli, S.K., Fredlund, D.G., and Pufahl, D.E. (1996). “The relationship between the soil-water characteristic curve and the shear strength of a compacted glacial till,” Geotechnical Testing Journal, 19(3), 259–268.

van Genuchten, M.T. (1980). “A closed-form equation for predicting the hydraulic conductivity of unsaturated soils,” Soil Sci. Soc. Am. J. 44, 892–898.

Vega, A. and McCartney, J.S. (2014). “Cyclic heating effects on thermal volume change of silt.” Environmental Geotechnics. 1-12. doi.org/10.1680/envgeo.13.00022.

Villar, M.V. (2000). Caracterización Termo-hidro-mecánica Deuna Bentonita de Cabo de Gata. Ph.D. Thesis, Universidad Complutense de Madrid, Madrid, Spain.

Wheeler, S.J., Sharma, R.S., and Buisson, M.S.R. (2003). “Coupling of hydraulic hysteresis and stress–strain behaviour in unsaturated soils,” Géotechnique, 53(1), 41-54.